Development Of A High Throughput Facility For The RF Characterisation Of Superconducting Thin Films

Daniel Seal, MPhys (Hons)

Engineering Department

Lancaster University

A thesis submitted for the degree of

Doctor of Philosophy

December 2025

This thesis is dedicated to my parents — to my Mum, for her constant encouragement and support, and to my Dad, whose memory has been a guiding presence throughout my studies.

Development Of A High Throughput Facility For The RF Characterisation Of Superconducting Thin Films

Daniel Seal, MPhys (Hons).

Engineering Department, Lancaster University

A thesis submitted for the degree of *Doctor of Philosophy*. December, 2025

Abstract

Superconducting radio frequency cavities are used in particle accelerators because they can accelerate charged particles efficiently with high duty cycle or continuous wave operation. For more than 60 years, bulk niobium has been the material of choice for these cavities; however, these require large capital and operational costs and now perform close to their theoretical limits. With future accelerators requiring more sustainable technology, an alternative approach using thin film superconductors deposited on copper cavities is being explored. This would allow significant capital savings, and the use of alternative materials, such as Nb_3Sn, NbTiN, V_3Si, offer the potential for higher temperature operation and accelerating gradients that exceed Nb.

The development of thin film coatings on full-sized cavities is expensive and time-consuming. Therefore, optimising deposition parameters in cavities alone is not viable. Instead, thin film optimisation should be performed on planar samples, which are quicker, easier and cheaper to develop. For this, quick measurements of the superconducting properties is vital. Most importantly, measurements of the RF properties of samples, such as surface resistance, are vital to predict the RF performance before cavity depositions.

A handful of dedicated RF test facilities have been designed around the world; however, many offer a slow sample turnover rate. In order to speed up the rate of thin film development, a new RF facility was developed and commissioned using a unique 7.8 GHz Choke Cavity design. A simple sample mounting procedure and

low-effort operation allow for RF measurements of up to three samples per week in this facility, thus providing an important tool in the multi-parameter optimisation process of thin films. It is capable of testing samples $90 - 130\,\mathrm{mm}$ in diameter to measure the average surface resistance as a function of either sample temperature or peak sample magnetic field.

This work presents details of the Choke Cavity and simulations that demonstrate its operation. The design and operation of the cryogenic facility are then presented with details of a sample workflow from substrate preparation and deposition to RF testing. Measurements of bulk Nb and thin film Nb on Cu samples were performed to commission the system and demonstrate the capabilities of the system. This demonstrated the ability to measure surface resistance at temperatures in the range $4 - 20\,\mathrm{K}$ and sample peak magnetic fields up to $3\,\mathrm{mT}$, with a minimum resolvable surface resistance of $\sim 0.1\,\mu\Omega$ and typical uncertainties of $\approx 14\%$.

Additional studies, with further superconducting measurements and surface analysis, have been performed with Nb and Nb_3Sn thin films on Cu to demonstrate how the system can be used to optimise deposition parameters. For samples produced at Daresbury Laboratory, the Nb/Cu study demonstrated optimal RF performance can be achieved for a deposition temperature of $530\,^{\circ}\mathrm{C}$, whilst the RF performance for the Nb_3Sn/Cu samples is optimal for lower magnetron powers down to $50\,\mathrm{W}$. In addition, samples deposited with a Nb_3Sn-Nb-Cu bilayer showed a decrease in RF performance compared with the single layer Nb_3Sn.

Acknowledgements

Firstly, I wish to thank Prof Graeme Burt for giving me the opportunity to undertake this work as well as providing excellent supervision and support throughout. I also thank Dr Oleg Malyshev for daily supervision at the lab and invaluable help with cryogenics and vacuum.

I would also like to thank other current and former members of the Daresbury Laboratory thin film research group as well as the many staff and students who helped make this an enjoyable experience. In particular, Dr Reza Valizadeh for providing thin film samples and surface analysis. Dr Philippe Goudket for invaluable support and knowledge on RF and the Choke Cavity. Dr Taaj Sian for support with the Choke Cavity facility during the early development stages. James Conlon for his invaluable technician support - the many hours of overtime for sample loading and switching off sample depositions were much appreciated. Liam Smith for his regular support in the cryolab. Dr Dan Turner for his support in the cryolab during my first couple of years. Dr Chris Benjamin for providing SEM images and XPS analysis.

I wish to acknowledge the support received by other members of the Cockcroft Institute and STFC. Tony Palmer, Andrew Wootten, Patrick McGuinness and James Gawthorpe in the electronics group for providing many cables and circuit boards. Steve Bibby-Trevor, Ray McAllister and Will Marshall in the Engineering Technology Centre workshop providing many key components of the Choke Cavity facility. Katy Clarke and her team in the vacuum processing laboratory for cleaning of components. Katie Morrow and Mark Roper for support with the WLI. Dr Gavin Stenning for training and support on the MPMS3 at RAL.

Outside of the lab, I would also like to thank colleagues in the IFAST collaboration. Dr Cristian Pira, Dr Eduard Chyhyrynets, Davide Ford and Alessandro Salmaso at INFN for providing chemical treatments of the Choke Cavity and sample disks. Dr Eugen Seiler and Dr Ratislav Ries at IEE for providing VSM sample measurements. Dr Oleksandr Hryhorenko and Dr David Longuevergne at

IJCLab for metallographic polishing of sample disks. Also, thanks to Prof Gianluigi Ciovati at ODU for providing the WinSuperFit code.

I would like to thank family and close friends for your support during this time. You all made the last few years extremely enjoyable. In particular, many thanks to my friends at UMHC. Hiking and climbing provided the perfect balance during my PhD and I am proud to have been your vice-chair and weekends secretary during this time.

Above all, my biggest thanks is to my Mum for her unwavering help and support throughout my scientific career to date, and to the memory of my Dad, whose influence and encouragement continue to inspire me.

Declaration

I declare that the work presented in this thesis is, to the best of my knowledge and belief, original and my own work. The material has not been submitted, either in whole or in part, for a degree at this, or any other university. This thesis does not exceed the maximum permitted word length of 80,000 words including appendices and footnotes, but excluding the bibliography. A rough estimate of the word count is: 63878

Daniel Seal

Publications

One publication, shown below, has been created directly from the thesis, from which large portions of this published work is used within chapters 4, 5, 6:

D. Seal, O. B. Malyshev, P. Goudket, et al. "A high throughput facility for the RF characterisation of planar superconducting thin films". In: *Superconductor Science and Technology* 37.11 (Oct. 2024), p. 115012. DOI: 10.1088/1361-6668/ad7643

The following proceedings have been generated while developing the thesis, which are either wholly the authors own work or that which the author contributed to:

D. Seal, C. Benjamin, O. B. Malyshev, et al. "Upgraded multiprobe sample inserts for thin film SRF cavity developments". In: *Proc. 15th International Particle Accelerator Conference (IPAC '24)* (Nashville, TN, USA). May 2024, pp. 2775–2778. DOI: 10.18429/JACoW-IPAC2024-WEPS38

C. Benjamin, R. Valizadeh, D. Seal, et al. "V_3Si: an alternative thin film material for superconducting RF cavities". In: *Proc. 15th International Particle Accelerator Conference (IPAC'24)* (Nashville, TN, USA). May 2024, pp. 2779–2781. DOI: 10.18429/JACoW-IPAC2024-WEPS39

D. Seal, G. Burt, J. A. Conlon, et al. "Optimisation of Niobium Thin Film Deposition Parameters for SRF Cavities". In: *Proc. 21st International Conference on RF Superconductivity (SRF'23)* (Grand Rapids, MI, USA). June 2023, pp. 253–258. DOI: 10.18429/JACoW-SRF2023-MOPMB062

N. Leicester, G. Burt, D. Seal, et al. "Development and testing of split 6 GHz cavities with niobium coatings". In: *Proc. 21st International Conference on RF Superconductivity (SRF '23)* (Grand Rapids, MI, USA). June 2023, pp. 51–55. DOI:

10.18429/JACoW-SRF2023-MOPMB001

C. Benjamin, G. Burt, D. Seal, et al. “Deposition and Characterisation of V_3Si Films for SRF Applications”. In: *Proc. 21st International Conference on RF Superconductivity (SRF'23)* (Grand Rapids, MI, USA). Sept. 2023, pp. 84–87. DOI: 10.18429/JACoW-SRF2023-MOPMB011

C. Pira, O. Azzolini, D. Seal, et al. “Progress in European Thin Film Activities”. In: *Proc. 21st International Conference on RF Superconductivity (SRF'23)* (Grand Rapids, MI, USA). June 2023, pp. 607–614. DOI: 10.18429/JACoW-SRF2023-WECAA01

D. Seal, C. Benjamin, G. Burt, et al. “Characterisation Facilities For Evaluating Superconducting Thin Films For SRF Cavities”. In: *Proc. 14th International Particle Accelerator Conference (IPAC'23)* (Venice, Italy). May 2023, pp. 2983–2986. DOI: 10.18429/JACoW-IPAC2023-WEPA141

T. Sian, J. Conlon, D. Seal, et al. “Split 6 GHz SRF thin film cavities”. In: *Proc. 14th International Particle Accelerator Conference (IPAC '23)* (Venice, Italy). May 2023, pp. 3074–3077. DOI: 10.18429/JACoW-IPAC2023-WEPA185

C. Benjamin, R. Valizadeh, D. Seal, et al. “V_3Si Thin Films for SRF Applications”. In: *Proc. 14th Internation Particle Accelerator Conference (IPAC'23)* (Venice, Italy). Sept. 2023, pp. 3071–3073. DOI: 10.18429/JACoW-IPAC2023-WEPA184

T. Sian, G. Burt, D. Seal, et al. “Split thin film SRF 6 GHz cavities”. In: *Proc. 31st International Linear Accelerator Conference (LINAC '22)* (Liverpool, UK). Sept. 2022, pp. 814–817. DOI: 10.18429/JACoW-LINAC2022-THP0GE09

D. Seal, O. B. Malyshev, R. Valizadeh, et al. "RF Characterisation of Bulk Niobium and Thin Film Coated Planar Samples at 7.8 GHz". In: *Proc. 31st International Linear Accelerator Conference (LINAC '22)* (Liverpool, UK). Sept. 2022, pp. 818–821. DOI: 10.18429/JACoW-LINAC2022-THPOGE10

C. Z. Antoine, S. Berry, D. Seal, et al. "Thin Film Activities in the IFAST Program". In: *Proc. 65th ICFA Adv. Beam Dyn. Workshop High Luminosity Circular e e Colliders (eeFACT2022)* (Frascati, Italy). Sept. 2022, pp. 818–821. DOI: 10.18429/JACoW-eeFACT2022-WEYAS0104

D. Seal, T. Sian, O. B. Malyshev, et al. "First RF Measurements of Planar SRF Thin Films with a High Throughput Test Facility at Daresbury Laboratory". In: *Proc. 13th International Particle Accelerator Conference (IPAC'22)* (Bangkok, Thailand). June 2022, pp. 1283–1286. DOI: 10.18429/JACoW-IPAC2022-TUPOTK033

O. B. Malyshev, P. Goudket, D. Seal, et al. "Main Highlights of ARIES WP15 Collaboration". In: *Proc. 20th International Conference on RF Superconductivity (SRF'21)* (East Lansing, MI, USA). June 2021, p. 571. DOI: 10.18429/JACoW-SRF2021-WEPFDV007

D. Seal, T. Sian, O. B. Malyshev, et al. "A Low Power Test Facility for SRF Thin Film Testing with High Sample Throughput Rate". In: *Proc. 20th International Conference on RF Superconductivity (SRF'21)* (East Lansing, MI, USA). June 2021, p. 100. DOI: 10.18429/JACoW-SRF2021-SUPFDV016

R. Valizadeh, A. Hannah, D. Seal, et al. "Synthesis of Nb and Alternative Superconducting Film to Nb for SRF Cavity as Single Layer". In: *Proc. 20th International Conference on RF Superconductivity (SRF'21)* (East Lansing, MI, USA). 20. June 2022, p. 893. DOI: 10.18429/JACoW-SRF2021-FROFDV06

Contents

List of Tables

List of Figures

Chapter 1

Introduction

1.1 Particle Acceleration

Particle accelerators are machines that use electromagnetic fields to propel charged particle beams to very high energies. Such machines have existed for almost 100 years [18]. Today, these are found all over the world in industries such as healthcare (e.g., cancer treatment and sterilisation) [19] and security (e.g., cargo scanning) [20]. However, for most people, the idea of particle acceleration is commonly associated with large-scale particle colliders, such as the Large Hadron Collider (LHC) at CERN [21]. Despite the different shapes and sizes of these machines and their different applications, they all typically have the same basic structure: a particle source, a method of controlling the particle path, and a method of accelerating and transferring energy to the particles. For particle acceleration, electric fields are required. These can be produced electrostatically or electrodynamically. UK-based examples of both types of accelerator are shown in Figure 1.1.

Electrostatic accelerators use direct current (DC) electric fields to accelerate particles under high voltage potentials. This formed the basis for the early particle accelerators. It is based on the concept of a capacitor, which is made up of two electrodes separated by a dielectric or vacuum. A potential difference applied across the gap will accelerate charged particles between them toward the oppositely

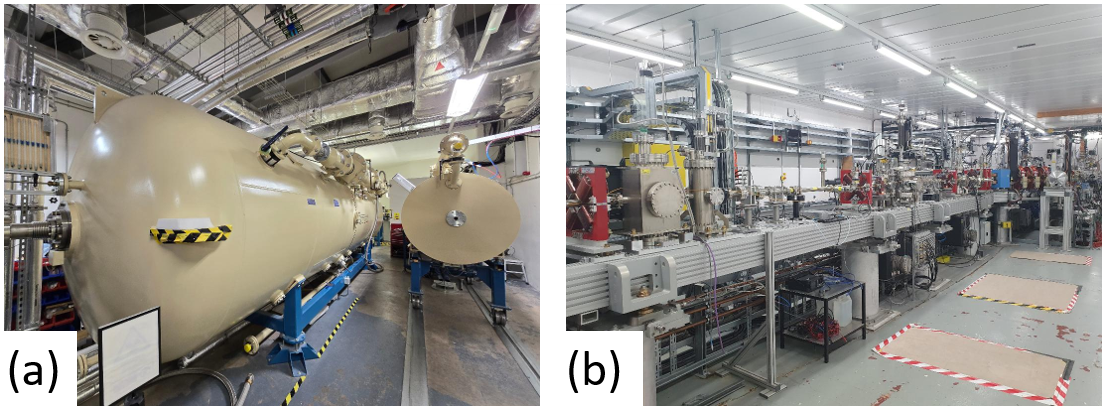

Figure 1.1: Examples of accelerators in the UK: (a) the 5 MV tandem pelletron at the Dalton Cumbrian Facility (electrostatic), (b) CLARA at Daresbury Laboratory (electrodynamic).

charged electrode. The particles will gain an energy proportional to the voltage applied. The first particle accelerators used this concept, dating back to 1897 with the invention of the cathode ray tube by Ferdinand Braun [22]. In the 20th century, other electrostatic accelerators were invented, including the Van de Graaff generator (by Robert J. Van de Graaff in 1929) [23] and the Cockcroft-Walton generator (by John Douglas Cockcroft and Ernest Thomas Sinton Walton in 1932) [24]. However, these machines are limited to around $20 - 30$ MV due to electrical breakdown at high voltages. The Nuclear Structure Facility (NSF) at Daresbury Laboratory, for example, was regularly operated at 20 MV during operation from 1983 to 1992 [25]. Despite this limitation, because these machines are simple and low-cost, they are still widely used today in research and industry, e.g., X-ray machines, and other applications that require up to MeV energy beams. An example of an electrostatic accelerator used today is a 5 MV tandem pelletron used to accelerate ion beams at the Dalton Cumbrian Facility, shown in Figure 1.1(a).

To exceed the maximum voltage limitations of these electrostatic machines, electrodynamic accelerators were developed. These use time-varying electromagnetic (or electrodynamic) fields to generate the electric fields required for acceleration.

The most common type of electrodynamic accelerator is the radio frequency (RF) accelerator. These utilise alternating electric fields generated in closed, hollow metallic structures excited by oscillating RF fields. These are known as RF cavities. The first RF accelerator was a linear accelerator (LINAC) developed by Rolf Wideröe in 1928 [26]. An example of a LINAC used today is shown in Figure 1.1(b). This is the Compact Linear Accelerator for Research and Applications (CLARA) at Daresbury Laboratory. It uses copper (Cu) RF cavities to accelerate electrons up to 250 MeV [27].

In addition to LINACs, circular accelerators were also developed in the 1920s, starting with the development of the cyclotron in 1929 by Ernest Lawrence [28]. Later, in the 1940s, another type of circular accelerator was developed to achieve even higher energies by accelerating particle beams in fixed circular paths. This became known as the synchrotron. The synchrotron principle was invented by Vladimir Veksler in 1944 [29], whilst Edwin McMillan built the first electron synchrotron in 1945 [30]. This later resulted in the development of high-energy colliders, such as the LHC, that are at the forefront of modern-day high-energy particle physics.

Scientists soon realised that bending charged particles travelling close to the speed of light produces high-intensity photons, which became known as synchrotron radiation. This synchrotron light was first harnessed in 1956 by Diran Tomboulian and Paul Hartman for X-ray spectroscopy using a 320 MeV electron synchrotron at Cornell University (a first-generation light source) [31]. The first dedicated X-ray synchrotron light source (a second-generation light source) was the Synchrotron Radiation Source (SRS) at Daresbury Laboratory, which operated from 1980 to 2008 [32]. Later, a third generation of light sources were built using insertion devices (undulators or wigglers) to create more intense light beams [33], an example being the Diamond Light Source in the UK [34]. Most recently, X-ray free-electron lasers (XFEL) (examples of fourth-generation light sources), have been constructed that produce light intensities many times brighter than synchrotron sources [35].

Both LINACs and synchrotrons use RF cavities to provide the required energy to a particle beam that passes through. If excited at their resonant frequency, these structures have low loss with intrinsic quality factors, $Q_0 \sim 10^4$ if they are made of Cu. They are made of Cu as this is the best usable normal conducting metal with low electrical losses. However, achieving the high particle energies required for high-energy machines, such as XFELs and colliders, means that cavities require electric fields $> 10\,\mathrm{MV/m}$. Cu cavities operating continuously at this gradient would have 100s of kW wall losses, which could destroy the cavity. Accelerators therefore require RF cavities made from metals with extremely low electrical loss.

1.2 Superconducting Radio Frequency Cavities

To achieve very low electrical loss, RF cavities made from superconductors are required. These are known as superconducting radio frequency (SRF) cavities. They have been used for many years in various particle accelerators around the world. These are typically made of bulk niobium (Nb). An example of an SRF cavity for testing at Daresbury Laboratory for the Proton Improvement Plan-II (PIP-II) at Fermilab is shown in Figure 1.2(a). The surface resistance of such cavities is typically up to six orders of magnitude lower than Cu, which means that much less power is dissipated in the walls of the cavity [36]. For bulk Nb, this minimal power dissipation is achievable only when the metal is superconducting, that is, when it is cooled below the critical temperature ($T_\mathrm{c} = 9.2\,\mathrm{K}$ for Nb). To achieve the operating requirement of $Q_0 > 10^{10}$, these cavities are installed in liquid helium (LHe) jackets and cooled to around 2 K because below this temperature cavities are limited by residual resistance not BCS resistance. An example of jacketed cavities is shown in Figure 1.2(b) for the European Spallation Source (ESS) high-beta cavities, which were tested at Daresbury Laboratory prior to assembly at CEA. Multiple jacketed cavities are then integrated into a cryomodule prior to installation in the accelerator, as shown in Figure 1.2(c) for the ESS high-beta cavities.

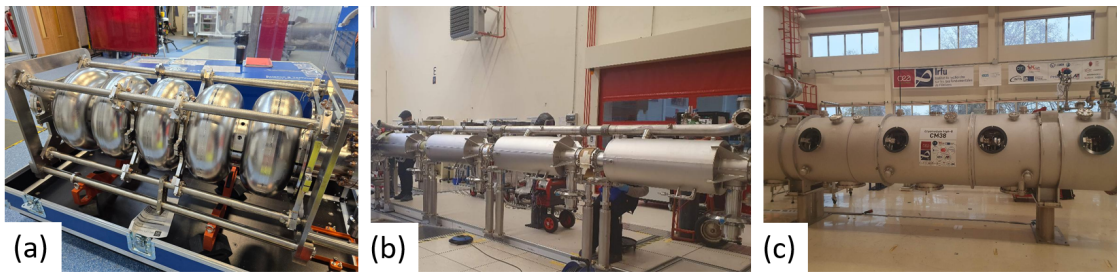

Figure 1.2: Examples of bulk Nb cavities and cryogenic infrastructure: (a) a PIP-II 650 MHz bulk Nb cavity at Daresbury Laboratory, (b) an ESS high-beta jacketed cavities and (c) an ESS high-beta cryomodule built at CEA.

The main advantages of SRF cavities are that it allows the cavities to be operated with high duty cycle or continuous wave (CW) operation with negligible power dissipated in the cavity walls. However, despite the advantages, bulk Nb comes at a significant cost for both cavity production and cryogenic operation. The construction of future accelerators and the upgrades of current accelerators demand more sustainable technology to reduce cost and energy consumption during operation. In addition, significant improvements in the RF performance of bulk Nb 1.3 GHz cavities in recent years have brought them very close to their theoretical limit in accelerating gradient (57 MV/m at 2 K [37]). For example, 1.3 GHz TESLA shaped single-cell cavities have demonstrated gradients up to 50 MV/m at 2 K [38].

An alternative to bulk Nb is to use a Cu cavity with a few micron thick superconductor coated on the inside. Cu is significantly less expensive than Nb, whilst a thin film coated on the inside should exhibit properties similar to those of a bulk Nb cavity. Using thin films has also opened up the exploration of other superconducting materials with higher T_c (e.g. NbTiN, Nb_3Sn, NbN, V_3Si, MgB_2) [39]. These materials have the potential to match or exceed Q_0 of bulk Nb at higher temperatures than the typical 2 K operation. They may also sustain higher peak magnetic fields than Nb resulting in higher accelerating gradients. This may allow for shorter accelerating structures, thus resulting in further infrastructure savings, e.g., fewer cryomodules and less concrete shielding.

However, developing thin film cavities is not easy. It requires significant levels of research in both substrate production and deposition techniques. For this purpose, it would be ideal to deposit films on multiple cavities and perform SRF testing as a function of coating parameters. However, this approach is too costly and time consuming. In addition, any material analysis is difficult without cutting the cavity, which would make it non-reusable. Instead, the materials should first be deposited on small, planar samples and then tested to investigate different deposition parameters and to obtain knowledge and experience to later coat the curved surface of an SRF cavity. Most importantly, superconducting tests on these samples should include measurements of RF properties, such as surface resistance, which is typically more difficult to achieve than measurements of DC properties, such as T_c.

In recent decades, some facilities have been developed that can measure the RF properties of samples, e.g., the quadrupole resonator [40]. However, in order to quickly optimise deposition parameters and identify candidate thin film parameters for test cavity production, high-throughput RF sample test facilities are required. These facilities are very useful for the initial characterisation of material parameters, providing a starting point for cavity depositions, however cavity tests should still be performed to assess whether a film can perform similarly on a complex, curved geometry.

1.3 About This Thesis

The focus of this thesis is on the development of a high-throughput RF test facility used to measure superconducting thin film samples. This would provide Daresbury Laboratory with its first dedicated RF sample test facility and provide the main tool for the optimisation of thin film deposition parameters.

Chapter 2 begins by introducing the theory of RF acceleration, key figures of merit and principles of cavity testing. The chapter continues by explaining the importance of SRF in accelerators, including a brief overview of the theory

of superconductivity. The final part of the chapter discusses the theory and development of thin film SRF cavities and their importance for the development of new accelerators and upgrades of existing facilities.

For thin film SRF research, RF sample testing is vital. Chapter 3 introduces and compares the different measurement methods and techniques for RF sample testing. The different facilities available are introduced and compared followed by an outline of the main considerations for a new facility.

Chapter 4 describes the novel Choke Cavity previously developed at Lancaster University/STFC Daresbury Laboratory which provides an alternative method for the RF sample testing, utilising RF chokes as its main feature. The RF performance of this cavity is analysed via electromagnetic simulations to show the benefits of using chokes as well as the key advantages compared to other facilities introduced in the previous chapter. Simulations showing the addition of RF couplers are also presented.

With the ability to input and measure RF power through the Choke Cavity, a cryogenic facility has been developed that houses it to characterise samples. Chapter 5 describes this facility that houses along with the procedures and calculations required for sample measurements under RF conditions.

Chapter 6 describes how the Choke Cavity facility was commissioned. Measurement capabilities were performed with bulk and thin film Nb on Cu samples. The commissioning procedure first highlights issues with microphonics and also demonstrates the capabilities of the facility with a detailed error analysis and repeatability study for sample measurements.

Having commissioned the facility, Chapter 7 demonstrates thin film optimisation studies that have used the commissioned Choke Cavity facility as the primary measurement technique. The first study looked at optimising the RF performance of Nb/Cu samples, specifically focussing on the effect of the deposition temperature. The second study looked at an alternative superconductor, Nb_3Sn/Cu, deposited with different magnetron powers and the effect of a Nb underlayer with

Nb_3Sn/Nb/Cu samples. This chapter also introduces the deposition methods and the additional techniques that are used to supplement the RF measurements.

The thesis concludes with Chapter 8 which summarises the importance of the new RF test facility and the results of the sample studies carried out. Then it highlights suggestions for further Choke Cavity facility upgrades and possible future studies.

Chapter 2

Superconducting Radiofrequency Theory

The following chapter begins by describing how RF cavities operate as well as some of the important figures of merit for both cavity operation and testing. It continues by explaining why superconducting RF (SRF) cavities are required whilst outlining some of the theory of superconductivity that is important to understand their behaviour. The chapter will conclude by highlighting the motivation for transitioning from bulk Nb cavities to Cu cavities coated with thin film superconductors.

2.1 Radiofrequency Cavity Theory

2.1.1 Key Concepts

RF cavities are some of the main components in modern-day particle accelerators. Their fundamental design consists of a hollow, highly electrically conductive metallic structure with open beam pipes allowing a particle beam to pass through. Most RF cavities operate under vacuum to reduce electrical breakdown and minimise beam losses. Electromagnetic (EM) waves input into the cavity are reflected back and

forth by the conductive walls, creating standing waves of an infinite number of EM eigenmodes. If the frequency coincides with the fundamental cavity resonant frequency (f_0) a large build-up of stored energy results. In an accelerator, this energy will be transferred to a charged particle beam passing through with the correct timing and be accelerated by the electric field component.

The simplest cavity design is a 'pillbox' cavity, shown in Figure 2.1 (with radius R and length d). The design is based on a cylindrically symmetric hollow waveguide that is mostly closed with a small aperture at each end for beam entry and exit. Under RF excitation, the EM eigenmodes in the cavity are solutions to the wave equation derived from Maxwell's equations [37]:

$$\left(\nabla^2 - \frac{1}{c^2}\frac{\partial^2}{\partial t^2}\right)\begin{pmatrix}\boldsymbol{E}\\ \boldsymbol{H}\end{pmatrix} = 0, \tag{2.1}$$

where c is the speed of light in a vacuum and the electric ($\boldsymbol{E}$) and magnetic ($\boldsymbol{H}$) fields satisfy the boundary conditions given by

$$\hat{\boldsymbol{n}} \times \boldsymbol{E} = 0,\ \hat{\boldsymbol{n}} \cdot \boldsymbol{H} = 0, \tag{2.2}$$

where $\hat{\boldsymbol{n}}$ is the unit normal to the surface of the cavity wall.

There are two types of eigenmode solution to Equation 2.2 depending on whether the E-field is longitudinal (E_z) or the H-field is longitudinal (H_z), where the z-axis is the longitudinal axis of symmetry that coincides with the path of a beam.

- Transverse Magnetic (TM) - where a longitudinal component of E exists and $H_\mathrm{z} = 0$.
- Transverse Electric (TE) - where a longitudinal component of H exists and $E_\mathrm{z} = 0$.

The E-field required to accelerate the beam must be along the direction of the particle motion. Therefore, a TM_{mnp} mode can be used, where the indices represent the number of sign changes of E_z in the ϕ, ρ and z directions, respectively (illustrated

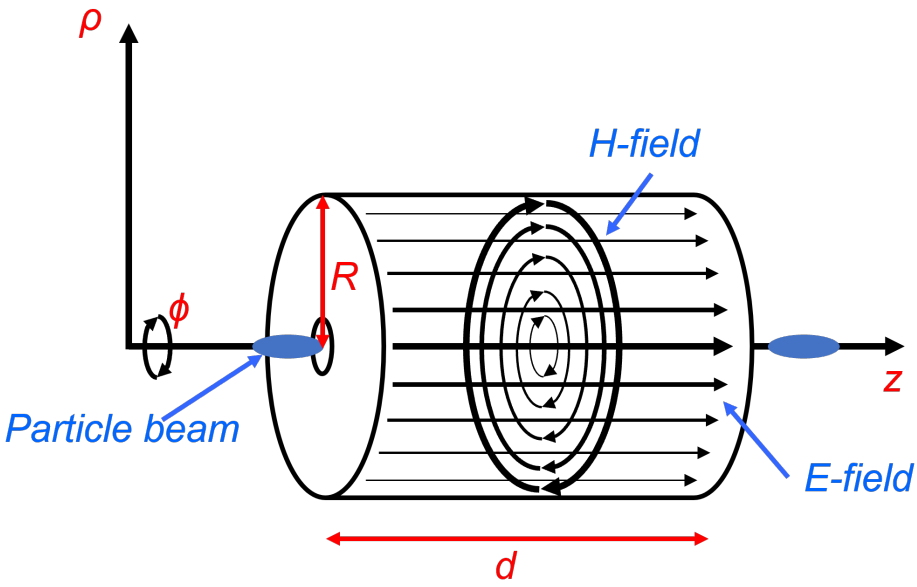

Figure 2.1: A basic illustration of a pill-box cavity showing the axes of interest, path of a particle beam and the E- and H-field profiles.

in Figure 2.1). A similar definition is used to describe H_z in a TE_{mnp} mode. For TM modes, the induced H-field is orthogonal to the E-field and parallel to the outer walls of the cavity. The accelerating mode is typically TM_{010}, as this has the lowest eigenfrequency. In this mode, the peak E-field (E_{pk}) is on-axis and the peak H-field (H_{pk}) is on the cavity equator. The resonant frequency is inversely proportional to the size of the cavity and does not depend on its length. For the pill-box cavity (without an iris), the resonant frequency (i.e. frequency of the TM_{010} mode) is an exact solution given by

$$f_0 = \frac{2.405c}{2\pi R}, \tag{2.3}$$

where 2.405 is the approximate value of the first root of the zeroth order Bessel function, J_0.

Unfortunately, SRF cavity structures cannot be made using simple pill-box shapes. Sharp edges would lead to field emission at high field (introduced in Section 2.3.2.3). Also, if free electrons in the cavity vacuum are accelerated by the electric

field, this can lead to the release of secondary electrons upon collisions with the cavity walls which may result in an exponential increase in accelerated electrons. This is known as multipactor (introduced in Section 2.3.2.1), which can be difficult to avoid in a cylindrically symmetric cavity. These two effects severely limit the performance of the cavity. Instead, the edges of cavities are rounded to avoid field emission and the equator is elliptical to suppress multipacting [41]. An example of a modern-day cavity is the TESLA elliptical cavity [42, 43], for which the EM fields for a 1.3 GHz design are shown in Figure 2.2. Due to the complex designs of these cavities, EM simulations are required, for example, using CST Studio Suite (described later in Section 4.3.1) [44], as there are no simple analytical solutions as with the pillbox cavity. These are needed to design such a cavity, determine the eigenmodes and calculate figures of merit, e.g. f_0, to parameterise the cavity design.

2.1.2 Figures of Merit

The most important figures of merit for an RF cavity are its accelerating gradient (E_{acc}) and intrinsic quality factor (Q_0). A Q_0 vs E_{acc} measurement of a cavity at fixed temperature is the main set of measurements for cavity qualification because it indicates how the RF losses in the cavity walls vary with changing accelerating gradient and what the maximum gradient is the cavity can reach. In addition, it is important to understand the relationship between E_{acc}, E_{pk} and H_{pk}. However, in practical terms, these figures of merit are ultimately limited by the cavity material and preparation.

For a relativistic electron travelling through a cavity of length d (iris to iris) at the speed of light, its transit time $T_{\mathrm{cav}} = d/c$. To receive maximum acceleration from the time-varying E-field, it needs to traverse the cavity for exactly one half of an RF period to avoid deceleration. This transit time is, therefore, given by

$$T_{\mathrm{cav}} = \frac{d}{c} = \frac{\pi}{\omega_0}, \tag{2.4}$$

where $\omega_0 = 2\pi f_0$ is the angular frequency of the accelerating mode.

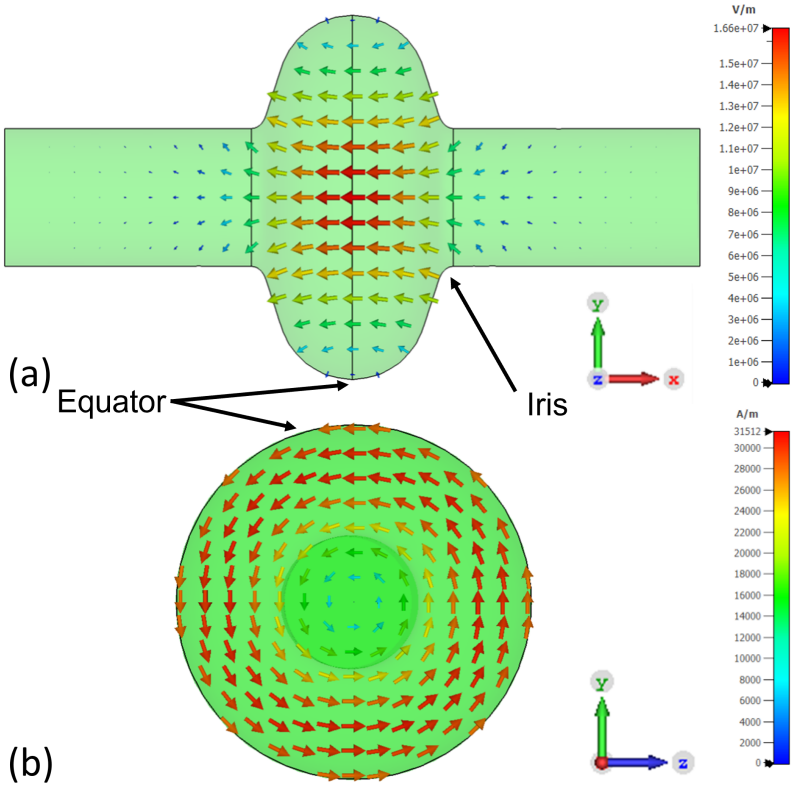

Figure 2.2: Field distribution from CST eigenmode simulations showing the magnitude of the EM fields for the TM_{010} mode of a single-cell 1.3 GHz TESLA cavity: (a) E-field (in XY plane), (b) H-field (in YZ plane).

To calculate E_{acc}, the accelerating voltage (V_{acc}) is first calculated. An electron in a cavity gains energy provided the E-field is in the direction of travel. The accelerating voltage is given by the line integral of the E-field seen by the electron (E_{z}) travelling in direction z:

$$V_{\mathrm{acc}} = \left| \int_0^{\mathrm{d}} E_z(z) e^{i\omega z/c} \mathrm{d}z \right| = dE_0T, \tag{2.5}$$

where T is the transit time factor which accounts for the time variation of the field during the particle transit through the cavity and E_0 is the maximum on-axis E-field in the pillbox cavity.

Typically, the accelerating gradient (often just referred to as the gradient) is of

interest as it accounts for the length of the cavity. This is given by

$$E_{\mathrm{acc}} = \frac{V_{\mathrm{acc}}}{d}. \tag{2.6}$$

The other main parameter used to characterise a cavity is its Q_0 (also known as the unloaded or Ohmic quality factor). It is a measure of how well the cavity can store EM energy and how much power is dissipated in the cavity walls due to Ohmic losses. For a cavity operating at its ω_0, it is defined as

$$Q_0 = 2\pi \frac{\text{Energy stored per cycle}}{\text{Energy dissipated per cycle}} = \frac{\omega_0 U}{P_{\mathrm{c}}}, \tag{2.7}$$

where U is the total stored energy in the cavity and P_{c} is the average power dissipated in the walls of the cavity. An ideal cavity should maximise U whilst minimising P_{c}, therefore it is desirable to maximise Q_0. This is a universal quantity for all resonators and is a measure of the number of oscillations that a cavity will go through before dissipating all of its stored energy.

The total stored energy in the cavity is given by

$$U = \frac{1}{2}\mu_0 \int_{\mathrm{V}} |\boldsymbol{H}|^2 \mathrm{dV} = \frac{1}{2}\epsilon_0 \int_{\mathrm{V}} |\boldsymbol{E}|^2 \mathrm{dV}, \tag{2.8}$$

where the integrals are performed inside the volume (V) of the cavity, μ_0 is the vacuum permeability and ϵ_0 is the vacuum permittivity. The second equality exists because the time-averaged energy in the E-field equals that in the H-field.

As will be discussed in Section 2.1.5, a small fraction of the RF input into a cavity will penetrate a thin surface layer of the cavity wall. This will induce wall currents and dissipate energy. Therefore, the cavities exhibit a surface resistance (R_{s}). The dissipated power in the wall of the cavity is given by

$$P_{\mathrm{c}} = \frac{1}{2} R_{\mathrm{s}} \int_{\mathrm{S}} |\boldsymbol{H}|^2 \mathrm{dS}, \tag{2.9}$$

where the integrals are performed over the interior surface area (S) of the cavity. This calculation assumes that there are no variations in R_{s} over the cavity surface by keeping this factor outside the integral.

The Ohmic heating limits the stored energy in the cavity. A higher cavity R_s increases P_c, resulting in less power used to accelerate the beam. This dissipated power will heat up the cavity, causing an increase in temperature. Due to the higher R_s of normal conducting cavities compared to superconducting ones operating below their T_c (as shown later in Figure 2.6), continuous operation can result in power losses of several hundred kilowatts. Without adequate cooling, typically provided by water, this level of heat dissipation can cause severe damage to the cavity.

Equations 2.8 and 2.9 can be combined with Equation 2.7 to give

$$Q_0 = \frac{\omega_0 \mu_0 \int_\mathrm{V} |\boldsymbol{H}|^2 \mathrm{dV}}{R_\mathrm{s} \int_\mathrm{S} |\boldsymbol{H}|^2 \mathrm{dS}}. \tag{2.10}$$

This clearly shows how Q_0 is dependent on the quality of the surface (R_s) and the geometry of the cavity (represented by the ratio of the H-field integrals). As a result, Equation 2.10 can be simplified to give

$$Q_0 = \frac{G}{R_\mathrm{s}}, \tag{2.11}$$

where G is the geometry factor given by

$$G = \frac{\omega_0 \mu_0 \int_\mathrm{V} |\boldsymbol{H}|^2 \mathrm{dV}}{\int_\mathrm{S} |\boldsymbol{H}|^2 \mathrm{dS}}. \tag{2.12}$$

The geometry factor can be determined from EM simulations. Unlike f_0, this term depends only on the shape of the cavity but not on its size or material. It is therefore a useful quantity for both the comparison of cavity geometries and a simple calculation of R_s once Q_0 has been determined experimentally.

Another useful quantity is the accelerator shunt impedance ($R_\mathrm{a,acc}$), used to characterise cavity losses. It is defined as

$$R_\mathrm{a,acc} = \frac{|V_\mathrm{acc}|^2}{P_\mathrm{c}}, \tag{2.13}$$

where P_c is the power dissipated per cavity cell.

The ideal cavity maximises the accelerating voltage whilst minimising the power dissipated in the walls. The ratio of $R_{\mathrm{a,acc}}/Q_0$ is often used which is given by

$$\frac{R_{\mathrm{a,acc}}}{Q_0} = \frac{V_{\mathrm{acc}}^2}{\omega_0 U}. \tag{2.14}$$

If one scales the linear dimensions of a cavity by factor a: $V_{\mathrm{acc}} \propto a$ (from Equation 2.6), $U \propto a^3$ (from Equation 2.8) and $\omega_0 \propto 1/a$ (from Equation 2.3). Therefore, combining this into Equation 2.14, $R_{\mathrm{a,acc}}/Q_0$ is independent of the cavity size.

Finally, E_{pk} and H_{pk} on the inside surface of the cavity walls are important to consider. The upper limit to H_{pk} for a superconducting cavity is the RF critical magnetic field (described in Section 2.2.3). Above this limit, the cavity material can no longer sustain the superconducting state. Even close to this limit, a thermal quench or field penetration is possible depending on the surface properties of the cavity. Ideally H_{pk} should be minimised to restrict possible heating. For E_{pk}, fields above 100 MV/m have been reported. For example, a bulk Nb RF quadrupole achieved 128 MV/m in CW operation and 210 MV/m in pulsed mode [45]. However, a high E_{pk} can lead to field emission (described later in Section 2.3.2.3) and even higher fields can lead to voltage breakdown.

In general, to maximise experimentally determined Q_0 and E_{acc}, the cavity should maximise G and R_{a}/Q_0, whilst minimising $E_{\mathrm{pk}}/E_{\mathrm{acc}}$ and $H_{\mathrm{pk}}/E_{\mathrm{acc}}$.

2.1.3 Circuit Theory

During the initial stages of cavity design, modelling a cavity using circuit theory can be useful. Circuit analysis is best used when the dimensions of the cavity are small compared to the RF wavelength. For this, the various properties of the cavity are analogous to a resistance, inductance, and capacitance (or RLC circuit) arranged in parallel, as shown in Figure 2.3. Each component represents different cavity properties:

- Resistance, R - ratio of cavity voltage to dissipated power in cavity walls due

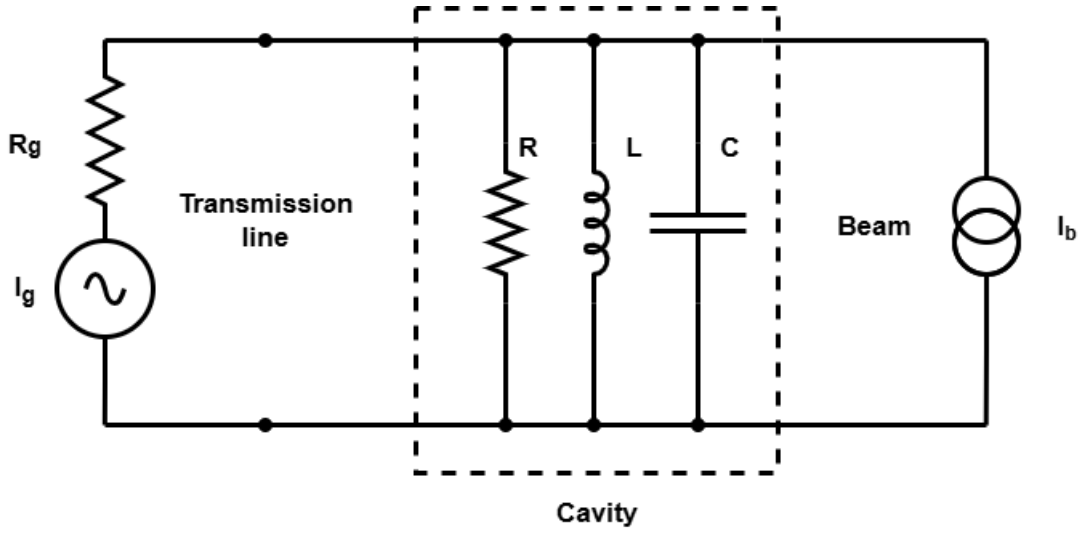

Figure 2.3: An equivalent RLC circuit of a cavity coupled via a transmission line to an RF generator (with current I_{g}) and to the beam (with current I_{b}).

to surface current, i.e. the shunt impedance.

- Inductance, L - the surface current travels around the cavity walls giving rise to the magnetic field which stores energy.

- Capacitance, C - the cavity has two conducting plates at either end with an electric field between the two.

These parameters can be used to calculate Q_0 and R_{a}/Q_0 given the relations:

$$\omega_0 = \frac{1}{\sqrt{LC}}, \tag{2.15}$$

$$U = \frac{CV_{\mathrm{c}}^2}{2}, \tag{2.16}$$

and

$$P_{\mathrm{c}} = \frac{V_{\mathrm{c}}^2}{2R}. \tag{2.17}$$

Combining these equations with Equation 2.7 yields

$$Q_0 = \frac{\omega_0 U}{P_\mathrm{c}} = R\sqrt{\frac{C}{L}}, \tag{2.18}$$

and with the circuit theory definition of shunt impedance ($R_{\mathrm{a,circuit}}$) yields

$$\frac{R_{\mathrm{a,circuit}}}{Q_0} = \frac{V_\mathrm{c}^2}{2\omega_0 U} = \frac{1}{\omega_0 C} = \sqrt{\frac{L}{C}}. \tag{2.19}$$

Both provide simplified calculations of key cavity figures of merit.

2.1.4 Coupling Power into a Cavity

For cavity testing and cavity operation in an accelerator, power must be driven into the cavity. For this, a cavity must be connected to a transmission line (shown in Figure 2.3), which is either a waveguide or a coaxial line. The power is coupled from the transmission line to the cavity via an input coupler. An output (or pickup) coupler can also be connected to measure the transmitted power. The addition of these couplers to a cavity results in additional energy losses that must be separated from the cavity losses to measure Q_0. The strength of coupling, i.e., how well the cavity fields overlap with the leaked fields into the coupler, can be varied by adjusting the penetration depth of the inner conductor of the coupler into the cavity. This is discussed further in Section 4.4.

The addition of couplers means that the total power lost from the cavity (P_{tot}), when the RF is switched off, is the sum of the Ohmic losses and the power flowing through both the input coupler (P_e) and the pickup coupler (P_t). Instead of directly measuring Q_0, a loaded quality factor (Q_L) is measured that combines all these losses. This is defined as

$$Q_\mathrm{L} = \frac{\omega_0 U}{P_{\mathrm{tot}}}, \tag{2.20}$$

where, by conservation of energy,

$$P_{\mathrm{total}} = P_\mathrm{c} + P_\mathrm{e} + P_\mathrm{t}. \tag{2.21}$$

For a non-power driven cavity, power will flow out proportional to the rate of change in stored energy, given by

$$\frac{\mathrm{d}U}{\mathrm{d}t} = -P_{\mathrm{tot}} = -\frac{\omega_0 U}{Q_{\mathrm{L}}}. \tag{2.22}$$

Solving this 1st-order differential equation gives

$$U = U_0 \cdot \exp\left(-\frac{\omega_0 t}{Q_{\mathrm{L}}}\right), \tag{2.23}$$

where U_0 is the initial stored energy.

Therefore, the stored energy decays with a time constant (τ_{L}) given by

$$\tau_{\mathrm{L}} = \frac{Q_{\mathrm{L}}}{\omega_0}. \tag{2.24}$$

Thus, measurement of this time constant allows Q_{L} to be determined.

Combining Equations 2.20 and 2.21 gives

$$\frac{1}{Q_{\mathrm{L}}} = \frac{1}{Q_0} + \frac{1}{Q_{\mathrm{e}}} + \frac{1}{Q_{\mathrm{t}}}, \tag{2.25}$$

where external quality factors have been defined for the input coupler (Q_{e}) and for the pickup coupler (Q_{t}) analogously to Q_0, as

$$Q_{\mathrm{e}} \equiv \frac{\omega_0 U}{P_{\mathrm{e}}}, \tag{2.26}$$

and

$$Q_{\mathrm{t}} \equiv \frac{\omega_0 U}{P_{\mathrm{t}}}. \tag{2.27}$$

Useful quantities known as coupling strengths can be defined for each coupler as the ratio of losses through the coupler to the ratio of Ohmic losses. For the input (β_1) and the pickup (β_2) these are given by:

$$\beta_1 \equiv \frac{Q_0}{Q_{\mathrm{e}}} = \frac{P_{\mathrm{e}}}{P_{\mathrm{c}}} \tag{2.28}$$

and

$$\beta_2 \equiv \frac{Q_0}{Q_\mathrm{t}} = \frac{P_\mathrm{t}}{P_\mathrm{c}}. \tag{2.29}$$

Therefore, using Equations 2.25-2.29 gives

$$Q_0 = Q_\mathrm{L}(1 + \beta_1 + \beta_2). \tag{2.30}$$

Typically, the pickup is designed such that $P_\mathrm{t} \ll P_\mathrm{c}$, therefore, $\beta_2 \ll 1$. That is, the pickup is very weakly coupled. For now, it is assumed that $\beta_2 \ll 1$ and its influence can be ignored. Later, Section 5.3.2 provides details on calculations without this assumption.

When driving power into a cavity, there are three powers to consider:

- P_f - forward power going into the cavity.
- P_r - reverse power coming back from the cavity.
- P_e - emitted power leaking through the coupler from the cavity stored energy.

At the coupler-cavity boundary, there is a large impedance mismatch resulting in a reflection out of phase to the input signal. By conservation of energy,

$$P_\mathrm{r} = \left(\sqrt{P_\mathrm{f}} - \sqrt{\frac{\omega_0 U}{Q_\mathrm{e}}}\right)^2. \tag{2.31}$$

By conservation of energy, change in stored energy over time is equal to the sum of the power flowing into the cavity and the power flowing out, as well as Ohmic losses:

$$\begin{aligned}
\frac{\mathrm{d}U}{\mathrm{d}t} &= P_\mathrm{f} - \left(\sqrt{P_\mathrm{f}} - \sqrt{\frac{\omega_0 U}{Q_\mathrm{e}}}\right)^2 - \frac{\omega_0 U}{Q_0} \\
&= \sqrt{\frac{4P_\mathrm{f}\omega_0 U}{Q_\mathrm{e}}} - \omega_0 U\left(\frac{1}{Q_0} + \frac{1}{Q_\mathrm{e}}\right) \\
&= \sqrt{\frac{4P_\mathrm{f}\omega_0 U}{Q_\mathrm{e}}} - \frac{\omega_0 U}{Q_\mathrm{L}},
\end{aligned} \tag{2.32}$$

where Equation 2.20 has been used.

In steady state, $\mathrm{d}U/\mathrm{d}t = 0$ and $U = U_0$ (the maximum stored energy). Solving Equation 2.32 and using Equations 2.28 and 2.30 gives

$$U_0 = \frac{4P_\mathrm{f}\beta_1 Q_0}{(1+\beta_1)^2\omega_0}, \tag{2.33}$$

which can be used to calculate the stored energy in a cavity which is maximal when $\beta_1 = 1$ and there is matched coupling.

A reflection coefficient (Γ) is defined as the ratio of the reflected wave voltage to that of the incident wave. For a cavity in steady state, this is given by

$$\Gamma(\omega) = \frac{\beta_1 - 1 - iQ_0\delta}{\beta_1 + 1 + iQ_0\delta}, \tag{2.34}$$

where

$$\delta = \frac{\omega}{\omega_0} - \frac{\omega_0}{\omega}. \tag{2.35}$$

Therefore, on resonance $\omega = \omega_0$ and Γ becomes

$$\Gamma(\omega_0) = \frac{\beta_1 - 1}{\beta_1 + 1}. \tag{2.36}$$

P_r is calculated from Γ on resonance:

$$P_\mathrm{r} = \Gamma^2(\omega_0)P_\mathrm{f}, \tag{2.37}$$

and using Equation 2.36 and solving for β_1 gives

$$\beta_1 = \frac{1 \pm \sqrt{P_\mathrm{r}/P_\mathrm{f}}}{1 \mp \sqrt{P_\mathrm{r}/P_\mathrm{f}}}, \tag{2.38}$$

where +/- is used for the overcoupled state and -/+ is the undercoupled state. The three possible states are:

- Undercoupled: $\beta_1 < 1$, most power is reflected at the cavity/coupler boundary.
- Overcoupled: $\beta_1 > 1$, most of the power is emitted from the cavity.

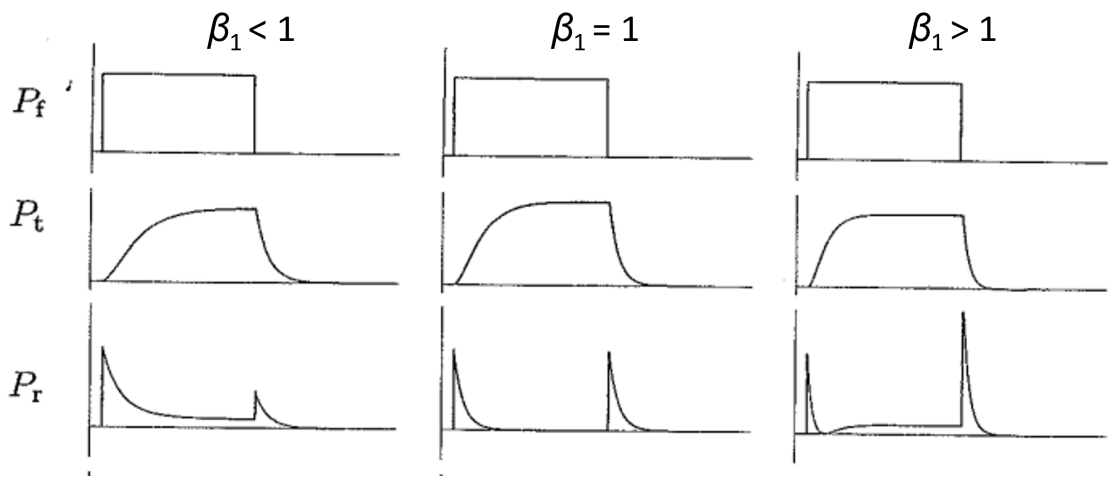

Figure 2.4: The response of P_r and P_t to a rectangular pulse, P_f. Adapted from [37].

.

- Critical or matched: $\beta_1 = 1$, the coupler impedance matches the cavity impedance, the emitted power is equal to the reflected power, and the signals are 180° out of phase.

Figure 2.4 shows how a rectangular RF pulse leads to different responses in P_r and P_t depending on the coupling state. Later, Section 4.4.1 shows how using polar plots from a vector network analyser (VNA) is a possible method to determine the coupling state, as this cannot be determined from P_r/P_f alone.

2.1.5 Normal Conductors

In Section 2.1.1, it was shown that the E-field component accelerates charged particles along the longitudinal axis of the cavity. However, the EM fields will also interact with a thin surface layer of the conducting walls, causing currents to flow and a surface resistance to be induced. This EM response of the cavity walls can be described by a complex surface impedance (Z_s), which is analogous with the DC resistance. It is defined as the ratio of E_0, to the total current in the conductor (I). The total current is equal to the integrated current density ($J(z)$) as a function of depth (z). Therefore, Z_s is given by

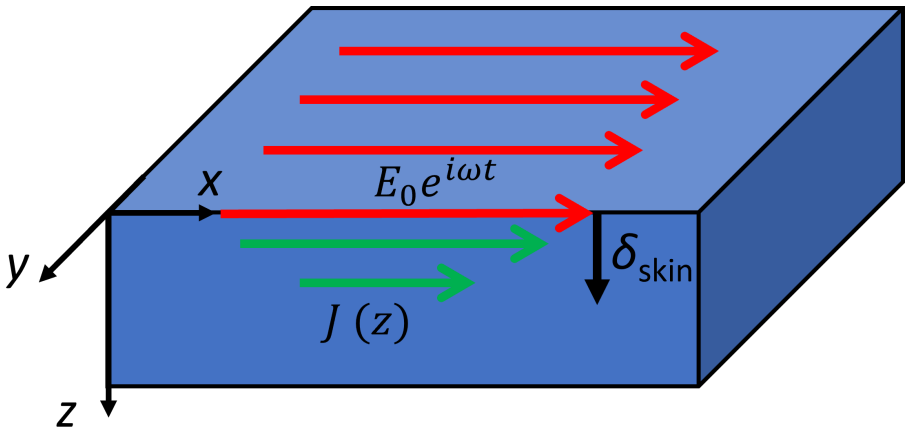

Figure 2.5: An illustration of RF penetration into a conductor.

$$Z_s = \frac{E_0}{\int_{-\infty}^{\infty} J(z)\mathrm{d}z} = \sqrt{\frac{i\omega\mu}{\sigma}} = R_s + iX_s, \tag{2.39}$$

where R_s is the real surface resistance, X_s is the imaginary surface reactance, μ is the permeability and σ is the electrical conductivity of the cavity material.

For normal conductors, an alternating E-field will decay exponentially within the material over the distance of the skin depth (δ_{skin}) as illustrated in Figure 2.5. From Equation 2.39, R_s is given as:

$$R_s = \sqrt{\frac{\omega\mu}{2\sigma}} = \frac{1}{\sigma\delta_{skin}}, \tag{2.40}$$

where, the skin depth is defined as

$$\delta_{skin} = \sqrt{\frac{2}{\omega\mu\sigma}}. \tag{2.41}$$

For example, for a 1.3 GHz Cu cavity with $\sigma = 5.8 \times 10^7$ Sm^{-1} at room temperature, $\delta = 1.8\,\mu$m and $R_s = 9.4$ mΩ. Equation 2.9 showed that $P_c \propto R_s$, therefore the relatively high R_s of a normal conducting cavity leads to substantial wall heating under CW operation, with RF losses $\sim$kW for $E_{acc} \sim$MV/m. Thermal expansion from this heating detunes the cavity, reflecting an increasing fraction of the incident RF power, thereby limiting further power deposition in the cavity

walls. While this detuning provides a degree of self-protection, the associated thermal stresses and non-uniform heating still render CW operation impractical. Consequently, such cavities are generally operated in pulsed mode with active water cooling to manage the thermal load.

Equation 2.41 is valid in the regime where the skin depth is much larger than the electron mean free path (l), i.e. $\delta \gg l$. This is known as the 'normal skin effect'. However, at very low temperatures and/or high frequencies, the skin depth might become shorter than the electron mean free path. In this case, the current and fields become non-local and Ohm's law is no longer valid. This is the 'anomalous skin effect'. The surface resistance is then dependent on ρl (where $\rho = 1/\sigma$ is the resistivity) which is a material constant independent of temperature. In the extreme anomalous limit ($\delta \ll l$), $l \to \infty$, and the resistance can be described by [46, 47]

$$R_{\mathrm{s}}(l \to \infty) = \frac{8}{9}\left(\sqrt{3}(\rho l)\omega^2\left(\frac{\mu_0^2}{16\pi}\right)\right)^{1/3}. \tag{2.42}$$

In the classical skin effect regime (described in Equation 2.40), $R_{\mathrm{s}} \propto \rho^{1/2}$, therefore improvements in material purity directly reduce RF losses with square-root dependence. However, in the anomalous skin effect regime (described in Equation 2.42), the scaling reduces to $R_{\mathrm{s}} \propto \rho^{1/3}$. Therefore, the weaker, non-linear dependence on ρ means that further reducing ρ yields diminishing returns compared to the classical regime.

The alternative to normal conductors is to use superconductors. As shown in Equation 2.40, for a normal conducting cavity, $R_{\mathrm{s,NC}} \propto \sqrt{f}$. In Section 2.2.2, it will be shown that $R_{\mathrm{s,SC}} \propto f^2$ for a superconducting cavity. However, these cavities must be cooled to a few degrees above absolute zero to have the required level of R_{s} providing $Q_0 > 10^{10}$. Figure 2.6 shows the dependence of R_{s} on f for both a superconducting Nb ($RRR = 400$) cavity at both 2 K and 4.2 K compared with a normal conducting ($RRR = 100$) Cu cavity at both < 10 K (where $R_{\mathrm{s,NC}}$ has virtually no temperature dependence) and room temperature (300 K). The residual resistance ratio (RRR) is a useful quantity used to define the purity of a metal, and

is defined as:

$$RRR \equiv \frac{\rho_{300\,\mathrm{K}}}{\rho_{T_\mathrm{c}}}, \tag{2.43}$$

where $\rho_{300\,\mathrm{K}}$ is the room temperature resistivity and $\rho_{\mathrm{T_c}}$ is the resistivity just above T_c. For a normal conductor the denominator is instead the resistivity at 0 K.

To have low-frequency CW operation ($< 4\,\mathrm{GHz}$), only SRF cavities are really viable due to their $6-7$ orders of magnitude lower R_s. At higher frequencies, the R_s of Nb is only a couple of orders of magnitude lower than Cu; therefore, it is not cost-effective to cryogenically cool cavities at these frequencies when instead normal conducting Cu cavities at room temperature can be used.

2.2 Superconductivity

In April 1911, the Dutch physicist Heike Kammerlingh Onnes performed some experiments measuring the electrical resistance of solid mercury at LHe temperatures of 4.2 K [48]. His experiments successfully demonstrated that the DC resistance of mercury abruptly disappeared at this temperature. This temperature later became known as the critical temperature. This incredible discovery gave birth to a new field in physics - known later as superconductivity. Subsequent experiments found that this property was not unique to mercury. Experiments in 1913 found that lead and tin exhibit similar properties when cooled below 7 K [49]. In fact, in subsequent decades, many other materials were found to exhibit superconducting properties. However, it would not be for another forty years since Onnes' discovery that the reasons for superconductivity could be explained at a microscopic level.

Many steps were taken since the 1910s to try and understand superconductivity. Up until the early 1930s, people only understood superconductivity as a vanishing electrical resistance. However, in 1933, Fritz Wather Meissner and Robert Ochsenfeld performed experiments on superconducting tin and lead in the presence of an external magnetic field. Initially, this field fully penetrated the samples.

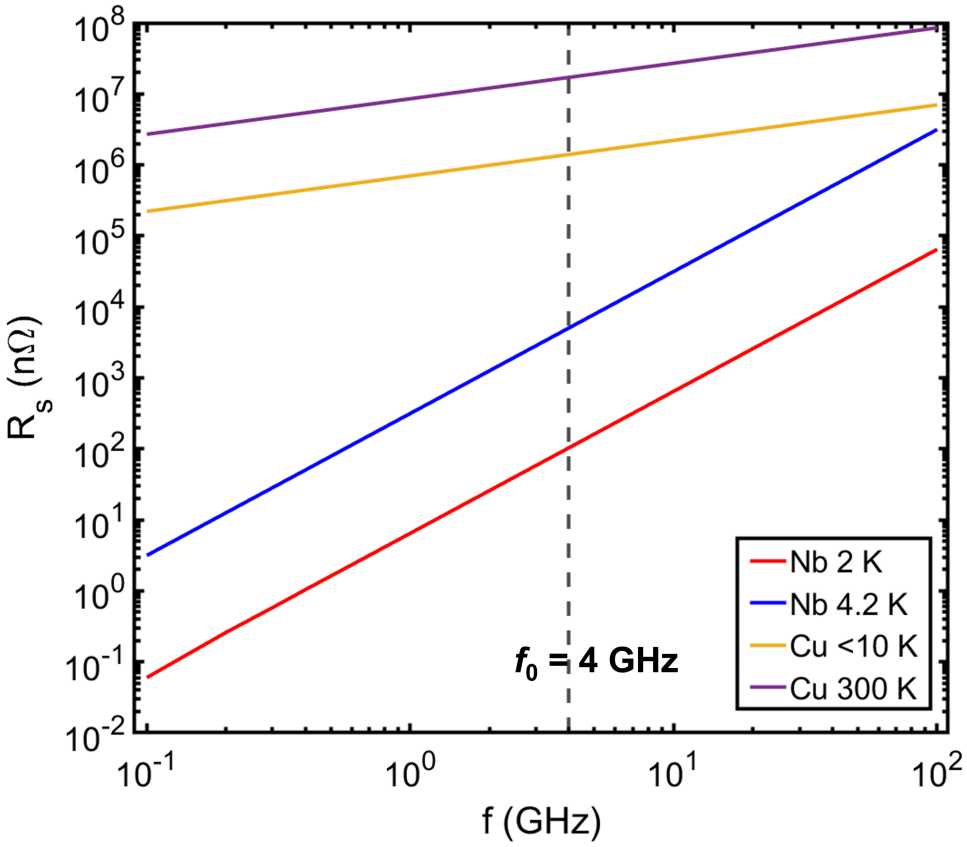

Figure 2.6: Surface resistance as a function of frequency of a superconducting bulk Nb cavity at both 2 K and 4.2 K compared to a normal conducting Cu cavity at both < 10 K and 300 K.

However, when cooled below their critical temperature, Meissner and Ochsenfeld indirectly detected that the field was almost completely expelled [50]. The cause of this effect was later explained to be due to supercurrents within the surface layer of the superconductor that act to shield the external magnetic field. The material exhibited perfect diamagnetism, which later became known as the Meissner effect. Diamagnetism is a property of a material that causes weak repulsion to a magnetic field whereas perfect diamagnetism is only experienced by superconductors.

The Meissner effect is illustrated in Figure 2.7 that compares the behaviour of a perfect conductor and a superconductor cooled to temperatures below T_c in the presence of a H-field. Below T_c, field still penetrates the perfect conductor whilst

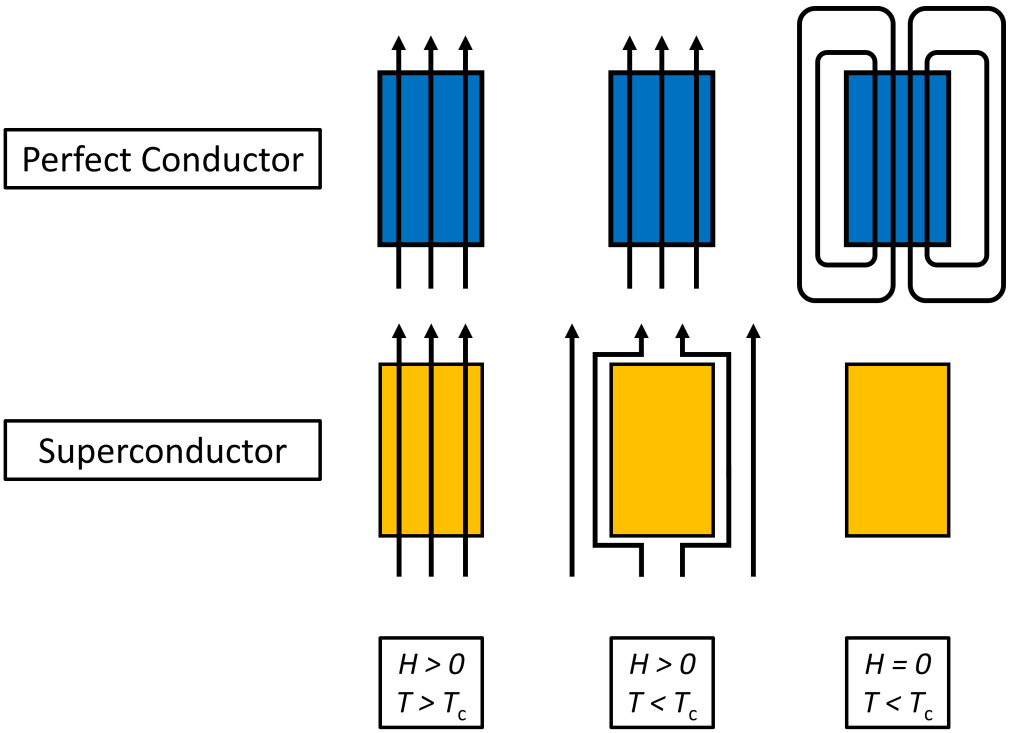

Figure 2.7: The behaviour of a perfect conductor and superconductor during cooldown below T_c in both the presence of an external magnetic field and with removal of the magnetic field.

it is expelled from the bulk of the superconductor. Upon removal of the H-field, the perfect conductor remains magnetised whilst the superconductor returns to the normal state. It will be shown later that, because of both impurities and the critical fields of the material, there is a limit to the maximum magnetic field that can be expelled. This ultimately limits the maximum E_{acc}.

2.2.1 Two-Fluid Model and London Theory

Below T_c, some electrons become tightly bound in pairs, known as Cooper pairs. This attraction happens by an exchange of phonons between the two electrons which becomes energetically favourable to overcome their electrostatic repulsion. At $T = 0\,\mathrm{K}$, all electrons are in Cooper pairs, whist at temperatures from $0 < T < T_c$ some electrons are bound in Cooper pairs and the remaining behave as normal free

electrons.

Gorter and Casimir described this using a two fluid state with both normal conductivity and superconductivity [51]:

- Normal conductivity - electron number density n_{n} and normal current density $\boldsymbol{j}_{\mathrm{n}}$.
- Superconductivity - Cooper pair number density n_{s} and superconducting current density $\boldsymbol{j}_{\mathrm{s}}$.

The superconducting behaviour is different depending on whether a DC or RF field is applied:

- DC - the Cooper pairs are a superfluid that carry the whole DC current which flows without resistance, analogous to a superfluid liquid with zero viscosity. In the superfluid state, the two bound electrons behave as a boson with integer spin.
- RF - the Cooper pairs have mass and inertia therefore do not screen an applied time-varying field perfectly. A time-varying electric field is induced in the skin layer by a time-varying magnetic field. The imperfect shielding means that this time-varying electric field couples to the normal electrons, causing small power dissipation as the electrons accelerate and decelerate. This is the mechanism giving rise to the superconducting surface resistance.

In 1935, a quantitative explanation of the Meissner effect was modelled by brothers Fritz and Heinz London [52]. They described the Meissner effect as follows:

$$\nabla \times \boldsymbol{j}_{\mathrm{s}} + \frac{n_{\mathrm{s}} e^2}{m} \boldsymbol{B} = 0, \tag{2.44}$$

which is the second London equation, where e is the electron charge and m is the electron mass.

The second London equation combined with Maxwell's equations gives

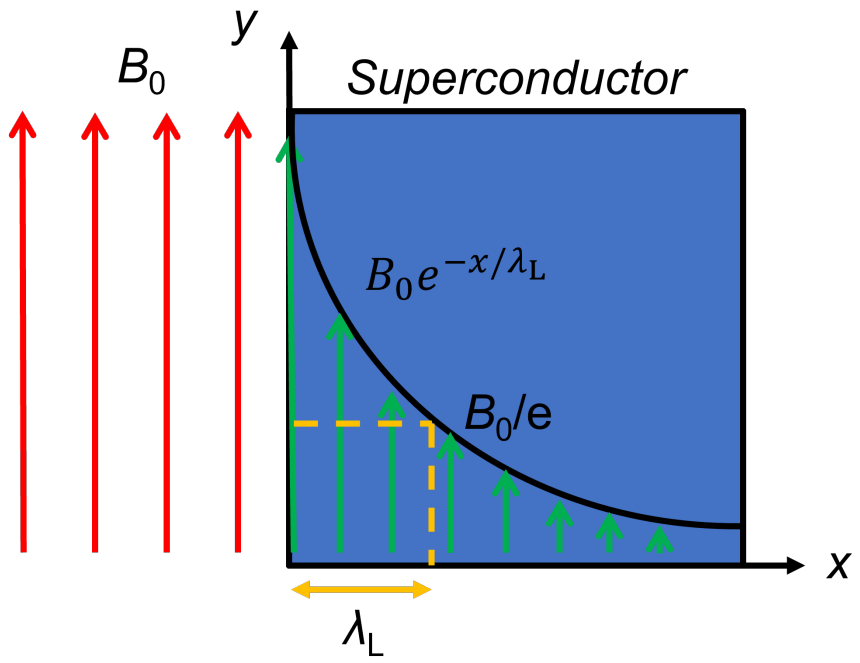

Figure 2.8: The decay of the parallel RF magnetic field into the surface of a superconductor.

$$\nabla^2 \boldsymbol{B} = \frac{1}{\lambda_{\mathrm{L}}^2} \boldsymbol{B}, \tag{2.45}$$

where λ_{L} is the London penetration depth given by

$$\lambda_{\mathrm{L}} = \sqrt{\frac{m}{n_{\mathrm{s}} e^2 \mu_0}}. \tag{2.46}$$

This characterises the penetration depth of the parallel RF magnetic field component, illustrated in Figure 2.8. The solution to Equation 2.45 is

$$B_x = B_0 \exp\left(-\frac{x}{\lambda_{\mathrm{L}}}\right), \tag{2.47}$$

where x is the distance from the surface. Therefore, by definition, λ_{L} is the distance over which the applied magnetic field B_0 decays by a factor 1/e. For example, $\lambda_{\mathrm{L}} = 36\,\mathrm{nm}$ for high-purity bulk Nb [53].

Another equation was derived by equating the electromagnetic force on an electron from the Lorentz force law to Newton's second law. The result was an equation that describes the time-varying behaviour of the supercurrent in an applied E-field:

$$\frac{\partial \boldsymbol{j}_{\mathrm{s}}}{\partial t} = \frac{n_{\mathrm{s}} e^2}{m} \boldsymbol{E}, \tag{2.48}$$

which is the first London equation. This shows that a supercurrent is freely accelerated by an applied voltage. By taking the curl of Equation 2.48 and using Faraday's law, it is possible to obtain the second London equation.

2.2.2 BCS Theory

The first theory to describe superconductivity at the microscopic level was developed by John Bardeen, Leon Cooper and John Robert Schrieffer in 1957 [54, 55]. This became known as the BCS theory.

The fundamental concept of BCS theory is based on the formation of Cooper pairs. Electrons moving through a metal lattice distort the positive ions. The accumulation of positive charge in the deformed region attracts a second electron. Phonons mediate the attraction between the two electrons that can overcome the electrostatic repulsion leading to the formation of a Cooper pair which acts as a boson. For a Cooper pair to form, a strong electron-phonon interaction is required. For electrons to condense into Cooper pairs, they need to be within an energy

$$k_{\mathrm{B}} T_{\mathrm{c}} \approx \hbar \omega_{\mathrm{D}} \tag{2.49}$$

of the Fermi level, where $\hbar\omega_{\mathrm{D}}$ is the maximum phonon energy, ω_{D} is the Debeye frequency and $\hbar$ is the reduced Planck constant. This results in a redistribution of the Fermi energy distribution resulting in the formation of an energy gap (Δ) in which there is an absence of energy levels. This gap dictates the pairing energy and has a temperature dependence approximated by:

$$\Delta(T) \approx \Delta(0)\sqrt{\cos\left(\frac{\pi}{2}\left(\frac{T}{T_\mathrm{c}}\right)^2\right)}, \tag{2.50}$$

where $\Delta(0)$ is the value of Δ at $T = 0\,\mathrm{K}$ and near T_c, $\Delta \to 0$.

The spatial extent (or mean length scale) of a Cooper pair is dervied from Bose-Einstein statistics and Heisenberg's uncertainty principle. This is known as the coherence length (ξ). At 0 K this is denoted by ξ_0 and can be related to the Fermi velocity (v_F) and T_c:

$$\xi_0 = \frac{\hbar v_\mathrm{F}}{k_\mathrm{B} T_\mathrm{c}}. \tag{2.51}$$

For high RRR bulk Nb, $\xi_0 \approx 39\,\mathrm{nm}$ [53].

The BCS theory gives an approximate relation for the surface resistance of a superconductor in RF fields, which is known as the BCS resistance (R_BCS). At low field, a basic relation for R_BCS is given by

$$R_\mathrm{BCS} = \frac{A\omega^2}{T}\exp\left(-\frac{\Delta(0)}{k_\mathrm{B}T}\right), \tag{2.52}$$

valid for $T < T/T_\mathrm{c}$ where $\Delta \to \Delta(0)$. Here A is a material dependent constant and the exponential term is a factor proportional to n_n [37].

Equation 2.52 shows the two main features of the superconducting surface resistance that differ from the normal conducting resistance:

1. $R_\mathrm{BCS} \propto f^2$.

2. R_BCS increases exponentially with temperature.

These two features are illustrated in Figure 2.9 for a Nb cavity, indicating variations in both R_BCS and Q_0 (assuming only BCS losses). Figure 2.9(a) is shown as a function of frequency for $T = 2\,\mathrm{K}$ and Figure 2.9(b) is as a function of temperature for a 1.3 GHz cavity. Both are for a cavity with $G = 270\,\Omega$. For all cavities, $R_\mathrm{s} > R_\mathrm{BCS}$. This is due to the presence of a temperature-independent

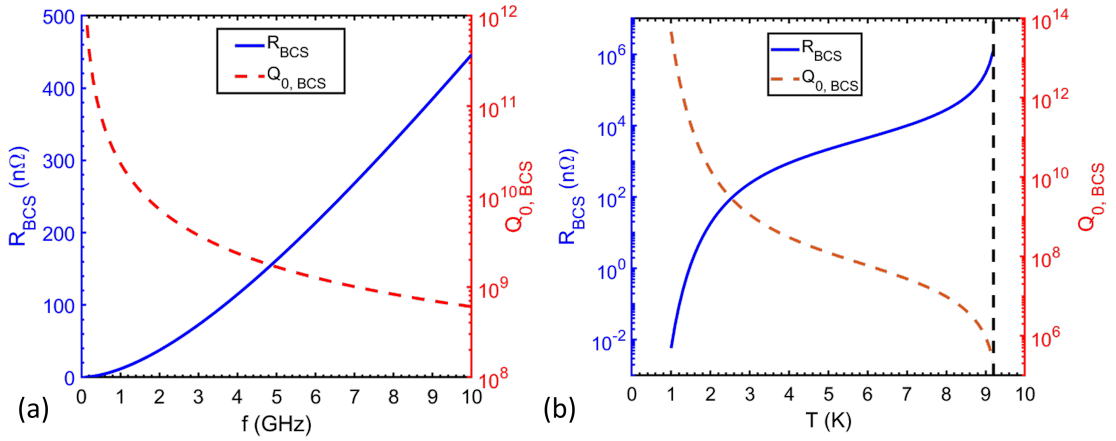

Figure 2.9: BCS resistance and intrinsic quality factor for a bulk Nb cavity as a function of (a) frequency at 2 K, (b) temperature for 1.3 GHz (calculated in SRIMP [56] with material parameters: $\Delta(0)/k_{\mathrm{B}}T_{\mathrm{c}}$,=1.86, $\lambda_{\mathrm{L}} = 32\,\mathrm{nm}$; $\xi_0 = 39\,\mathrm{nm}$, $T_{\mathrm{c}} = 9.2\,\mathrm{K}$).

residual resistance (R_{res}) which can be attributed to material impurities and trapped flux (detailed later in Section 2.3.3).

The constant A in Equation 2.52 depends on various material parameters. As well as the Fermi velocity and penetration depth, this term depends on:

- Electron mean free path, l:

  This is the average distance a normal electron travel before a collision. It can be compared to the coherence length to determine whether a superconductor is in the 'clean' limit or 'dirty' limit:

  - Clean limit: $l \gg \xi_0$
  - Dirty limit: $l \ll \xi_0$

  It is possible to reduce l and make the surface layer 'dirty' by adding impurities to the material. Therefore, given that there is a minimum R_{BCS} for low l, it is possible to tune a material to reduce R_{BCS} and hence maximise Q_0. This is what Nb/Cu thin film cavities can achieve, as detailed in Section 2.4.1.

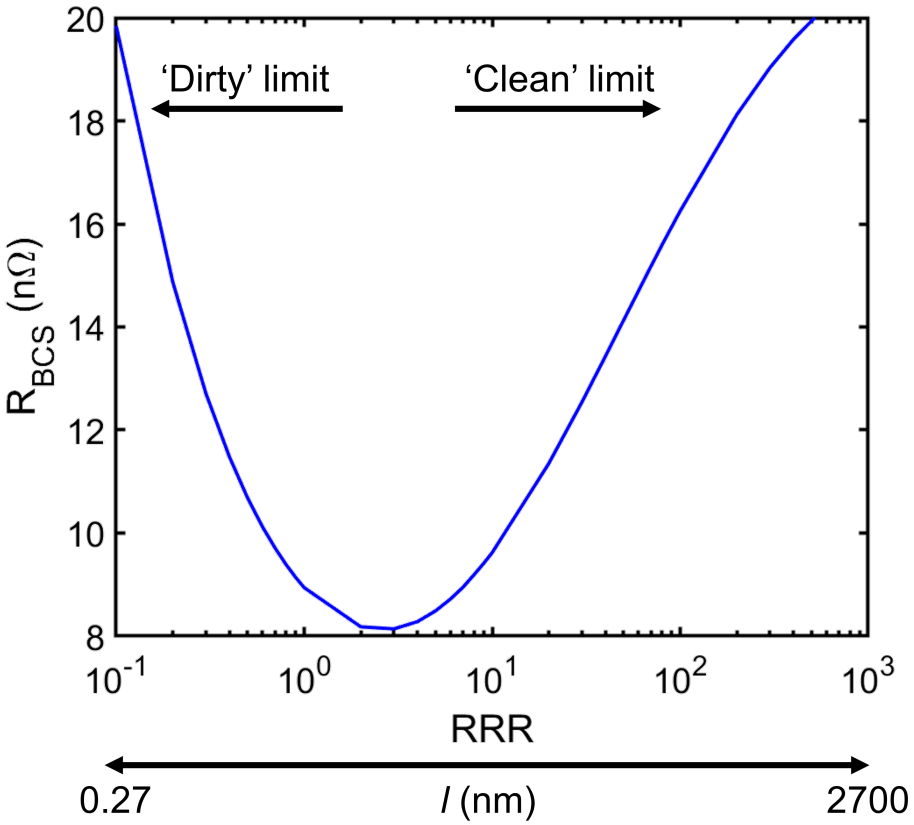

Figure 2.10: BCS resistance as a function of RRR for bulk Nb at 1.3 GHz and 2 K, showing also the relation between RRR and l (calculated in SRIMP [56] with material parameters: $\Delta(0)/k_{\mathrm{B}}T_{\mathrm{c}}$,= 1.86, $\lambda_{\mathrm{L}} = 32\,\mathrm{nm}$; $\xi_0 = 39\,\mathrm{nm}$, $T_{\mathrm{c}} = 9.2\,\mathrm{K}$).

- The effective coherence length, ξ:

  The actual coherence length depends on impurities, therefore $\xi = \xi(l)$ and is given by:

$$\frac{1}{\xi} = \frac{1}{\xi_0} + \frac{1}{l}. \tag{2.53}$$

  In the clean limit, $\xi \approx \xi_0$. However, in the dirty limit, $\xi(l) \approx l$ whereby ξ becomes shorter with decreasing l.

  The two limits are demonstrated in Figure 2.10 where $l \propto RRR$ [57] and a minimum R_{BCS} exists when $\xi_0 \approx l$.

- The penetration depth, λ:

  As discussed in Section 2.2.1, the distance over which the magnetic field penetrates into a superconductor is dictated by λ_{L}. The penetration depth is related to the coherence length by

  $$\lambda = \lambda_{\mathrm{L}} \sqrt{\frac{\xi_0}{\xi}}, \tag{2.54}$$

  therefore, $\lambda \approx \lambda_{\mathrm{L}}$ at 0 K for a clean superconductor.

  Near T_{c}, the penetration depth for a clean superconductor has a temperature dependence, derived from the two-fluid model

  $$\lambda(T) = \frac{\lambda_{\mathrm{L}}}{\sqrt{1 - (\frac{T}{T_{\mathrm{c}}})^4}}. \tag{2.55}$$

The full calculation for R_{BCS} with the dependence on these material parameters cannot be solved analytically. It requires numerical codes. Often the SRIMP code [56] is used to calculate R_{BCS} based on input values of l, ξ_0, λ_{L}, $\Delta(0)/k_{\mathrm{B}}T_{\mathrm{c}}$, T_{c}, T and f_0. This user-friendly programme is based on a code written by Halbritter [58]. For Figures 2.9(a), 2.9(b) and 2.10 the SRIMP code was used with material parameters: $\Delta(0)/k_{\mathrm{B}}T_{\mathrm{c}}$,= 1.86, $\lambda_{\mathrm{L}} = 32\,\mathrm{nm}$; $\xi_0 = 39\,\mathrm{nm}$, $T_{\mathrm{c}} = 9.2\,\mathrm{K}$ [53] as well as the fixed values of f_0, T and RRR where applicable.

2.2.3 Critical Magnetic Fields

As discussed previously, superconductors exhibit different behaviours in magnetic fields compared to normal conductors. For an SRF cavity, the maximum H_{pk}, and therefore the maximum E_{acc}, that the superconductor can exhibit is limited by the material's ability to maintain the Meissner state.

In superconductivity, 'Gibbs free energy' represents the amount of energy required to do useful work and is related to the transition between normal and superconducting states. The superconducting state is more ordered than the normal

state, therefore, having lower free energy. However, the increase of an external DC magnetic field (H_{ext}) causes supercurrents to flow in the penetration depth to cancel out the field in the interior, creating an increase in free energy as there is an increase in work done to expel the magnetic field. At a value $H_{\text{ext}} = H_{\text{c}}$, the free energy of the superconducting and normal conducting phases are in equilibrium. When $H_{\text{ext}} > H_{\text{c}}$, the system is pushed out of equilibrium and it is energetically favourable that all flux enters the superconductor, and superconductivity is broken. Due to fact that $\Delta \to 0$ as $T \to T_{\text{c}}$, the critical field has a temperature dependence given by

$$H_{\text{c}}(T) = H_{\text{c}}(0)\left[1 - \left(\frac{T}{T_{\text{c}}}\right)^2\right]. \tag{2.56}$$

For this reason, H_{c} is known as the thermodynamic critical field.

At the phase boundary between the superconducting and normal conducting states, there is a surface energy barrier. The behaviour of the magnetic field depends on whether the superconductor behaves as a Type-I or Type-II superconductor. It is possible to distinguish between them by calculating the Ginzburg-Landau parameter (κ_{GL}):

$$\kappa_{\text{GL}} = \frac{\lambda_{\text{L}}}{\xi_0}. \tag{2.57}$$

The difference between these types of superconductor is as follows and is shown in Figure 2.11:

- Type-I - positive surface energy, fields enter at H_{c}, $\kappa_{\text{GL}} < 1/\sqrt{2}$, e.g., Pb.
- Type-II - negative surface energy, it is energetically favourable for flux to enter at a lower critical field (H_{c1}) forming a mixed state, $\kappa_{\text{GL}} > 1/\sqrt{2}$, e.g., Nb.

For a Type-I superconductor, when the applied magnetic field $H > H_{\text{c}}$, flux fully penetrates the material and it transitions to the normal state. On the other hand, when flux enters a Type-II superconductor at $H = H_{\text{c1}}$, a lattice of vortices form.

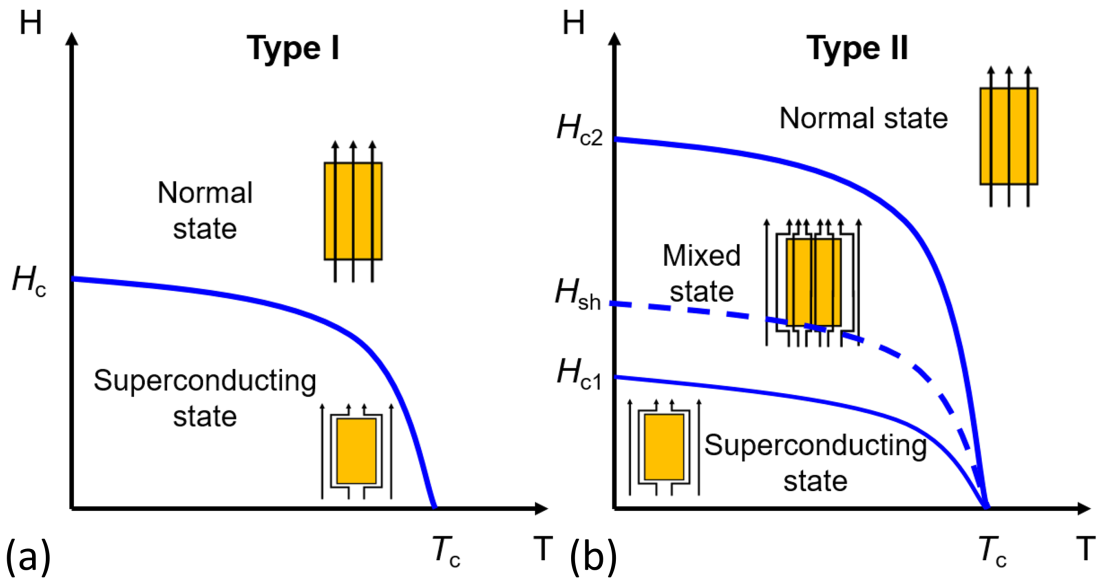

Figure 2.11: The magnetic field phase diagrams for: (a) Type-I, (b) Type-II superconductors.

The core of each vortex is normal conducting with radius ξ whilst the region between them remains superconducting. At increasing H, flux entry rises and vortex density increases until a field higher than H_c is reached, known as the upper critical field (H_{c2}) In this 'mixed' state, SRF cavity operation can continue, but with more losses.

Vortices that penetrate at $H > H_{c1}$ in a Type-II superconductor are pinned to the surface. In an SRF cavity, the magnetic field is parallel to the inside surface, however the vortices must enter perpendicular, but they can bend when inside the surface. The vortices do not enter the bulk due to the Bean-Livingston barrier formed by screening currents [59]. It is possible for the Meissner state to exist metastably above H_{c1} up to a superheating field (H_{sh}), which is approximately equal to the critical RF magnetic field and less than H_{c2}. For bulk Nb cavities, this provides the theoretical limit $E_{acc} = 57\,\mathrm{MV/m}$ at $2\,\mathrm{K}$ [37].

2.3 Superconducting RF Cavity Performance

2.3.1 Cryogenics

A superconducting cavity typically has a Q_0 around a factor of 10^5 higher than a normal conducting cavity. This means that the dissipated power in the walls of the cavity is reduced by $\approx 10^5$. However, in order to reach this level, a superconducting cavity must be cooled to 2 K with LHe, which requires significant AC (or wall plug) power to produce or recondense the LHe.

The main challenge to overcome is the cryogenic efficiency. The total refrigerator efficiency (η_{tot}) is dependent on the product of the thermodynamic Carnot efficiency (η_{c}) and the technical efficiency of the cooling system (η_{t}), i.e.,

$$\eta_{\text{tot}} = \eta_{\text{c}}\eta_{\text{t}}. \tag{2.58}$$

For a refrigerator operating at temperature T_{hot} cooling a load to temperature T_{cold}, η_{c} is given by

$$\eta_{\text{c}} = \frac{T_{\text{cold}}}{T_{\text{hot}} - T_{\text{cold}}}. \tag{2.59}$$

Therefore, for a cavity being cooled from $T_{\text{warm}} = 300$ K to $T_{\text{cold}} = 2$ K, $\eta_{\text{c}} = 0.6\%$. The technical efficiency is usually around $20 - 30\%$, therefore this gives $\eta_{\text{tot}} = 0.12 - 0.18\%$, demonstrating the inefficiency of the cryogenic system.

Once the total efficiency is known, it is possible to calculate the total cryogenic power (P_{cryo}) required for cooling. This must take into account the total heat load on the cavity at cryogenic temperatures (P_{cold}). This is not only dependent on the RF power dissipated in the cavity walls but also on static heat loads due to heat leaks from higher temperature stages (e.g. via RF and electrical cables). As a result, P_{cryo} is given by

$$P_{\text{cryo}} = \frac{P_{\text{cold}}}{\eta_{tot}}. \tag{2.60}$$

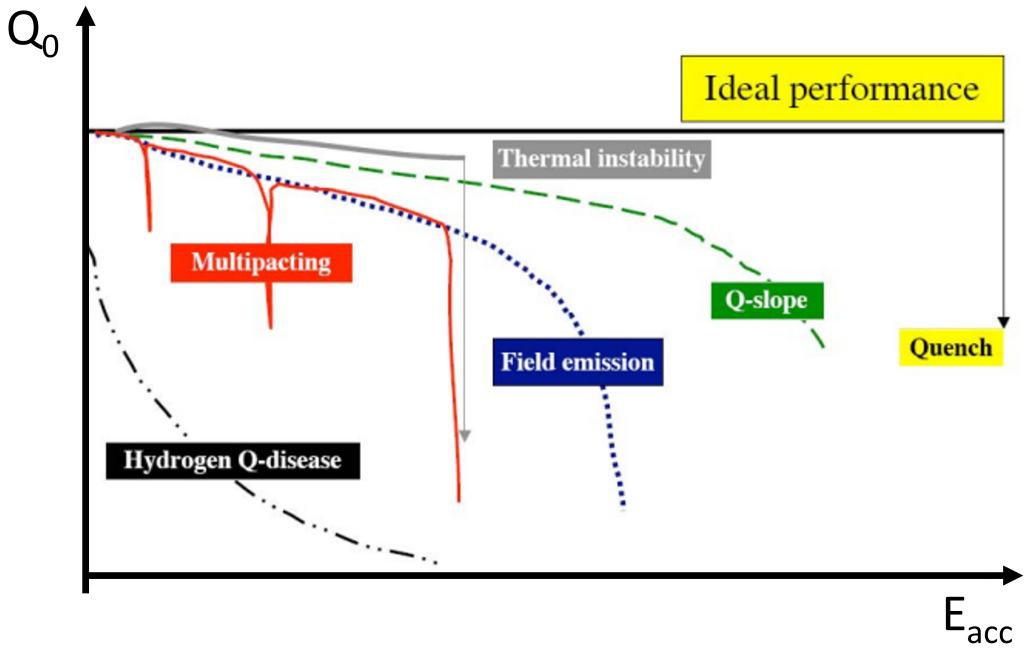

Figure 2.12: SRF cavity loss mechanisms [60].

For example, for an SRF cavity operating at 2 K with a total heat load $P_{\text{cold}} = 10\,\text{W}$, $P_{\text{cryo}} = 5.6 - 8.3\,\text{kW}$ (depending on the technical efficiency).

2.3.2 Limiting Factors

Testing SRF cavities will produce typical shapes of the $Q_0(E_{\text{acc}})$ curve. Some of these curves that might be observed are illustrated in Figure 2.12 [60]. An ideal cavity should have a horizontal $Q_0(E_{\text{acc}})$ curve at its maximum Q_0 reaching its maximum E_{acc} (limited by the B_{sh} of the material). However, cavity tests will always deviate from this ideal performance due to one or more loss mechanisms which will quickly lead to thermal runaway, cavity quenching and a rapid drop in Q_0 (Q-slope). This makes the cavity unable to sustain RF energy.

2.3.2.1 Multipacting

Multipacting is a resonant phenomenon in which a large number of electrons can build up at a point within the cavity surface. The process starts with an electron emitted from the cavity surface. This emitted electron is accelerated by the RF fields within the cavity before it impacts another portion of the cavity wall. The key multipacting phase condition is that the electrons must return at the same phase as they were emitted at. The phase relates the timing between the electron emission relative to the oscillation of the electric field. If the electrons are emitted at a time when the electric field accelerates them back towards the wall this will lead to more impacts and the release of secondary electrons in a resonant loop. These secondary electrons are then accelerated as well before impacting the wall and producing more electrons. This process keeps repeating, there is an exponential increase of electrons. The accelerated electrons absorb energy from the RF field and will deposit this energy as heat in the cavity walls after every collision. This can lead to a significant increase in the temperature of the cavity wall, resulting in thermal breakdown if the temperature rises above T_c. This mass of electrons then absorbs the RF power input into the cavity making it difficult to increase the cavity fields further with an increase in power.

The mean number of secondary electrons emitted per impact is known as the secondary emission coefficient (SEC, δ). This quantity varies for different materials but has a general functional shape, as shown in Figure 2.13. This firstly shows how SEC increases to 1 with increasing kinetic energy to a certain value, K_1. This is simply because each impacting electron loses all of its energy during impact and the mean number of electrons emitted is proportional to the impact energy of each electron. When the electrons have kinetic energy greater than K_1, $\delta > 1$, multipacting occurs if the electron transit time is an integer number of periods. This is the resonant phenomena for multipactor. When the energy increases past the peak, the electron penetrates further and fewer secondary electrons are able to escape, resulting in a decrease in δ. The value of δ then reaches 1 again once the

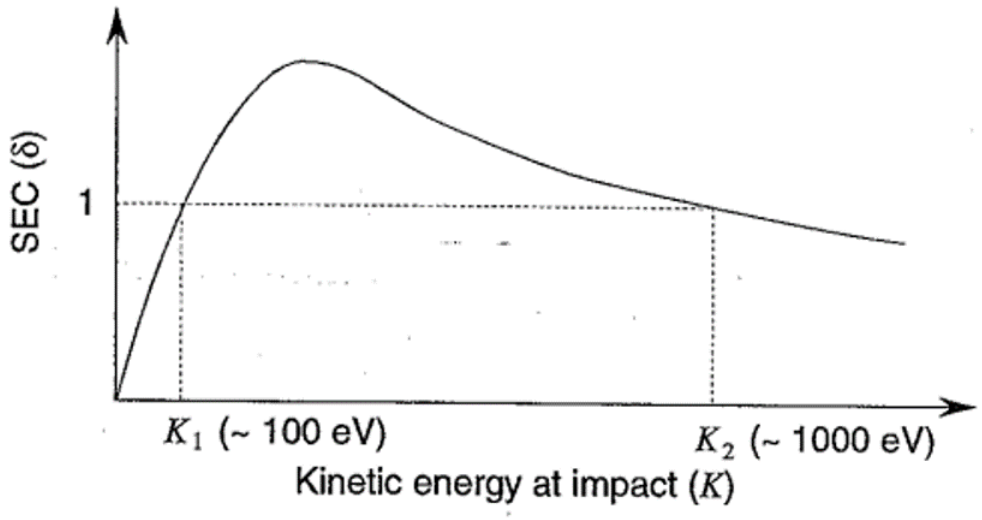

Figure 2.13: Secondary emission coefficient, δ, as a function of impact kinetic energy [37].

kinetic energy of electrons reaches K_2 [37].

The main way to minimise the risk of multipacting in RF cavities is to use cavities with rounded walls at the equator, as shown previously in Figure 2.2. In this configuration, the electrons are deflected to the equator whereby the electric field perpendicular to the cavity is very low. At this point multipacting ends because the electrons cannot gain enough energy to release secondary electrons [61]. In addition, ideally one would use low-SEC materials, but one must also ensure that the materials are clean, e.g. by running a vacuum bakeout or argon discharge cleaning.

2.3.2.2 Thermal Breakdown

Thermal breakdown (or thermal quenching) typically originates at sub-millimetre sized regions (defects) within the cavity. It can also occur at regions with a high surface magnetic field. Within this region, the temperature is higher than in surrounding areas. As the field increases, the defect temperature can rapidly exceed T_c and therefore becomes normal conducting, thus limiting the maximum E_{acc}. The material near the defect also becomes normal conducting, resulting in a rapid increase in power dissipation and a decrease in Q_0. Defects can be caused by

contamination in the cavity, e.g., a particle of Cu. It is also possible to measure defects using a thermometric method (detailed later in Section 3.2.3) by measuring the variation in surface temperature in the cavity as the field increases.

A simple model is used to calculate the maximum field at which the defect will reach thermal breakdown. For a hemispherical defect of radius a, surface resistance R_{n}, cooled to bath temperature T_{b}, the maximum field reached before quenching is given by [62]

$$H_{\mathrm{max}} = \sqrt{\frac{4\kappa(T_{\mathrm{c}} - T_{\mathrm{b}})}{aR_{\mathrm{n}}}}, \tag{2.61}$$

where κ is the thermal conductivity.

From this, it is clear that the larger the defect, the lower the maximum field. However, the maximum field reached can be increased by using a material with higher thermal conductivity. These materials should be those with high RRR. More complex models simulate the onset of thermal breakdown by calculating the equilibrium temperature distribution on the Nb surface in the presence of a magnetic field by incorporating all the factors that influence heat production and heat transport [63].

However, there are various solutions to thermal breakdown. Any identified defects can be removed by mechanical grinding. This should work for defects on the order of sub-millimetres. Secondly, increasing the thermal conductivity of Nb by using higher material RRR would result in an increase in H_{max}, allowing higher powers to be input into the cavity before thermal breakdown. However, a higher RRR would result in a higher R_{BCS}, as illustrated previously in Figure 2.10. A third option is to use Nb thin films coated on Cu cavities because of the higher thermal conductivity of the substrate Cu allowing for more efficient heat dissipation (detailed later in Section 2.4).

2.3.2.3 Field Emission

Thermal breakdown relates to the surface magnetic field, however, there are also limitations associated with the surface electric field. This mainly occurs due to electron emission from regions of high electric field within the cavity. These regions are known as field emitters and will lead to temperature a rise.

The theory of field emission can be understood by considering the electrostatic potential of electrons in a metal. Electrons are confined within specific energy levels inside a potential well such that, under normal circumstances, they have insufficient energy to escape. However, in the presence of an electric field, the work function (ϕ) is lowered, meaning that electrons can tunnel through the potential well and escape from the metal.

The current of tunnelling electrons as a function of applied electric field, E, has been derived by Fowler and Nordheim [64] and is given by

$$I(E) = \frac{A_{\mathrm{FN}} A_{\mathrm{e}} (\beta_{\mathrm{FN}} E)^2}{\phi} \exp\left(-\frac{B_{\mathrm{FN}} \phi^{3/2}}{\beta_{\mathrm{FN}} E}\right), \tag{2.62}$$

where A_{e} is the effective emitting area, A_{FN} and B_{FN} are the Fowler Nordheim parameters which can be determined experimentally and β_{FN} is the field enhancement factor.

Understanding β_{FN} is key to understanding field emission. The field enhancement could be explained by defects or contaminations, however these are not usually found under microscopic examination. In fact, field emission can be explained by the microgeometry of particles on the surface of cavities, which can be introduced by contamination. This theory models β_{FN} as a contribution from both the particle as a whole and smaller protrusions on the particle [65]. In superconducting cavities, this emission is observed from localised sites. As with thermal breakdown, these can be monitored using the thermometric method as well as measuring X-ray flux due to bremsstrahlung radiation.

2.3.2.4 Q Disease

One loss mechanism that can limit Q_0 at low E_{acc} is known as Q disease. This occurs because of the presence of hydrogen dissolved in the bulk Nb that that has the ability to form lossy Nb hydrides at the surface during cooldown. The concentration of hydrogen required to form the hydride phases decreases with temperature. However, at temperatures between 150-70 K, the required concentration of hydrogen to form hydrides is low enough such that the rate of hydride formation becomes significant. Therefore, the cooldown rate over this temperature range must be fast enough to limit hydride formation.

Figure 2.14(a) shows an experiment with different cooldown times of a 1.5 GHz Nb cavity in the $150 - 75$ K 'danger zone' with measurements of Q_0 shown in Figure 2.14(b). The cavity was first rapidly cooled to base temperature before being warmed to a temperature within the 'danger zone' and subsequently cooled to base temperature before being repeated with various hold times within the 'danger zone'. It is clear that an increase in the time spent within this zone leads to a degradation of Q_0 [66]. In addition to adjusting the cooldown time, a 600 °C or higher temperature bake for several hours can promote the diffusion and outgassing of hydrogen in UHV conditions.

2.3.3 Residual Resistance

The measured R_{s} of SRF cavities is always higher than R_{BCS}. The additional losses cannot be explained by the BCS theory; therefore, they are represented by an additional loss factor known as the residual resistance, R_{res}, which is temperature independent. As a result

$$R_{\mathrm{s}} = R_{\mathrm{BCS}} + R_{\mathrm{res}}. \tag{2.63}$$

Over the years, these residual losses have been accounted for by several sources that normally arise from cavity preparation and treatment, including the effects of

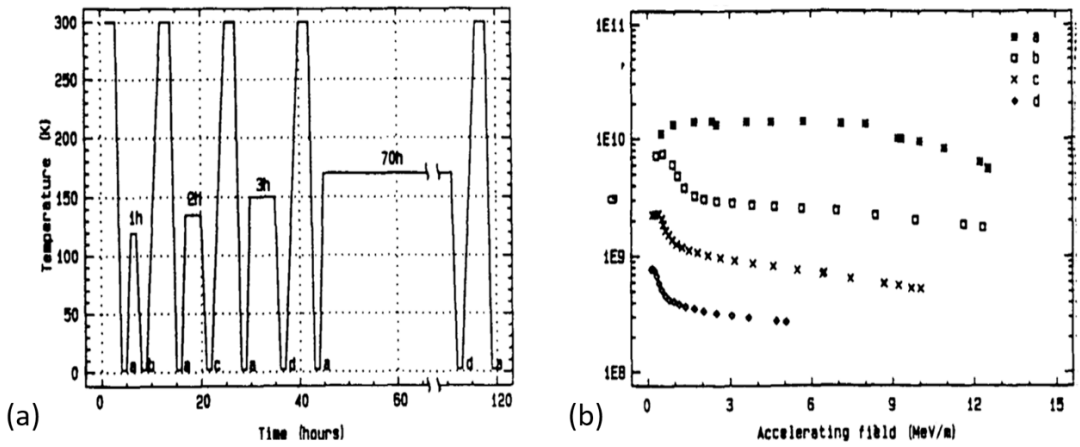

Figure 2.14: Q-disease measurements: (a) different thermal cycles, (b) Q_0 as a function of accelerating gradient at 1.6 K measured after each thermal cycle [66].

Q-disease previously discussed. Failure to mitigate these factors will result in an SRF cavity that does not reach its theoretical maximum Q_0. However, as a result of several decades of research, it is possible to mitigate these losses if some key steps are taken during the cavity preparation procedure. Some of the sources of residual losses, as well as the steps taken to reduce them, are listed in Table 2.1

2.3.4 Bulk Niobium SRF

Significant improvements in cavity preparation procedures and methods to mitigate limiting factors and minimise residual losses have improved the RF performance of bulk Nb cavities in recent years. These treatments, detailed later in Section 7.1.1, include HPR with UPW, electropolishing (EP) or buffer chemical polishing (BCP), high temperature ($600 - 800\,^{\circ}$C) bakes and low temperature ($120\,^{\circ}$C) bakes.

In recent years, nitrogen infusion has produced cavities that regularly reach, $Q_0 = 10^{10} - 10^{11}$ and $E_{\mathrm{acc}} > 40\,\mathrm{MV/m}$ at 2 K [67]. In addition, 1.3 GHz TESLA shaped single-cell cavities have demonstrated $E_{\mathrm{acc}} > 50\,\mathrm{MV/m}$ at 2 K with a modified $75/120\,^{\circ}$C low-temperature bake procedure [38]. However, regularly achieving high quality bulk Nb cavity performance comes at a significant cost for the

Table 2.1: Sources of residual losses and mitigation methods.

Source	**Mitigation**
Large surface roughness.	Mechanical or chemical surface polishing.
Contaminants, chemical residues, condensed gases.	Light chemical etching and/or cleaning in a clean with UPW HPR.
Dissolved hydrogen forming lossy Nb hydrides in surface.	High temperature bake (e.g. 600 °C).
Dissolved oxygen forming lossy Nb oxides in surface.	Low temperature bake (e.g. 120 °C).
Trapped magnetic flux from external DC magnetic field during cooldown.	Fast cooldown and magnetic shielding.
Trapped flux generated by thermocurrents.	Uniform cavity cooling and controlled cooling rates to minimise thermal gradients.

raw materials, manufacturing, and liquid helium (LHe) cooling, therefore alternative methods should be considered.

2.4 Thin Film Superconducting RF

For all new accelerators and accelerator upgrades, the production and operational cost of the superconducting accelerating structures is a significant factor. There is now a growing push to investigate more sustainable solutions that are able to match or even exceed the performance of bulk Nb. In addition, with the increasing cost of raw Nb and LHe, as well as the unsustainable mining of bulk Nb, these structures are becoming increasingly less attractive for future accelerators. The focus is on lowering capital and reducing operating costs for improved sustainability whilst still meeting performance specifications. For facilities requiring CW operation, e.g., X-

ray free-electron lasers, higher temperature operation must be explored to reduce the high operational costs associated with 2 K operation.

An alternative pathway is to use thin film superconductors deposited on other substrates. In order to transition from bulk Nb to thin film SRF cavities, three main areas were identified as the key goals for thin film research and development [68]:

- Developing Nb-coated Cu (Nb/Cu) cavities.
- Developing Cu cavities coated with alternative superconductors, such as Nb_3Sn, NbTiN and MgB_2.
- Developing superconducting-insulating-superconducting (SIS) multilayers.

2.4.1 Niobium on Copper

As discussed in Section 2.2.1, the penetration of the RF and DC magnetic field components into a bulk Nb cavity is defined by λ_L, which is usually in the range of a few 10s of nm into the cavity surface. The remaining wall thickness of the cavity provides structural support and thermal conduction for cooling. Instead of bulk Nb, the RF layer is a thin film of Nb deposited with a thickness of a few μm on a substrate with optimised thermal conductivity, such as Cu. In theory, this should be sufficient to provide the same RF performance as bulk Nb whilst using considerably less Nb material. This could also form part of an SIS multilayer structure as illustrated in Figure 2.15, which is discussed briefly in Section 2.4.2. Additional thin film layers could also be applied to mitigate performance-degrading issues such as high SEY, gas diffusion, and poor thermal conductivity.

The cost of Nb cavity raw material and production and its relatively low cryogenic thermal conductivity are the main reasons why Cu is being studied as the base material for SRF cavity manufacture. Cu substrates have several advantages over Nb:

- Higher thermal conductivity at cryogenic temperatures resulting in improved cooling and thermal stability.

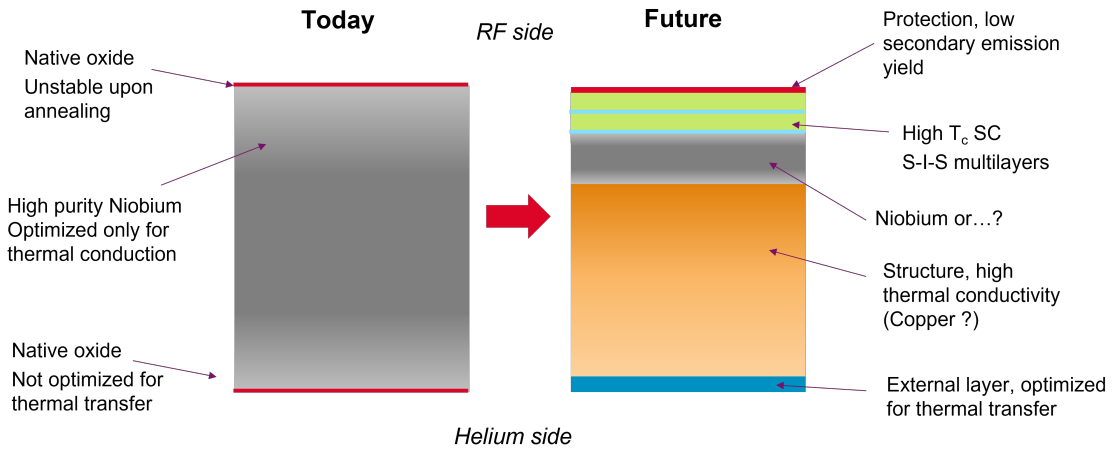

Figure 2.15: An illustration of an alternative pathway for thin film superconducting RF cavities instead of bulk Nb. Courtesy C.Z Antoine (CEA) [68].

- Wider availability of material.
- Lower material costs.
- More easily machinable.
- Less harsh chemicals required for polishing.

Figure 2.16(a) shows the effect of the normal state RRR (proportional to electron mean free path) on R_{BCS}. For bulk Nb, the RRR is usually $300 - 400$ in order to maximise the thermal conductivity. However, a factor 2.5 lower R_{BCS} is achievable for lower RRR, thus increasing Q_0 by the same factor assuming no change in R_{res}. The RRR of a thin film can be tuned to be closer to this minima if deposited on high thermal conductivity Cu. Figure 2.16(b) shows the effect of increasing frequency on R_{BCS}. Shown is the line below which, $Q_0 > 10^{10}$ for $G = 270\,\Omega$. For a bulk Nb cavity operating at 2 K it is possible to achieve this Q_0 for $f < 2\,\mathrm{GHz}$, however at 4.2 K this is only possible for much larger cavities in the range of $100 - 200\,\mathrm{MHz}$. The benefit of thin film Nb, is being able to achieve $Q_0 > 10^{10}$ up to $\approx 400\,\mathrm{MHz}$ at 4.2 K due to the lower R_{BCS} shown in Figure 2.16(a).

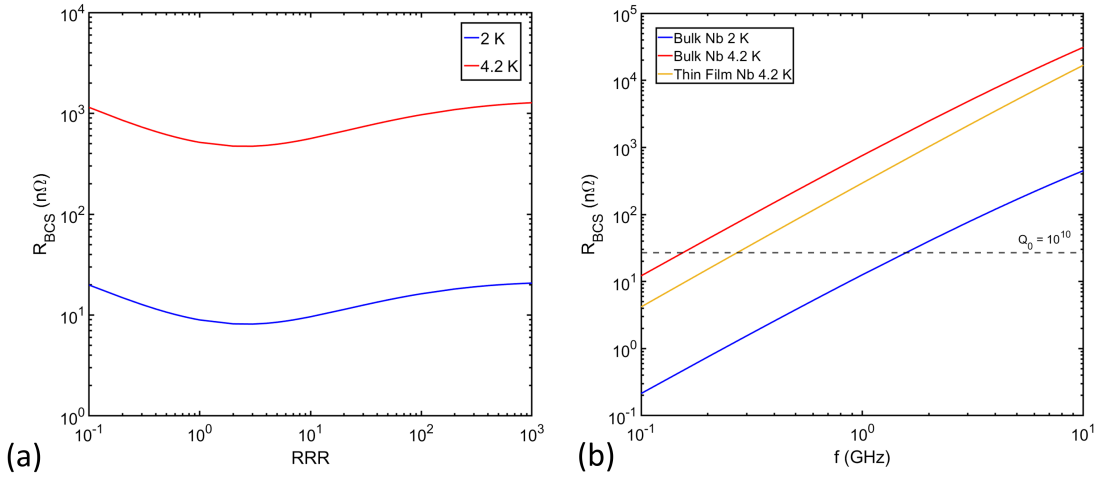

Figure 2.16: (a) Theoretical BCS resistance of bulk Nb as a function of RRR for a 1.3 GHz cavity at 2 K and 4.2 K. (b) Theoretical BCS resistance as a function of frequency for a bulk Nb cavity at 2 K and 4.2 K and a thin film Nb cavity at 4.2 K. The dashed line represents $Q_0 = 10^{10}$ for $G = 270\,\Omega$ (assuming minimal R_{res}) below which Q_0 increases. Both Calculated using SRIMP [56, 58] with material parameters: $\Delta(0)/k_{\mathrm{B}}T_{\mathrm{c}}$,$=1.86$, $\lambda_{\mathrm{L}} = 32\,\mathrm{nm}$; $\xi_0 = 39\,\mathrm{nm}$, $T_{\mathrm{c}} = 9.2\,\mathrm{K}$ [53].

Operation at $\approx 4.2\,\mathrm{K}$ allows for significant cost savings in cryogenic infrastructure. The higher temperature means that the cryogenic system can work with LHe instead of the superfluid He that is required for 2 K operation. This means that the complex addition of superfluid heat exchangers and additional pumps, which also require additional maintenance, is not required. Some cost estimates for the European Spallation Source (ESS) report possible cost savings of 15 M€ for cryogenic infrastructure if cavities were to be operated at 4.5 K instead of 1.8 K [69].

Another significant cost comes from the cryogenic operation of SRF cavities, which requires high-energy-consuming LHe cryogenic plants. To compensate for heat loads at cryogenic temperatures, the refrigerator needs to extract wall-plug power. This is inversely proportional to refrigerator efficiency, which improves at higher temperatures. Section 2.3.1 detailed how the efficiency of a cryoplant can be calculated from the product of the Carnot efficiency and the technical efficiency.

Table 2.2: A comparison of the efficiency of a cryogenic system at 2 K and 4.2 K with η_t from [69].

	Efficiency (%)	
	2 K	4.2 K
η_c	0.7	1.4
η_t	$15-20$	$25-30$
η_{tot}	0.14	0.42

A comparison of the efficiency calculations for 2 K and 4.2 K operation is shown in Table 2.2. Here, η_t is estimated from [69]. Therefore, a factor 3 lower plug power consumption for the higher temperature operation is possible. Although the operation of 4.2 K is still fairly inefficient, significant savings can be expected for the electrical operation of thin film cavities at this temperature in addition to infrastructure costs. The cost savings for ESS are estimated to be $3-5$ M€ per year if a higher temperature operation were possible [69].

Research into the use of thin film Nb began in the 1980s with the use of Nb/Cu cavities for the Large Electron Positron Collider (LEP) at CERN [70]. Since then, 400 MHz Nb/Cu cavities have been installed in the Large Hadron Collider (LHC) [71] and, most recently, Nb thin film technology has been used for the 100 MHz quarter-wave resonator (QWR) cavities used in the High Intensity and Energy Isotope Separator On Line DEvice (HIE-ISOLDE) at CERN [72]. However, despite achieving higher Q_0 compared to bulk Nb cavities at low field, Nb/Cu cavities suffer from steep Q-slope at intermediate E_{acc} [73]. This effect currently limits Nb/Cu cavities to operation at $E_{acc} \leq 10$ MV/m [74], which is approximately a factor 5 lower than the maximum achievable with bulk Nb. The hope is to use this technology in future accelerators, such as the Future Circular Collider (FCC) at CERN.

Further research and development, for example at CERN [75] and JLab [76], is ongoing with the aim of understanding this Q-slope and techniques to overcome it, as the technology is still a long way from matching the maximum achievable

gradient of bulk Nb. In hope of reaching that level, several research pathways are being explored:

- Improving film quality - the early Nb/Cu cavities were deposited with DC magnetron sputtering (DCMS). More energetic deposition techniques are being explored, such as high-power impulse magnetron sputtering (HiPIMS) that aim to yield films with higher density and overall quality [75, 77, 78] (detailed later in Section 7.2).

- Seamless cavities - these have been explored to remove defects around the cavity welds, which can be a source of poor film adhesion and significantly increase RF losses. For example, HIE-ISOLDE seamless cavities have demonstrated improved accelerating gradients [79] and both electroformed and bulk machined seamless 1.3 GHz cavities at CERN have been shown to be comparable to bulk Nb at low field [80].

- Additive manufacturing - being investigated at INFN [81] as a method to simplify and reduce the cost of manufacturing seamless structures. However, these might not all be ideal techniques for manufacturing a large number of cavities, so classical methods such as spinning and hydroforming continue to be investigated.

- Split cavities - these are being explored to see if Cu cavities can be manufactured in either halves or quarters. The parts would then be bolted together without a physical weld. This allows for easier depositions and inspection of the film post-deposition, and the removal of defects as with seamless cavities. It is being explored at CERN with 600 MHz and 1.3 GHz Slotted ELLiptical (SWELL) cavities [82, 83] and at Lancaster University/STFC with longitudinally split 1.3 and 6 GHz cavities [5, 9, 11]

- Improving substrate quality - the film growth is ultimately dictated by the substrate quality [84]. The crystal structure of the substrate and the level

of roughness will strongly affect the initial film nucleation, which will dictate the growth of the film. In addition, any impurities on the substrate may be incorporated into the film. Therefore, surface preparation research is vital. For example, sustainable methods, such as plasma electrolytic polishing (PEP), are being developed using more environmentally friendly diluted salt solutions compared to the harsh acids typically used with electropolishing [85, 86]. Mechanical polishing methods such as centrifugal barrel polishing (CBP), diamond turning and metallographic polishing are also being explored [87–90].

2.4.2 Alternative Superconductors

It has been demonstrated with Nb/Cu that operation at 4.2 K is highly desired to reduce both cryogenic infrastructure and operational costs. However, for Nb, this is only possible with low-frequency structures. For higher frequency machines, e.g., 1.3 GHz, alternative superconducting materials must be investigated for 4.2 K operation if one wants to match or exceed Nb Q_0 at 2 K. In addition, for new accelerators (e.g., for high energy physics (HEP) applications or machines requiring more compact accelerating infrastructure) it is desirable to increase E_{acc}.

Research into alternative superconductors has been ongoing in recent decades. Importantly, these materials must be able to be deposited on a substrate material without delamination. They must also have high T_{c} and large Δ to minimise R_{BCS} at 4.2 K. To exceed the accelerating gradients of Nb, these materials should also have higher H_{c} and H_{sh}.

Only a small number of superconducting compounds have been found to be viable candidate materials. These include NbTiN, Nb_3Sn, V_3Si, MgB_2, which all have higher H_{sh}, T_{c} and Δ in their optimal composition. They have lower H_{c1} than Nb [39], however, as detailed in Section 2.2.3, a low H_{c1} is not a limiting factor for the maximum RF field. Research on some of these materials has been ongoing since the 1970s, however, RF performance beyond bulk Nb has not yet been achieved. The superconducting material parameters of these alternative materials are shown

Table 2.3: Superconducting parameters from literature for some of the alternative superconductors being studied at Daresbury Laboratory ((0) denotes the value at 0 K).

Material	T_c (K)	λ_L (nm)	ξ_0 (nm)	$\Delta(0)$ (meV)	$B_{c1}(0)$ (mT)	$B_{sh}(0)$ (mT)	$B_c(0)$ (mT)	Ref.
Nb	9.25	24-30	39	1.5-2.5	174	199	240	[75, 91]
NbTiN	17.3	150-170	2-3	2.8	24	439	500	[39, 92]
Nb_3Sn	18	65-89	5-7	3-3.4	38	440	520	[91–93]
V_3Si	17	179	3.5	2.5	72	490	720	[39, 94]
MgB_2	40	185	4.9	1.7/7	18	210	260	[95, 96]

in Table 2.3.

Of these materials, Nb_3Sn has received the most attention. This belongs to the class of A15 compounds with a stoichiometric composition of A_3B which are of interest due to their T_c approximately twice that of Nb [97]. This class of materials, as well as the other candidate materials, are too brittle to form a bulk cavity structure on their own; therefore, they must be developed as a thin film, or as metallic vapour diffusion into bulk Nb. With a theoretical $T_c \approx 18\,\mathrm{K}$, and $H_{sh} \approx 400\,\mathrm{mT}$, Nb_3Sn offers the potential for high Q_0 and operation with higher E_{acc} [37]. It is thought that $E_{acc} \approx 100\,\mathrm{MV/m}$ is the theoretical maximum at 4.2 K [98]. As well as the 4.2 K operation described previously, this offers the potential for machines needing fewer superconducting cavities. This would not only save significant capital cost of the accelerating structure and required cryogenic plants but also reduce the size of the overall accelerator, thus reducing other costs elsewhere, e.g. length of beam pipes, vacuum infrastructure, length of tunnel/shielding, etc. Ultimately, the design goals of the accelerator will dictate whether its high Q_0 or high E_{acc} that is prioritised.

The most promising alternative material that has provided RF performance

comparable to a Nb cavity is Nb_3Sn. The technique used was tin (Sn) vapour diffusion which forms a thick Nb_3Sn film on the surface of a bulk Nb cavity by heating a cavity above 950 °C in the presence of a heated Sn source. A set of cavity measurements, in Figure 2.17(a), shows how it is possible to achieve a $Q_0 > 10^{10}$ at higher temperature than Nb due to nearly double the T_c. Here, the roll off in Q_0 at low T is due to the cavity R_s being dominated by an $R_{res} = 9.5\,n\Omega$ at these temperatures. Figure 2.17(b) shows that the inverse coefficient of performance (COP^{-1}), defined as the watts of wall power required to remove one watt of heat), is around a factor of 3 lower at 4.2 K than 2 K, consistent with the efficiency calculations in Table 2.2 [99].

The vapour diffusion technique was successfully applied in the 1990s at The University of Wuppertal, achieving Q_0 up to 10^{11} at 2 K and above 10^{10} at 4.2 K on a 1.5 GHz cavity with maximum $E_{acc} = 15\,MV/m$ at 2 K [100]. A more recent achievement is a high performing 1.3 GHz Nb_3Sn cavity that has demonstrated $Q_0 \approx 10^{10}$ at $E_{acc} > 10\,MV/m$ at 4.2 K in early 2010s at Cornell [101]. Most recently, a 1.3 GHz cavity has shown $E_{acc} = 24\,MV/m$ at 4.4 K and 1.3 GHz 9-cell cavities have been demonstrated for potential use in European XFEL and LCLS-II [102].

Alternative materials are also being investigated as part of multilayer structures. For this, the cavities are coated with superconductor-insulator-superconductor (SIS) layers, with superconducting layers smaller than λ. This principle was first theorised by Gurevich [103] as being a way of screening the underlying thick superconductor (or bulk Nb) from a higher H_{app}. This prevents vortex penetration into the bulk superconductor, which could allow fields $> H_{c,Nb}$ to be sustained within the cavity and therefore increase E_{acc}.

As of 2024, an alternative superconducting thin film sputtered on Cu has yet to demonstrate performance matching or exceeding Nb_3Sn/Nb produced by Sn vapour diffusion. This should be the initial goal for an alternative superconducting on Cu. Given the small coherence length of Nb_3Sn (and other alternative compounds), one of the main limiting factors for cavity performance has been identified as surface

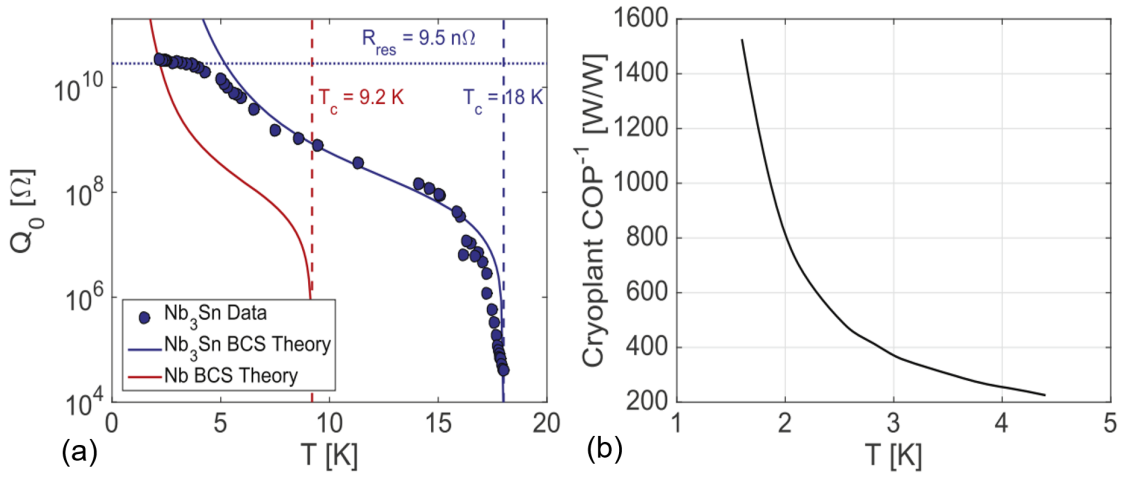

Figure 2.17: (a) Q_0 as a function of cavity temperature for a 1.3 GHz Nb_3Sn cavity compared to Nb_3Sn and Nb BCS theory, (b) the inverse coefficient of performance as a function of temperature [99].

roughness [104] as well as ensuring strong film adhesion and low residual resistance. Therefore, optimising the deposition parameters and substrate preparation are two key areas of research. Research at STFC Daresbury Laboratory has been ongoing for more than a decade on the use of Nb_3Sn [17, 105], V_3Si [3, 6, 10, 106], NbTiN [107, 108], NbN [107, 109, 110], MgB_2 [111] and SIS multilayers [112]. Progress has mainly been made on planar samples and small 6 GHz cavities, although there are plans to scale this to 1.3 GHz and larger cavities in the near future. One of the main bottlenecks for this research is the ability to provide rapid superconducting testing of candidate coatings.

Chapter 3

RF Characterisation of Planar Samples

A vital part of thin film research and development for SRF cavities is cryogenic testing of superconducting properties. This must include testing under RF conditions to measure Q_0 and/or R_s to understand the performance of the material. A cost-effective research pathway must include optimisation of substrate preparation techniques and thin film deposition parameters on small, planar samples prior to cavity development.

The following chapter provides a brief overview of the motivation for small-sample cryogenic testing. It includes details on why an RF test facility was required at Daresbury Laboratory in addition to the existing DC test facilities. There are typically three main measurement methods to characterise samples under RF conditions which are described and compared. Details and comparisons of the different vertical test facilities worldwide that use these measurement methods are shown, whilst highlighting what must be considered to build an RF test facility for small sample tests.

3.1 Planar Sample Testing

3.1.1 Motivation For Small Sample Testing

As discussed in Section 2.4, thin film SRF cavities offer a promising alternative to bulk Nb cavities to improve the sustainability profile of all future accelerator builds and upgrades. However, thin film coated cavities are very sensitive to preparation procedures and thin film deposition parameters, making it difficult to produce cavities that match or exceed the RF performance of bulk Nb. These must be optimised to maximise Q_0 and also mitigate the effects of the limiting factors discussed in Section 2.3.2 that result in a Q-slope and limit the maximum E_{acc}.

Attempting to develop thin film cavities may be possible by performing and testing countless thin films deposited on full-sized cavities manufactured to the shape and frequency required for the application. Typical high-power SRF tests would be performed to compare $Q_0(E_{\mathrm{acc}})$ for each cavity. This approach has typically been used for the optimisation of bulk Nb cavities in the past 60 years. However, the time and effort required to manufacture, polish, coat, and test cavities for thin film testing makes this approach much too costly and time-consuming. The RF testing alone could easily take one week, including cavity loading, cooling, and performing all the RF calibrations and measurements. Additional time-consuming steps then exist to remove a film and re-polish the cavity for more tests.

Coating on a curved surface has added complexities. The main one being that some of the alternative superconductors being studied might not be developed enough to be deposited on a full-sized cavity. It might also be difficult to control film thickness, uniformity and adhesion.

There are also issues with post deposition analysis. Once a thin film is deposited on the inside of a cavity, it is very difficult to analyse the surface structure and morphology of the film to help understand the measured results. For surface analysis, a cavity would have to be cut, meaning that it could not be reprocessed for future depositions, again increasing the cost. For deposition and substrate preparation

processes that have not been optimised, it is vital that results from RF measurements are compared with results from many other analysis techniques to help improve the thin film parameter optimisation.

The best approach requires depositing on a versatile open geometry that can be used for a range of analysis techniques. Typically, thin films are first deposited on small planar substrates (a few cm diameter maximum). Such a geometry allows for a much higher throughput of sample production compared to cavity production. The samples can then be analysed using a variety of superconducting and surface characterisation techniques, with the priority being RF measurements. This allows identification of candidate thin films before the processes are repeated on curved surfaces, which is always more difficult.

The main benefits of using small samples instead of cavities are:

- Significant cost savings as a result of a reduction in raw material.
- Easier to achieve consistent surface finishes during substrate preparation and polishing. This means that performance differences between samples can be attributed to the thin film deposition processes only.
- A wide range of deposition parameters can be studied quickly, as deposition facilities often use loadlock chambers to deposit multiple samples sequentially without breaking the vacuum in the deposition chamber [113].
- It is simpler to deposit on a flat surface than on a curved surface and achieve a uniform coating [114]. Therefore, it is easier to attribute sample performance to the intrinsic properties of the film.
- Easier production of planar target materials than that of cylindrical targets and easier to control magnetic field. This allows for better control of target stochiometry and purity prior to deposition [115].
- Sample testing requires a less complicated cryogenic vessel due to easier sample cooling and less space required.

- Samples can be easily transferred to other facilities for further superconducting measurements and surface analysis.

Having prepared the samples, it must be possible to measure their performance using a variety of methods. These measurements should allow for characterisation of both the surface and the superconducting properties. Surface analysis can study the substrate before and after film growth to analyse the film characteristics that may lead to a higher than expected R_s or Q-drop at lower than expected E_{acc}. These measurements alone provide useful information on the surface characteristics of the films produced; however, this analysis is only useful when combined with measurements of the superconducting and thermo-mechanical properties under cryogenic conditions.

In general, the development of thin film samples consists of five main areas:

1. Substrate preparation.
2. Thin film deposition.
3. Superconducting RF measurements.
4. Superconducting DC measurements.
5. Surface characterisation.

3.1.2 DC Sample Characterisation

Many superconducting properties, such as T_c and B_c, can be measured using DC magnetic or resistive techniques. These can be performed fairly easily on small samples with standard four-point probes and magnetic probes [2] or commercial magnetometry (e.g. SQUID VSM) [116].

At Daresbury Laboratory, it has been possible for many years to characterise the DC superconducting properties of thin film samples [112, 117–120]. These are currently performed in two in-house developed cryogenic facilities based on LHe-free

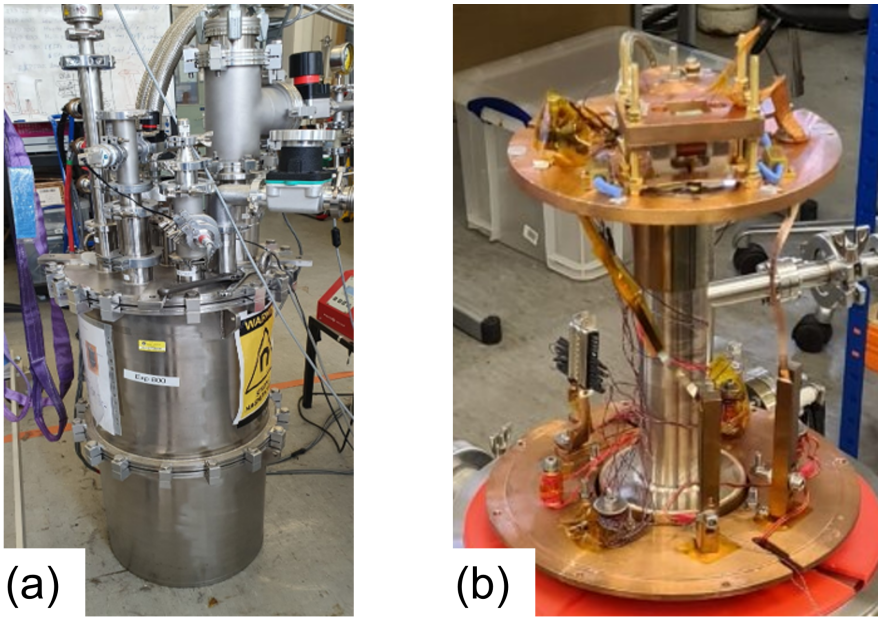

Figure 3.1: The two facilities in use at Daresbury Laboratory for measuring the DC superconducting properties of small samples: (a) the multiprobe facility [8], (b) the magnetic field penetration facility [119].

cryocoolers, as shown in Figure 3.1 [8]. These facilities are used to measure the T_c, RRR and the field of first flux penetration of the DC magnetic field applied parallel to sample (B_{fp}).

The quick sample testing process in these two cryogenic facilities provides useful information on film quality and behaviour under DC conditions. However, these do not provide an analysis under RF conditions. There is no evidence yet that these methods allow prediction of thin film behaviour under RF conditions.

3.1.3 RF Sample Characterisation

An RF test on a small sample is vital to assess whether a film might perform well as a coating on the inside a cavity when excited with an RF signal. It is important that superconducting RF measurements are performed soon after deposition to minimise any contamination that could increase the RF losses. Only after satisfactory results are obtained at each stage in the development pathway should all knowledge and

experience be applied to coat the curved surface of a cavity.

For planar samples, these RF measurements are typically more difficult than DC measurements due to the requirement to combine the sample with a bespoke resonator and measure sample losses independent of the resonator with minimal RF leakage. Several laboratories around the world have tried and tested methods to characterise planar samples under RF conditions [121]. The goal is to be able to calculate RF-related quantities such as R_s, f_0, λ, etc., all as a function of variables such as sample temperature and peak RF magnetic field on the sample surface.

The main aim at Daresbury Laboratory was to develop such a facility for the RF characterisation of planar thin coated samples to work alongside the existing DC characterisation facilities. Eventually, all facilities should be used in sequence to determine whether there is a correlation between RF and DC measurements on the same samples. To develop a new RF test facility, it is important to understand both the main RF sample measurement techniques and the existing facilities worldwide that use them.

3.2 RF Measurement Techniques

Measurement of RF losses on the sample surface requires the sample to be part of a resonant structure. Early experiments used simple pillbox cavity-like resonators [122], however, further developments have resulted in more complex cavity geometries.

When the resonator is excited at a specific EM mode based on its design, it should be possible to measure the sample R_s. Two main techniques can be used:

- End-plate replacement (indirect),
- RF-DC compensation (direct).

The common outcome for these two techniques is that they calculate the average R_s of the sample. They are unable to distinguish local variations in R_s; however,

this is not usually an issue for comparing samples. For measuring local variations, a third technique, known as the thermometric method, is sometimes used.

The eventual choice of method is made by balancing factors such as the required turnaround time, measurement range and resolution. These factors ultimately influence the design of the resonator, as will be clear later in Section 3.3.

3.2.1 End-Plate Replacement

The easiest way to measure the surface resistance of samples is with the end-plate replacement technique which has been used for more than 50 years [122]. An illustration of this method is shown in Figure 3.2. The resonator for this technique is typically a test cavity with an open end face. The test sample is mounted at this open-end to close the cavity and form a complete resonant structure. This technique requires two measurements of intrinsic quality factor to calculate the average sample R_s: (a) the first measurement is with a reference sample made from the same material and treated in the same way as the test cavity ($Q_{0,\mathrm{ref}}$), and second, (b) the reference sample is replaced with the sample of interest (Q_0).

Using this method, Q_0 is given by the combination of the cavity quality factor (Q_{cav}) and the sample quality factor (Q_{sam}):

$$\frac{1}{Q_0} = \frac{1}{Q_{\mathrm{cav}}} + \frac{1}{Q_{\mathrm{sam}}}, \tag{3.1}$$

where Q_{cav} does not include the sample.

Using the fact that surface resistance and quality factor are related by a geometry factor (Equation 2.11), it is possible to calculate Q_0:

$$Q_0 = \frac{1}{\frac{R_{\mathrm{s,cav}}}{G_{\mathrm{cav}}} + \frac{R_{\mathrm{s,sam}}}{G_{\mathrm{sam}}}}, \tag{3.2}$$

where $R_{\mathrm{s,sam}}$ is the surface resistance of the sample being tested and $R_{\mathrm{s,cav}}$ is the surface resistance of the test cavity. Furthermore, G_{sam} and G_{cav} are the geometry factors for the cavity and sample, respectively, which can be calculated using CST

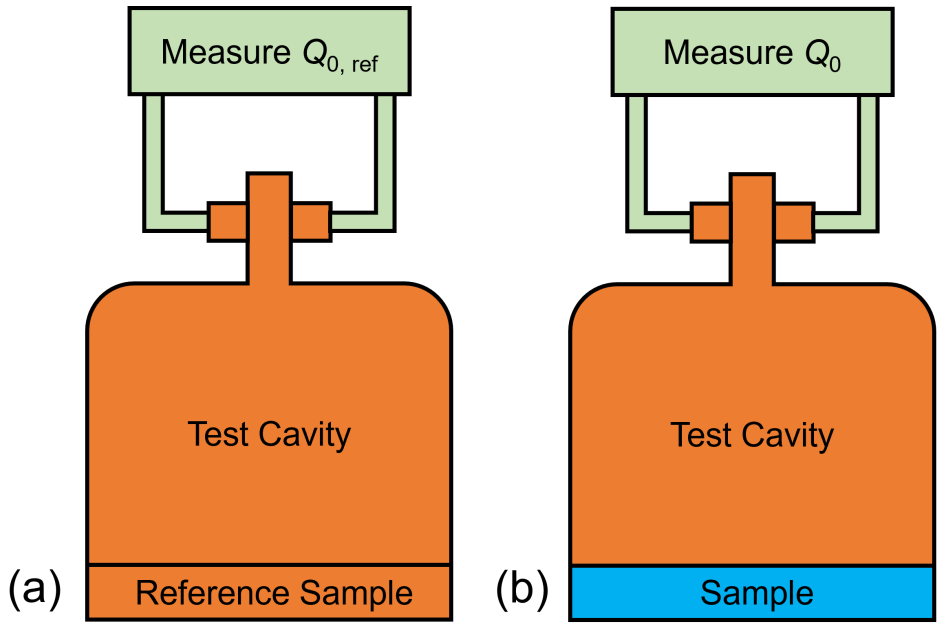

Figure 3.2: The two step process to measure the surface resistance of a sample using the end-plate replacement technique with: (a) the reference sample mounted to the test cavity, (b) the sample of interest mounted to the test cavity.

[44]. Using Equations 2.11 and 2.12, G_{sam} and G_{cav} are defined as:

$$G_{\text{sam}} = R_{\text{s,sam}} Q_{\text{sam}} = \frac{2\omega_0 \mu_0^2 U}{\int_{\text{sam}} |\mathbf{B}|^2 \text{dS}}, \tag{3.3}$$

and

$$G_{\text{cav}} = R_{\text{s,cav}} Q_{\text{cav}} = \frac{2\omega_0 \mu_0^2 U}{\int_{\text{cav}} |\mathbf{B}|^2 \text{dS}}. \tag{3.4}$$

Equation 3.2 requires knowledge of $R_{\text{s,cav}}$. This can only be calculated using a reference sample made from the same material and treated in the same way as the test cavity. For the case with a reference sample, it is assumed that $R_{\text{s,cav}} = R_{\text{s,sam}}$. Using Equation 3.2 for a test cavity loaded with the reference sample, $R_{\text{s,cav}}$ is given by

$$\begin{aligned} R_{\mathrm{s,cav}} &= \frac{1}{\left(\frac{1}{G_{\mathrm{cav}}} + \frac{1}{G_{\mathrm{sam}}}\right) Q_{0,\mathrm{ref}}} \\ &= \frac{G}{Q_{0,\mathrm{ref}}}, \end{aligned} \tag{3.5}$$

where G is the geometry factor for the entire cavity-sample system.

By substituting Equation 3.5 into Equation 3.2, $R_{\mathrm{s,sam}}$ can be calculated using a simple relation:

$$R_{\mathrm{s,sam}} = G_{\mathrm{sam}} \left(\frac{1}{Q_0} - \frac{1}{Q_{0,\mathrm{ref}}} \right) + \frac{G}{Q_{0,\mathrm{ref}}}. \tag{3.6}$$

Therefore, after initial calibration with a reference sample, calculating $R_{\mathrm{s,sam}}$ requires only Q_0. However, periodic re-calibration checks are advised.

3.2.2 RF-DC Compensation

The second technique is an RF-DC power compensation method, also known as the calorimetric method. The basic setup required for this is shown in Figure 3.3(a). For this, the sample must be connected directly to a DC heater and a temperature sensor to maintain a set temperature. This is usually done through a sample holder that is well thermalised to the sample, since it is often difficult to mount the required measurement devices to the sample directly. The sample must also be physically and thermally isolated from the test cavity in order to measure the RF losses on each of the surfaces independently of each other. This is also to ensure that there is no additional heat flow between the two via thermal conduction.

Control of the sample temperature is performed by varying the DC power applied to the sample heater. From measurements of DC power before and after RF is input at constant sample temperature, it is possible to directly measure the RF power dissipated on the sample surface. Then, combining DC measurements with RF measurements allows the average sample R_{s} to be calculated using Equation 2.9, assuming thermal gradients are the same or minimised under both DC and RF.

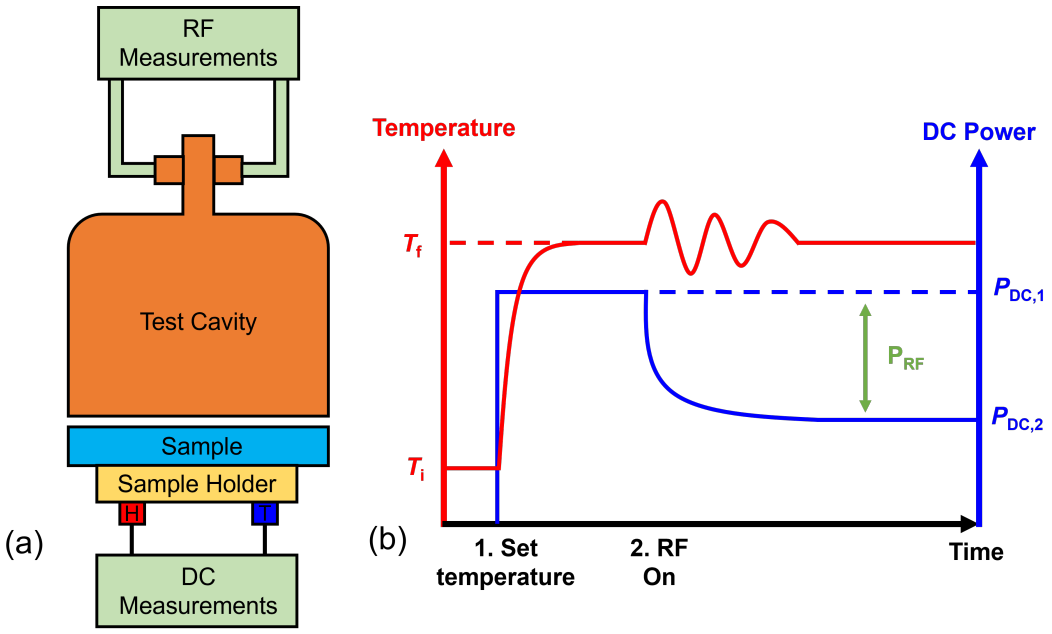

Figure 3.3: The RF-DC compensation method: (a) a sample mounted to a sample holder physically isolated from the test cavity (H and T represent the heaters and thermometers), (b) the RF-DC compensation method.

A two-step measurement process is required (illustrated in Figure 3.3(b)):

1. The sample is heated from an initial temperature (T_i) to a set temperature (T_f) by applying a current through the sample heater. The heater power ($P_{\mathrm{DC},1}$) is then calculated after the temperature and power have reached steady state.

2. RF power is then turned on. If the applied RF is at the resonant frequency of the test cavity, there will be RF dissipation on the surfaces of both the cavity and sample causing both temperatures to increase. The current through the sample heater is reduced to maintain the set T_f as in step 1. At steady state, the heater power is again measured ($P_{\mathrm{DC},2}$), where $P_{\mathrm{DC},1} > P_{\mathrm{DC},2}$.

Combining the measurements of $P_{\mathrm{DC},1}$ and $P_{\mathrm{DC},2}$ with Equation 2.9, the RF power dissipated on the sample, P_RF, is given by

$$P_\mathrm{RF} = P_{\mathrm{DC},1} - P_{\mathrm{DC},2} = \frac{1}{2\mu_0^2}\int_\mathrm{Sample} R_\mathrm{s}(B)|\boldsymbol{B}|^2 \mathrm{dS}, \tag{3.7}$$

where $\boldsymbol{B}$ is the magnetic field strength on the sample surface.

The integral in Equation 3.7 contains $R_{\mathrm{s}}(B)$ indicating local variations of R_{s} as a function of magnetic field on the surface of the sample. However, since the calorimetric measurement process measures the average powers and hence the average P_{RF} throughout the sample, it is not possible to measure these variations using this method. Therefore, to simplify the measurements, R_{s} is assumed to be constant over the sample surface area and independent of the magnetic field. Therefore, Equation 3.7 can be rearranged giving:

$$R_{\mathrm{s}} = \frac{2\mu_0^2(P_{\mathrm{DC},1} - P_{\mathrm{DC},2})}{\int_{\mathrm{Sample}} |\boldsymbol{B}|^2 \mathrm{dS}}. \tag{3.8}$$

It is not possible to experimentally calculate the denominator in Equation 3.8. Instead, this can be calculated using a combination of RF calibrations and electromagnetic simulations, detailed later in Section 5.3.

3.2.3 Thermometric Method

The end-plate replacement and RF-DC compensation techniques will provide only information on the average R_{s}. For the purpose of sorting and comparing samples, this is usually sufficient. However, in reality, the surface of the samples is not uniform, resulting in localised variations in temperature. These variations can be regions of thermal breakdown (detailed previously in Section 2.3.2.2) that will lead to thermal quenches. To map this out, a third technique, known as the thermometric method, is sometimes employed. This is also known as temperature mapping and would usually be used to supplement average any R_{s} calculations using the previous two methods, as it cannot resolve the absolute R_{s} alone.

The thermometric method requires an array of temperature sensors to be placed at different positions on the back of the sample. For this, a similar test cavity/sample setup can be used as the previous two methods, as shown in Figure 3.4(a). The main difference is the number of thermometers connected to the sample holder. Given that many are required, Allen-Bradley resistors, diodes or ruthenium dioxide sensors

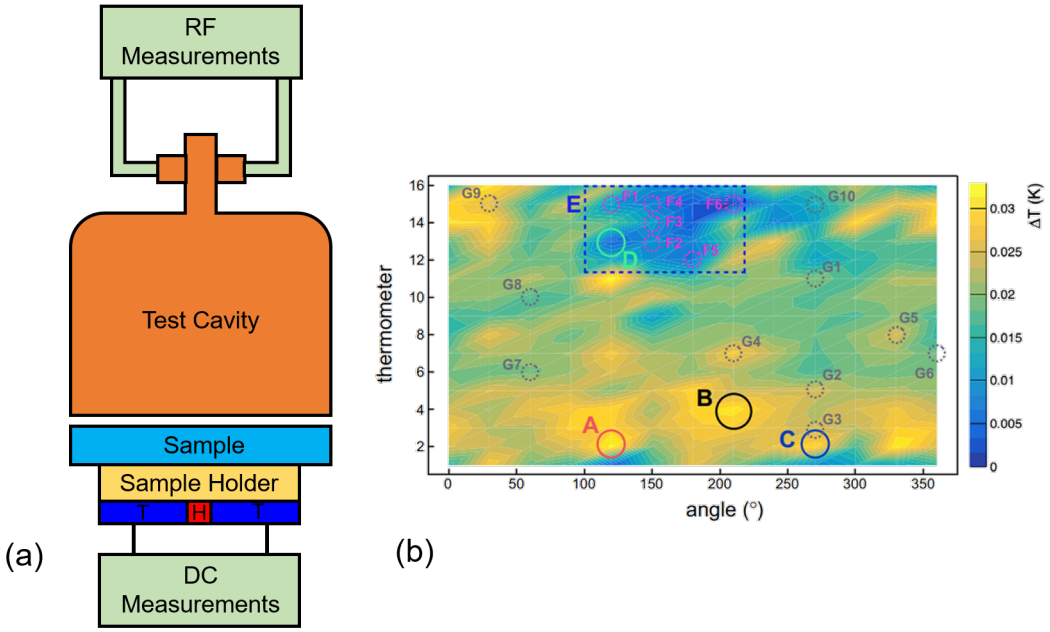

Figure 3.4: An example of a possible setup and measurements using the thermometric method: (a) the sample mounted to a sample holder underneath a test cavity, (b) an example of a 1.3 GHz Nb/Cu temperature map for with various hotspots and regions of interest highlighted [123].

are typically used because of their low cost. These, along with a data acquisition system, can map out local variations in temperature (ΔT) caused by local variations in RF losses on the sample surface.

An example of how the results might look is shown in Figure 3.4(b). This example shows a temperature map of a 1.3 GHz Nb/Cu cavity; however, similar plots are possible for sample tests. Here, sites of interest and regions with localised heating are circled [123]. Another example includes the addition of thermometer arrays to multicell 1.3 GHz bulk Nb cavities at Cornell University [124]. In addition, a calibration with DC heaters may be used for calculations of the RF power dissipated at various points on the sample as a function of the temperature change. This, along with knowledge of the heat capacity and thermal conductivity of the sample, allows measurements of the variation in R_s.

3.2.4 Comparison

As has been discussed, there are three main methods to measure the surface resistance of small samples: end-plate replacement, RF-DC compensation and thermometric. The end-plate replacement and RF-DC compensation methods are mainly used because average R_s all that is required. Sometimes, these are supplemented with the thermometric method if an understanding of the uniformity of the surface and localised effects is required. The design of a test resonator and the overall facility is ultimately dictated by the testing method. As a result, it is important to consider the benefits and drawbacks of each method.

First, the main reason why the end-plate replacement technique is used is that it only requires a basic cavity geometry, such as mushroom/hemispherical cavities (see Section 3.3.1) and cylindrical cavities (see Section 3.3.4). These geometries make for fairly straightforward manufacturing. In addition, with these designs, there are few complexities in sample mounting. This reduces the overall testing time and effort per sample. For these reasons, it is historically the oldest method used and is a common approach for laboratories that require quick tests.

The main disadvantage is that it requires that the reference sample be of the same ingot of material as the cavity and be treated in the same way. This is to ensure that the condition $R_{s,cav} = R_{s,sam}$ is met during the test cavity calibration with a reference sample and the uncertainty on a measurement $Q_{0,ref}$ is minimised. To improve measurement reliability, the reference sample and the cavity should be produced at the same time. Furthermore, there is also a high risk of contamination of the test cavity and sample during sample changeovers because of direct contact between both components, which may require the use of indium (In) seals. This join may also require more complex sample designs in order to provide a sufficient vacuum seal if the cavity-sample system is immersed in LHe for 2 K measurements; however, this could be avoided if a minimum of 4 K is tolerable, which is achievable with a cryocooler. It is usually not possible to avoid this contact as the seal is also required to minimise RF electrical currents leaking out to avoid perturbing the measurement.

Also, the join must be designed so that it cannot increase the RF losses and increase the thermal contact resistance. If steps are not taken to minimise contamination, particulates on the surface of the cavity can increase the cavity R_s, thus changing Q_{cav} and affecting the accuracy of the sample measurement. Therefore, this could lead to false conclusions about the quality of the sample. It may be possible to assess contamination in-situ by connecting a residual gas analyser (RGA) and/or a particle counter to the test facility.

The resolution on surface resistance ($|\Delta R_s|$) is given by differentiating Equation 3.6 with respect to Q_0 and $Q_{0,ref}$:

$$|\Delta R_s| = \sqrt{\left(\frac{G_{sam}\Delta Q_0}{Q_0^2}\right)^2 + \left(\frac{G\Delta Q_{0,ref}}{Q_{0,ref}^2}\right)^2 + \left(\frac{G_{sam}\Delta Q_{0,ref}}{Q_{0,ref}^2}\right)^2} \tag{3.9}$$

where ΔQ_0 and $\Delta Q_{0,ref}$ are the uncertainties on Q_0 and $Q_{0,ref}$ respectively.

This technique has the advantage of allowing the use of Cu test cavities. This significantly reduces their cost compared to bulk Nb. However, in this case, even with a superconducting sample, RF losses on the surface of the cavity will always dominate at temperatures below the sample T_c. As a result, Q_0 will not be much greater than $Q_{0,ref}$. As an example, for a Cu cavity operating at 1.3 GHz with $Q_{0,ref} \approx 10^6$, $G = 300\,\Omega$ measuring a superconducting sample with $Q_0 \approx 5 \times 10^5$ gives $|\Delta R_s| = 0.22\,\text{m}\Omega$ (assuming an uncertainty on Q_0 and $Q_{0,ref} = 5\%$). Given that bulk Nb 1.3 GHz cavities typically operate with $Q_0 > 10^{10}$ at 2 K [67], resulting in an $R_s \sim$ few nΩ, the R_s of high-quality superconducting samples would not be resolvable.

Instead of Cu, bulk Nb can be used for the test cavity. In this case, assuming both $Q_{0,ref}$ and $Q_0 \approx 10^{10}$ for a 1.3 GHz cavity operating at 2 K with a sample of comparable quality, the resolution improves by almost three orders of magnitude, reaching $|\Delta R_s| = 2.1\,\text{n}\Omega$. This resolution is highly sensitive to cavity quality and will degrade if the cavity resistance varies by just a few nΩ. Furthermore, the limiting factors described in Section 2.3 may differ between the cavity and the reference sample, meaning the uncertainties in $Q_{0,cav}$, and thus in R_s for a sample, could

increase and be difficult to quantify.

The RF-DC compensation method is a simple calorimetric method that has the advantage of allowing direct measurements of RF losses on the sample without a reference sample. This removes any complexities in ensuring that the reference sample has been chemically or mechanically treated exactly the same way as the test cavity, as well as the risk of contamination. Ultimately, this method is used when high-resolution R_s measurements are required, for example, to resolve the residual resistance of 1.3 GHz cavities. For this method, $|\Delta R_\mathrm{s}|$ is given by differentiating Equation 3.7 with respect to $P_{\mathrm{DC},1}$ and $P_{\mathrm{DC},2}$:

$$|\Delta R_\mathrm{s}| = \frac{2\mu_0^2}{\int_{\mathrm{Sample}} |\boldsymbol{B}|^2 \mathrm{dS}} \sqrt{\Delta P_{\mathrm{DC},1}^2 + \Delta P_{\mathrm{DC},2}^2}. \tag{3.10}$$

where $\Delta P_{\mathrm{DC},1}$ and $\Delta P_{\mathrm{DC},2}$ are the uncertainties in $P_{\mathrm{DC},1}$ and $P_{\mathrm{DC},2}$ respectively.

Clearly, from Equation 3.10, the resolution of R_s using this method depends on the minimum heating power that can be measured. Providing that precise measurements of current, voltage, and temperature are taken, $|\Delta R_\mathrm{s}|$ can be down to nΩ levels. Systems using this method can mainly be improved by using higher resolution voltmeters and ammeters and improving the stability of DC power measurements. This can lead to $|\Delta R_\mathrm{s}| \sim$ sub-nΩ. Therefore, the main advantage of this method is up to $1-2$ orders of magnitude higher resolution than the end-plate replacement method, meaning that it can measure alternative superconductors with a BCS resistance lower than Nb.

The main disadvantage of this technique is the physical isolation required between the test cavity and the sample. This means that the test cavity design is often more complicated, and a simple cylindrical or mushroom shape cannot be used if the RF leakage is to be minimised. Additionally, the requirement that thermometers and heaters be mounted on the back of the sample can also lead to more complex sample holder designs. It is also assumed that the temperature distribution on the sample is the same with DC and RF heating, which can lead to an additional uncertainty. These difficulties have led to more complicated test

cavity geometries, for example quadrupole resonators (described later in Section 3.3.2) and the surface impedance characterisation (SIC) system (described later in Section 3.3.3).

Finally, the thermometric method is the only technique that measures local variations in R_s. The main advantages of this method are that it allows for both local and overall measurements of sample R_s, meaning that regions with higher than average RF losses can be identified. This can be very useful when combined with surface analysis techniques to understand the causes of these variations. The main drawback is the requirement for a complex temperature mapping system to be designed and implemented, which can sometimes be impractical, depending on the test cryostat used. Good thermal contact between each sensor and the sample might also be difficult to achieve. All of this would require significant additional wiring and programming effort. For quick comparisons of sample performance, this extra effort required for this method can be considered unnecessary.

A summary of the different methods is shown in Table 3.1. In general, a new facility will choose between using the end-plate replacement and RF-DC compensation methods. For existing facilities, if the focus has been on quick measurements with simple cavity designs, the end-plate replacement method has been chosen. If the focus has been on high-resolution measurements, without worrying about measurement time, the RF-DC compensation method has been used. An ideal future system should look to combine the advantages of both methods to achieve quick sample tests with high-resolution measurements.

3.3 RF Characterisation Facilities

To use the characterisation methods discussed, several RF test systems have been designed [121, 125]. These devices date back to the early 1970s with a lead-plated 2.85 GHz cylindrical cavity operating at $1.5 - 4.2$ K in a TE_{011} mode [122]. As with the lead cavity, facilities that use the end-plate replacement technique typically

Table 3.1: A summary of the methods for the RF testing of small samples.

Method	Advantages	Disadvantages	$\lvert\Delta R_s\rvert$
End-plate Replacement	Simple cavity designs Cu or Nb cavities Quick sample turnover Cu is cheaper than Nb	Requires reference sample Risk of contamination Lowest resolution (Cu)	Few-μΩ (Cu) Few-nΩ (Nb)
RF-DC Compensation	Direct measurements of RF losses Highest resolution	Requires sample holders Complex design Only SC cavities	Sub-nΩ
Thermometric	Only method for measuring local variations in R_s	Complex sample holder Additional wiring Additional data acquisition	Few-nΩ

use cavities with simple designs operating in TE_{0np}-type modes. These include mushroom cavities at SLAC [126, 127], Cornell [128], TAMU [129] and SARI/IMP [130, 131] and a cylindrical cavity at Orsay [132]. On the other hand, the RF-DC compensation method requires more complex designs. These include the commonly employed quadrupole resonator (QPR) at CERN [40, 133], HZB [134] and DESY [135] and the SIC system at JLab [136].

3.3.1 Mushroom Cavities

The simplest design for the end-plate replacement method is a cylindrically symmetric cavity operating in a TE_{0np} type mode. The major benefit of these modes are that the E-field lines form closed loops around the axis of symmetry, helping to maximise the H-field on the sample end plate and avoid problems such as RF breakdown and multipacting due to surface E-fields. With these modes, there are no surface E-fields on the sample and no surface currents where the sample and the host cavity join, thus reducing the chance of losses on the joint. The surface H-fields on the cavity wall are also low, whilst the peak H-field is in the centre of the cavity. This allows for cavities with high geometry factor and high Q_0. However,

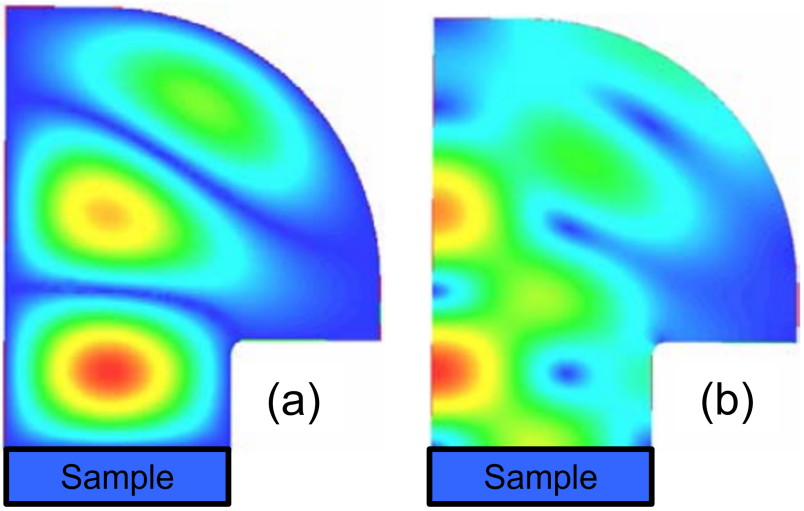

Figure 3.5: The concept of a mushroom cavity showing (a) the E-field and (b) the H-field for the TE_{013} mode where the left hand side of each plot is the axis of symmetry and the sample is placed over the bottom opening where the H-field is maximal. Adapted from [126].

by symmetry, this approach also leads to an undesirable high H-field on the cavity at the end opposite the sample. To overcome this, various TE-mode, mushroom-shaped cavities have been designed to ensure that the H-field is much higher on the sample plate compared with everywhere else on the cavity.

The first mushroom cavity was initially designed at SLAC in 2005 [126]. This cavity was designed to operate in a TE_{013} mode at 11.4 GHz and originally test sample disks $51 - 76$ mm in diameter at temperatures > 4 K. This geometry, shown in Figure 3.5, resulted in an H-field that was 75% higher on the sample plate than anywhere else on the cavity and an E-field that was zero everywhere on the cavity surface, thus avoiding issues due to RF breakdown and multipacting.

The first cavity design was made of Cu [137, 138] which allowed for high field measurements without cavity quenching. This cavity was later replaced by a hemispherical cavity to increase the maximum H-field on the sample [127, 139, 140]. This design has a peak magnetic field on the sample approximately 2.5 times greater than that on the cavity. RF tests demonstrated the ability to measure the samples

at temperatures in the range $3 - 300\,\mathrm{K}$ and maximum sample surface $B = 360\,\mathrm{mT}$. The low Q_0 meant that RF losses on the host cavity always dominate, limiting the sensitivity on R_s to $0.1\,\mathrm{m\Omega}$ at $360\,\mathrm{mT}$ [141]. The cavity was later redesigned using a Nb/Cu cavity with significant improvements in R_s measurement resolution, down to $0.7\,\mu\Omega$ at $4\,\mathrm{K}$, however this is still not enough for bulk Nb at $1.8\,\mathrm{K}$ [142].

More recently, the SLAC design formed development of a mushroom-shaped cavity at Utsunomiya University [143]. Several years of development led to a 5.2 GHz Nb cavity [144, 145]. The peak sample B-field was reported to be 75.4 mT with 1 W of RF input power and has been able to reach 383 mT with 5.1 W input power, which is sufficient to measure the RF critical field of NbN [146].

At a similar time, another TE-mode cavity was being developed at Cornell University. Three generations of cavity were built: the pillbox cavity, mushroom cavity and bulge/onion/bulb (BOB) cavity [147]. All three (shown in Figure 3.6) were made from bulk Nb and designed to test 124 mm diameter sample disks. The resulting third-generation BOB cavity was designed to operate at 4 GHz [147, 148]. A temperature mapping system was also added. This redesign, allowed a peak field of 106 mT at 1.6 K with a maximum of $Q_0 = 4.1 \times 10^{10}$ and R_s on the order of $\mathrm{n\Omega}$ [149, 150].

A third mushroom cavity, based on the SLAC cavity, was designed at Texas A&M University (TAMU) [129, 151]. This design, shown in Figure 3.7, consists of a half-cell bulk Nb TESLA cavity made into a mushroom cavity that operates in a TE_{011} mode at 2.2 GHz, testing 150 mm diameter samples. As with the surface impedance characterisation system (detailed later in Section 3.3.3) this cavity is dielectrically loaded with a sapphire rod. This acts as a dielectric lens to focus the electromagnetic fields on the sample and has allowed the system to reach a maximum surface B-field of 3.75 times higher than anywhere else on the cavity[129, 152]. An upgraded design at the Thomas Jefferson National Accelerator Facility had a theoretical maximum field of 162 mT however it only reached a $Q_0 = 3.96 \times 10^8$ at 2.73 K and 6.6 mT, limited by multipacting in the cavity or the couplers [153].

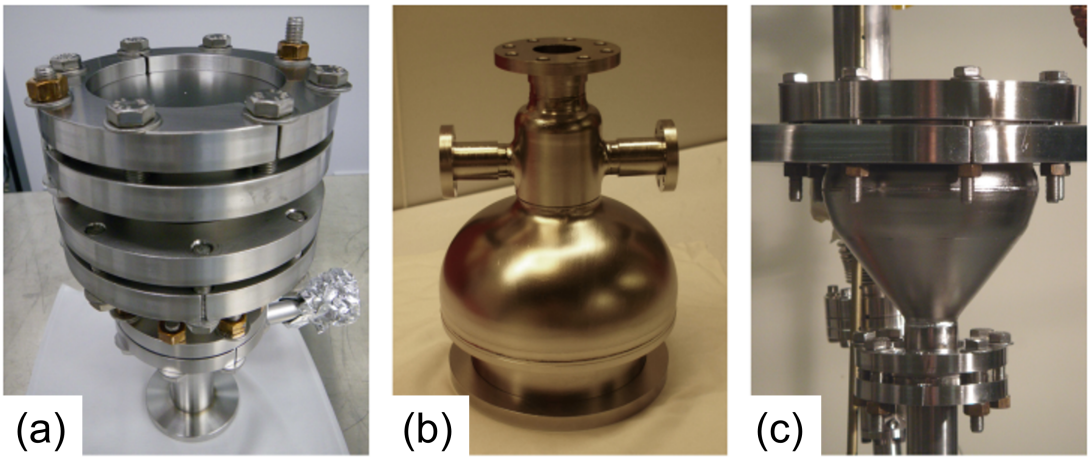

Figure 3.6: The development of TE-mode cavities at Cornell: (a) the original pillbox cavity, (b) the mushroom cavity, (c) the 'bulge/onion/bulb design [147].

Most recently, another cavity has been developed between the Shanghai Advanced Research Institute (SARI) and the Institute of Modern Physics (IMP) based on the Cornell design [130, 131]. This cavity has been manufactured from bulk Nb and operates at 3.9 GHz in a TE_{011} mode to test 110 mm diameter samples. It has been designed to theoretically reach a peak sample $B = 126$ mT with a ratio of peak magnetic field on the sample to the cavity of 0.895. So far this cavity has quenched at 24 mT at 2 K while only reaching $Q_0 = 7 \times 10^9$.

3.3.2 Quadrupole Resonators

For the RF-DC compensation method, slightly more complex resonator designs are required to achieve the necessary thermal and physical isolation between it and the sample. The most widely used test resonator design is the Quadrupole Resonator (QPR). The QPR was originally designed at CERN in the late 1990s to allow field concentration on a 75 mm diameter sample size. It was designed to operate in the TE_{210} mode at 400 MHz - the frequency of the RF cavities in the LHC [40].

A typical QPR system is shown in Figure 3.8(a). The basic design consists of two 2 mm thick Nb cylinders connected through stainless steel flanges at the base

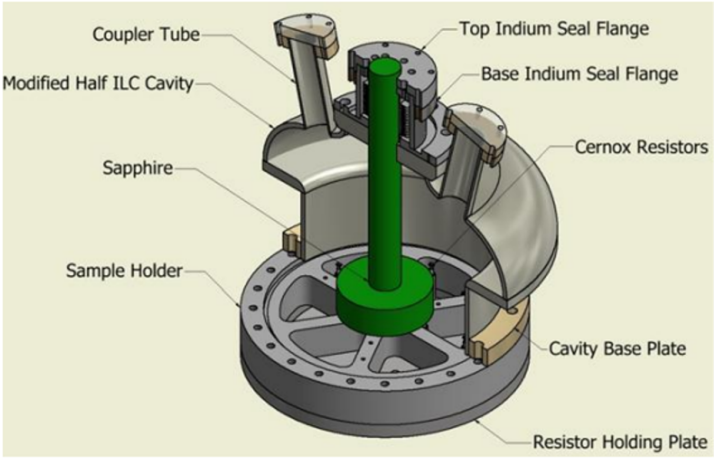

Figure 3.7: A cross-section of the TAMU test cavity which shows the sapphire rod suspended above the sample [153].

of the resonator. The larger of the cylinders is the host cavity whilst the other is the cylindrical sample connected to a calorimetry chamber with the required thermometers and heaters. Inside these cylinders are four hollow Nb rods which form a transmission line colinear with the vertical axis of the cylinder. The ends of the rods are bent into half-rings of 25 mm radius at a distance of 1 mm above the sample to be measured. The four-rod transmission line is excited in a symmetric quadrupole mode which is of the type TE_{2np}, hence the name quadrupole resonator. The resulting RF magnetic field profile is shown in Figures 3.8(b) and 3.8(c) and the ratio of peak magnetic field on the sample to the cavity is 1.16 [154]. Later, extensions of the CERN QPR were made to allow for excitations at 800 MHz (TE_{211}) and 1200 MHz (TE_{212}), whilst not breaking vacuum, removing the sample and risking contamination [155].

Given that the sample and rods are thermally isolated, the system can to calculate R_s at temperatures down to $\approx$ 1.85 K[154]. The design of the QPR is such that the screening current due to the fields in the cylinder vanishes at the flange between the two Nb cylinders at 400 MHz and 1200 MHz and that the fields decay exponentially along the walls of the sample cylinder. The screening current is a maximum at the flange at 800 MHz, however, the presence of a small 1 mm gap

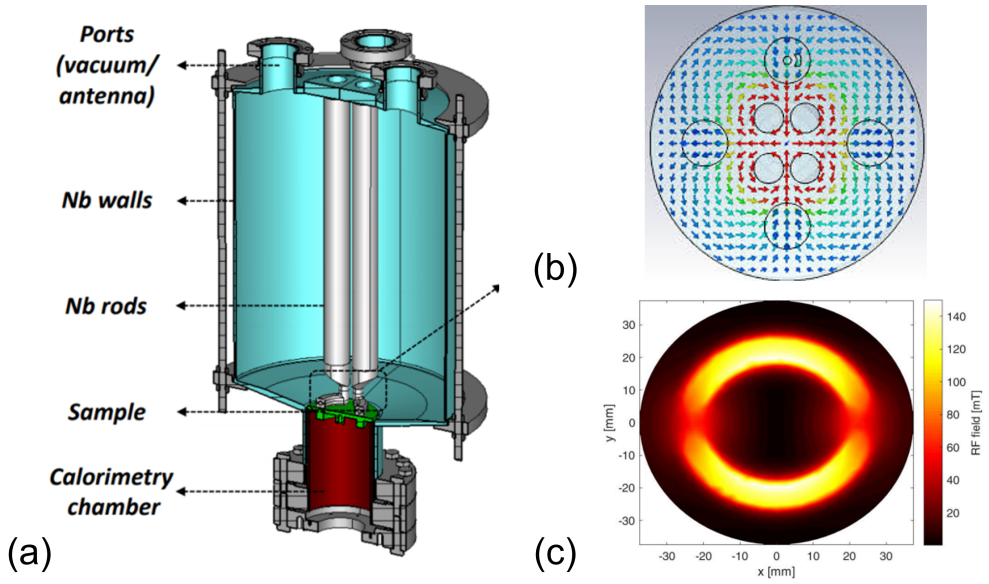

Figure 3.8: (a) A typical QPR design (this at DESY) [156]. (b) The magnetic field distribution of the DESY QPR at 424 MHz [157]. (c) The RF magnetic field on the sample for the HZB QPR showing the first quadrupole mode, which is similar to the other modes [134].

allows the concentration of high fields on the sample. With this setup, the maximum field on the sample surface was 60 mT at 400 MHz [36]. With a peak magnetic field on the sample surface of 5 mT, the R_s resolution was measured to be 0.44 nΩ at 2 K. The achievement of a higher resolution than regular cavity measurements has allowed this system to study the effect of trapped flux and the effect of thermal cycling on bulk Nb and Nb/Cu samples [73, 158].

Other laboratories have also designed their own versions of the QPR. This began at HZB [134, 159] with the aim of improving the resolution at higher peak sample H-fields, reducing the peak E-field and improving the mechanical stability [159]. The aim was to overcome limitations of field emission and multipacting in the CERN QPR and reduce sensitivity to microphonics [36].

In the HZB design, the radius of the rod was increased, gap decreased and the thickness of the rod increased compared to the CERN design. This resulted in a

reduction in E_{pk}, an increase in the maximum B_{pk} on the sample to 120 mT and reduced vibrational noise [160]. This design also has slightly different quadrupole frequencies of 433 MHz up to 1.3 GHz. For the CERN and original HZB QPRs, the sample disk has to be electron beam welded to the sample cylinder. To avoid this potentially sample-contaminating process, an alternative calorimetry chamber was designed that is bolted to the main resonator body with an In gasket and allows sample exchange between HZB and CERN [161]. Initial RF measurements with the new sample holder showed a higher R_{s} with a strong dependence on magnetic field strength and temperature, which was partly associated to losses at the In gasket joint between the sample holder and the Nb tube [161]. However, performance exceeding Nb was later shown with measurements of Nb_3Sn coatings [162].

The QPR has a measurement sensitivity higher than that of the mushroom cavities. The R_{s} is able to reach sub-nΩ resolution, which is mainly a result of the minimum detectable heater power difference as a function of temperature and field when calculating the R_{s} from the RF-DC compensation method [163]. More recently, the HZB QPR has also used Cu substrates electron beam welded to Nb cylinders to test the performance of Nb/Cu samples in addition to films deposited on bulk Nb [164].

A third QPR test facility at UHH/DESY, based on the other designs, has been in development since 2019 [135, 156]. It was recently commissioned in 2023 and has shown improved mechanical stability, resulting in reduced detuning and minimisation of parasitic heat loading on the sample [157]. This work led to the upgrade of the QPR at CERN in 2017 [133] and also formed the basis of an optimised geometry for a fourth QPR currently being developed at JLab [165].

3.3.3 Surface Impedance Characterisation System

A second system utilising the RF-DC compensation method was designed and built at Jefferson Lab. This system, originally commissioned in 2005, was developed from a modified cylindrical Nb cavity operating in the TE_{011} mode at 7.4 GHz [166]. It

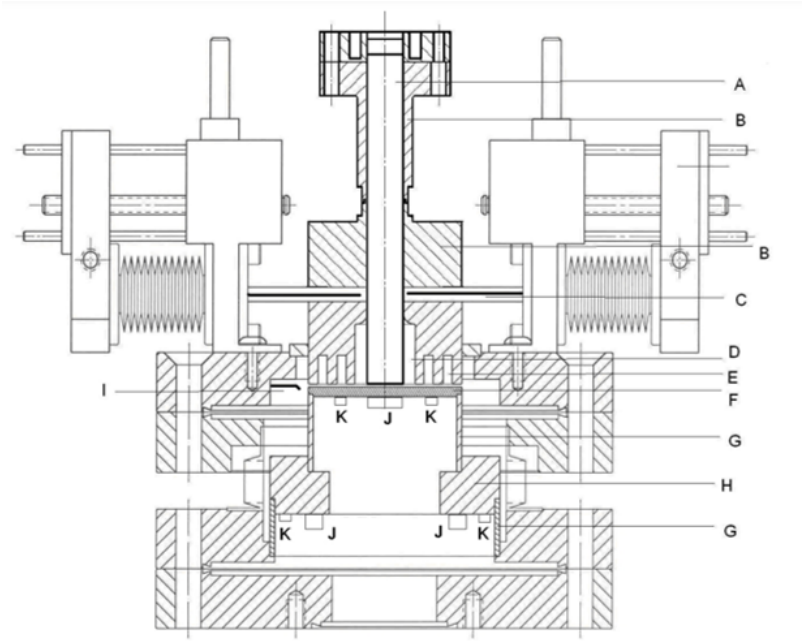

Figure 3.9: The design of the SIC system: A - sapphire rod, B - parts of the Nb system, C - input coupler, D - cylindrical TE_{011} cavity, E - a choke, F - Nb sample on Cu plate, G - stainless steel thermal insulation, H - Cu ring, I - pickup coupler, J - heater, K - thermometer [167].

became known as the Surface Impedance Characterisation (SIC) system.

The SIC system is shown in Figure 3.9 [136, 167, 168]. To keep sample sizes small, the cylindrical cavity was designed with a diameter of 20 mm with a sapphire rod inserted into the centre of the cavity (similar to the TAMU mushroom cavity) to reduce the frequency from around 20 GHz to 7.4 GHz. Sapphire is used because of its high electrical permittivity, high thermal conductivity and low dielectric loss factor [166]. It also ensures that RF fields are confined to a small central area of 80 mm^2 on the sample. This, along with two 10 mm deep RF choke structures, results in minimal RF field leakage.

RF is input via an adjustable loop coupler. A sample disk, up to 50 mm in diameter, is placed at the open end of the cavity with a small 20 mm gap between the two for thermal isolation [136]. The sample is bonded to a dedicated OFHC Cu

sample holder with heaters and thermometers. This small sample size was chosen because it can be easily accommodated in laboratory deposition and surface analysis equipment. The sample mounting system ensures quick sample changeover.

The SIC system originally reported temperatures of $2 - 20\,\mathrm{K}$. Given its high frequency, it has reached peak field sample magnetic fields up to 14 mT and reported R_s resolution down to $1.2\,\mathrm{n\Omega}$ at 5 mT and 2 K [136]. The peak field on the sample is approximately 1.04 times higher than the peak field on the cavity [167]. As with mushroom cavities, the use of a TE_{011} cavity mode is advantageous as it means that there are no electric fields incident on the sample, therefore reducing the likelihood of multipacting issues. The choke joints also prevent high RF fields at the sample edges, therefore avoiding anomalous heating from vortex entry [166].

During the design and commissioning phase, the SIC system was used primarily to test bulk Nb [136, 167–170]. Since then, the system has been used to test a wide range of single and multilayer thin film samples. Of the single layers, thin film Nb [171], $\mathrm{Nb_3Sn}$/Nb [170, 171] and $\mathrm{MgB_2}$ have been tested [170, 172, 173], with the latter also demonstrating the ability of the SIC system to reach 40 K. Of the multilayers, NbTiN/AlN/Nb, NbTiN/AlN/Nb/$\mathrm{Al_2O_3}$ [171], $\mathrm{MgB_2}$/MgO/Nb/MgO [174] and $\mathrm{Nb_3Sn}$/$\mathrm{Al_2O_3}$/Nb [175] have all been tested.

3.3.4 Orsay Cylindrical Cavity

In the early 1990s, a cylindrical pillbox cavity operating at 4 GHz in the TE_{011} mode and 5.6 GHz in the TE_{012} mode was developed between CEA Saclay and IPN Orsay to measure R_s of bulk Nb and Nb thin films using the end-plate replacement technique [176]. With this design, a sample to cavity magnetic field ratio of 1.43 was achievable. This technique gave accuracy on R_s of $\pm 1\ \mu\Omega$ at 4.2 K, therefore it was later developed to measure the R_s of thin films of Nb and NbTiN/Cu disks using a thermometric system inside a vacuum chamber [132]. This system allows for measurements of absolute values of R_s using the end-plate replacement technique and local variations in R_s via the thermometric method.

The RF properties of Nb/Cu samples were initially studied with this cavity. The results demonstrated that the thermometric method could provide more 3 times more accurate calculations of R_s than the end-plate replacement method. They also showed a correlation between R_s and substrate roughness [177].

Several years later, the cavity was slightly redesigned with a curved shape to avoid overlap with the TM_{111} and TM_{112} modes. This design operated at 3.9 and 5.1 GHz with a sample/cavity magnetic field ratio of 1.35 and aimed to investigate alternative superconducting thin films such as MgB_2 and Nb_3Sn [178]. The experimental set up, shown in Figure 3.10(a), consists of a bulk Nb cavity with a removable end plate. The removable end-plate is clamped to the cavity with an In gasket. This is where sample disks of 126 mm diameter are mounted. The magnetic field profile is shown in Figures 3.10(b) and 3.10(c) which illustrate that the field is maximal at the intersection between the top of the cavity and the bottom of the feedthroughs. The thermometric part contains a static heater and an array of 30 thermometers allowing for calorimetric and thermometric measurements of R_s. The expected sensitivity was calculated to be 1.43 nΩ at 1.8 K and 45 nΩ at 4.2 K at 5 mT [178, 179].

This modified system was the first to study NbN/MgO/Nb samples [180], demonstrating a μΩ lower R_s above 3 K compared to bulk Nb. In addition, recent results of a bulk Nb sample have demonstrated the ability to measure R_s at temperatures from $1.5-4.5$ K and fields up to 20 mT. Temperature mapping has also demonstrated the ability to map sample defects and sample thermal conductivity [179].

3.3.5 Comparison

For an ideal facility, the resonant frequency is in the range of accelerating cavities and the field distribution should maximise the peak magnetic field on the sample (B_{sam}) and maximise the ratio of B_{sam} to the peak magnetic field on the cavity (B_{cav}). In addition, the range of measurement temperatures is dictated by the cooling

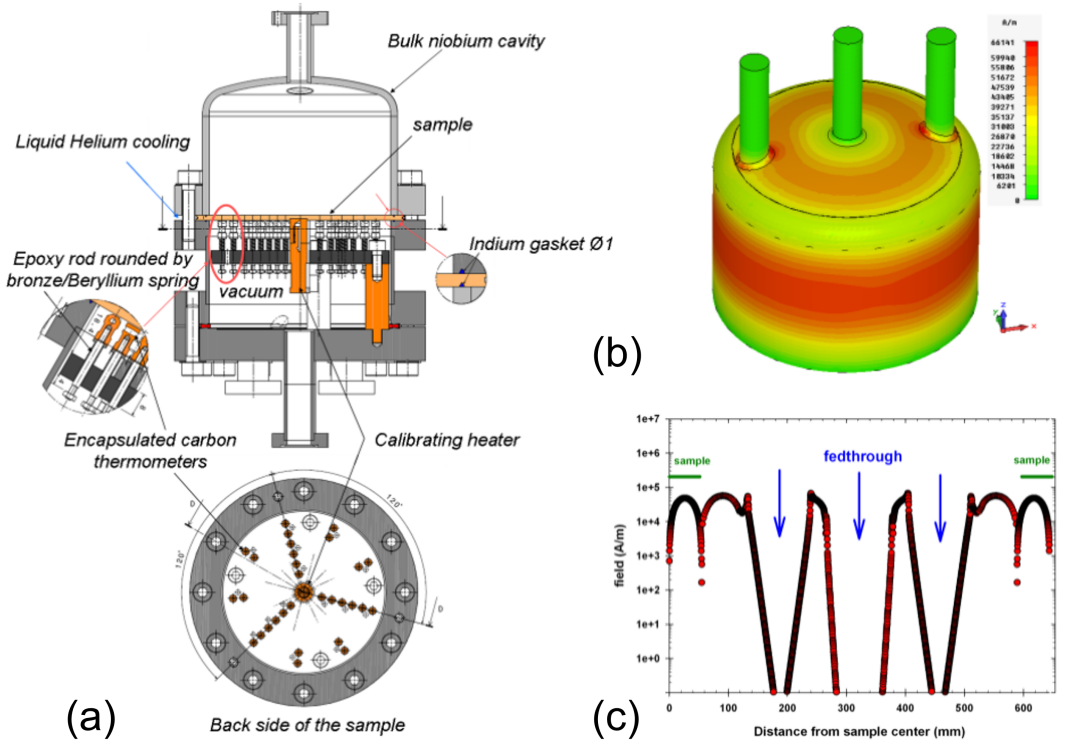

Figure 3.10: (a) The setup of the Orsay system, showing the bulk Nb cavity and the underside of the sample with the heater and array of thermometers, (b) the tangential magnetic field of the TE_{012} mode on the cavity surface, (c) surface magnetic field along the XZ plane [178].

method, the sensitivity/minimum resolvable R_s depends on both f_0 and $B_{sam,max}$, the sample shape and diameter is dictated by the cavity design and available deposition facilities. A full comparison of these parameters for each of the systems presented in this section is shown in Table 3.2 separated into their main characterisation techniques and completed as best as possible based on the available data. Ideally, the system should also have a high sample throughput rate to optimise thin film deposition parameters quickly. An estimate of the average sample throughput rate is shown for each system where 'high' is the ability to test more than 2 samples per week, 'med' is 1 sample per week and 'low' is less than 1 sample per week.

The simplicity of mounting a sample is an important factor when designing a

Table 3.2: A comparison of RF test facilities for small samples.

	End-plate replacement				RF-DC Compensation				Thermometric
	SLAC	Cornell[a]	TAMU[a]	SARI/ IMP	CERN QPR	HZB QPR	DESY QPR	SIC	Orsay[b]
f_0 (GHz)	11.4	4.78 6.16	2.2	3.9	0.4 0.8 1.2	0.4 0.9 1.3	0.4 0.9 1.3	7.4	3.9 5.1
Mode	TE_{013}	TE_{012} TE_{013}	TE_{011}	TE_{011}	TE_{210} TE_{211} TE_{211}	TE_{210} TE_{211} TE_{212}	TE_{210} TE_{211} TE_{212}	TE_{011}	TE_{011} TE_{012}
$\Delta R_{s,min}$ ($\mu\Omega$)	100[c] 0.7[d]				$< 10^{-3}$	$< 10^{-3}$	$< 10^{-3}$	10^{-3}	10^{-3}
$B_{sam,max}$	360	106	162	126	70	120	120	14	20
$B_{sam,max}/B_{cav,max}$	2.5	1.24 1.74	3.75	0.895	0.81	0.89		1.04	1.35
T_s (K)	3-300	1.6-4.2	> 2	> 2	2-20	2-20	1.8-20	2-40	1.5-4.5
Cooling	LHe[c] Cryocooler[d]	LHe	LHe	LHe	LHe	LHe	LHe	LHe	LHe
Sample diam. (mm)	$51-76$	124	150	110	75	75	75	50	126
Sample shape	Disk	Disk	Disk	Disk	Cylinder	Cylinder	Cylinder	Disk	Disk
Sample through-put	Med	Med	Med	Med	Low	Low	Low	High	Med

a Also, thermometric.
b Also, end-plate replacement.
c Cu cavity.
d Nb cavity.

test facility. The simplest solutions have been the facilities that use the end-plate replacement method at SLAC, Cornell, TAMU and SARI/IMP. The cylindrical and mushroom-shaped cavity design can be easily manufactured and do not require a great deal of effort for sample mounting. The use of TE-modes means that there is no need to worry about RF losses at the sample-cavity join. This sample mounting process has the benefit of being able to test many samples in a short time allowing for fast optimisation of deposition parameters.

The main downside of these facilities is the requirement for direct sample-cavity

contact (often with the use of an In seal). This risks cavity contamination during sample changeover, which could change the cavity Q_0 and affect the reliability of sample measurements. In addition, for the calibration, a reference sample must be produced from the same ingot might not always be possible to control. Also, to keep the sample size small, a high resonant frequency would be required and the Cu cavity is unsuitable for sensitive measurements of R_s. Testing with a Nb cavity is possible, but requires two cooldowns per sample if both high field and high resolution R_s measurements are required. The Cornell design benefits from a lower frequency and temperature mapping, but at the cost of a lower sample peak magnetic field and a larger sample size. The TAMU cavity has the lowest frequency of the mushroom designs, allowing for sample evaluation much closer to cavity frequencies, but this means that a large sample is required.

The RF-DC compensation method solves these issues with physical sample-cavity separation. The QPR is the most popular facility because it performs measurements at a range temperatures, multiple low frequencies close to those of SRF cavities and the highest peak magnetic field limit of any system using the calorimetric technique. By probing R_s to sub-nΩ level, these facilities can be used to detect small changes in residual resistance that would be undetectable with other facilities.

However, one of the main issues of the QPR is the risk of contamination during sample preparation. This was later overcome with an alternative calorimetry chamber. The main disadvantage is the complex sample design, which may require more complicated deposition facilities compared to the ones for sample disks. In addition, the extra effort required means that sample preparation and testing can easily take at least two weeks. To improve turnaround time, a Rapid Superconductor Test Apparatus (RaSTA) is in development to help sort through candidate samples using a 4.8 GHz TM_{020} mode cavity [181].

Overcoming the issues with a complex sample design means using planar disks. This has been achieved at JLab with the SIC system. However, issues with choke leakage were not taken into account, as these losses did not radiate out of the

closed system, thus adding uncertainty. Despite also being able to achieve sub-nΩ resolution, a higher frequency is used and almost an order of magnitude lower peak magnetic fields are achievable compared to the QPR.

The third technique, temperature mapping, is very useful for mapping out variations in R_s on the sample surface that can be supplemented with surface analysis. However, the extra effort required for the manufacture and wiring of a mapping system as well as the development of data acquisition software is not necessary for simple comparisons of samples under RF conditions. Therefore, this method is not worth pursuing.

The cooling method is also a vital consideration for a test facility. LHe based systems allow for the cooling of samples to temperatures down to at least 2 K and can operate at higher cooling capacities in the cryogenic system. However, this restricts the rate of sample turnover. In contrast, a cryocooler-based system is not dependent on LHe supply. It has a simpler design and fewer cryogenic health and safety risks, However, it is limited by the cooling power and typically restricted to $T > 3.5 - 4\,\mathrm{K}$.

From the review of existing test facilities, an ideal system should provide:

- Low frequencies $< 1.5\,\mathrm{GHz}$.
- Sub-nΩ resolution.
- High sample turnover.
- Small samples with simple mounting.
- High maximum sample peak magnetic field.
- Wide sample temperature range.
- Good thermal control of sample.

From the comparisons made, no system can perfectly cover all requirements. The design of a system should match the main objective of the facility. If the

main aim is to study the residual resistance with sub-nΩ resolution, this is only achievable using the RF-DC compensation method. If measuring the quench field is desirable, a design such as a Cu mushroom cavity might be considered. However, if the main aim is to perform mass deposition parameter optimisation studies, a high-throughput facility, such as a mushroom cavity, might be more suitable despite a higher frequency. Also, if the primary objective is to test and compare alternative superconductors, higher base temperatures of 4 K would be sufficient and would reduce cooling infrastructure and costs.

Overall, no single system can comprehensively satisfy all experimental requirements. The optimal design must therefore be determined by prioritising the facility's primary scientific objectives while balancing precision and practical constraints such as infrastructure required.

Chapter 4

The Choke Cavity

The main aim for a new RF test facility at Daresbury Laboratory was a high sample testing rate whilst still being able to measure the surface resistance with high resolution. To achieve these goals, a new cavity was designed by G. Burt and P. Goudket, which became known as the Choke Cavity.

This chapter begins by describing the initial motivation for the design of this cavity. Electromagnetic simulations in CST were performed after manufacture to analyse different iterations of the cavity design and demonstrate how this cavity works. Finally, further simulations were performed to determine the best positions for the RF couplers prior to developing the Choke Cavity into a fully operational sample measurement facility.

4.1 Motivation for a New Test Cavity

The review of existing RF test facilities in Chapter 3 demonstrated that achieving the criteria set out to produce the optimal sample test cavity is very difficult to achieve in practice. Each of the facilities meets one or more of the criteria, but not all. For example, the most commonly used facility, the QPR, can measure the surface resistance with high sensitivity at low resonant frequencies and high peak magnetic fields. However, a complex sample preparation and mounting procedure

limits the sample turnover rate. In addition, most test facilities use LHe to achieve base temperatures $< 2\,\mathrm{K}$. Despite being able to reach the operating temperature of bulk Nb cavities, this increases sample testing times as a result of the availability of the liquid cryogens, cooldown times, added complexities with helium pumps, and the requirement to have multiple members of staff for safe facility operation.

Given the growing desire to use thin film SRF cavities in new accelerators and accelerator upgrades to meet sustainability goals, it is now increasingly desirable to have sample test facilities that are able to produce results rapidly. This is a must to increase the rate of thin film development. To develop the best performing thin films, a lot of fine tuning of both substrate preparation and deposition parameters must be carried out. Given the large number of parameters that can be varied, this means that a lot of test samples must be produced quickly. High-throughput test facilities are therefore a key requirement to aid this process, match the rate of sample production, and enable rapid evaluation at each stage of the optimisation process. In addition, with the desire to operate thin film SRF cavities at 4.2 K, having a LHe cryogenic sample test facility operating at 2 K should only be reserved for the best samples. Quicker sample comparisons at 4.2 K can be achieved with LHe or closed-cycle cryocoolers to first filter out samples with poor RF performance.

For the purpose of RF testing, a new test facility was developed at Daresbury Laboratory with the main aim of maximising the sample turnover rate without compromising measurement accuracy. The ultimate goal is to use this new facility in conjunction with the available DC measurement facilities (discussed in Section 3.1.1) to determine whether there is any correlation between the DC and RF measurements. Only by combining DC and RF measurements with surface analysis on each sample can a full conclusion be made about whether the thin film is a potential candidate for full cavity deposition.

For this facility, a new test cavity design was required with the following criteria:

- Ability to directly measure RF losses on a simple planar sample design separately from the test cavity:

  - Using the RF-DC compensation method.
  - A low-cost sample design.
  - A simple cavity design.

- Fast sample turnaround:
  - No welding, vacuum, or RF seals between the test cavity and the sample.
  - The possibility to reuse the sample for additional coatings and further tests.

- A vacuum system that is easy to vent, open, close, and pump.
- Easy and safe cryogenic operation from $4 - 20\,\mathrm{K}$.

To meet this set of criteria, a novel test cavity was designed and previously manufactured. This became known as the Choke Cavity. To be able to quickly sort through samples and allow for fast optimisation of deposition parameters, the facility would need to be low maintenance and simple to operate.

4.2 Choke Cavity Design

The starting point for a test cavity was the combination of a small pillbox cavity with a sample mounted underneath. The cavity would operate in a TM_{010} mode to best replicate the fundamental mode of acceleration in an accelerating cavity. Basing the design on a TE_{011} mode mushroom cavity was originally considered, however this would have needed a larger cavity size for given frequency and there were space constraints in the cryostat. An iris could have been used to keep the same sample size but the peak field would not have been on the sample, thus limiting the maximum magnetic fields. To establish a resonance, the sample would need to close the open end of the cavity, similar to one of the mushroom cavities described in Section 3.3.1. However, this would not provide the thermal isolation required for the RF-DC compensation method. The addition of a small gap with a TM_{010} mode

would lead to significant RF leakage. Therefore, when considering the test cavity design, a method was required to contain the RF fields within the cavity and sample to avoid RF leakage through the gap.

Whilst considering test cavity designs, the sample design was also important. The simplest sample design that could be tested is a planar disk. Planar samples are easier to manufacture from a metal sheet than cavities and cylindrical samples, making them more cost-effective to mass-produce. They are also much easier to deposit a thin film on compared to curved structures. When the test cavity was designed, the maximum sample diameter was limited to 100 mm considering the size of the load-lock chamber connected to the available deposition chamber (described later in Section 7.2) and the dimensions and cost of the deposition targets [113]. The diameter of the sample defined the maximum size of the test cavity. Furthermore, disks are versatile as they can easily be cut for further analysis without significant added cost.

To address RF leakage that would be introduced due to the sample-cavity gap, RF chokes were used. This became the main feature of the test cavity and is discussed in more detail in Section 4.3. In electronics, RF chokes are types of inductors or capacitors that filter either low or high frequency AC signals. That is, the impedance is high for the signals to be blocked. They are often used to protect networks where RF noise can interfere.

For an RF cavity, the choke dimensions should be tuned to the cavity resonant frequency (f_0) to ensure that unwanted frequencies pass through whilst the required cavity frequency is not allowed to pass and therefore does not leak out of the cavity. This means that the chokes should act as band-stop (or notch) filters to attenuate the passage of frequencies in a narrow range between a high frequency (f_H) and low frequency (f_L), reaching a minimum at a centre frequency (f_C). I.e. the ratio of the signal out (P_out) to signal in (P_in) should be minimised for $f_\mathrm{L} < f < f_\mathrm{H}$, as shown in Figure 4.1(a). The circuit diagram in Figure 4.1(b) shows that such a filter can be represented by a capacitor to block low frequencies and an inductor to block high

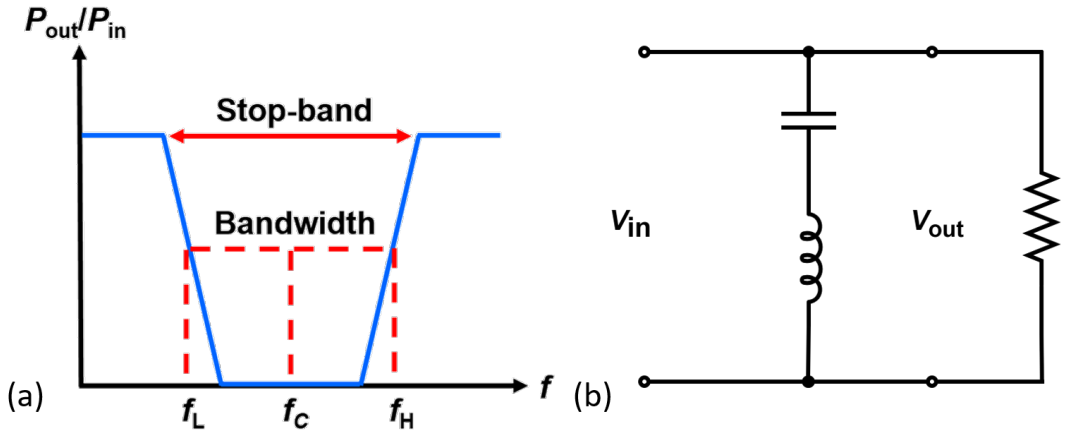

Figure 4.1: Band-stop filter: (a) frequency principle, (b) circuit diagram.

frequencies, resulting in an attenuation of frequencies between f_{H} and f_{L}.

Chokes have been proposed in the past for use in damping RF cavities to trap the accelerating mode within the resonator [182–184] and prevent Q_0 degeneration. As described in Section 3.3.3, the SIC system used them for small sample testing [136]. In RF engineering, chokes are designed to be transmission lines one quarter of a wavelength long, e.g. using coaxial cables or microstrips. With one end shorted, a closed circuit is created, and signals at the design frequency of the choke are reflected after travelling one quarter of a wavelength, whilst acting as a band-stop filter. With an RF cavity, this opens up the possibility of containing the fundamental mode frequency within the cavity whilst filtering out unwanted frequencies. The size of the chokes would be tuned to a specific frequency and gap size between the cavity and sample to minimise RF leakage whilst not having a physical RF seal. This would allow for the thermal isolation required for the RF-DC compensation method.

As is the case when designing an RF cavity, the starting point for the Choke Cavity design was a circuit model, shown in Figure 4.2. This design neglects the addition of RF couplers, for now, which are discussed in further detail in Section 4.4. The main part of the design consists of a standard LRC central cavity made up of inductive, resistive, and capacitive components, which is described in Section 2.1.3. The central cavity has the addition of one quarter-wavelength choke, represented

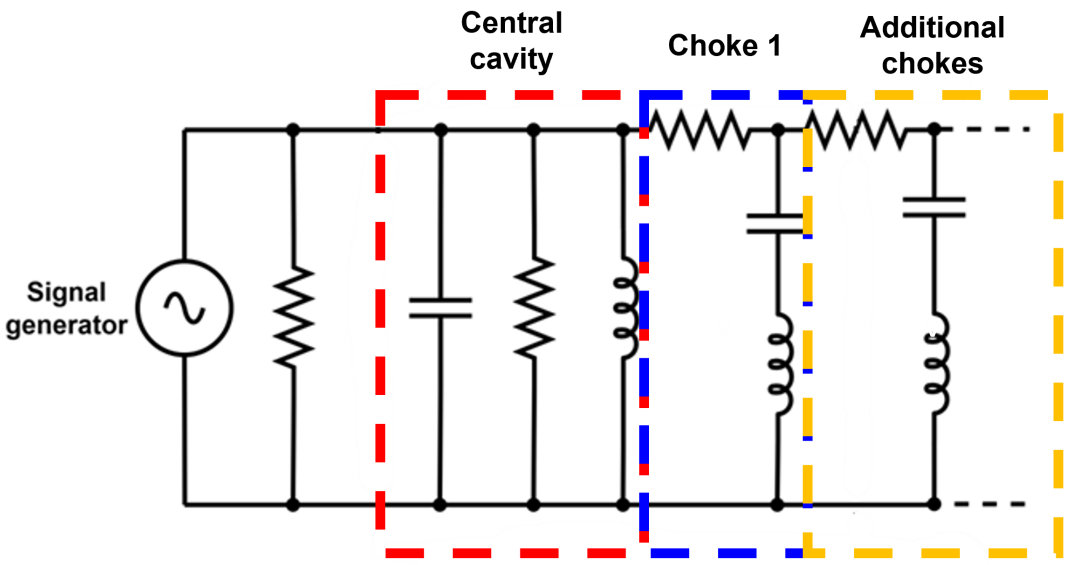

Figure 4.2: An RF circuit model of the Choke Cavity.

by an additional inductor and capacitor. This is done to create the fundamental resonance between the cavity and choke because of the requirement for a sample-cavity gap creating an open structure. Additional chokes should be a quarter-wavelength from the first choke to create overlap and trap any wanted frequencies in or close to the resonant frequency whilst allowing unwanted frequencies to pass. Any RF signals that pass through the chokes would be radiated through the gap; however, it is not possible to separate these losses from those of the cavity and chokes from RF measurements.

The first design phase resulted in a 3.9 GHz test cavity with two RF chokes, as shown in Figure 4.3 [185]. However, the size of the main part of the cavity and surrounding chokes meant that a sample larger than 100 mm diameter was required. This was too large for a simple installation in the deposition facilities available at Daresbury Laboratory. Given that the facilities could accommodate a maximum sample size of 100 mm diameter with ease, the resonant frequency was doubled to 7.8 GHz to reduce both the size of the central cavity and the surrounding chokes. The final cavity design is based on an elliptical half-cell cavity operating in the fundamental TM_{010} mode surrounded by three chokes. In this design, the central

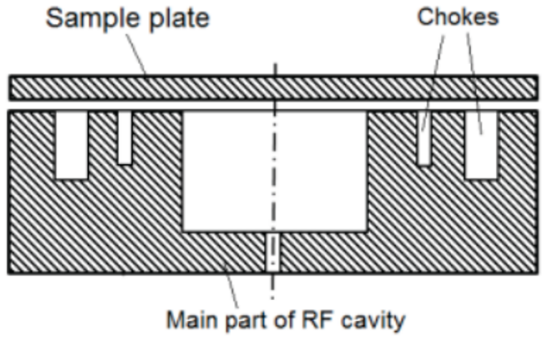

Figure 4.3: The initial 3.9 GHz two choke cavity design [185].

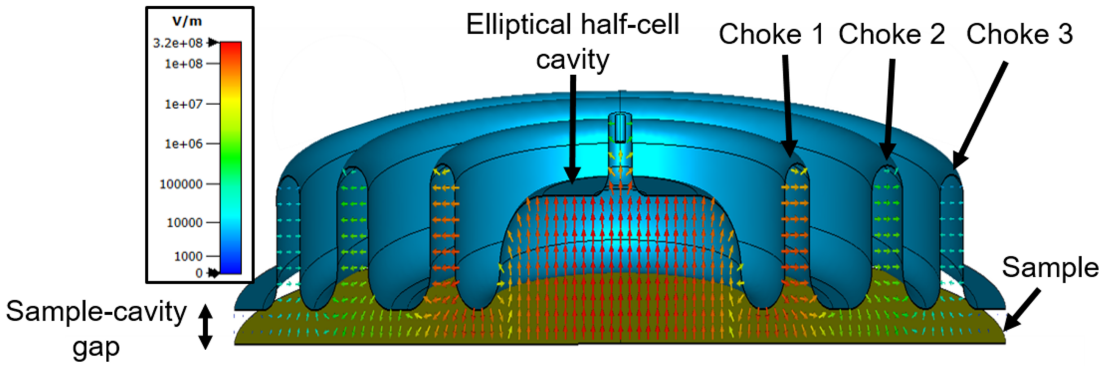

Figure 4.4: The current iteration of the Choke Cavity.

cavity and chokes are rounded to avoid possible complications due to multipacting that may have been present in the 3.9 GHz cavity.

The final design of the Choke Cavity was performed in CST [185]. This design is shown in Figure 4.4 which illustrates the Choke Cavity on top of a sample with a small gap. Standing waves, or a resonance, are set up between the central elliptical half-cell cavity, operating in the fundamental TM_{010} mode, and a single choke (choke 1). A second (choke 2) and third choke (choke 3) were added which surround choke 1 and the central cavity. These additional chokes maximise the fundamental RF fields contained within the system and ensure that the passage of frequencies of interest is further attenuated towards the edge of the cavity for minimal leakage.

4.3 Choke Cavity Performance

4.3.1 Electromagnetic Simulations Overview

Understanding the operation and performance of the complex Choke Cavity required calculating the cavity frequencies, E- and H-fields and losses for different iterations of the design in CST [44]. CST is one of many EM simulation codes that is based on solving the wave equation (Equation 2.1) inside electrically conductive structures. The infinite number of solutions define the set of eigenmodes that are excited in the cavity. These can then be used to calculate useful figures of merit such as H_{pk}, E_{pk}, U, G (defined in Section 2.1.1) and simulate values of Q_0 for given R_{s}.

These simulations required specifying material properties and boundary conditions prior to simulation. The CST model used is shown in Figure 4.5. The Choke Cavity and sample were simulated as lossy metals separated by a vacuum gap. Lossy metals are materials with finite electrical conductivities (σ) for which the electric fields penetrate a layer defined by the skin depth. For both parts, $\sigma = 7 \times 10^{13}\,\mathrm{Sm}^{-1}$ was used, corresponding to $R_{\mathrm{BCS}} \approx 20\ \mu\Omega$ (for $RRR = 300$ superconducting bulk Nb at 4.2 K and 7.8 GHz calculated using the SRIMP code [56]). An absorber, made from lossy dielectric, formed a tapered ring from the width of the gap to a short distance outside choke 3 to prevent reflections back into the cavity. Without this, total RF losses in the system would be underestimated as it would be difficult to properly account for radiative losses through the gap outside of choke 3. To simulate a material with high EM absorption, a material with relative permittivity, $\epsilon_{\mathrm{r}} = 4.3$ and a dielectric loss tangent, $\tan\delta = 0.2$ at 10 GHz, was used. Simulations assumed perfect surfaces with zero roughness. However, it is possible that real surfaces with a finite roughness may impede current flow.

A background material was defined in the shape of a box surrounding the Choke Cavity. For this, a perfect electrical conductor (PEC) was used because 100% lossless reflections of EM waves on the surface ensures that the EM fields are contained within the resonant structure. This means that the simulation accurately represents

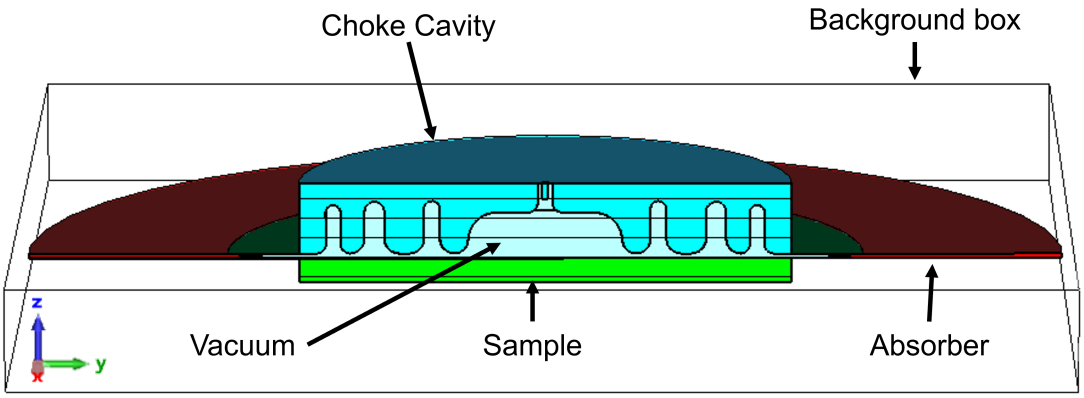

Figure 4.5: The Choke Cavity CST model.

the EM behaviour of the cavity modes without being influenced by external losses. This sets the boundary condition $E_{\parallel} = 0$ ($H_{\perp} = 0$) in all directions. As the Choke Cavity has axial symmetry, the two symmetry planes between the vertical axis and horizontal axes (i.e. YZ and XZ) had magnetic $H_{\parallel} = 0$ ($E_{\perp} = 0$) boundary conditions. This simplified the simulations to a quarter of the model, thus reducing the calculation time by a factor of 4.

In total, three types of CST solver were used for Choke Cavity simulations in this work:

- Eigenmode - to calculate H_{pk}, E_{pk}, U, G and Q factors (detailed in this section and Section 4.4).
- Frequency domain - to calculate S-parameters (detailed in Section 4.4).
- Thermal steady state - to calculate thermal distributions due to DC and RF heating (detailed in Section 6.5).

4.3.2 Figures of Merit

The design of the Choke Cavity focused on minimising RF leakage out of the system. To understand the EM performance of this design, eigenmode simulations were performed. The simulations started with the elliptical half-cell cavity and one choke

to understand the effect of varying the choke dimensions. Subsequent simulations were then performed with additional chokes.

Two figures of merit, in addition to f_0, were investigated:

- For the input of RF power into the system, some power is dissipated in the Choke Cavity, some on the sample (both Ohmic losses), and the rest are non-Ohmic losses radiated as leakage through the gap (P_{rad}). Currently, losses in RF couplers have been neglected. The main optimisation goal was to minimise total RF losses through the system. To quantify all RF losses, a quality factor was defined for the system (Q_{system}) which should be maximised to maximise the peak magnetic field on the sample surface ($B_{\mathrm{s,pk}}$) for a given input power. Its definition is analogous to the definition of Q_{L} in Equation 2.25:

$$\frac{1}{Q_{\mathrm{system}}} = \frac{1}{Q_0} + \frac{1}{Q_{\mathrm{rad}}}, \tag{4.1}$$

  where Q_0 is the quality factor of the combined Choke Cavity and sample.

  For non-Ohmic (radiative) losses, a quality factor was defined as Q_{rad} (analogous to Q_0 in Equation 2.7), which is given as

$$Q_{\mathrm{rad}} \equiv \frac{\omega_0 U}{P_{\mathrm{rad}}}, \tag{4.2}$$

  This should be maximised, as most of the input RF power should be dissipated on the sample and the Choke Cavity whilst minimising P_{rad}.

- Another measure of leakage is to monitor the magnitude of the E-field of the fundamental mode on the sample surface at the edge of the cavity (E_{edge}), i.e. just outside the position of choke 3, 50 mm from the centre. This is compared with the maximum E-field on the sample surface (E_{pk}). Therefore, $E_{\mathrm{edge}}/E_{\mathrm{pk}}$ should be minimised. To monitor the effectiveness of each choke cavity parameter in minimising leakage, an arbitrary comparison of parameter values was made at $E_{\mathrm{edge}}/E_{\mathrm{pk}} = -30\,\mathrm{dB}$.

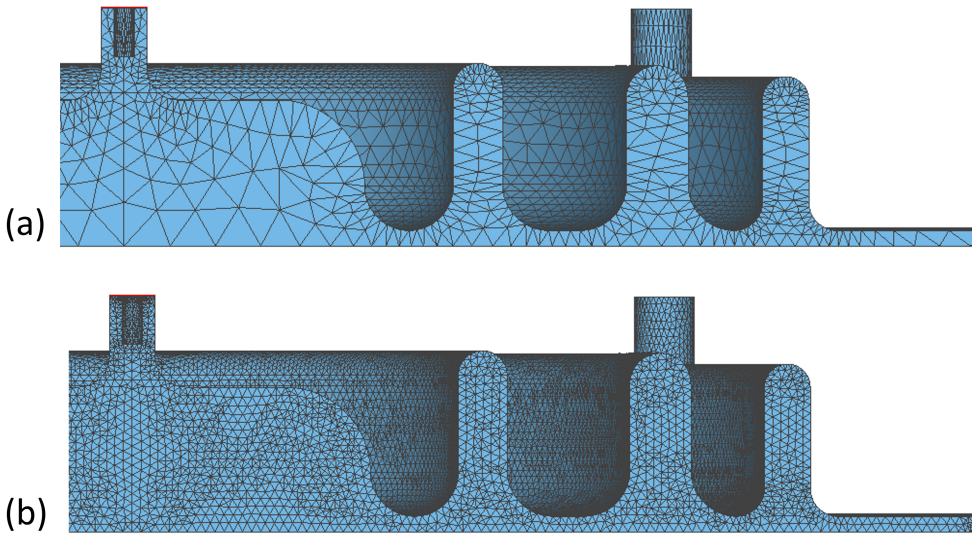

Figure 4.6: Examples of the Choke Cavity mesh: (a) course, (b) fine.

Given the complex geometries that are typically simulated, it is not possible to solve Equation 2.1 for a structure as a continuous geometry. Instead, the structure is subdivided into cells, known as a mesh. Maxwell's equations are then solved in each cell. A tetrahedral mesh was used for all simulations. This type of mesh divides the structure into tetrahedrons. Figure 4.6 shows two examples mesh generation. A fine mesh has a higher mesh density than a course mesh, leading to more accurate solutions. However, increasing the number of mesh cells requires more computer memory and increases the simulation time.

For the Choke Cavity, a set of eigenmode simulations were performed with varying numbers of mesh cells to determine the minimum number of mesh cells that should be used. Figure 4.7 shows the effect of increasing the number of mesh cells on f_0 and Q_{system}. These results show good convergence for both parameters when using above 1.5×10^6 mesh cells.

4.3.3 Single Choke System

For an RF cavity, the structure must be built so that EM waves can reflect back and forth from the walls of the cavity. If the EM waves have a frequency equal to

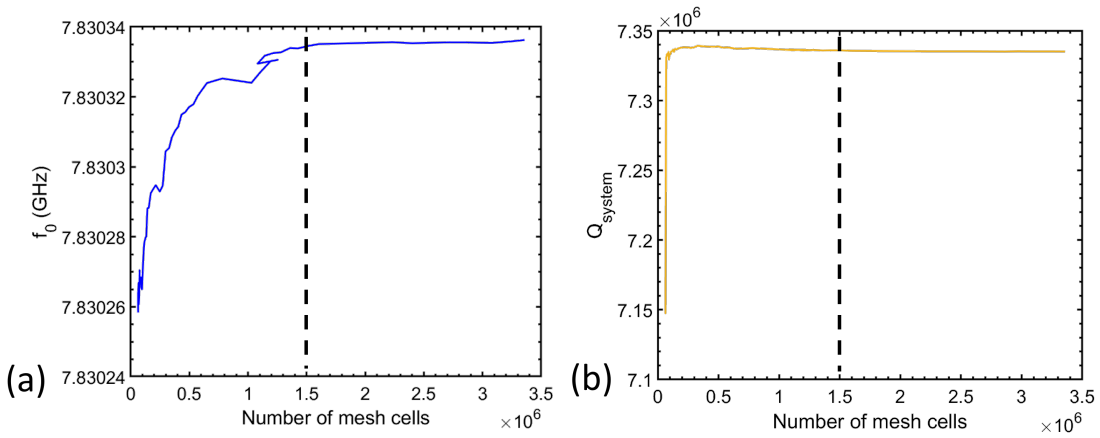

Figure 4.7: Results from mesh optimisation on: (a) f_0, (b) Q_{system} (the dashed line represents the level of mesh convergence).

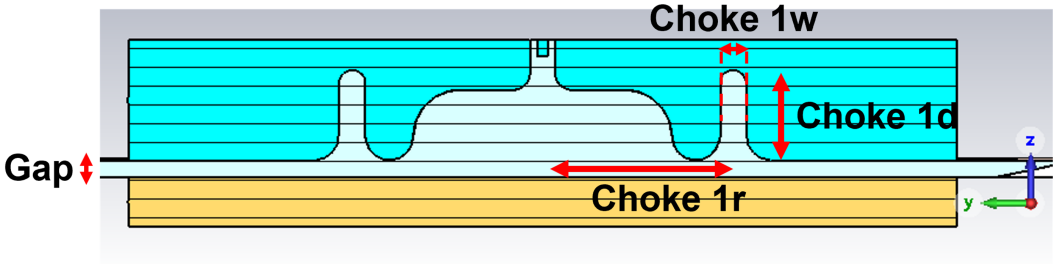

Figure 4.8: The initial single choke cavity design showing the choke parameters that can be varied.

the resonant frequency of the cavity, there is a large build-up of stored energy in the cavity. This happens because an RF cavity is a closed structure that allows these reflections to take place without any RF leakage. However, the main purpose of the Choke Cavity design was to have a physical gap between itself and the sample, and therefore, not be closed. The initial design used a central elliptical cavity and a single outer choke structure to establish the resonance as shown in Figure 4.8. In addition to the sample-cavity gap the choke depth, radial position and width are indicated and are denoted by choke 1d, choke 1r, choke 1w.

Firstly, a parameter sweep was performed in the z-plane by varying choke 1d for different values of the gap from $0.5 - 3.0\,\text{mm}$ whilst fixing choke $1\text{r} = 23\,\text{mm}$ and

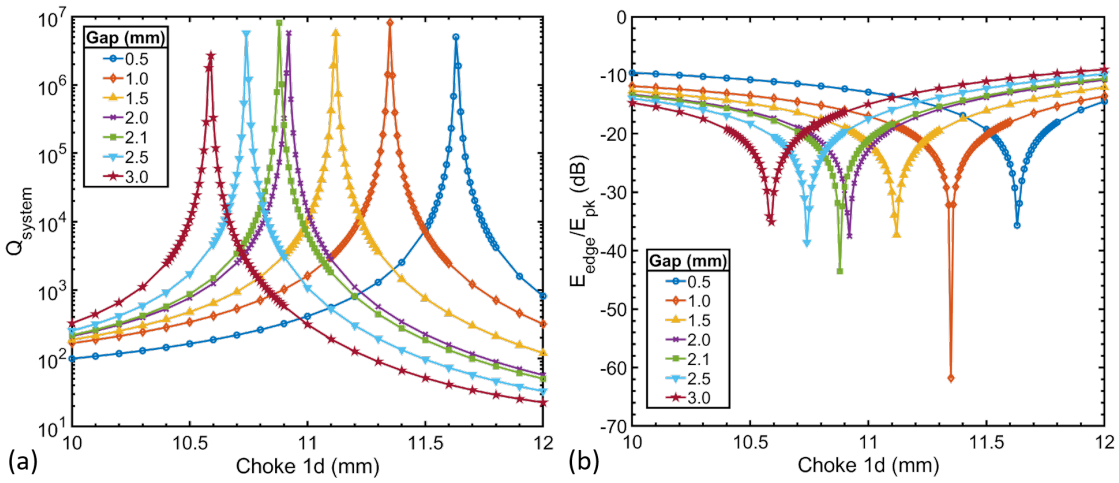

Figure 4.9: The effect of changing the choke 1 depth for a range of gap sizes from $0.5 - 3.0$ mm on: (a) Q_{system} and (b) $E_{\text{edge}}/E_{\text{pk}}$.

choke 1w = 3.2 mm (according to the final design). The results, shown in Figures 4.9(a) and 4.9(b), show that larger gaps require a smaller choke 1d to maximise Q_{system} and minimise leakage. The results illustrate that there exists an optimal value of choke 1d for each gap to maximise Q_{system} and minimise $E_{\text{edge}}/E_{\text{pk}}$. However, for each fixed gap, choke 1d is very sensitive to small variations. For example, a decrease in choke 1d from 11.35 to 11.34 mm with a 1 mm gap is enough to reduce Q_{system} from 8.1×10^6 to 1.4×10^6 due to an increase in leakage whilst increasing $E_{\text{edge}}/E_{\text{pk}}$ to > -30 dB. Figure 4.10 shows examples of magnitude of the E-field with the fundamental mode showing the effect of changing choke 1d for gaps of 0.5 mm and 3 mm. For the cases of minimum leakage with gap = 0.5 mm and choke 1d = 11.79 mm (Figure 4.10(a)(ii)) and gap = 3.0 mm and choke 1d = 10.59 mm (Figure 4.10(b)(ii)), the minimum E-field appears in the bottom right of the choke with minimal leakage beyond. For the choke 1d = 10 mm and choke 1d = 12 mm cases, the position of these minima change, thus increasing leakage. For the gap = 3 mm, the leakage is largest with a choke 1d = 12 mm, with a minimum far from the choke, whilst for the gap = 0.5 mm leakage is largest beyond the minima with a choke 1d = 10 mm.

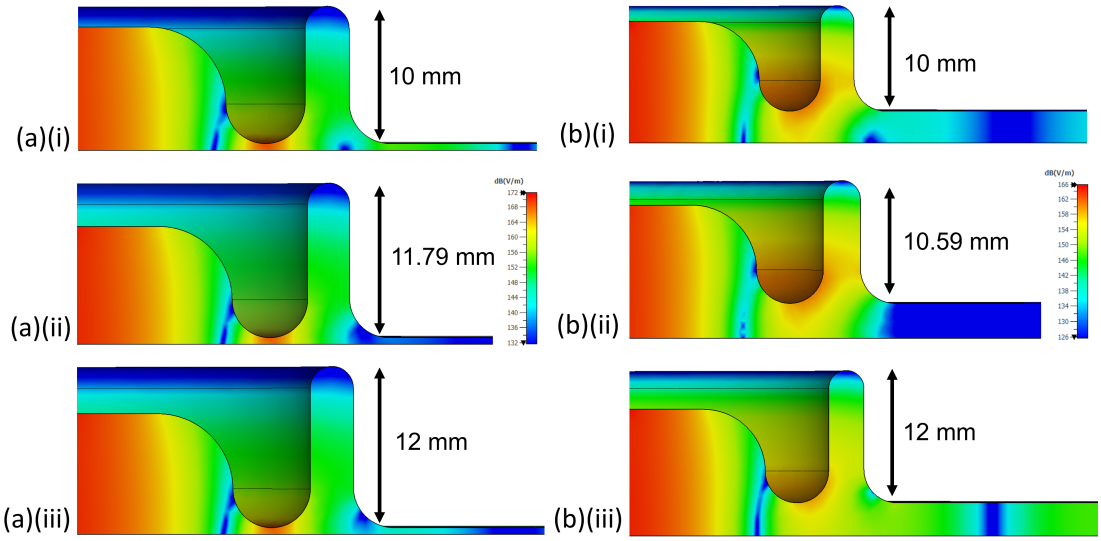

Figure 4.10: Examples of contour plots for the fundamental mode showing the effect of changing choke 1d on the magnitude of the E-field for: (a) gap = 0.5 mm and (b) gap = 3.0 mm. Minimum leakage is shown in (a)(ii) for choke 1d = 11.79 mm and (b)(ii) for choke 1d = 10.59 mm.

A second parameter sweep was performed in the xy-plane by varying choke 1r for values of choke 1w from $2-6$ mm whilst fixing choke 1d = 10.87 mm and gap = 2.1 mm (based on the final design). These results are shown in Figures 4.11(a) and 4.11(b). It can be seen that the maximum Q_{system} and minimum leakage require lower values of choke 1r for a larger choke 1w. Each value of choke 1w is sensitive to small changes in choke 1r, however, this sensitivity appears to decrease for larger choke 1w. For example, a change in choke 1r by ± 0.05 mm for choke 1w = 2 mm is enough to decrease in Q_{system} by an order of magnitude, whilst for a choke 1w = 6 mm, it is tolerant to changes in choke 1r of ± 0.14 mm. An increase in Q_{system} for choke 1w = 5.0 mm is also observed for choke 1r < 19.2 mm and for choke 1w = 6.0 mm with choke 1r < 19.6 mm. Both appear to coincide with choke 1 overlapping the central elliptical cavity, therefore they are not valid cavity designs. Examples of magnitude of E-field contour plots are shown in Figure 4.12. As in Figure 4.10, the minimum E-field appears in the bottom right of the choke with minimal leakage

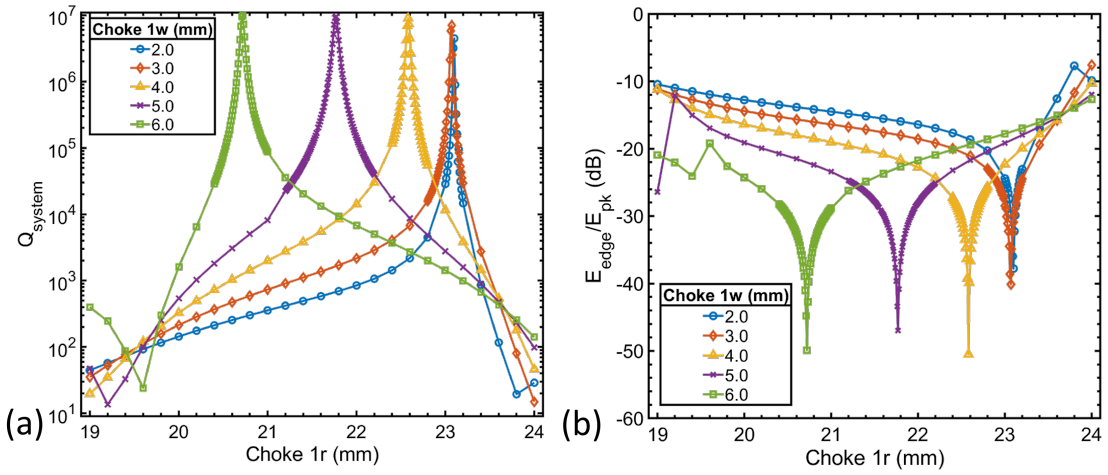

Figure 4.11: The effect of changing the choke 1r for choke 1w from $2-6$ mm on: (a) Q_{system} and (b) $E_{\text{edge}}/E_{\text{pk}}$.

beyond in Figures 4.12(a)(ii) and 4.12(b)(ii). Leakage beyond the choke is shown for the cases of choke 1r $= 19$ mm and choke 1r $= 24$ mm. Figure 4.12(b)(i) shows a weak E-field in the central cavity due to coupling with a nearby mode.

The values of choke 1d for each gap and choke 1r for each choke 1w corresponding to the maximum Q_{system} and the minimum $E_{\text{edge}}/E_{\text{pk}}$ are shown in Figures 4.13(a) and 4.13(b). It can be seen that for larger gaps, a smaller choke 1d should be used to minimise leakage. Likewise, a higher choke 1w should coincide with a smaller choke 1r. In addition, for each parameter, the widths of the curves at $E_{\text{edge}}/E_{\text{pk}} = -30$ dB are shown for comparison (denoted by Δ_{choke1d} and Δ_{choke1r}). This is used to compare the range over which the parameter is optimal to minimise leakage, i.e. an indication of the tolerance of each parameter. It can be seen that there is no significant change in the sensitivity of choke 1d, with an average $\Delta_{\text{choke1d}} \approx 0.04$ mm. Choke 1r can be seen to have a higher tolerance that increases with choke 1w to a maximum of $\Delta_{\text{choke1r}} = 0.44$ mm for a choke 1w $= 6$ mm and choke 1r $= 20.7$ mm.

The variation of each choke 1 parameter also changes f_0. For each gap size, there exists a value of choke 1d for which the target $f_0 = 7.8$ GHz can be achieved, as shown in Figure 4.14(a). For larger choke 1w, the value of choke 1r required to reach $f_0 = 7.8$ GHz increases, as shown in Figure 4.14(b). Therefore, despite the

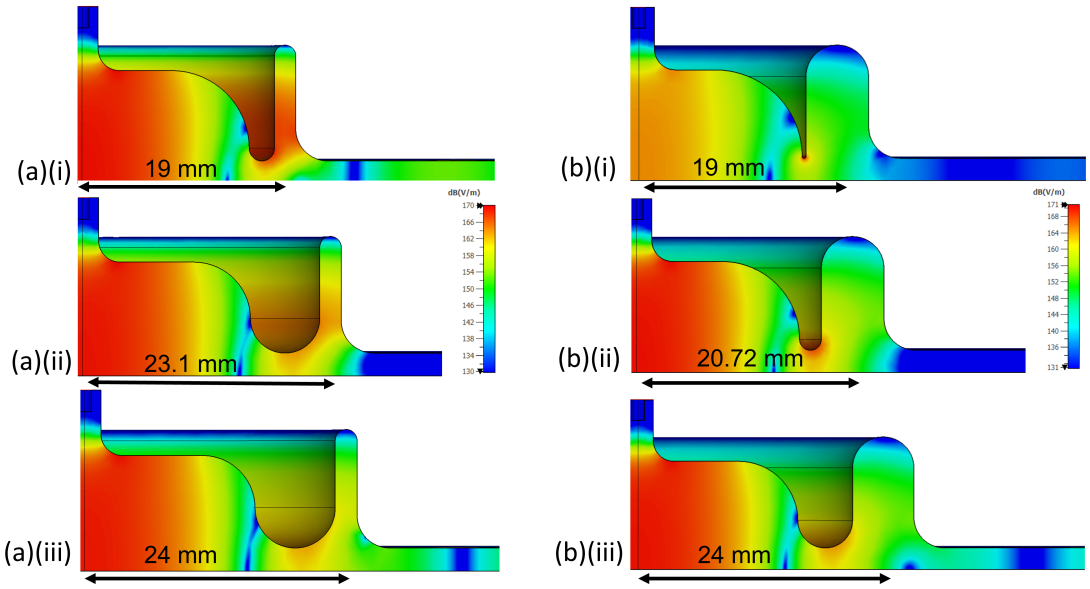

Figure 4.12: Examples of contour plots for the fundamental mode showing the effect of changing choke 1r on the magnitude of the E-field for: (a) choke 1w = 2.0 mm and (b) choke 1w = 6.0 mm. Minimum leakage is shown in (a)(ii) for choke 1r = 23.10 mm and (b)(ii) for choke 1r = 20.72 mm.

higher Δ_{choke1r} for lower values of choke 1r, the target $f_0 = 7.8$ GHz is only achievable for choke 1r > 22.8 mm for this range of choke 1w.

Overall, it would be difficult to manufacture a one-choke cavity because of the tight tolerances on the choke parameters. The addition of chemical etching or fractions of millimetre deviations from the original design would almost certainly lead to a cavity with significant leakage, thus reducing the maximum $B_{\text{s,pk}}$. Therefore, additional steps had to be considered to further mitigate leakage with more chokes being the only option.

4.3.4 Additional Chokes

As a result of the tight tolerances of the one choke system, additional chokes were subsequently added around choke 1 whilst ensuring that the total Choke Cavity structure did not significantly exceed 100 mm in diameter.

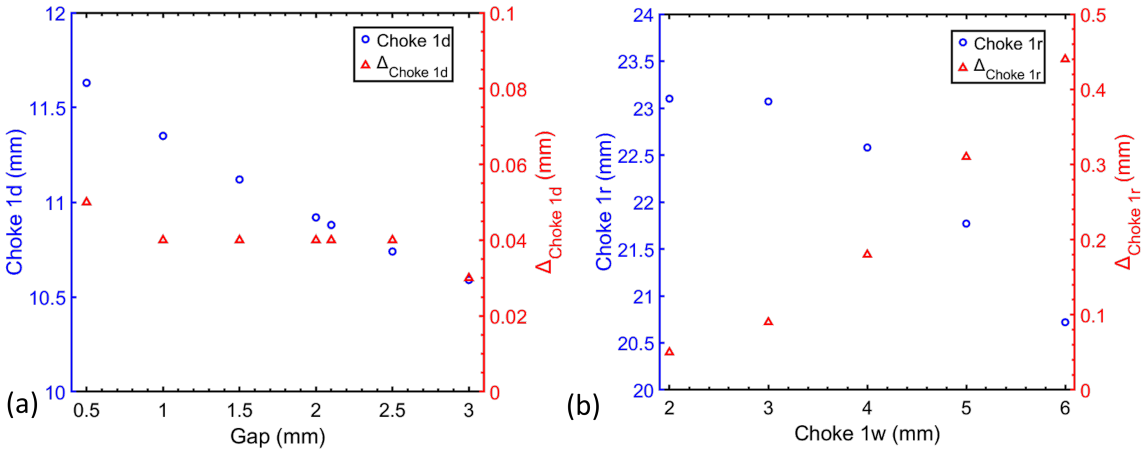

Figure 4.13: The combination of choke 1 parameters that produce the lowest leakage and the parameter range for which $E_{\text{edge}}/E_{\text{pk}} < -30\,\text{dB}$ (represented by Δ_{choke1d} and Δ_{choke1r}) for: (a) choke 1d as a function of gap and (b) choke 1r as a function of choke 1w.

Figures 4.15(a) and 4.15(b) show Q_{system} and $E_{\text{edge}}/E_{\text{pk}}$ as a function of choke 1d. These compare the 1 choke model (from Section 4.3.3) to models with the addition of a second (2 choke) and third choke (3 choke). This shows the clear benefits of adding two chokes around the central cavity and choke 1 if they are manufactured with the correct dimensions. The range of choke 1d for which $Q_{\text{system}} > 10^6$ increases dramatically between the three designs, meaning that the 3 Choke Cavity is less sensitive to small parameter changes.

Figure 4.16(a) shows Q_{system} and Figure 4.16(b) shows $E_{\text{edge}}/E_{\text{pk}}$, both as a function of gap for the three models. Changing the gap was investigated as this should detune all chokes. The simulations show that above gap $\approx 3.5\,\text{mm}$, all three chokes start to become significantly detuned. Provided the gap is uniform, it can be seen that the 1 choke design is very sensitive to small gap variations, whilst the 3 choke design is capable of maintaining a $Q_{\text{system}} > 10^6$ over a much wider range of gap sizes. The maximum $Q_{\text{system}} = 8.4 \times 10^6$. For this value, $Q_{\text{rad}} = 1.8 \times 10^9$ and $Q_0 = 8.5 \times 10^6$, therefore, the maximum achievable Q_{system} appears to be limited by ohmic losses. Interestingly, for the 2 choke design, an additional peak in

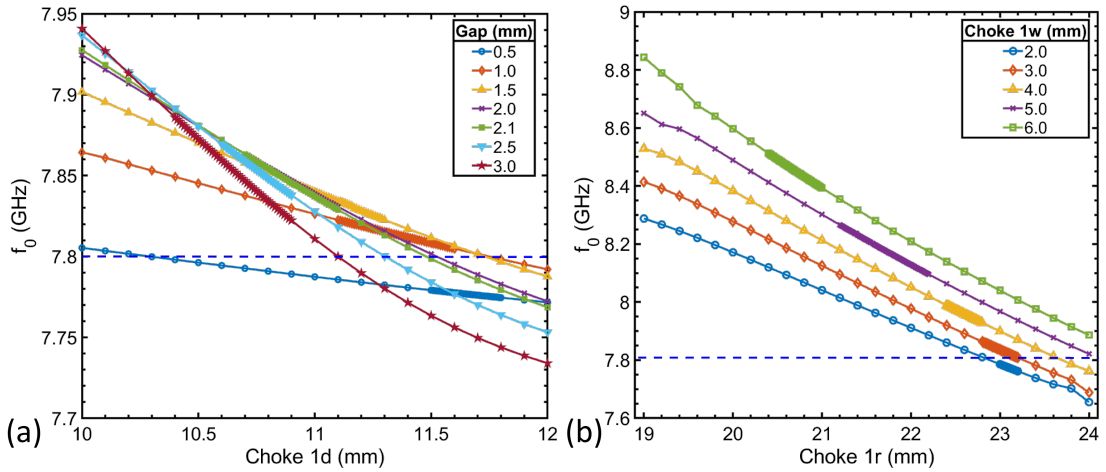

Figure 4.14: The effect of changing choke 1 parameters on f_0: (a) choke 1d and gap (b) choke 1r and choke 1w.

Q_{system} appears with a gap of 3.4 mm. This is a second mode of the choke passband. Experimentally, this could be confirmed by performing a beadpull experiment.

In both Figures 4.15(b) and 4.16(b), $E_{\text{edge}}/E_{\text{pk}} < -30\,\text{dB}$ across the full width of the curves indicating that leakage is minimised with a three choke system. The benefit of having multiple chokes is also illustrated in Figure 4.17. The addition of chokes reduce E/E_{pk} from -30 dB at the edge of the cavity for the 1 choke system to -45 dB for the 2 choke and -50 dB for the 3 choke systems.

For the final design, Figure 4.18 shows that the E-field at the edge of the cavity (i.e. 50 mm from the centre) is $\approx$ 50 dB lower than the E_{pk}. The E-field induces a B-field that is maximal on the sample surface and is responsible for sample heating. The peak magnetic field on the sample ($B_{\text{s,pk}}$) is approximately 1.07 times higher than the peak magnetic field on the Choke Cavity. The corresponding field profiles are shown in Figure 4.19.

It should be noted that without a physical joint between the sample and Choke Cavity, and despite the presence of chokes, there is still some radiation (or RF leakage), represented by Q_{rad}. If there are changes in leakage with each sample, Q_{rad} can never be truly separated out using a VNA S-parameter measurements, meaning that the end-plate replacement method is unsuitable for the Choke Cavity.

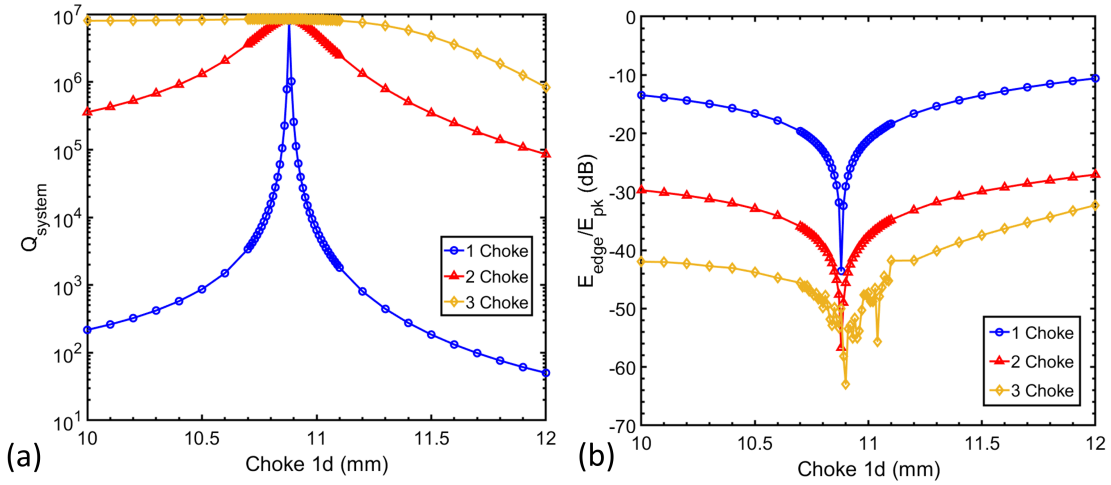

Figure 4.15: A comparison of the effect of changing choke 1d for the 1 choke, 2 choke and 3 choke models: (a) Q_{system}, (b) $E_{\text{edge}}/E_{\text{pk}}$.

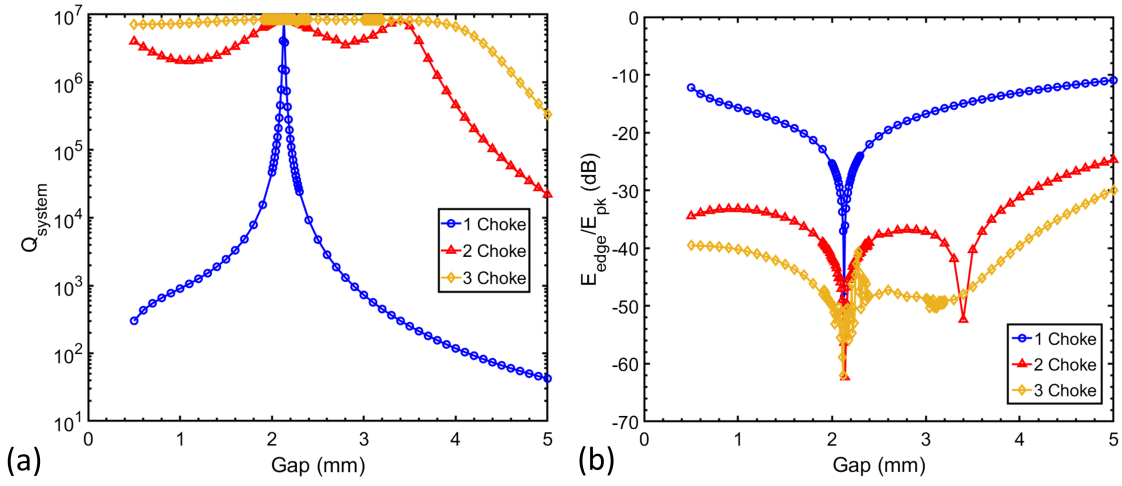

Figure 4.16: A comparison of the effect of changing gap for the 1 choke, 2 choke and 3 choke models: (a) Q_{system}, (b) $E_{\text{edge}}/E_{\text{pk}}$.

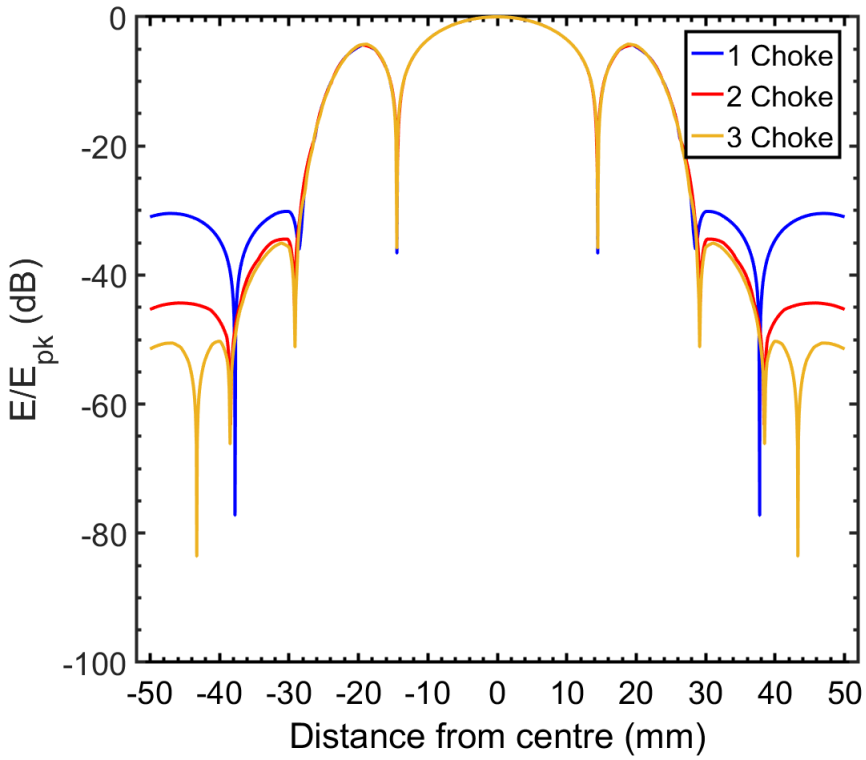

Figure 4.17: A comparison of E/E_{pk} simulated along the diameter of the sample surface for the 1 choke, 2 choke and 3 choke models.

Therefore, only the RF-DC compensation method is suitable for this cavity setup. For the RF-DC compensation method, only the RF heating on the sample needs to be measured. Any RF leakage still present after the addition of chokes would not limit the accuracy of measurements and the ability to measure samples. It would only affect the maximum achievable $B_{\mathrm{s,pk}}$.

4.3.5 Optimisation Of The Sample-Cavity Gap

For RF power input into the cavity, the total RF power dissipated is split between:

- RF dissipation on the Choke Cavity surface.
- RF power dissipation on the sample surface.
- RF power dissipated due to leakage through the sample-cavity gap.

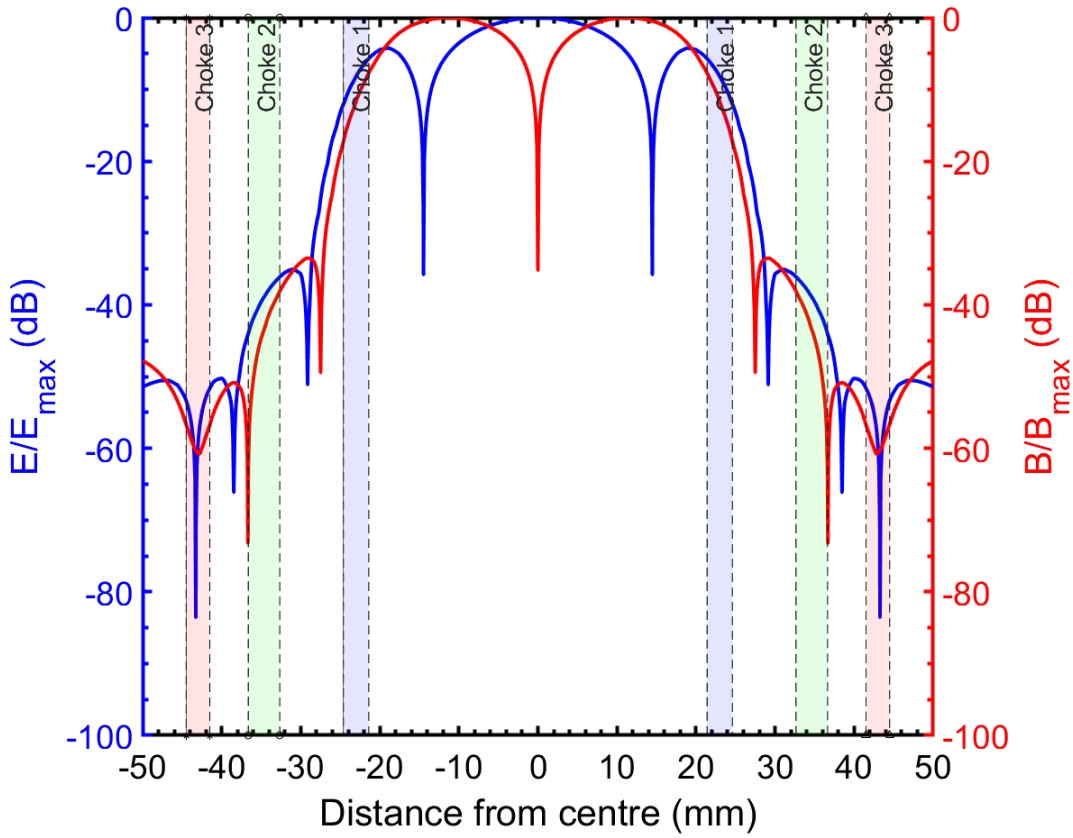

Figure 4.18: The E/E_{pk} and $B/B_{\mathrm{s,pk}}$ for the final Choke Cavity design simulated along the diameter of the sample surface. Also shown are the positions of the chokes.

The original Choke Cavity design minimised $E_{\mathrm{edge}}/E_{\mathrm{pk}}$ for a 2.1 mm gap; however, it was not known whether it would be possible to change the power dissipation ratios by tuning the sample-cavity gap size. The main reasoning behind this was to try and maximise the power dissipated on the sample in order to increase $B_{\mathrm{s,pk}}$.

Figure 4.20(a) shows the effect of increasing the sample-cavity gap size on power dissipation in the three areas, assuming the same R_{s}. As shown, a smaller gap size results in a higher percentage of power dissipation in the sample, allowing for higher values of $B_{\mathrm{s,pk}}$. Leakage dominates when the size of the gap is > 4 mm, therefore care should be taken to control the gap size. A gap size < 1 mm could risk direct contact between the sample and Choke Cavity. Therefore, a gap size of 1 mm was

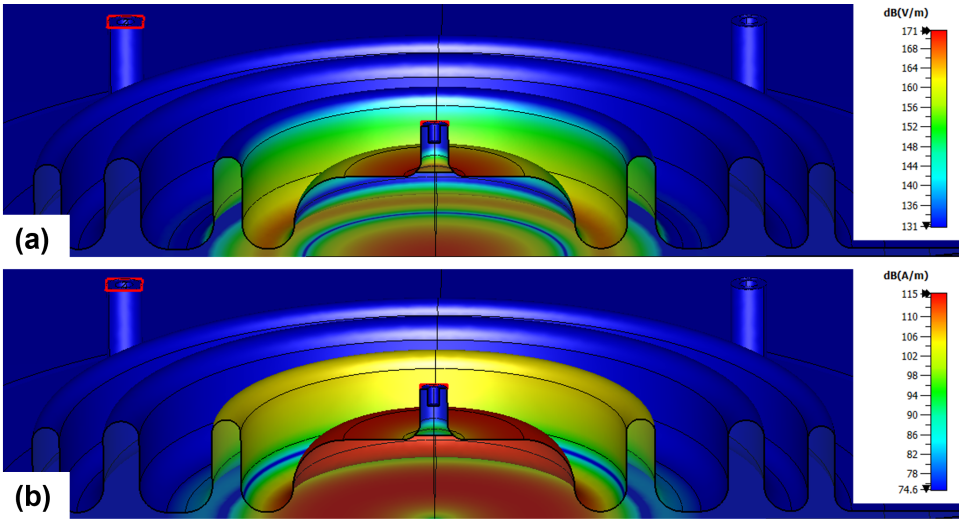

Figure 4.19: The magnitude of the EM fields on the Choke Cavity and sample illustrating the: (a) E-field and (b) B-field.

chosen, as this was considered the minimum size that is easiest to maintain with spacers (as detailed later in Section 5.1.1). The leakage with a gap = 1 mm is higher than for gap sizes $1.5 - 3.5$ mm because the Choke Cavity was originally designed for a larger gap; however, a smaller gap allows optimisation of sample losses. Figure 4.20(b) shows that changing the gap size also changes f_0. A peak in $f_0 \approx 7.85$ GHz is seen for a gap = 2 mm which decreases for gaps smaller and larger than this.

Simulations showing the effect of tuning the gap size on both Q_{system} and $B_{\text{s,pk}}$ are given in Figures 4.21(a) and 4.21(b). Despite a peak in Q_{system} around 2 mm, due to lower leakage, Q_{system} is fairly consistent until a gap > 4 mm. However, $B_{\text{s,pk}}$ is inversely proportional to the size of the gap. A 1 mm gap has 1.5 times higher $B_{\text{s,pk}}$ than a 5 mm gap. For a thin film sample test cavity, maximising $B_{\text{s,pk}}$ should be prioritised. This justified the decision to use a 1 mm gap size for sample tests. This gap size was used to simulate the coupler positions in Section 4.4. Overall, with this Choke Cavity configuration, approximately 34% of RF heating is on the sample with the rest being on the Choke Cavity and due to leakage.

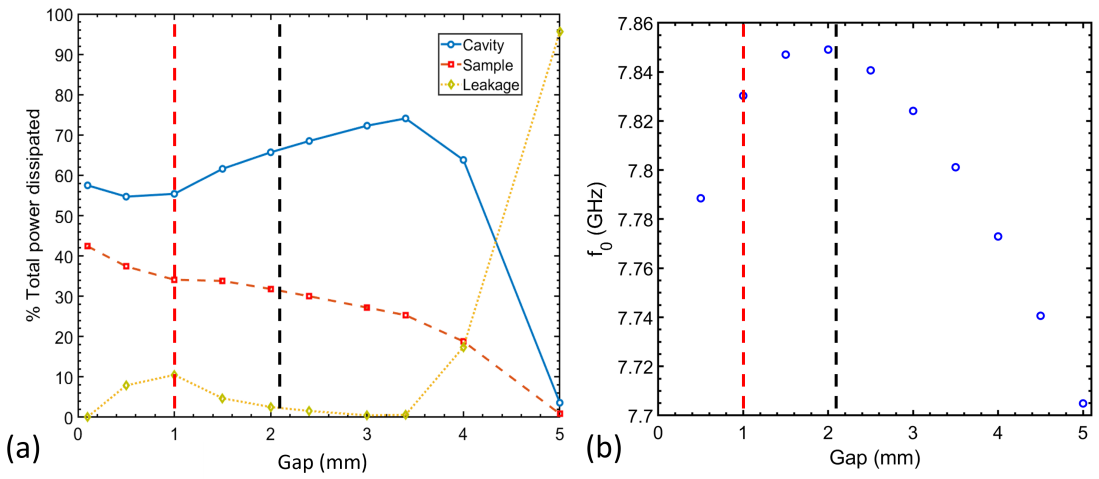

Figure 4.20: The effect of tuning the sample-cavity gap size on: (a) % of RF power dissipated on the sample, cavity and % of RF leakage as a function of sample-cavity gap and (b) resonant frequency (gaps of 1 mm and 2.1 mm are represented by the red and black lines respectively).

4.4 Couplers

RF power transmission to and from the cavity is vital for any cavity test if one wants to measure $Q_0(E_{\mathrm{acc}})$. These RF transmission lines are either waveguides or coaxial cables. Coaxial cables were chosen as they would be easier to mount in the cryostat and less costly. In addition, coupling power from these transmission lines to the cavity requires RF couplers. Input power is typically provided by a conductive rod mounted to the cavity beam pipe, acting as the input coupler. This operates like a coax whereby the conductive rod forms the centre conductor and the beam pipe forms the outer conductor, both separated by an insulating vacuum. This allows for E-field coupling whereby RF power travels to the cavity by coupling the TEM mode of the coupler to the TM mode of the cavity. I.e., both the coupler E- and H-fields are perpendicular to the direction of travel. To measure the transmitted power, a second coupler must be added, typically to the other beam pipe.

The design of the central conductor of the coax can be adjusted depending on the

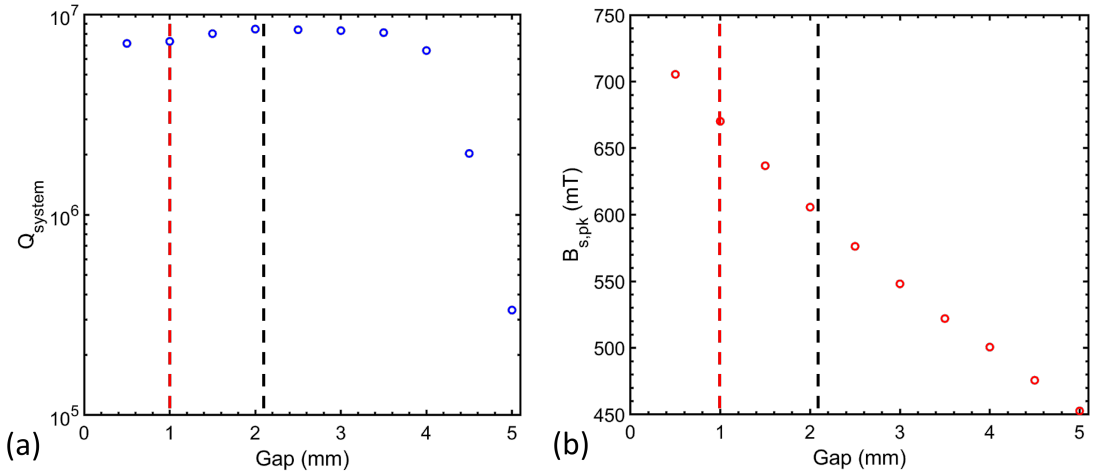

Figure 4.21: The effect of tuning the sample-cavity gap size on: (a) Q_{system} and (b) $B_{\text{s,pk}}$ (gaps of 1 mm and 2.1 mm are represented by the red and black lines respectively).

cavity design, field distribution, and required proper coupler positioning. The central conductor can be left open to form a probe, or shorted with the outer conductor to form a loop. The end of a probe will couple strongly to the E-field (capacitive), whilst a loop will couple strongly to the H-field (inductive). The design choice often depends on whether the coupler is being placed into a high E-field or high H-field region, as well the coupling strength requirement for the cavity.

The basis for adding couplers to the Choke Cavity was a modified RF circuit model, shown in Figure 4.22. This shows the coupling of the input to the central cavity and the coupling of the pickup to one of the chokes. Given the complex design of the Choke Cavity, further CST simulations were required. Both eigenmode and frequency domain simulations were performed. Eigenmode simulations were used to calculate Q_{system} as well as external quality factors, Q_{e} and Q_{t} (defined in Equations 2.26 and 2.27), for the input and pickup respectively. The frequency domain simulations provide details on how the S-parameters vary for each coupler, where S_{11} is the reflection parameter to and from the input port 1 whilst S_{21} is the transmission parameter from port 1 to the pickup port 2. Further details on

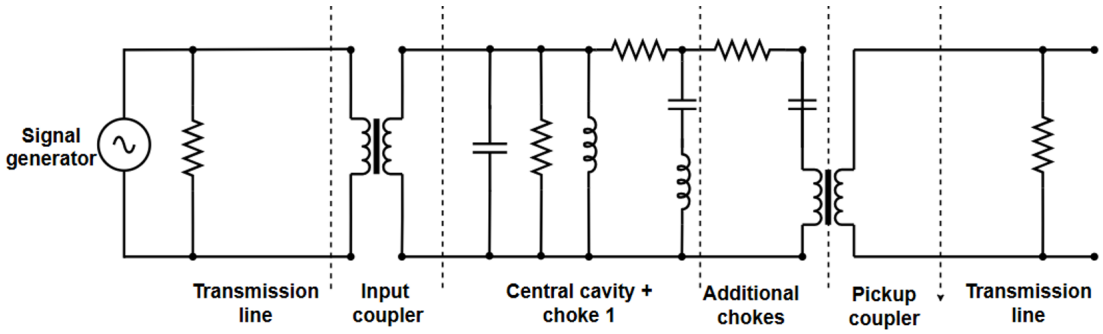

Figure 4.22: An RF circuit model of the Choke Cavity with couplers.

S-parameter measurements can be found in Section 5.3.2.

4.4.1 Input Coupler

For an RF cavity in an accelerator, the input coupler provides RF power to the cavity and subsequently to the beam. For the purpose of sample testing with the Choke Cavity, there is no beam. RF input into the system is still required to evaluate the power dissipated on both the sample and the cavity and to measure how well they perform under RF conditions. However, the presence of an input coupler will perturb the EM fields in the cavity, so its correct positioning should be considered.

For ease of mounting a coupler when the Choke Cavity is installed in a cryogenic facility, it was chosen to mount the input coupler in the centre of the central cavity. The simplest method to couple power is via the centre conductor of a coaxial cable, as shown in Figure 4.23(a). By geometry, having the coupler in the centre means that it is positioned on the axis of peak E-field, therefore, the strongest coupling would be capacitive coupling using a straight probe. The coupling between the TEM mode of the coupler to the TM_{010} mode in the cavity is shown in Figure 4.23(b).

Eigenmode simulations were performed to understand the coupling strength with the input in this position. As shown in Figure 4.23(c), Q_e is sensitive to the depth of penetration of the coupler into the cavity (measured from the top of the Choke Cavity). Q_e is shown to vary by 7 orders of magnitude over a coupler depth range of 5 mm. Given the short range over which Q_e varies significantly, precise control of

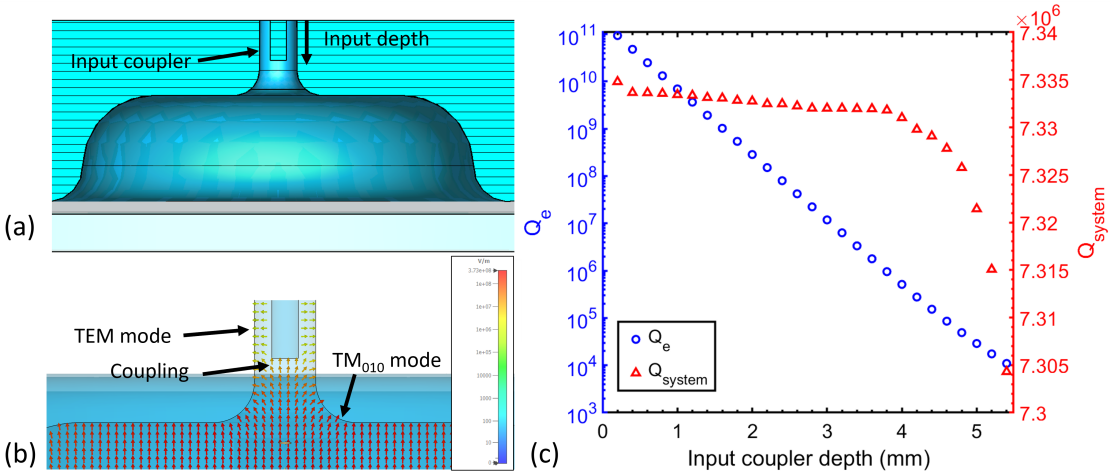

Figure 4.23: (a) Positioning of the input coupler in the Choke Cavity, (b) E-field profile around input coupler, (c) effect of input coupler depth on Q_{e}.

the coupler depth is vital. Also shown in Figure 4.23(c) is the effect of input coupler depth on Q_{system}. As will be shown later in Section 6.2.1, being able to overcouple the input ($Q_{\mathrm{e}} < Q_0$) will be vital. In addition, slight deterioration in Q_{system} is observed for coupler depths $> 4\,\mathrm{mm}$. Therefore, care should be taken not to insert the coupler too far and risk significant perturbation of the EM fields.

Coupling power into the cavity was initially described in Section 2.1.4. Having the ability to vary the depth of the coupler also results in a change of the input coupling factor, β_1, defined in Equation 2.28. Considering the losses defined by Q_{system}, this equation can be modified to

$$\beta_1 \equiv \frac{P_{\mathrm{e}}}{P_{\mathrm{system}}} = \frac{Q_{\mathrm{system}}}{Q_{\mathrm{e}}}, \tag{4.3}$$

where P_{system} is the average power dissipated in the Choke Cavity, sample and due to leakage.

However, it is not possible to measure Q_{system} directly. Instead, Q_{L}, is measured. For a single-coupler system (or when a second coupler is very weakly coupled), this is adapted from Equation 2.20 and is given by

$$Q_{\mathrm{L}} = \frac{\omega_0 U}{P_{\mathrm{system}} + P_{\mathrm{r}}} = \frac{Q_{\mathrm{system}}}{1+\beta_1} = \frac{f_0}{\Delta f}, \tag{4.4}$$

where Δf is the resonance bandwidth.

In addition to the ratio of the dissipated powers in Equation 4.3 and Δf in Equation 4.4, β_1 also defines the reflection coefficient, Γ, in Equation 2.34. This can be calculated using the reflection S-parameter, S_{11}, given by:

$$S_{11}(f) = \frac{\beta_1 - 1 - iQ_{\mathrm{system}}\delta}{\beta_1 + 1 + iQ_{\mathrm{system}}\delta}, \tag{4.5}$$

where δ was previously defined in Equation 2.35.

Later, in Section 6.2.1, it will be demonstrated that being able to adjust Δf, and hence vary Q_{e}, is vital to mitigate the effects of microphonics. The coupler position may also have to be varied for different values of Q_{system} with different samples to maximise input power.

Frequency mode simulations were performed to calculate $|S_{11}|$ for different coupler depths, as shown in Figure 4.24(a). This example shows an increase in Δf, due to a change of coupler depth of 1 mm, as a result of increasing β_1 from $0.2 - 5$, which corresponds to different coupling states described in Section 2.1.4.

As shown in Figure 4.24(a), similar values of $|S_{11}|$ exist for both the undercoupled ($\beta_1 < 1$) and overcoupled ($\beta_1 > 1$) cases; therefore, determining the coupling state requires a different plot. One of the simplest methods requires analysing S_{11} in the complex plane, as shown in Figure 4.24(b), where the real and imaginary components are denoted by $\mathrm{Re}(S_{11})$ and $\mathrm{Im}(S_{11})$ respectively. Out of resonance $|S_{11}| = 1$ and the circle in the complex plane intersects a unit circle, whilst at resonance S_{11} follows a circle towards the origin. For the overcoupled case, the circle includes the origin, whereas the undercoupled case does not. The approximate case of critical coupling ($\beta_1 \approx 1$) is shown where the circle crosses very close to the origin.

A bulk Nb Choke Cavity testing a bulk Nb sample with a critically coupled input (i.e. $Q_{\mathrm{e}} = Q_{\mathrm{system}} \approx 10^7$) is possible for a coupler depth ≈ 3 mm. As has been demonstrated, sub-mm tuning of the coupler is vital to be able to control β_1. The

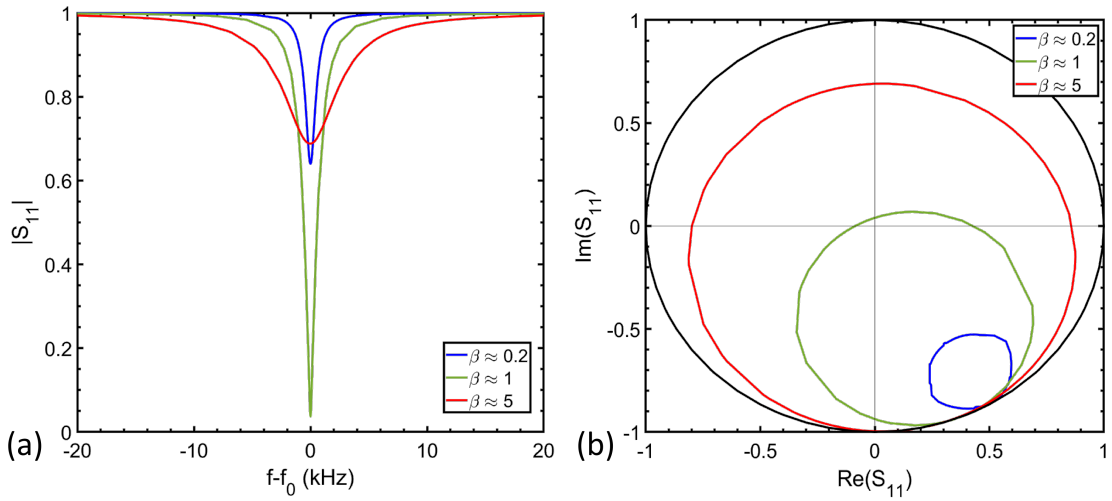

Figure 4.24: Effect of the coupling state on S_{11} for: (a) the magnitude illustrating the effect on the bandwidth with frequency centred at f_0 and (b) the effect on the real and imaginary components.

aim of operation is to perform sample tests with zero frequency span from the VNA or signal generator to ensure that the sample heating is constant when measuring R_s. Zero frequency span would allow the Choke Cavity to be excited at the resonant frequency ensuring that it absorbs maximum power. Therefore, the input should be overcoupled, with $Q_e < 0.1 \times Q_{system}$ to tolerate the effects of microphonics and keep the cavity excited on resonance.

4.4.2 Pickup Coupler

The initial Choke Cavity design used only the input coupler to estimate the stored energy. However, a pickup coupler was required for measurements of the transmitted power (P_t) through the cavity. The pickup coupling factor is denoted by β_2 and is defined as:

$$\beta_2 \equiv \frac{Q_{system}}{Q_t} = \frac{P_t}{P_{system}}. \tag{4.6}$$

Therefore, Q_L is defined as:

$$Q_{\mathrm{L}} = \frac{\omega_0 U}{P_{\mathrm{system}} + P_{\mathrm{r}} + P_{\mathrm{t}}} = \frac{Q_{\mathrm{system}}}{1 + \beta_1 + \beta_2} = \frac{f_0}{\Delta f}, \tag{4.7}$$

where P_{r} is with the RF off.

By calibrating Q_{t}, measuring P_{t} using a pickup allows for direct measurements of stored energy with a lower uncertainty than using a single-coupler system. In addition, future RF systems may incorporate a phase-locked loop (PLL) or self-excited loop (SEL) control system, which requires a signal from the pickup. A PLL compares the phase and amplitude of this signal to a reference signal to generate an error signal. This signal constantly adjusts the frequency of the RF source driving the cavity, ensuring the cavity locked to its resonant frequency. A SEL takes the signal from the pickup through amplitude and phase controllers before amplifying and feeding it back into the cavity as the drive signal, to keep the cavity locked onto the correct frequency.

The overall aim was to weakly couple the pickup ($Q_{\mathrm{t}} > 10 \times Q_{\mathrm{system}}$) to avoid perturbing the EM fields and to ensure sufficient power with a high signal-to-noise ratio for a power meter.

There are three main options for the positioning of a pickup:

- Central elliptical cavity.
- Sample-cavity gap.
- Choke 1, 2 or 3.

Ideally, the pickup would have been inserted into the central elliptical cavity. However, given the small diameter of this section, designed to accommodate the surrounding chokes, a pickup in the cavity would be too close to the input coupler. This could cause unwanted crosstalk between the couplers as a result of interference between the coupler signals.

The second option was to insert the pickup coupler in the gap from the side. However, this was considered a more complex mechanical solution with the added

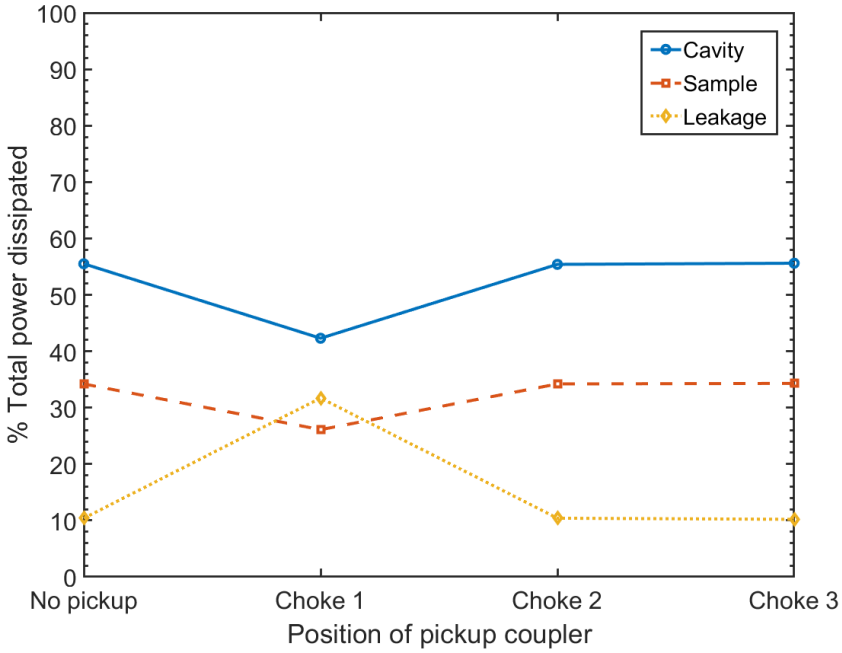

Figure 4.25: The dependence of % of RF power dissipated on the sample, cavity and % of RF leakage on the position of the hole for the pickup coupler.

risk of having the coupler touch the sample or cavity due to the difficult position in a 1 mm gap. It was also discounted as it detuned the chokes and resulting in an increase in leakage. The remaining option to investigate was to drill a hole in one of the three chokes to have the pickup coupler inserted vertically.

To begin this investigation, the first step was to investigate the effect of drilling a small hole in the top of each of the chokes to place the coupler. Figure 4.25 shows simulated measurements of % power dissipated in the cavity, sample, and leakage with a hole in each of the chokes compared to the original design without a hole. The results show that a hole in choke 1 leads to an 11% decrease in power dissipated on the Choke Cavity and an 8% decrease on the sample. This is due to an increase in leakage through the hole in choke 1 due to the high electric field in this region, resulting in degredation in the maximum achievable $B_{\mathrm{s,pk}}$. Meanwhile, having a hole in chokes 2 or 3 allows the cavity to operate with minimal extra leakage.

For simplicity, eigenmode simulations were performed with a straight probe

pickup. Figure 4.26(a) shows the effect of increasing the depth of the pickup coupler in each choke on Q_t. A maximum depth of 15 mm is possible to avoid direct contact with the sample. Given the higher magnitude of the E-field present in choke 1, it is possible to vary Q_t by 10 orders of magnitude over a depth range of 15 mm. A smaller range is covered by having the pickup in choke 2 or choke 3. A minimum $Q_t \approx 10^7$ in choke 2 meets the initial specification, whilst a minimum $Q_t \approx 10^9$ in choke 3 does not. The effect of increasing pickup depth on Q_{system} is also shown. At small depths < 5 mm, $Q_{\text{system}} \approx 7 \times 10^7$, which remains constant throughout the depth range for a pickup in choke 3. For choke 2, a degradation in Q_{system}, and therefore an increase in RF losses, appear for pickup depths > 13.2 mm, whilst this degradation starts earlier at depths > 5 mm in choke 1 with a significant decrease > 12.8 mm. Figure 4.26(b) shows the effect of increasing the depth of the pickup on f_0. A constant f_0 is observed for a pickup in chokes 2 and 3, with a slight increase observed for depths from $5 - 10$ mm before decrease at depths > 12.8 mm. These deviations in f_0 coincide with the degradation in Q_{system}. Overall, a pickup in choke 1 was not considered due to an increase in leakage and choke 3 was not considered due to not reaching the required Q_t for maximum depth. Therefore, given that a hole in choke 2 provided minimal extra leakage and a pickup in this position could reach the required Q_t, further investigations were carried out on the feasibility of a pickup in choke 2.

Simulations were performed in the frequency domain to investigate S_{21} with a pickup in choke 2 whilst using a gap size of 1 mm. The effect of a pickup on $|S_{21}|$ as a function of frequency is shown in Figure 4.27(a). The depth of the coupler was adjusted with $Q_t \approx 10^9$ to meet the initial target. For comparison, the results of a pickup in choke 1 with approximately the same Q_t are shown. For a pickup in choke 1, an ideal $|S_{21}|(f)$ Lorentzian shape is observed. However, in choke 2, as well as observing the mode at f_0, there appears to be an additional peak at ≈ 8.2 GHz. Additional modes can cause problems if their frequencies are too close to f_0. As a result, Fano resonances can arise, which are identifiable by their asymmetric

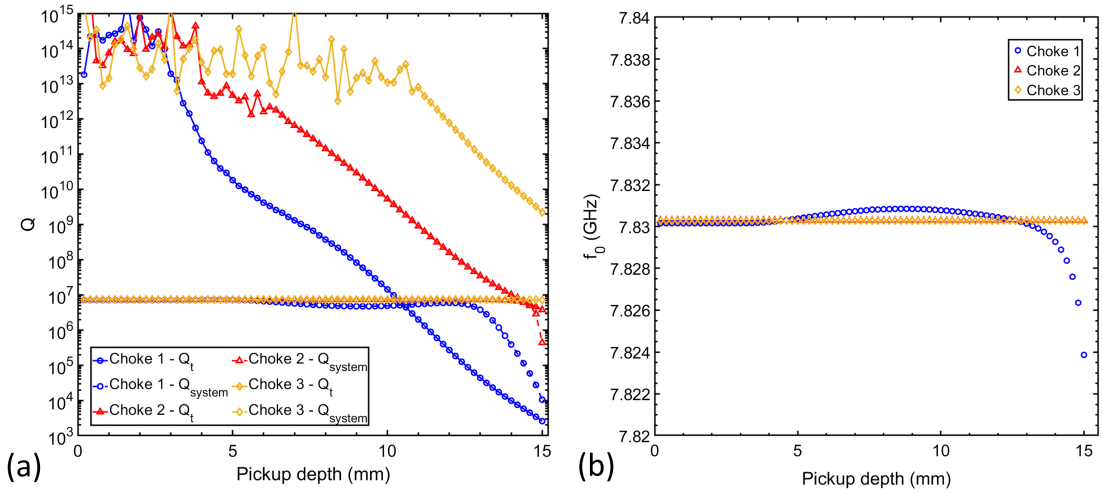

Figure 4.26: The effect of increasing the pickup depth in each of chokes on: (a) Q_{t} and Q_{system} and on (b) f_0.

line profile [186]. This only occurs when the two modes are close enough to cause destructive interference and peak distortion. If the modes are too close, this may lead to larger uncertainties, as the pickup could couple to the wrong mode, and thus provide inaccurate transmitted power measurements. It is also possible that the frequency of the additional mode is an underestimate or overestimate of the actual mode frequency. To avoid coupling issues, it was important to ensure that these additional modes are far away from the main cavity resonance.

Shown in Figure 4.27(b) is the effect of varying the gap size on f_0 and the nearby interfering mode, f_1. This shows that whilst there is little variation in f_0, consistent with Figure 4.20(b), f_1 decreases with increased gap size, with an overlap in peaks at a gap $\approx 2.1\,\mathrm{mm}$. Eigenmode simulations, shown in Figure 4.28(a), show that the pickup couples to a mode at 8.08 GHz. Eigenmode simulations without the addition of a third choke, in Figure 4.28(b), show a similar field pattern at 8.04 GHz and a Fano resonance in Figure 4.28(c). As a result of the consistency, the additional mode cannot be due to the addition of a third choke. f_1 can be attributed to a mode set up between choke 2 and the edge of choke 1. The frequency mode simulations, show that the Fano mode distortions create an overestimate of the frequency of this mode.

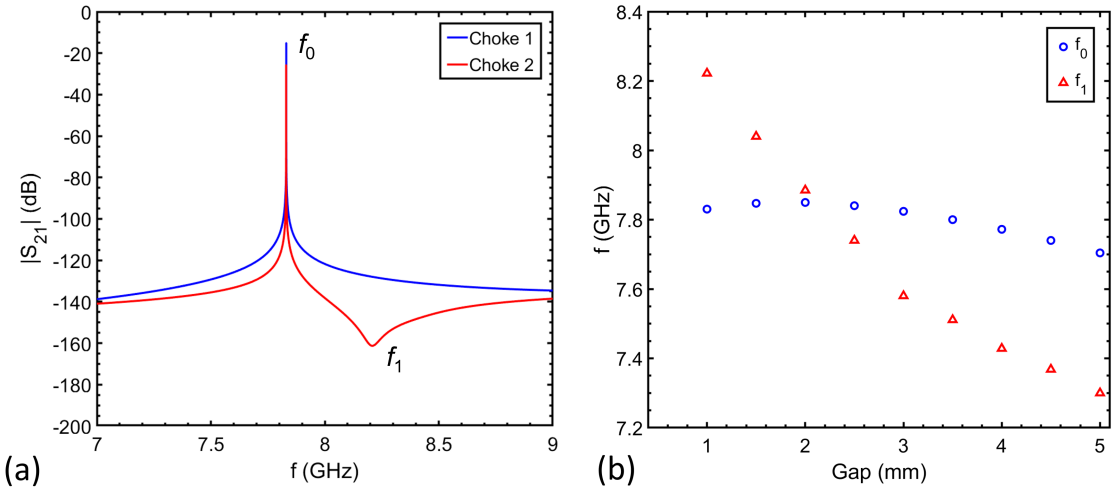

Figure 4.27: (a) $|S_{21}|$ as a function of frequency with a pickup in either choke 1 or choke 2. (b) The effect of increasing gap size on the fundamental mode (f_0) and additional mode (f_1) with a pickup in choke 2.

Overall, for the preferred Choke Cavity-sample configuration with a gap of 1 mm (detailed in Section 4.3.5), the additional mode is ≈ 300 MHz from the cavity mode, which is much higher than the typical cavity bandwidth ($\sim$ few kHz). Therefore, it is okay to position a pickup in choke 2 without fear of coupling to the wrong mode. The results of Figure 4.27(b) also justify the decision to use a smaller gap. However, care should be taken if samples are measured with different gap sizes.

4.5 Cavity Summary and Manufacture

The key figures of merit for the final Choke Cavity design are shown in Table 4.1. The values of Q_{system}, $B_{\text{s,pk}}$, and $B_{\text{cav,pk}}$ assume a bulk Nb cavity and bulk Nb sample, whilst $E_{\text{s,edge}}/E_{\text{s,pk}}$, sample geometry factor (G_{sam}), Choke Cavity geometry factor (G_{cav}) and the combined geometry factor (G) are material-independent. The Choke Cavity dimensions for this are shown in Table 4.2 and the technical drawings are shown in Appendix A.1.

The final design of the manufactured cavity is shown in Figure 4.29. It operates

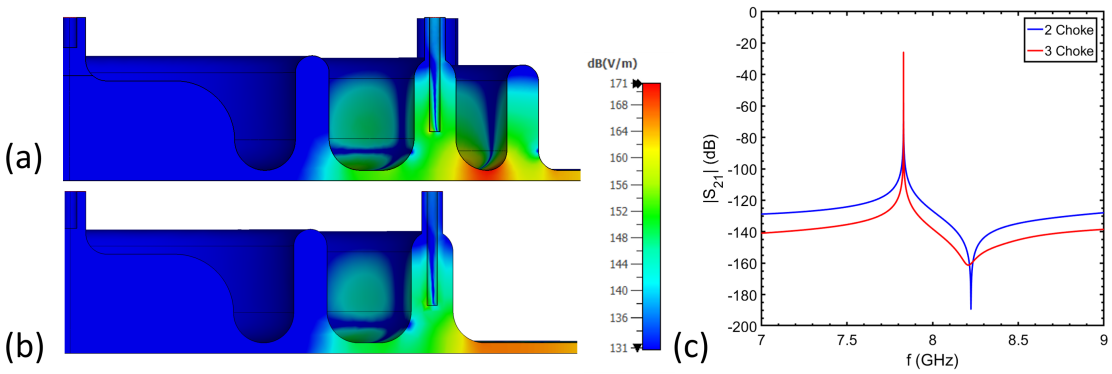

Figure 4.28: Contour plots showing additional mode coupled to by the pickup coupler: (a) final 3 choke design, (b) 2 choke design. (c) $|S_{21}|$ as a function of frequency with a pickup in choke 2 comparing the 3 choke and 2 choke designs.

in a TM_{010} mode at $f_0 = 7.8\,\text{GHz}$. Two parts are required for RF tests:

- Choke Cavity: A half-cell elliptical cavity surrounded by three quarter-wavelength RF chokes milled and machined from $RRR = 400$ bulk Nb manufactured by Niowave Inc [187]. Holes 3 mm in diameter are drilled into both the half-cell cavity and choke 2 for positioning of the RF couplers. The entire structure is 104 mm in diameter and 12 mm thick. The cavity received the following treatments:
  - A 600 °C bake to degas hydrogen.
  - A light 20 µm BCP etch at INFN to remove surface contaminants formed during heat treatment.
  - A 120 °C bake for 48 hours at Daresbury Laboratory to diffuse oxygen from the surface to the bulk.
- Planar sample: a $90 - 130\,\text{mm}$ in diameter and $1 - 10\,\text{mm}$ thick bulk Nb or thin film coated Cu disk separated from the Choke Cavity by a 1 mm gap.

Taking into account the RF losses on the Choke Cavity, sample and leakage, a maximum $Q_{\text{system}} \approx 10^7$ can be achieved using a bulk Nb Choke Cavity. It is possible that a thin film coated Choke Cavity, e.g. Nb_3Sn/Cu, might achieve $Q_{\text{system}} > 10^7$.

Table 4.1: A summary of the key Choke Cavity design parameters.

Parameter	**Value**
f_0 (GHz)	7.83
Q_{system}	7.3×10^6
$E_{\text{s,edge}}/E_{\text{s,pk}}$ (dB)	-50
$B_{\text{s,pk}}/\sqrt{U}$ (mT/J$^{0.5}$)	670
$B_{\text{s,pk}}/B_{\text{cav,pk}}$	1.07
G_{sam} (Ω)	452
G_{cav} (Ω)	279
G (Ω)	154

Table 4.2: A summary of the Choke Cavity dimensions.

Location	**Parameter**	**Dimension (mm)**
Central half-cell	Radius	15.638
	Depth	8.48
Choke 1	Choke 1d	10.87
	Choke 1r	23
	Choke 1w	3.2
Choke 2	Choke 2d	10.71
	Choke 2r	34.66
	Choke 2w	4
Choke 3	Choke 3d	10
	Choke 3r	43
	Choke 3w	3

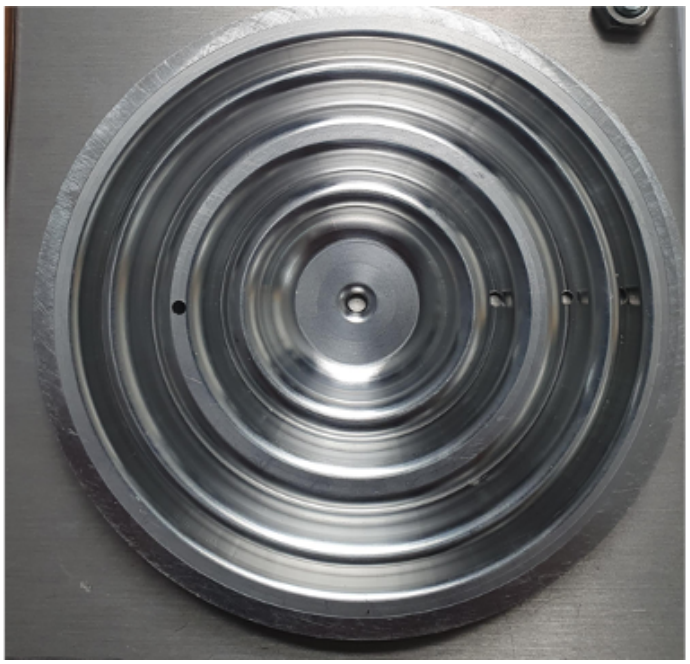

Figure 4.29: The manufactured bulk Nb Choke Cavity.

Chapter 5

Test Facility Design and Operation

RF testing of planar samples with the Choke Cavity requires a bespoke cryogenic vertical test facility design. With the primary goal of testing alternative superconducting thin films, the facility must be able to measure samples at temperatures down to at least 4.2 K. There must also be sufficient power to use the RF-DC compensation method (detailed previously in Section 3.2.2).

This chapter begins by describing the three main components of this facility: the cryogenic system, the vacuum system, and the RF system. A recently built cryostat has been modified and developed to its current iteration to successfully measure thin film samples. Details about the design and facility operation will be shown, including sample mounting procedures and a typical facility operation cycle. The final section of this chapter derives the required equations for calculating the stored energy of a 2-port system using a simple vector network analyser based RF system, and describes how this is used to calculate the surface resistance of samples.

5.1 Facility Design

Testing SRF samples using the Choke Cavity requires cryogenic cooling. The main aim whilst using this cavity design is to achieve a high sample turnover in order to test and compare multiple samples per week. To achieve this, a bespoke cryogenic facility was required. Developing such a facility requires three main components to be considered:

- Cryogenic System:

  The Choke Cavity and samples need to be tested in a cryostat, i.e., an insulated vacuum vessel that provides cooling with liquid cryogens or a cryocooler. Provided that the aim is to operate thin film cavities at 4.2 K, this is the minimum temperature requirement for the cryostat. It should also be possible to measure R_s over a wide temperature range, ideally covering the theoretical T_c of the material. With the primary objective of testing alternative superconductors, the maximum sample temperature of the facility should be at least the highest theoretical T_c of the materials of interest (e.g., 18.3 K for Nb_3Sn [188]). The facility should also be able to handle multiple thermal cycles per week to satisfy the desired sample testing rate.

- Vacuum System:

  If the facility does not use liquid cryogens, it needs to be pumped to high vacuum (HV), $10^{-3} - 10^{-7}$ mbar to provide thermal insulation and minimise convective heat loads and residual gas conduction. The system should be easy to operate and capable of handling regular pump and vent cycles. The types of pump used (e.g., dry or wet) should also be considered to minimise particulate contamination inside the facility that could pollute the sample.

- RF System:

  The design of an RF circuit should consider how much power can be input into the Choke Cavity without it heating up beyond the cryogenic cooling capacity.

The level of RF power input dictates the maximum $B_{\mathrm{s,pk}}$ that can be measured. An increase in $B_{\mathrm{s,pk}}$ results in an increase in power loss (from Equation 2.9) that will heat the sample (with a similar effect due to peak field on the Choke Cavity). The maximum RF power will therefore be limited by the cryogenic cooling capacity after static losses (e.g. radiation and thermal conduction through cabling) have been accounted for. One would expect field emission, and therefore radiation, at $E_{\mathrm{pk}} \approx 10\,\mathrm{MV/m}$. This scales to a $B_{\mathrm{pk}} \approx 18\,\mathrm{mT}$, corresponding to $P_{\mathrm{f}} \approx 10\,\mathrm{W}$ for a critically coupled input. Lab health & safety limited the $P_{\mathrm{f}} < 1\,\mathrm{W}$.

5.1.1 Cryogenic System

Designing a cryogenic system requires choosing whether to have a wet or dry system. A wet system is one that uses liquid cryogens, such as liquid nitrogen (LN) and liquid helium (LHe). In these systems heat transfer occurs via conduction through the liquid and gas phases of the cryogens, but also via convection. Meanwhile, a dry cryostat is a system that does not require liquid cryogens. Instead, it uses a mechanical cryocooler, typically Gifford-McMahon (GM) or Pulse-Tube Cryocooler (PTC), to cool the components via conduction through solid components. These systems will only reach base temperature if the system is under mid-HV such that there is negligible convective heat transfer.

If it is desirable to reach temperatures down to 2 K and operate with high cooling capacity, a wet system should be used. If a system requires a simple design with high sample turnover that is also easy to operate, a dry system is preferable. The advantages and disadvantages of using the two types of cryogenic system to test SRF samples are summarised in Table 5.1.

In 2015, a LHe-based cryostat for the Choke Cavity was commissioned [185, 189], as shown in Figure 5.1. The Choke Cavity was mounted to a Cu heat sink in direct contact and conduction cooled with a LHe vessel. The sample was mounted under the cavity on a separate Cu base plate supported by thin-wall stainless steel

Table 5.1: The advantages and disadvantages of wet and dry cryogenic systems for SRF sample testing.

	Advantages	Disadvantages
Wet	High cooling powers.	LHe needs refilling.
	Low base temperatures.	Complex design and
	Can measure quench fields.	operation.
		Rising LHe costs.
		Additional safety concerns.
		Multiple staff operation.
Dry	No liquid cryogens.	High initial cost.
	Only require electrical power.	Low cooling powers.
	Continuous cooling.	Higher base temperature.
	Simple design and turn-key	One person operation.
	operation.	

tubes to minimise thermal conduction between the sample and cavity. Both sat within a small vacuum chamber. Initially, this chamber was filled with He gas for cooling. The chamber was then evacuated ensuring that the cavity and sample were thermally and electrically isolated via a vacuum gap with no physical connection. This was important to allow for direct measurements of RF losses on the sample in order to calculate its surface resistance independent of the Choke Cavity. Pumping on the LHe allowed base temperatures $< 2\,\mathrm{K}$ and control of temperature was through heaters and thermometers.

Despite successfully measuring a bulk Nb sample, a lot of effort was required to change the samples and prepare the facility for testing. This was ultimately due to the time-consuming nature of forming additional vacuum seals inside the cryostat and the requirement for LHe and LN, which often had supply problems. This restricted the turnover rate to just one sample every two weeks.

To simplify the measurements and allow for a high sample testing rate, it was

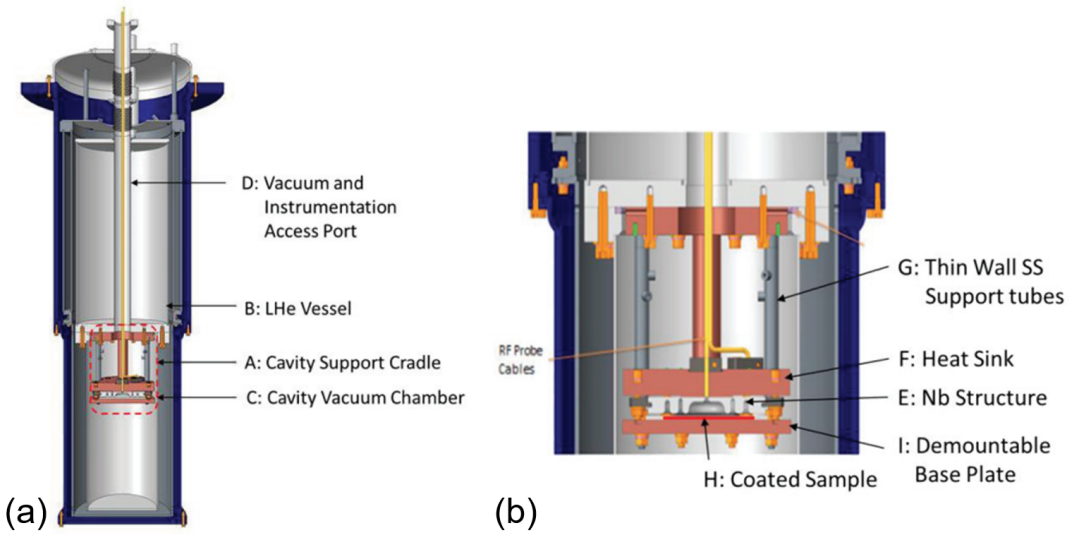

Figure 5.1: A schematic of the original cryostat: (a) the LHe cryostat, (b) mounting of the Choke Cavity and sample.

decided that a dry cryogenic facility built around a cryocooler would be the best option. This was considered a cheaper long-term option compared to the wet system because of the increasing cost of LHe. Furthermore, in the absence of LHe, the time-consuming vacuum joints that need to be sealed within the cryogenic vessel were not required. The main issue was creating a thermally insulating vacuum seal between the Choke Cavity and sample. With a dry cryostat, the Choke Cavity and sample would share the same vacuum as all other components in the facility, meaning that the sample change over procedure would be much more straightforward and only one vacuum seal for the main chamber would need to be made.

The resulting LHe-free dry cryostat, shown in Figure 5.2, is the result of several years of development and recent modifications since the first design of this system [190]. The facility is easy to operate and safe with minimal training requirements. Furthermore, a new method of sample mounting (discussed later in Section 5.2.1) allows reliable measurements of RF losses on the sample independently of the Choke Cavity to calculate the sample R_s.

This facility is built around a two-stage GM cryocooler (Sumitomo RDK-415D2).

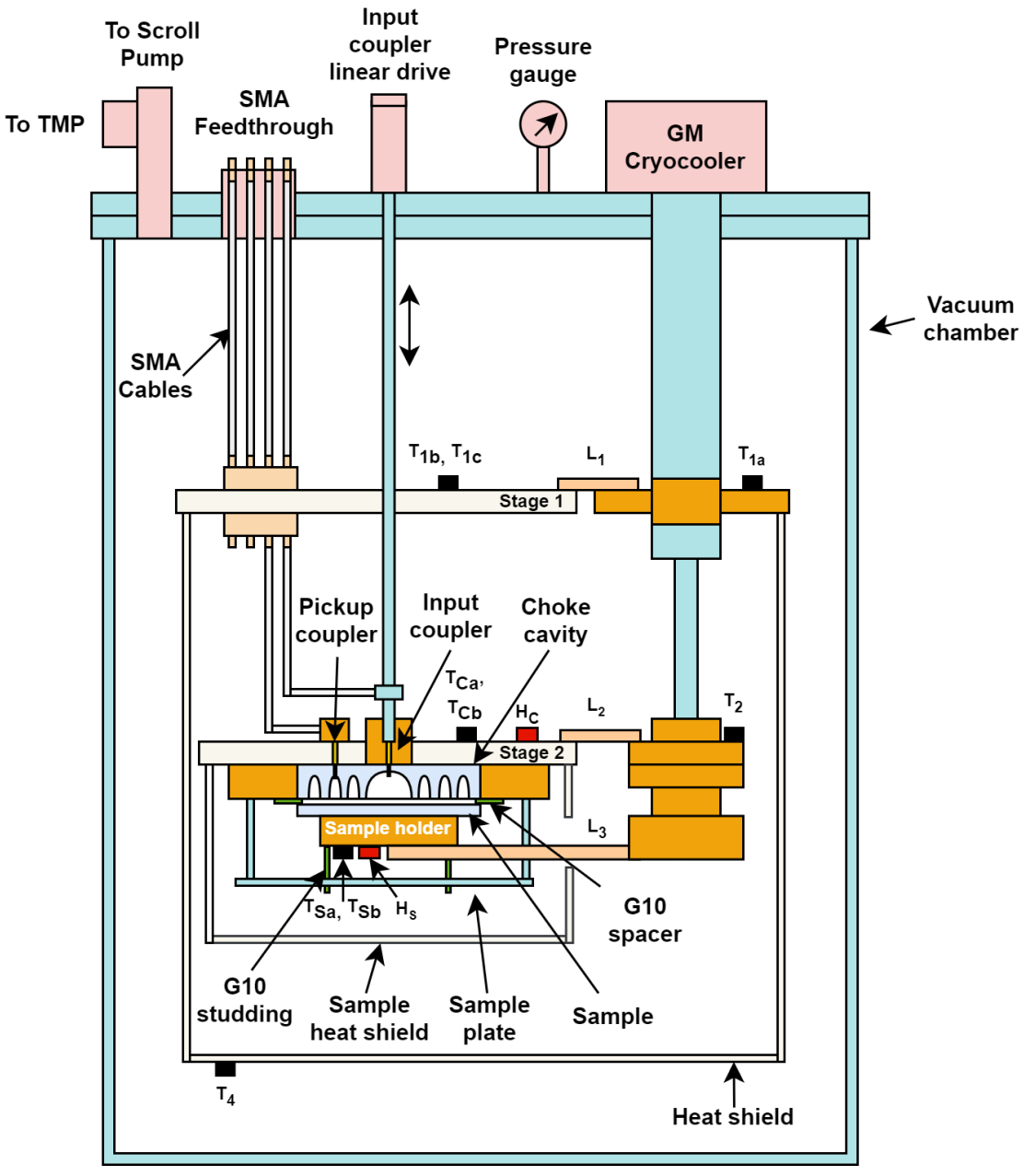

Figure 5.2: A schematic of the Choke Cavity cryostat.

A cryocooler of this type circulates He gas within a closed cycle to produce cooling in two stages. The cryocooler is connected to a Sumitomo F-50 water-cooled compressor, which supplies high-pressure gas to the cryocooler and receives low-pressure gas back. This combination of a cryocooler and a compressor produces a maximum cooling power of 35 W at 50 K (stage 1) and 1.5 W at 4.2 K (stage 2).

The main advantage of this setup is the simple operation to start the cooling process, which only requires switching on the compressor (either with a mechanical switch or remote control). This requires no training, unlike the LHe cryostat operation. The main disadvantage of using a GM cryocooler is vibrations due to the cooling cycle and moving parts that operate at a frequency of 1 Hz. Mechanical vibrations can be transferred through the Choke Cavity, sample and couplers, which could affect the level and stability of RF power input into the Choke Cavity. This is known as microphonics and will be addressed later in Section 6.2.1. The alternative is to use a PTC. This is typically more expensive than a GM however, it has less vibration at stages 1 and 2 due to no low temperature moving parts. Future upgrades or new cryogenic facilities for SRF cavity testing would benefit from using a PTC.

The GM cryocooler is mounted on an upper flange of an outer vacuum chamber (OVC) made of 304L stainless steel (SS). SS is used because of its high mechanical strength and low cryogenic thermal conductivity. The cryocooler is thermally connected by flexible Cu heat links (L_1 and L_2) to two large Cu plates: stage 1 plate and stage 2 plate. Typically, oxygen-free high conductivity (OFHC) is the grade of choice for all cryogenic Cu due to its high thermal conductivity at cryogenic temperatures. The two stage plates have many tapped through holes and feedthroughs to mount and heat sink the electronics (i.e. thermometers, heaters, connectors, cable cooling bobbins, etc.).

During upgrades, the internal and external wiring was completely re-made. Originally, the thermometers were soldered directly to D-25 connectors (shown in Figure 5.3(a)), which meant that any subsequent repairs would be difficult. The thermometry wiring was re-organised used breakout boards mounted to the

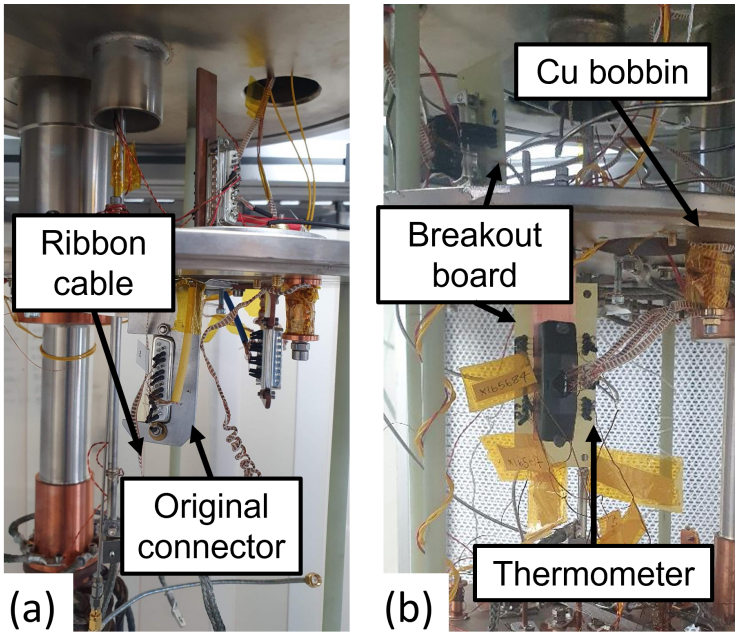

Figure 5.3: (a) Original wiring, (b) uprgraded wiring using breakout boards.

underside of stage 1 (shown in Figure 5.3(b)). These are PCBs with a D-25 connector wired to 6 sets of 4 sockets. Each of the sockets corresponds to a thermometer and allows for easy connecting and disconnecting of thermometers whenever a sample is mounted. The D-25 is wired to the room temperature flange with a twisted pair ribbon cable to minimise conductive heat load. The heaters were wired separately with D-9 connectors, again with twisted pairs to minimise electrical interference. Wrapping ~~as~~ the wires coming from room temperature around the cooling bobbins on stage 1 ensure good thermal anchoring and minimise heat conduction to stage 2.

Mechanically, the stage 1 plate is mounted with four G10 supports on the OVC top flange, and the stage 2 plate is mounted with another four G10 supports to the stage 1 plate. G10 is a fibreglass epoxy material that has good mechanical stability and low thermal conductivity. It also has a high dielectric strength, which makes it very suitable as an electrical insulator. Therefore, it is used in cryogenic environments where high thermal and electrical insulation as well as high mechanical strength are required. All G10 used was cleaned with isopropyl alcohol and ultrapure

water prior to installation to minimise particulate contamination.

For any cryogenic system, heat transfer due to thermal radiation is typically the dominant heat load and therefore must be mitigated. According to the Stefan-Boltzmann law, the heat transfer between two bodies is proportional to the difference between the fourth power of their temperatures. This means that the heat load from room temperature (300 K) to cold stages (4.2 K) is significant unless thermal intercepts are installed, i.e., heat shields. If, for example, a LN cooled shield at 77 K is placed between 300 K and 4.2 K, the 4.2 K surface would receive a radiative heat load approximately 230 times less than a system with no shield.

Due to the significant difference in radiation head loads from different temperature stages, a Cu heat shield is mounted on the stage 1 plate to reduce the radiation heat load to stage 2 (including the sample). The heat shield is also covered with multi-layer thermal insulation (MLI). MLI consists of thin layers of highly reflective aluminised Mylar placed in the vacuum between the hot OVC and cold Cu heat shield. Each layer acts as radiation shield, and layers of non-conducting mesh are placed between them to minimise thermal conduction. In addition, any holes on stage 1 are covered with Al plates or reflective tape to avoid a direct line of sight between the room temperature OVC and 4.2 K stage 2 plate. An additional heat shield was added to the stage 2 plate around the sample and cavity to minimise radiation from stage 1. The mounting of the heat shields is shown in Figure 5.4.

The facility uses several thermometers, typically resistance temperature detectors (RTDs), at different points within the cryostat. With RTDs, the resistance of the sensor varies with temperature and can be used, provided that they have been calibrated. The temperature of the stage 1 cold head (T_{s1}) is monitored with platinum RTDs (Pt100). Four of these temperature sensors are used (T_{1a} to T_{1d}) and are connected to a Lakeshore 218 temperature monitor. Pt100 sensors are used because they provide high repeatability and are typically suitable for measurements down to 20 K. They are not as accurate as other cryogenic thermometers; however, they are a significantly cheaper alternative where high accuracy is not necessary,

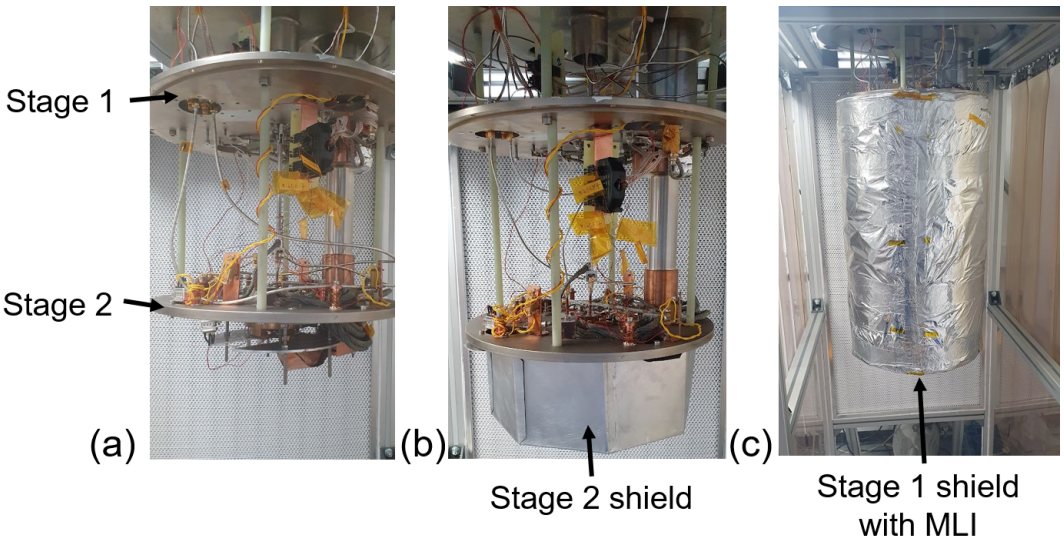

Figure 5.4: (a) Open cryostat, (b) mounting of the stage 2 heat shield, (c) mounting of the stage 1 heat shield.

such as monitoring the stage 1 plate temperature. All thermometers use 4-wire measurements to ensure that only the voltage drop across the sensor is measured and the measurement accuracy is not limited by the resistance of the wires. All wires are also twisted pairs to reduce electrical noise. The use of Cu bobbins allows wires to be heat sunk to minimise heat leak from the wires to the sensors, avoiding warming of the sensor and inaccurate temperature readings.

The Choke Cavity is mounted directly on the bottom of the stage 2 plate, as shown in Figure 5.5, with two Cu mounts that allow cooling from the top and the edge of the cavity. Thin strips of high purity indium (In) foil are placed between the cavity, Cu supports and stage 2 plate to maximise thermal conductance between different components. Additional In foil is used at the boundary between any components to minimise contact resistance, which may arise from a number of factors including surface roughness and contact pressure. The use of cryogenic vacuum grease (e.g. Apiezon N grease) is an alternative option; however, this was not chosen as the risk of sample contamination was not known. The sample itself is mounted on top of a Cu sample holder (see Section 5.2.1) that sits underneath the

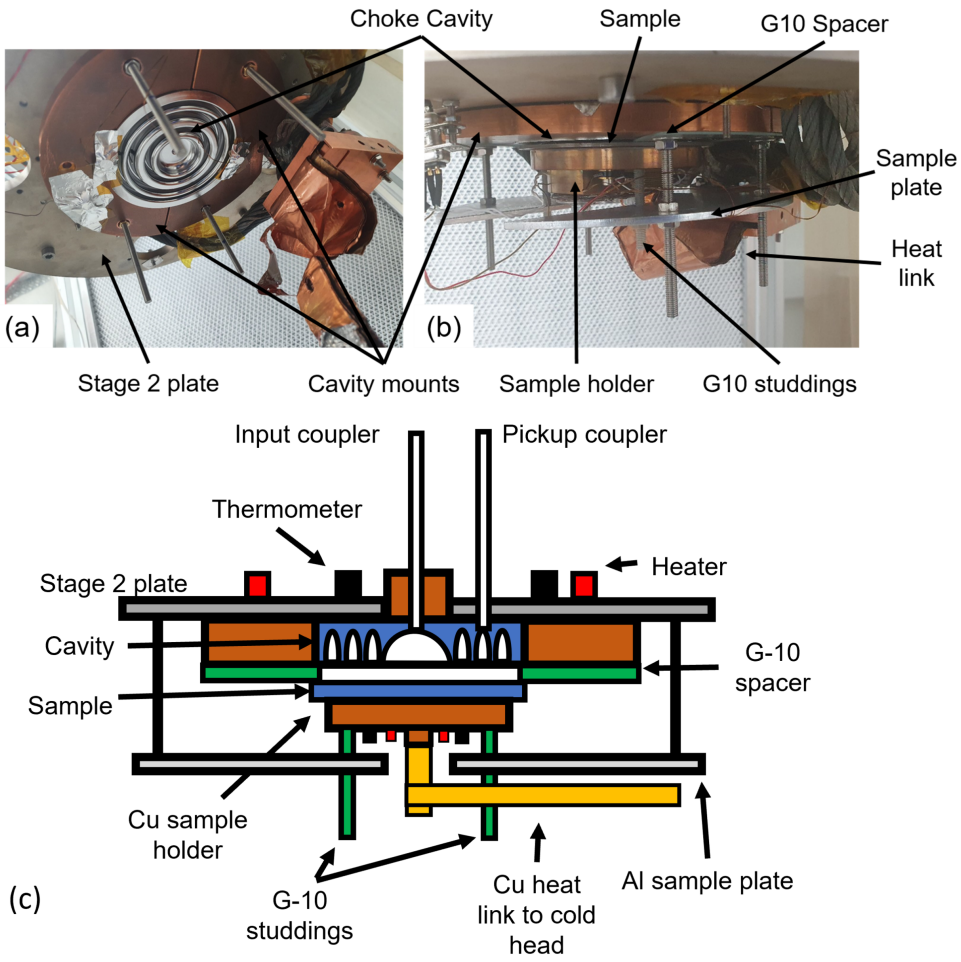

Figure 5.5: (a) The underside of the stage 2 plate showing the Choke Cavity mounted to the stage 2 plate, (b) mounting of a sample underneath the cavity, (c) a schematic of the sample mounting system.

cavity and is supported by three G10 studdings connected to an Al sample plate.

Separation of RF losses on the sample from the Choke Cavity is required for the RF-DC compensation method, previously discussed in Section 3.2.2. For this, a physical gap between the two is required for thermal isolation. Spacers ensure that there is always a constant gap for every sample. A quick study was conducted in which the sample was mounted under the cavity using two different spacer materials to maintain the required 1 mm gap. G10 was compared with Al as the material of choice with no heat links connected the sample to the cold head. The comparison is

Table 5.2: A comparison of the minimum sample temperature, cavity temperature and difference between the Choke Cavity and sample for the two spacer materials without additional cooling.

Spacer	$T_{\mathrm{s,min}}$ **(K)**	T_{cav} **(K)**	ΔT **(K)**
Al	4.5	4.4	0.1
G10	8.2	4.2	4.0

shown in Table 5.2 where both the Choke Cavity temperature (T_{cav}) and the sample temperature (T_{s}) were measured. The minimum temperature ($T_{\mathrm{s,min}}$) reached on the sample with G10 was 3.7 K higher than with Al and the temperature difference (ΔT) between the sample and the cavity was 3.9 K higher due to thermal conduction between the two. The larger temperature difference showed that G10 minimises the thermal conduction pathway and therefore better thermal isolation between the sample and the Choke Cavity. This meant that 1 mm thick G10 could be used confidently to maintain the 1 mm gap and allow control and measurement of T_{s}. The spacers are mounted between the sample and the Choke Cavity outside of choke 3 where dielectric losses due to the spacers are negligible.

The cooling of the sample holder is provided by a separate heat link, L_3, (shown in Figure 5.5) to the cold head to increase the thermal path between the sample and the Choke Cavity. Given that the two are thermally isolated with a vacuum gap, conductive heat flow is only from each component to the cold head, which is the coldest part of the system. A sufficient amount of cooling power is needed across L_3 in order for the sample to reach $T_{\mathrm{s,min}} < 4$ K and also produce a detectable change in temperature with the applied heater power to use the RF-DC compensation method. It was decided that a level of 1 K temperature increase was required for 1 W of power as this would allow much lower levels of RF power dissipation, e.g., $\sim$mW level, to be detected which would produce $\sim$mK temperature fluctuations. The heat link is made from multiple Cu strips sealed with In foil at each end to provide the flexibility required between the cold head and the sample holder. For a heat link with cross-

sectional area A and length L, with one end at temperature T_1 and the other end at T_2 (where $T_2 > T_1$), the rate of heat transfer ($\dot{Q}$) is given by

$$\dot{Q} = \frac{A}{L}\int_{T_1}^{T_2} k(T)\mathrm{dT}, \tag{5.1}$$

where $k(T)$ is the temperature dependent thermal conductivity of the material. For small temperature differences, k was assumed to be constant, giving

$$\dot{Q} = k\frac{A(T_2 - T_1)}{L}. \tag{5.2}$$

From the literature, for OFHC Cu ($RRR = 100$), k $\approx 10^3\,\mathrm{Wm^{-1}K^{-1}}$ [191]. For $L = 100\,\mathrm{mm}$ (approximate distance between the cold head and the sample holder) and for a Cu width of 50 mm, using Equation 5.2 with $\dot{Q} = 1$ W and $T_2 - T_1 = 1\,\mathrm{K}$, this gives a required heat link thickness of 1 mm. Assuming that the Cu strips each have a thickness $\approx 0.1\,\mathrm{mm}$, this means that 10 Cu strips are required for the heat link. This rough calculation provided a starting point for the design of L_3.

Originally, silicon (Si) diode temperature sensors (Lakeshore DT-670) were used to monitor stage 2 and sample temperatures. Si diodes are an alternative to RTDs with a higher precision of $\pm 12\,\mathrm{mK}$ at 4.2 K. However, the manufacturer does not recommend their use in magnetic fields at temperatures below 60 K due to large calibration shifts [192]. As a result, these were replaced by Lakeshore Cernox temperature sensors (CX-1050-CU-HT-1.4L). These are less affected by magnetic fields at temperatures higher than 1 K and have a precision of $\pm 5\,\mathrm{mK}$ at 4.2 K. Two Cernox sensors ($\mathrm{T_{CA}}$ and $\mathrm{T_{CB}}$) are used to monitor stage 2 temperature, while a third Cernox ($\mathrm{T_2}$) is used to monitor stage 2 cold head temperature (T_{s2}). The sample holder is also equipped with two Cernox thermometers ($\mathrm{T_{SA}}$ and $\mathrm{T_{SB}}$).

For measurements of R_s as a function of sample temperature, a way to control the temperature of the Choke Cavity (T_cav) and the sample temperature (T_s) is required. For the control of T_cav, three $10\,\Omega$ heaters mounted to the stage 2 plate are used and are connected to a Lakeshore 331 temperature controller. For the control of T_s, two heaters are used and are connected to a second temperature controller. These

controllers use a proportional, integral, derivative (PID) algorithm to make slight adjustments to the heater power in order to maintain the temperature set point. For both the cavity and sample controllers, the PID parameters were set as: $P = 50$, $I = 100$ and $D = 0$. The power dissipated by the sample and cavity heaters is measured by 4-wire measurement. Measurements of heater current (I_{h}) and voltage (V_{h}) are made using two Multicomp Pro (MP730424) digital multimeters connected to each of the heater sets. Thus, the dissipated power, P_{DC}, is given by

$$P_{\mathrm{DC}} = I_{\mathrm{h}} \cdot V_{\mathrm{h}}. \tag{5.3}$$

5.1.2 Vacuum System

The OVC is a 304L SS cylinder, shown in Figure 5.6, and is sealed to the top plate using an ISO-400 nitrile O-ring. It is equipped with a 67 L/s Pfeiffer (HiPace 80) turbomolecular pump (TMP) backed with a 6 m^3/s Edwards (nXDS6i) scroll pump (SP). A dry pump, such as a SP, is preferred over oil-based pumps (e.g., rotary-vane pumps) because the presence of oil leads to a risk of contamination. Pressure control is achieved by In-Line and angle vacuum valves and two Agilent (FRG-700) full-range pirani inverted magnetron gauges.

It takes approximately 1 hour to rough the system down to a pressure $P \approx 10^{-2}$ mbar with the SP. The TMP is then activated and it takes another 3 hours to reach $\approx 10^{-5}$ mbar. At this point, the cryocooler is turned on and the system reaches a minimum $P \approx 10^{-7}$ mbar at base temperature due to cryopumping of the cold components.

At the end of a sample test, the facility is kept under vacuum and pumping until all parts are warmed to room temperature. A N_2 gas injection system allows venting to atmosphere. The cryostat vacuum chamber is equipped with a pressure relief valve to protect the system from overpressurisation during warm up and venting.

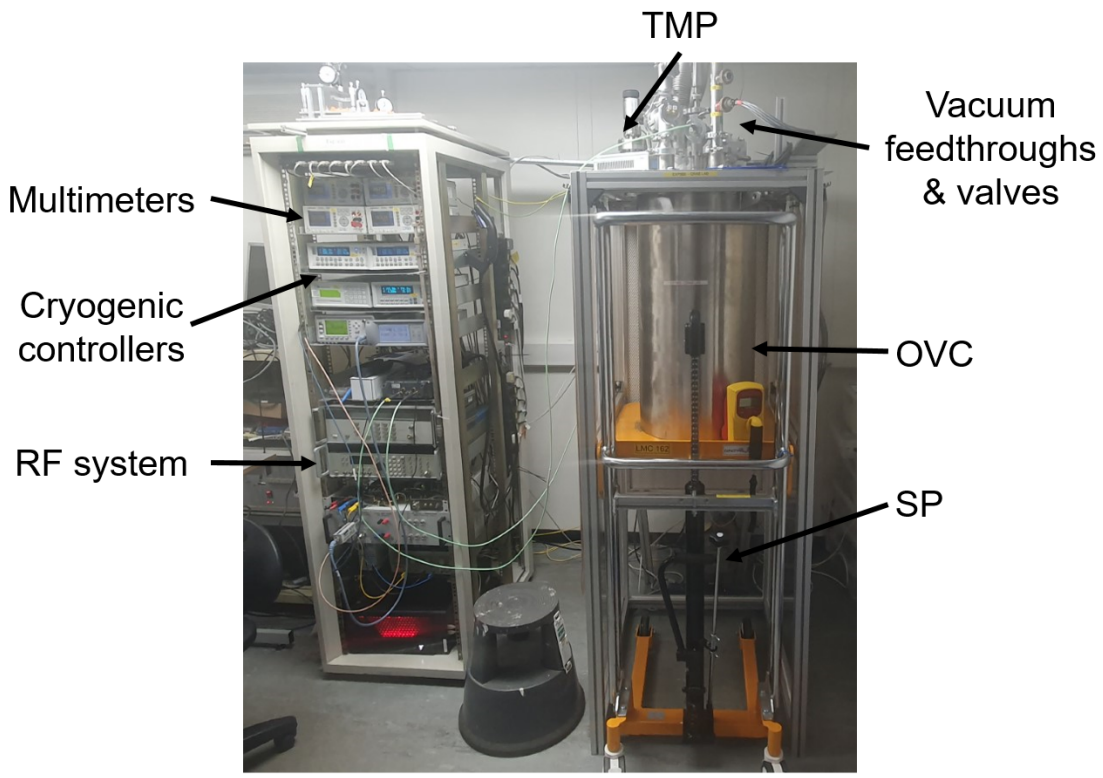

Figure 5.6: The Choke Cavity cryostat and control system.

5.1.3 RF system

RF is input into the centre of the cavity through a short semi-rigid Cu-coated SS coax that acts as an RF input coupler. This is attached by a long, thin-walled SS rod to a linear drive micrometer, as illustrated in Figure 5.2. Manual vertical movement using this drive allows for variable coupling of the input coupler to the cavity. Later, Section 5.3.2 explains the variable coupling strengths in more detail.

A second, short, semi-rigid Cu-coated SS coax is inserted into choke 2 and mounted in a fixed position with an Al clamp. For this, the inner conductor forms a closed loop with the outer conductor to allow the pickup coupler to couple to the magnetic field. The configuration of the couplers is shown in Figure. 5.7. RF is input to the couplers via coaxial cables from a room temperature SMA feedthrough. The cables are mounted to an adapter plate on stage 1 for thermalisation. This is shown in Figure 5.2. Unlike external coaxial cables, these are made from uncoated

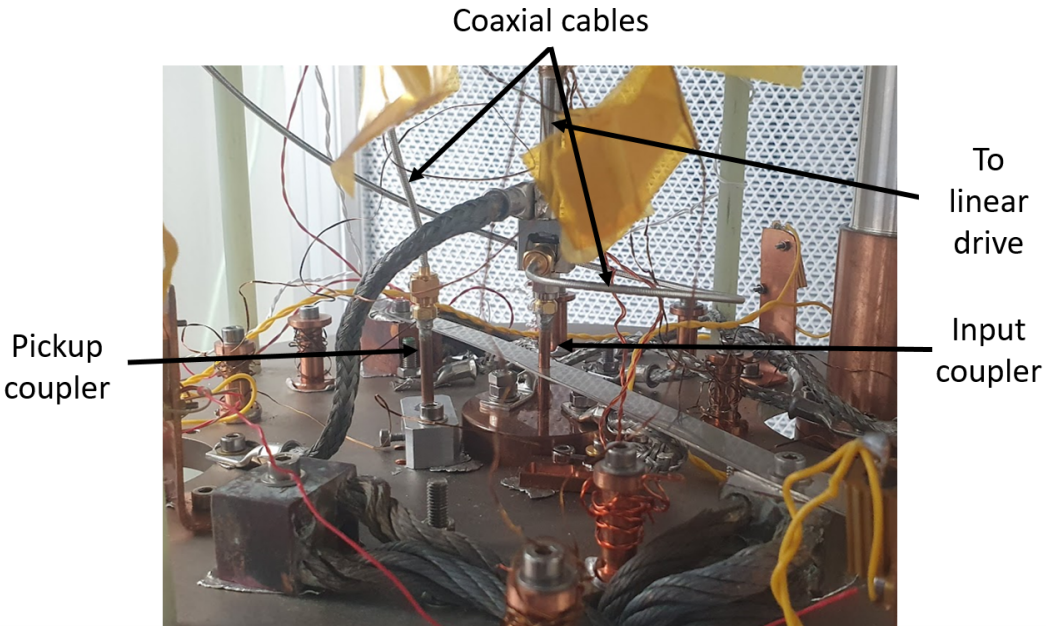

Figure 5.7: Mounting of the input and pickup couplers to the stage 2 plate.

SS to minimise thermal conductance; however, this results in higher RF cable signal losses.

Originally, the facility only had a single coupler acting as the input. It was possible to measure the stored energy from the reflected signal due to the low Q_{system} of the cavity. A pickup coupler (with the design study detailed in Section 4.4.2) was added that allows measurements of transmitted power. Given the wide bandwidth of this cavity (typically $\sim$ 1 kHz at 4.2 K with a Nb sample), RF measurements can be made without the need for a low-level RF (LLRF) system (either a PLL or SEL). Despite this, the future development of a LLRF system might be required for the testing of alternative superconducting thin films with $R_{\text{BCS}} < R_{\text{BCS,Nb}}$. Instead of using a PLL or SEL, a simple RF system was developed based on a vector network analyser (VNA) as the RF source. Initially, only a VNA was used with the single-coupler system; however, the RF power provided was insufficient to produce a detectable amount of heating on the sample, so an amplifier was added.

A schematic of the RF system is shown in Figure 5.8. The RF power is provided by a VNA (Keysight P5024A) that provides a maximum output power of 12 dBm

Table 5.3: The key specifications of the Microwave Amps AM43-7.8S-35-43 amplifier.

Parameter	**Value**
Frequency range (GHz)	$7.74 - 7.94$
Gain (dB)	50.5
Max output power (dBm)	43

at 7.8 GHz. Power is input into an RF amplifier (Microwave Amps AM43-7.8S-35-43) through fixed attenuators. The key specifications of this amplifier are shown in Table 5.3. Fixed attenuators are used to restrict the maximum input power in the cryostat to 1 W to meet the RF health and safety requirements to limit radiation in the lab from field emission. This restriction will be higher after moving to a radiation test bunker in the future. A circulator (Aaren Technology AT11B-GX250-AF) with 50 Ω load is used at the output of the amplifier to prevent amplifier reflections and damage. RF power from the amplifier system at A is input to the cryostat via a room temperature coaxial cable. The transmitted power is directed through another room temperature coaxial cable through the coupled port of a 20 dB directional coupler to a power sensor (Keysight E9326A) connected to a power meter (Keysight E4416A). A signal from the output port of the directional coupler goes to port 2 of the VNA.

For any set of measurements with this facility, a calibration of the room temperature and cryogenic cables and couplers for the input and pickup are required as well as the directional coupler. An estimate of cable losses can be made directly with the VNA. These losses are measured by connecting the cable end of the room temperature cables at points A and B shown in Figure 5.8 directly to ports 1 and 2 respectively on the VNA. Measurements of the out of band $|S_{11}|$ and $|S_{22}|$ signals (examples of which are shown from 7.8 to 7.85 GHz in Figure 5.9) are made and the losses are given by:

$$\text{Input Loss} = \frac{|S_{11}|(\text{dB})}{2} \tag{5.4}$$

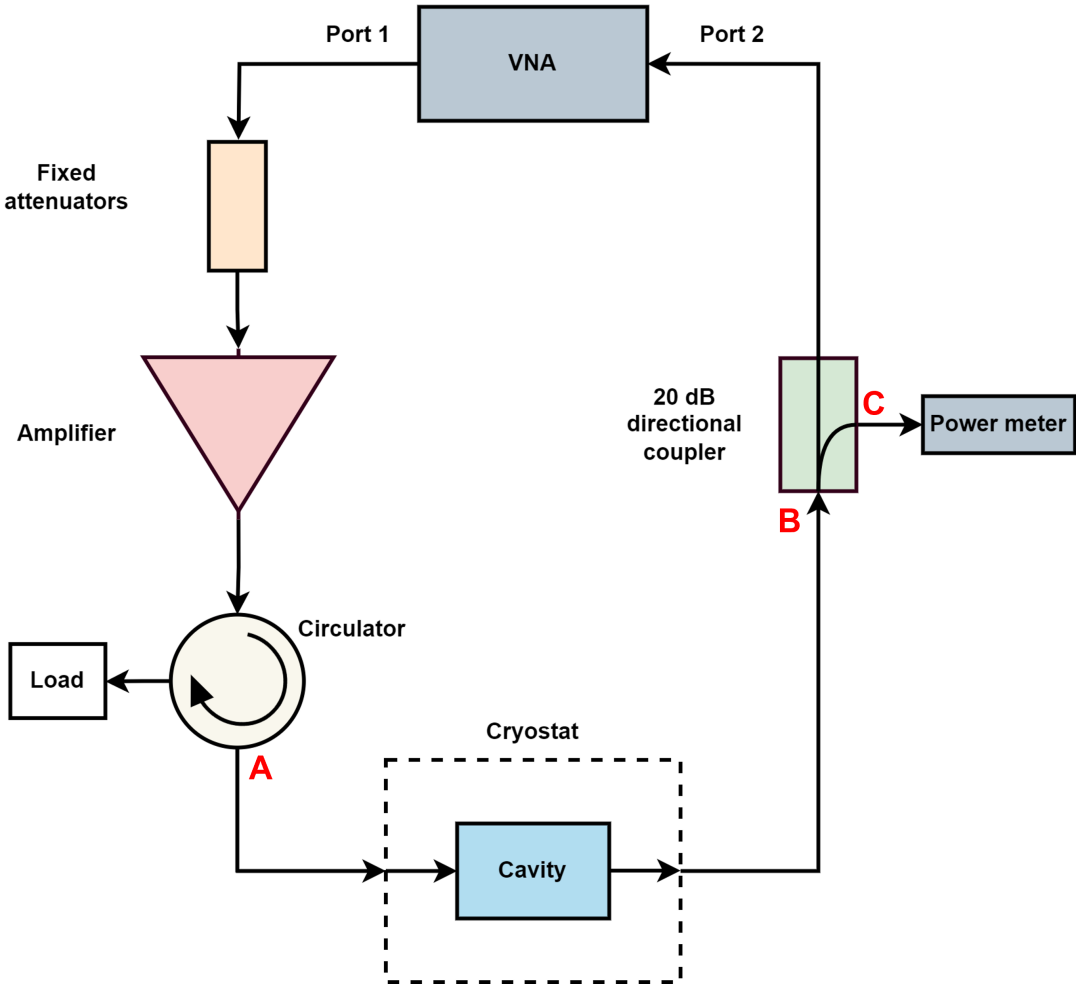

Figure 5.8: A schematic of the RF system.

and

$$\text{Pickup Loss} = \frac{|S_{22}|(\text{dB})}{2}. \tag{5.5}$$

Due to thermal contraction, for the Choke Cavity $f_0 \approx 7.83\,\text{GHz}$ during cryogenic testing. A summary of typical calibration measurements at this frequency is shown in Table 5.4.

Table 5.4: A summary of typical calibration loss and gain values for the RF system.

Calibration	Value (dB)
Cable from VNA to attenuators	-1.01
Attenuators	-26
Cable from attenuators to amplifier	-1.33
Amplifier	+ 50.5
Cable from amplifier to circulator	-0.8
Circulator	-0.15
Cable from A to cavity	-6.3
Cable from cavity to B	-6.8
Directional coupler B to C	-21.5

5.2 Facility Operation

5.2.1 Sample Mounting

In order to use the RF-DC compensation method, it must be possible to accurately control and measure the temperature of the sample. This requires the sample to be mounted to heaters, thermometry, and a heat link to the cold head for cooling. Attaching all these components directly to the sample is difficult to achieve; therefore, facilities such as this will use custom designed sample holders to mount all electronics. The main difficulty is ensuring good thermal contact with the sample.

The original sample holder, shown in Figure 5.10(a) was deemed too large and it was difficult to achieve good thermalisation with the sample. Due to the large thermal mass, it was difficult to accurately measure the small temperature and power differences when the RF-DC compensation method was tried. As a result, a smaller sample holder was designed, as shown in Figure 5.10(b). A technical drawing of this sample holder is provided in Appendix A.2.

The modified sample holder had the advantage of a simple and cost-effective

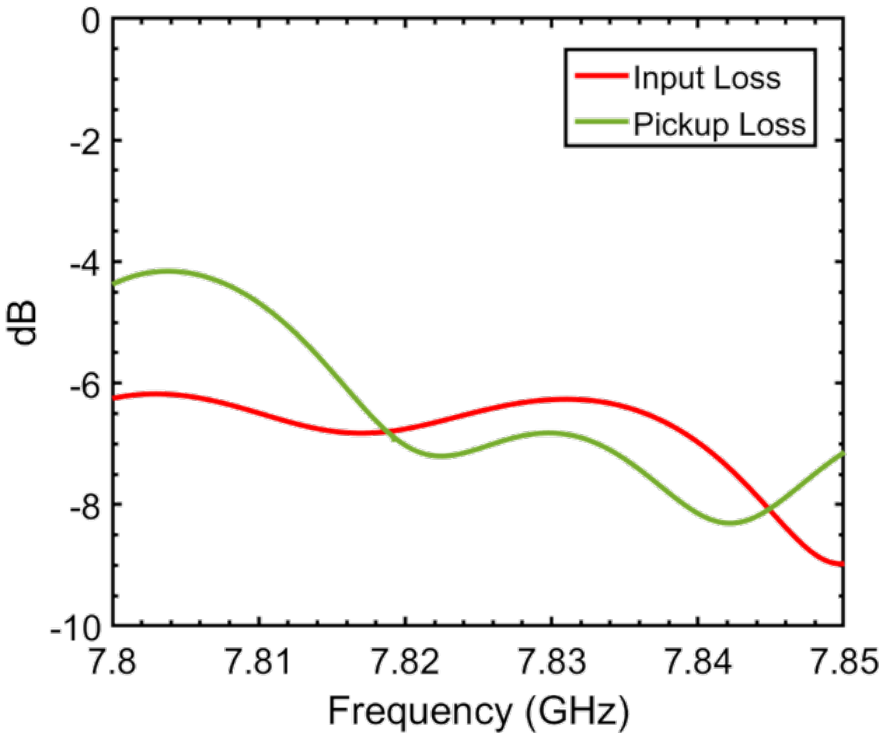

Figure 5.9: Typical measurements of input and pickup calibrations.

design so that multiple copies could be made. Also, it could be easily In-brazed to the back of the sample to ensure good thermalisation and temperature control. The downside was that the size of it meant that the sample would be thermalised from the centre to the edge, and it was difficult to predict whether this would cause temperature gradients. To achieve better temperature control and thermal stability, two new types of sample holder were designed, accommodating two sample designs, shown in Figure 5.11, which would provide more uniform thermalisation with the entire sample.

- Design 1: the sample holder (Figure 5.11(a)) is In-brazed to sample disks that are $90 - 130$ mm diameter and $2 - 3$ mm thick (Figure 5.11(b)).
- Design 2: the sample holder (Figure 5.11(c)) is bolted to a bespoke 110 mm diameter, 10 mm thick sample disk (Figure 5.11(d)).

Technical drawings of both designs are provided in Appendix A.2. Design 1

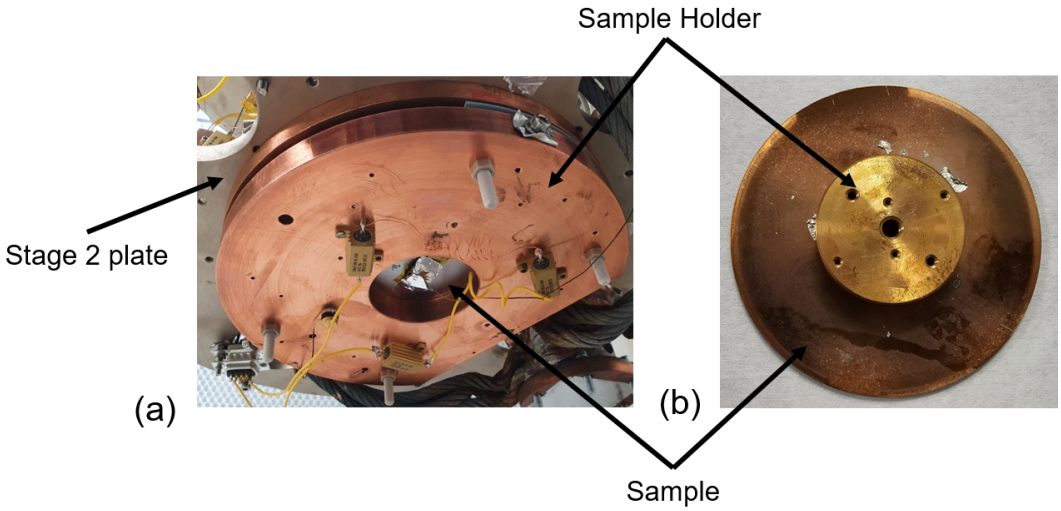

Figure 5.10: Sample holder designs:(a) original, (b) first redesign.

has the main advantage of being able to test simple sample disks. These disks are easy to manufacture in bulk, are simple to polish mechanically and chemically, and can easily be cut for additional superconducting measurements and surface analysis. This is the main configuration used for the samples tested in Chapters 6 and 7. This design allows for a better distribution of heat and improved sample alignment with the Choke Cavity due to the groove around the edge, which aligns with the G10 studdings on the sample plate.

For this design, the sample must be mounted within a separate, small vacuum chamber (as shown in Figure. 5.12). The sample is first loaded into this chamber, with the sample holder placed on top of the uncoated side of the sample. Strips of 99.99% In foil are placed between the sample and the sample holder. Heaters mounted to the sample holder allow it to be heated to above the melting point of indium (156 °C) under vacuum. Temperature monitoring of the sample/sample holder is provided with thermocouples. The heating is turned off when the sample and the sample holder are in thermal equilibrium at $\approx$ 160°C to ensure that the sample is fully brazed to the sample holder. The purpose of this method is to fully spread the In across the surface of the sample/sample holder to provide a strong physical connection and good thermalisation between the sample and the sample

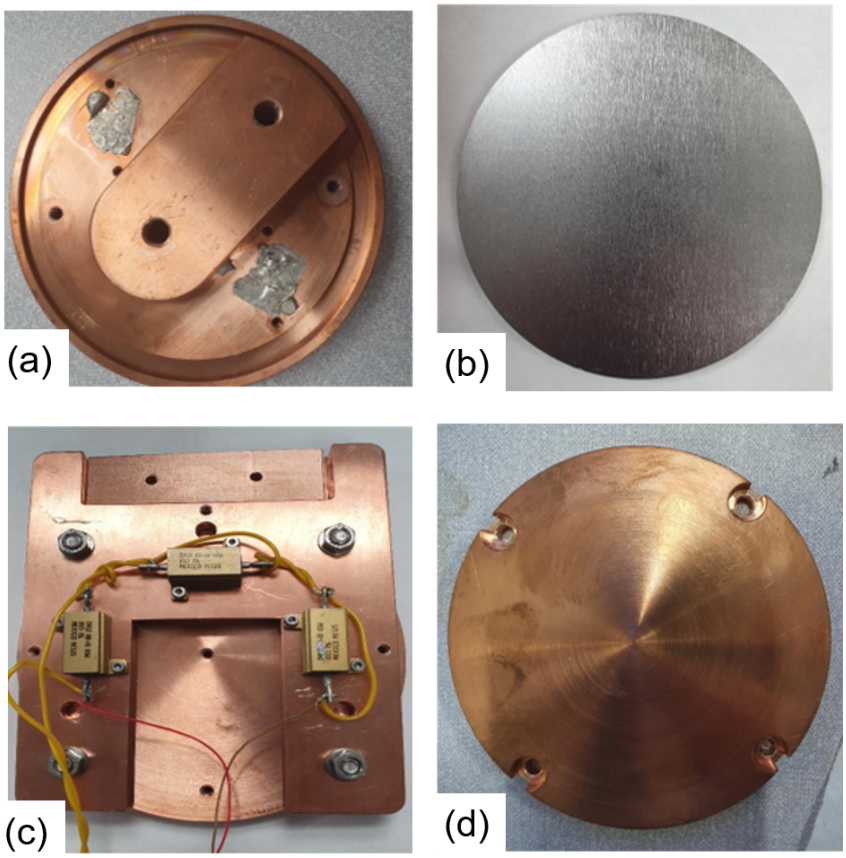

Figure 5.11: The final iteration of sample holders and samples: (a) Design 1 - sample holder, (b) Design 1 - sample, (c) Design 2 - sample holder, (d) Design 2 - sample.

holder. The downside of this method is that the sample must be prepared a day in advance for full heating and cooling of the sample prior to installation. No In contamination on the film, after using this method, has been detected using the surface analysis techniques detailed later in Section 7.3.

The main advantage of design 2 is that it does not require the In-brazing process. Good thermal contact between the sample and the sample holder is achieved simply by tightening four bolts around the edge of the sample with strips of In sandwiched between the contact faces. Given the greater thickness of the sample, tapped holes are present on the underside of the sample, as well as on the sample holder to measure temperature at multiple points. The downside of this design is the added weight of the sample, which means that it might not be suitable for some deposition

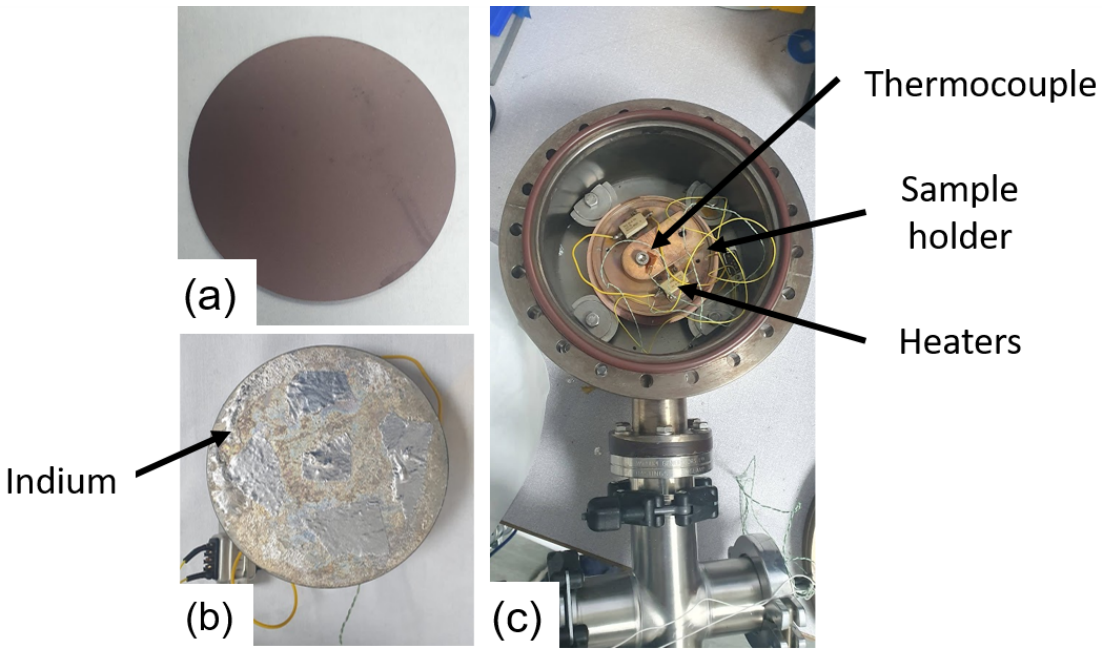

Figure 5.12: The process of In-brazing a design 1 sample to sample holder: (a) sample ready for mounting, (b) strips of In foil placed on the sample, (c) sample holder placed on top with heaters and thermocouple ready for pumping/heating.

facilities. The sample is also slightly more expensive to manufacture than the design 1 sample and is less versatile for analysis with additional techniques. This design is therefore restricted to RF measurements only; however, the film can be removed, allowing the substrate to be reused.

5.2.2 Experiment Operation Cycle

The main purpose of having a dry cryostat is simple operation with minimal training requirements. The usual operation cycle (with estimated timescales), after mounting a sample to a sample holder and opening the system, is as follows:

- Remove the previous sample (15 minutes).
- Blow new sample with ionising N_2 gun to remove any particulates on the surface that may have accumulated from the deposition system or sample

transfer and mount the new sample (15 minutes).

- Close the cryostat vacuum chamber (< 1 hour).

- Pump down to $< 10^{-4}$ mbar (4 hours).

- Switch on the compressor and cool down (approximately 12 hours). A typical cooldown is shown in Figure. 5.13. The sample cools at a faster rate than the Choke Cavity as a result of having a lower thermal mass. The sample reaches a base temperature of ≈ 3.6 K, whilst the Choke Cavity reaches ≈ 4.1 K.

- Sample measurements (up to 8 hours)

  - $R_{\mathrm{s}}(B_{\mathrm{s,pk}})$ - vary the input RF power at fixed T_{s} and T_{cav} ($0.1 < P_{\mathrm{in}} < 1$ W).

  - $R_{\mathrm{s}}(T_{\mathrm{s}})$ - vary the temperature at fixed power and fixed T_{cav} ($4.2 \leq T_s \leq 20$ K - higher if necessary).

  - $f_0(T_{\mathrm{s}})$ at fixed T_{cav} - measure the shift in resonant frequency and the change in penetration depth at fixed Choke Cavity temperature.

- Warm up (12 hours - overnight) - this can be assisted with both the stage 2 and sample heaters.

- Vent with N_2 to atmosphere.

- Open the cryostat vacuum chamber and remove the heat shields (30 minutes).

This cycle thus allows for the RF characterisation of up to 3 samples per week with minimal effort.

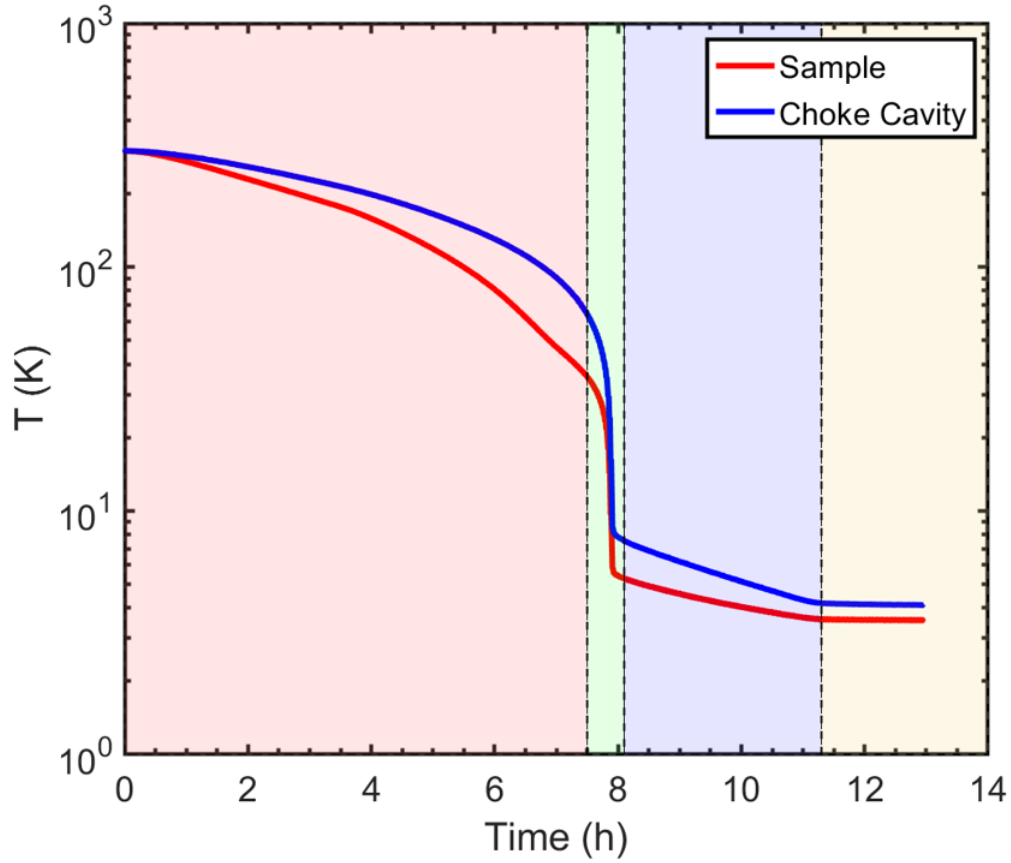

Figure 5.13: A typical cooldown curve for the sample and Choke Cavity (stage 2 plate).

5.3 Surface Resistance Measurements

5.3.1 Using the RF-DC Compensation Method

The R_s of samples is measured using the simple RF-DC compensation method, briefly introduced in Section 3.2.2. This uses the heaters connected to both the cavity and the sample, ensuring that measurements can be made at both fixed sample and fixed Choke Cavity temperature.

The RF-DC compensation procedure is described in more detail as follows, an example of which is illustrated in Figure 5.14:

(i) For the first step, the RF power is switched off. Starting at an initial sample

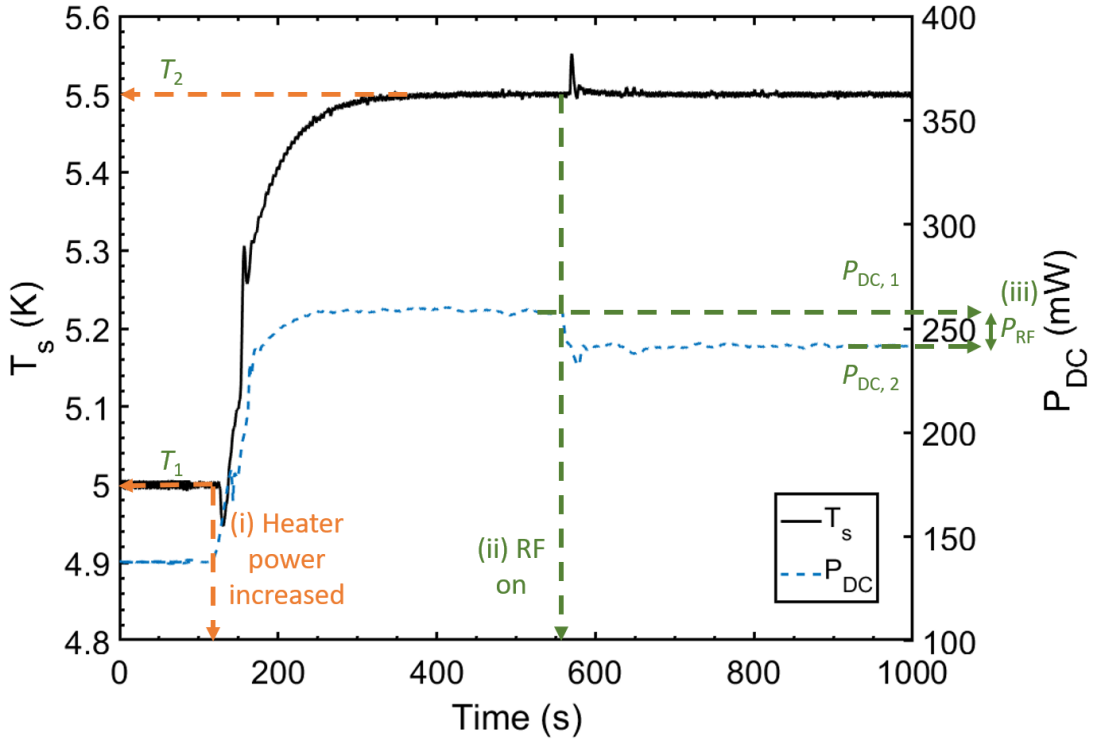

Figure 5.14: An example of the RF-DC compensation method in operation where the temperature has been increased from $T_1 = 5.0\,\mathrm{K}$ to $T_2 = 5.5\,\mathrm{K}$.

temperature (T_1), the sample temperature of interest (T_s) is set to T_2 using the sample temperature controller. Once T_s and the heater power (P_DC) have stabilised (after a few minutes), the first measurement of the heater power ($P_{\mathrm{DC},1}$) is made. During this time, the Choke Cavity temperature is also set to a constant temperature (T_cav) using the cavity temperature controller.

(ii) The RF power is then switched on at low power from the VNA with a narrow frequency span. This is done to locate and centre the output signal at f_0. From sample to sample, f_0 can vary by a few 100 kHz, likely due to different film thicknesses, material parameters and different positions of the variable input coupler. The frequency span is then set to zero at f_0 and the power is increased to the desired level. At zero span, f_0 is typically stable to within $\pm 1.5\,\mathrm{kHz}$ due to microphonics (explained in more detail later in Section 6.2.1

and there are no detectable frequency shifts due to Lorentz force detuning at such low RF fields. The input of RF power causes a momentary increase in both T_s and T_cav due to RF heating. The PID algorithm in the temperature controller reduces the heating power to bring the sample temperature back to T_2. After a few minutes, once T_s has stabilised to within $\pm 5\,\mathrm{mK}$ of the setpoint, a second measurement of the heater power is made ($P_\mathrm{DC,2}$).

(iii) The RF power dissipated on the sample, P_RF, is equivalent to the difference in the two heater power measurements:

$$P_\mathrm{RF} = P_\mathrm{DC,1} - P_\mathrm{DC,2}. \tag{5.6}$$

where $P_\mathrm{DC,1}$ and $P_\mathrm{DC,2}$ are measured using Equation 5.3.

(iv) Steps (ii) and (iii) can be repeated at a range of RF powers and a range of T_2. Each time, a new value of $P_\mathrm{DC,2}$ is measured. Varying the RF power allows measurements at different peak magnetic fields on the sample surface ($B_\mathrm{s,pk}$).

From Equation 2.9 P_RF is defined as

$$P_\mathrm{RF} = \frac{1}{2\mu_0^2} R_\mathrm{s} \int_\mathrm{sample} |\boldsymbol{B}|^2 \mathrm{dS}. \tag{5.7}$$

This equation assumes that R_s is constant on the sample surface.

Steps (i) to (iii) allow for direct measurements of R_s from a rearrangement of Equation 5.7:

$$R_\mathrm{s} = \frac{2\mu_0^2 P_\mathrm{RF}}{\int_\mathrm{sample} |\boldsymbol{B}|^2 \mathrm{dS}}. \tag{5.8}$$

The surface integral in Equation 5.8 cannot be determined experimentally; therefore, a constant must be defined to calculate R_s. This constant, c_1, is defined and calculated from eigenmode simulations in CST [44] as:

$$c_1 = \frac{2B_\mathrm{s,pk}^2}{\int_\mathrm{Sample} |\boldsymbol{B}|^2 \mathrm{dS}} = \frac{B_\mathrm{s,pk,CST}^2 R_\mathrm{S,CST}}{\mu_0^2 P_\mathrm{s,CST}} = 2.63 \times 10^3 \ \mathrm{m}^{-2}. \tag{5.9}$$

The second part of Equation 5.9 uses Equation 5.8 where $B_{\mathrm{s,pk,CST}}$, $P_{\mathrm{s,CST}}$ and $R_{\mathrm{s,CST}}$ are values of the magnetic field, power dissipated on the sample, and surface resistance, respectively, from an eigenmode simulation in CST [44] normalised to a stored energy of 1 J.

In addition, it is possible to calculate $B_{\mathrm{s,pk}}$, given as

$$B_{\mathrm{s,pk}} = B_{\mathrm{s,pk,CST}} \times \sqrt{U}, \tag{5.10}$$

where $B_{\mathrm{s,pk,CST}} = 670\,\mathrm{mT}$ for the Choke Cavity from simulations and U is the experimental stored energy from RF power measurements.

Substituting Equation 5.9 into Equation 5.8 gives a simple equation that can be used to calculate R_{s}:

$$R_{\mathrm{s}} = \frac{c_1 \mu_0^2 P_{\mathrm{RF}}}{B_{\mathrm{s,pk}}^2}. \tag{5.11}$$

One assumes that the manufactured Choke Cavity is identical to the simulated cavity, meaning that a reliable value of c_1 has been calculated. Later, Section 6.5.1 shows that small uncertainties in c_1 should be accounted for due to slight variations in cavity parameters, e.g. after chemical etching.

5.3.2 Stored Energy Measurements With The VNA

From Equations 5.10 and 5.11 and , it can be seen that, in addition to a measurement of P_{RF}, a measurement of U is required to determine R_{s}. Using the simple RF system described in Section 5.1.3, these measurements can be made using the VNA, which measures S-parameters. S-parameters are used to describe the relationship between ports in an electrical circuit with signals travelling between them. The S-parameter contains information about the amplitude and phase of the voltage of the travelling waves. For RF measurements with the Choke Cavity, 2 port measurements are required. A typical 2 port system for some device under test (DUT) is shown in Figure 5.15. This can be described by the S-parameter matrix given by:

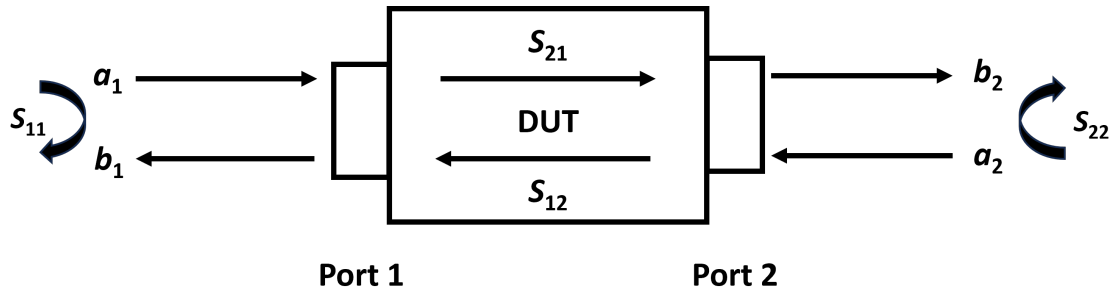

Figure 5.15: A 2 port network.

$$\begin{pmatrix} b_1 \\ b_2 \end{pmatrix} = \begin{pmatrix} S_{11} & S_{12} \\ S_{21} & S_{22} \end{pmatrix} \begin{pmatrix} a_1 \\ a_2 \end{pmatrix}, \tag{5.12}$$

where a_1 and a_2 the incident waves at ports 1 and 2, respectively, and b_1 and b_2 are the output/reflected waves from either port. The S-parameters are usually described as:

- S_{11} - input reflection coefficient.
- S_{12} - reverse transmission coefficient.
- S_{21} - forward transmission coefficient.
- S_{22} - output reflection coefficient.

For sample testing with the Choke Cavity, RF power is input from port 1 and the transmitted signal is measured at port 2. One can define the network using the forward voltage (V_f), reverse voltage (V_r) and transmitted voltage (V_t). The signals of interest for cavity testing are:

$$a_1 = \frac{V_\mathrm{f}}{\sqrt{Z}}, b_1 = \frac{V_\mathrm{r}}{\sqrt{Z}}, b_2 = \frac{V_\mathrm{t}}{\sqrt{Z}}, \tag{5.13}$$

where Z is the impedance of the port.

The S-parameters are defined by first expanding Equation 5.12

$$b_1 = S_{11}a_1 + S_{12}a_2, b_2 = S_{21}a_1 + S_{22}a_2. \tag{5.14}$$

S_{11} and S_{21} are defined when the output of port 2 is terminated with a matched load ($a_2 = 0$) and the impedance is identical at each port:

$$S_{11} \equiv \frac{b_1}{a_1} = \frac{V_\mathrm{r}}{V_\mathrm{f}}, \tag{5.15}$$

and

$$S_{21} \equiv \frac{b_2}{a_1} = \frac{V_\mathrm{t}}{V_\mathrm{f}}, \tag{5.16}$$

where Z cancel in both cases and similar definitions are possible for S_{22} and S_{12}.

For SRF cavity testing, power levels are typically measured; therefore, it is useful to express the magnitude of Equations 5.15 and 5.16 using powers, where:

- P_f: the forward power coming from the RF system to the Choke Cavity.
- P_r: the total reverse power made up of the vector sum of the emitted power back out of the input coupler and reflected power at the cavity-coupler boundary.
- P_t: the transmitted power out of the cavity through the pickup coupler.

The relevant S-parameters defined using the powers are:

$$|S_{11}|^2 \equiv \frac{P_\mathrm{r}}{P_\mathrm{f}}, \tag{5.17}$$

and

$$|S_{21}|^2 \equiv \frac{P_\mathrm{t}}{P_\mathrm{f}}, \tag{5.18}$$

It is important to note that these are measured at the VNA, therefore, cable losses (calculated using Equations 5.4 and 5.5) must be accounted for.

Measurements of U in a 2-port system can be made directly from measurements of S_{11}, S_{22} and S_{21} using the VNA in combination with measurements of P_t using the power meter. This requires a calibration of Q_t defined previously in Equation

2.27. For the 2-port system, each of the couplers have individual coupling factors and quality factors. For the input coupler, this is denoted by β_1 and Q_e (defined in Equation 4.3), and for the pickup coupler as β_2 and Q_t (defined in Equation 4.6).

Q_t can be calculated from Equation 4.6 provided that Q_system is calculated. It is defined using the loaded quality factor, Q_L, as

$$\frac{1}{Q_\mathrm{L}} = \frac{1}{Q_\mathrm{system}} + \frac{1}{Q_\mathrm{e}} + \frac{1}{Q_\mathrm{t}}, \tag{5.19}$$

Using Equations 4.3 and 4.6, Equation 5.19 can be rewritten using the coupling factors as

$$Q_\mathrm{system} = Q_\mathrm{L}(1 + \beta_1 + \beta_2). \tag{5.20}$$

The three variables in Equation 5.20 can be calculated from the measurements of $|S_{21}|$ and $|S_{11}|$ which are defined in Equations 5.17 and 5.18. A measurement of Q_L requires measuring the ratio of f_0 to the cavity bandwidth. Specifically, the bandwidth is measured at the half-power points or full-width half-maximum. This is measured when the voltage has dropped to $1/\sqrt{2}$ of its maximum and the power has dropped by half ($\approx 3\,\mathrm{dB}$). The 3 dB bandwidth (Δf_3dB) is measured using the $|S_{21}|$ trace and is illustrated in Figure 5.16. Q_L is therefore

$$Q_\mathrm{L} = \frac{f_0}{\Delta f_\mathrm{3dB}} = \frac{f_0}{f_2 - f_1}, \tag{5.21}$$

where f_1 and f_2 are the frequencies at the 3 dB points.

Next, to find an equation in terms of S-parameters for β_2 one starts by noting that in steady state with RF on, the total cavity power is conserved, i.e. the forward power is equal to the sum of the power dissipated in the system, the reverse power and the transmitted power:

$$P_\mathrm{f} = P_\mathrm{system} + P_\mathrm{r} + P_\mathrm{t}. \tag{5.22}$$

Substituting Equation 5.22 into the inverse of 5.18 gives

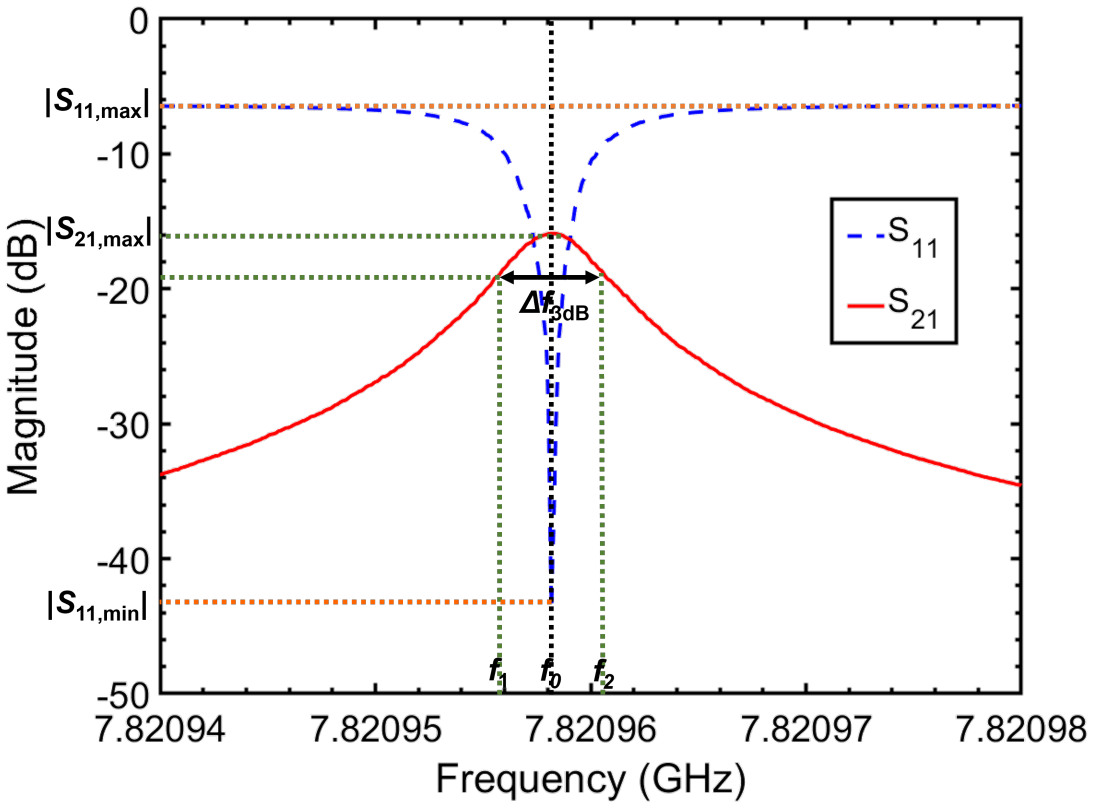

Figure 5.16: An example of $|S_{11}|$ and $|S_{21}|$ as a function of frequency.

$$\begin{aligned} \frac{1}{|S_{21}|^2} &= \frac{P_{\text{system}}}{P_{\text{t}}} + \frac{P_{\text{r}}}{P_{\text{t}}} + \frac{P_{\text{t}}}{P_{\text{t}}} \\ &= \frac{1}{\beta_2} + \frac{|S_{11}|^2}{|S_{21}|^2} + 1, \end{aligned} \tag{5.23}$$

where Equations 4.6, 5.18 and 5.17 have been used.

This can be rearranged to give an equation for β_2 in terms of S-parameters only:

$$\beta_2 = \frac{|S_{21,\text{cav}}|^2}{1 - |S_{11,\text{min}}|^2 - |S_{21,\text{cav}}|^2}, \tag{5.24}$$

with

$$|S_{21,\text{cav}}| = |S_{21,\text{max}}| - \text{Input Loss} - \text{Pickup Loss}, \tag{5.25}$$

where $|S_{11,\text{min}}|$ is the minimum value of $|S_{11}|$ and $|S_{21,\text{max}}|$ is the maximum value

of $|S_{21}|$, both measured at f_0 and illustrated in Figure 5.16. $|S_{21,\mathrm{cav}}|$ accounts for losses in the input and pickup cables calculated in Equations 5.4 and 5.5. Typically, the pickup probe will be very weakly coupled, i.e. $\beta_2 \ll 1$, to ensure that the signal does not affect the cavity's RF performance.

In order to derive an equation for β_1, one starts by noting that, for a two-port system, the input coupler cannot distinguish P_t from P_system. A new coupling coefficient, β^* is defined (modified from Equation 4.3):

$$\begin{aligned}\beta^* &= \frac{P_\mathrm{e}}{P_\mathrm{system} + P_\mathrm{t}} \\ &= \frac{1/Q_\mathrm{e}}{1/Q_\mathrm{system} + 1/Q_\mathrm{t}} \\ &= \frac{\beta_1}{1+\beta_2},\end{aligned} \tag{5.26}$$

β^* is calculated from the definition of S_{11} in Equation 4.5 for $\beta_1 = \beta^*$, which reduces to

$$S_{11} \equiv \frac{\beta^* - 1}{\beta^* + 1}, \tag{5.27}$$

when $f = f_0$ on resonance.

Substituting Equation 5.27 in 5.17, rearranging and taking the square root gives an equation for β^* in steady state

$$\begin{aligned}\beta^* &= \frac{1 \pm \sqrt{\frac{P_\mathrm{r}}{P_\mathrm{f}}}}{1 \mp \sqrt{\frac{P_\mathrm{r}}{P_\mathrm{f}}}} \\ &= \frac{1 \pm |S_{11}|}{1 \mp |S_{11}|}.\end{aligned} \tag{5.28}$$

Equating Equations 5.27 and 5.28 and accounting for cable losses give an equation for β_1 in terms of S-parameters only:

$$\beta_1 = \frac{|S_{11,\max}| \pm |S_{11,\min}|}{|S_{11,\max}| \mp |S_{11,\min}|} \cdot (1 + \beta_2), \tag{5.29}$$

where $|S_{11,\max}|$ which is the maximum off-band measurement of the $|S_{11}|$ trace to account for cable loss. The input coupler will be more strongly coupled to the cavity than the pickup ($\beta_1 > \beta_2$). The ratio of sign changes in Equations 5.28 and 5.29 depend on whether the coupler is overcoupled (+/-) or undercoupled (-/+). This can be inferred from the S_{11} polar plots, as explained previously in Section 4.4.1.

As a result, from Equations 4.6, 5.20, 5.24 and 5.29, it is possible to calibrate Q_t using the VNA. This value is not temperature or power dependent and so will not vary during a measurement run. Therefore, with a calibration of Q_t, it is possible to measure U with Equation 2.27 from simple measurements of P_t and calculate $B_\mathrm{s,pk}$ from Equation 5.10. These two equations can be combined, giving the following.

$$B_\mathrm{s,pk} = B_\mathrm{s,pk,CST} \left(\frac{Q_\mathrm{t} P_\mathrm{t}}{\omega_0} \right)^{\frac{1}{2}}. \tag{5.30}$$

From Equations 5.11 and 5.30, it can be seen that R_s measurements only require measurements of $P_\mathrm{DC,1}$, $P_\mathrm{DC,2}$, P_t and Q_t, making the measurement process fairly straightforward.

Table 5.5: A summary of the measurement observables and derived quantities.

	Symbol	Quantity	Equation
Observables	$P_{\mathrm{DC},1}$	DC heater power, RF off	
	$P_{\mathrm{DC},2}$	DC heater power, RF on	
	P_{t}	Transmitted power	
	f_0	Resonant frequency	
	Δf_{3dB}	3 dB bandwidth	
	$\lvert S_{11}\rvert$	Input reflection coefficient	
	$\lvert S_{21}\rvert$	Forward transmission coefficient	
Derived quantities	P_{RF}	RF power dissipated on the sample	5.6
	Q_{L}	Loaded quality factor	5.21
	β_1	Input coupling factor	5.29
	β_2	Pickup coupling factor	5.24
	Q_{system}	Choke Cavity-sample system quality factor	5.20
	Q_{t}	Pickup external quality factor	2.27
	$B_{\mathrm{s,pk}}$	Peak magnetic field on sample surface	5.30
	R_{s}	Sample surface resistance	5.8

Chapter 6

Choke Cavity Test Facility Commissioning

The aim of the Choke Cavity test facility is to be able to perform quick RF evaluation of thin film coated samples. The main benefit will be the ability to use RF measurements as the main tool for mass parameter optimisation of deposition processes at Daresbury Laboratory. Sample tests in this facility should be able to provide surface resistance measurements as a function of both sample temperature and sample peak magnetic field, as well as measurements of resonant frequency shift and change in penetration depth as a function of sample temperature.

Bulk Nb and thin film Nb/Cu samples have been used in this chapter to commission this facility and see whether the facility make reliable and repeatable RF measurements, as well as accurate temperature measurements. Surface resistance and resonant frequency shift measurements of these samples are used to characterise the RF measurement system and provide in-depth error analysis and repeatability studies.

6.1 Sample Preparation

To demonstrate the capability of the facility, five samples were measured: one bulk Nb and four Nb/Cu.

The bulk Nb sample used was a 100 mm diameter × 2.8 mm thick disk cut from a $RRR = 300$ Nb sheet, manufactured by Niowave, Inc [187]. The sample was subjected to four separate treatment processes: a heavy Buffered Chemical Polish (BCP) at INFN using a HF:HNO_3:H_3PO_4 = 1:1:2 solution for 60 minutes to remove $\approx 100\,\mu$m of material; (2) a 120 °C bake in ultra-high vacuum (UHV) for 48 hours; (3) a 600 °C bake in UHV for 6 hours to release mechanical stress and degas hydrogen from the bulk; (4) a second 600 °C bake in UHV for 6 hours. This was a non-standard order due to the availability of these facilities at the time for these treatment processes. Full details of bulk Nb preparation are found later in Section 7.1.1.

For the Nb/Cu samples, both the Design 1 and Design 2 OFHC Cu substrates (introduced in Section 5.2.1) were used. These were manufactured at the Daresbury Laboratory workshop. Two Design 1 Cu disks (DT1 and DT2) were diamond turned (DT) at STFC RAL Space using the process described later in Section 7.1.2.1. Given the more complex Design 2 substrate, this (MP2), along with a Design 1 disk (MP1), were metallographically polished (MP) at IJCLab using the process described later in Section 7.1.2.2[89]. The DT substrates had a mean surface roughness, $S_a \approx 3$ nm, and root-mean squared roughness, $S_q \approx 6$ nm. Meanwhile, the MP substrates had a slightly higher $S_a \approx 6$ nm and $S_q \approx 20$ nm. Both were measured using a white-light interferometer (WLI), detailed later in Section 7.3.2.

Each of the Nb/Cu samples made for commissioning was deposited inside the Daresbury Laboratory UHV deposition facility, detailed later in Section 7.2. For these samples, the high-power impulse magnetron sputtering (HiPIMS) technique was used with a Nb magnetron. The deposition parameters used are shown in Table 6.1. Kr was used as the discharge gas for all depositions with a pressure of 2×10^{-3} mbar. The set temperature was maintained during a 4.5 hour deposition.

Table 6.1: The deposition parameters for the Nb/Cu samples used for facility commissioning.

Deposition Parameter	**Value**
Base pressure (mbar)	10^{-9}
Initial heating time (h)	20
Initial temperature (°C)	530, 570, 620
Pressure with heating (mbar)	10^{-7}
Average target power (W)	400
Pulse duration (μs)	80
Pulse frequency (kHz)	1
Discharge gas	Kr
Deposition pressure (mbar)	2×10^{-3}
Substrate temperature (°C)	530, 570, 620
Deposition time (h)	4.5

The set temperatures before and during deposition for each of the samples are summarised in Table 6.2. The purpose of the bulk Nb, DT1 and DT2 samples was to demonstrate the capability of the facility, error analysis, measurement resolution, measurement repeatability and ability to distinguish between samples of different quality. As well as performing further repeatability studies, the addition of MP1 and MP2 was to demonstrate the ability to make measurements with alternative polishing techniques and different sample designs.

Figure 6.1 shows cross-sectional SEM measurements on the DT samples, performed at Daresbury Laboratory by C. Benjamin (STFC). The thickness of the DT1 and DT2 films was $\approx 1.5\,\mu$m. Given that samples have to be cut into $10 \times 10\,\text{mm}^2$ squares for SEM cross-section measurements, a thickness measurement of the MP2 film was not possible as this substrate was designed to be reused fully for future RF measurements only. However, given that the deposition time was the same for all four thin film samples, and assuming a constant deposition rate, it can

Table 6.2: The polishing method and deposition temperature used for the Nb/Cu samples for facility commissioning.

Sample	Polishing Method	Deposition Temperature (°C)
DT1	Diamond Turned	570
DT2	Diamond Turned	620
MP1	Metallographic	530
MP2	Metallographic	530

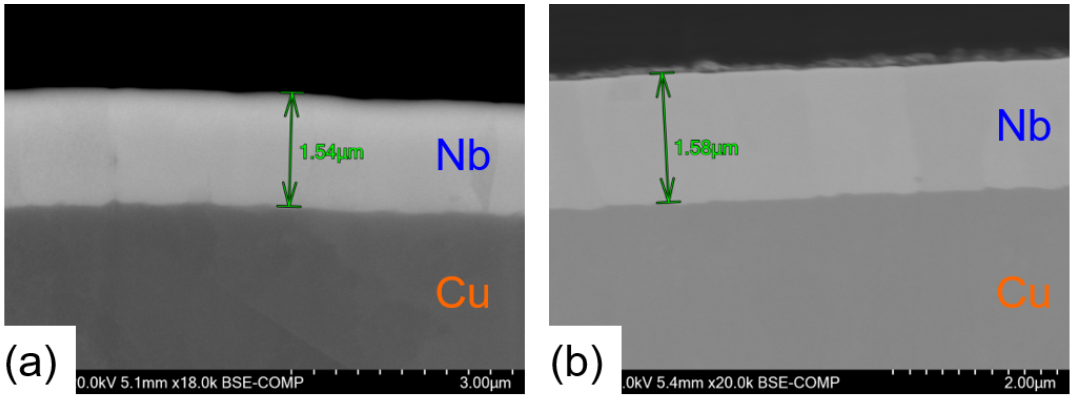

Figure 6.1: Cross-sectional SEM images of the Nb/Cu samples: (a) DT1, (b) DT2. Image courtesy: C. Benjamin (STFC).

be assumed that the MP1 and MP2 films had similar thicknesses. Details on the SEM measurement process can be found later in Section 7.3.3.

6.2 RF Commissioning

6.2.1 Microphonics

As discussed briefly in Section 5.1.1, a common issue with SRF cavity testing is the effect of microphonics. Microphonics are time domain variations of the cavity resonant frequency caused by internal or external vibrations or various instabilities within the system [193]. Typical sources of this, for both cavity test facilities and

accelerator cryomodules, include LHe pressure fluctuations and vacuum pump noise. This unwanted noise can affect the stability of the RF signal. It is problematic because it will induce shifts in the resonant frequency (known as detuning), making it difficult to maintain the cavity fields exactly on resonance. This can lead to a distortion of the cavity E-field and a reduction in acceleration efficiency. If external vibrations excite a cavity mechanical eigenmode, the detuning amplitude can increase significantly and the measured bandwidth on a VNA increases. For LHe-free systems operated with a cryocooler, microphonics is also likely to be an issue due to mechanical vibrations from the cold head operation.

Microphonics levels have been studied in SRF cavity cryomodules. For example, CBETA Linac 1.3 GHz cavity cryomodules were measured to have detuning ± 50 Hz, caused by pressure fluctuations in the LHe bath [194]. Meanwhile, 1.3 GHz TESLA cavities were measured to have ± 5 Hz level of detuning [195]. Even this level of detuning is an issue for SRF cavity testing. Bulk Nb 1.3 GHz cavities, for example, can regularly reach $Q_0 = 10^{10} - 10^{11}$ at 2 K [67]. Ideally, such cavities should be operated with $Q_\mathrm{L} \sim Q_0$ to minimise reflected power (i.e. $Q_0 \approx Q_\mathrm{e}$). However, with a critically coupled input coupler, this would decrease the bandwidth to $\sim 0.01 - 0.1$ Hz, which is much lower than the typical level of detuning. Without the addition of a PLL or SEL, this would reduce the possibility of stable testing, whilst significantly reducing the level of RF power entering the cavity. In a beamline, this would result in a reduction in field stability and, in the worst case, a loss of beam. In addition, overcoupling the RF antenna may help mitigate the microphonics by increasing the cavity bandwidth to better tolerate the detuning, however this would also increase the required RF power.

Microphonics does not only affect cavity testing and operation. It is also an issue for SRF sample testing facilities. For example, the QPR at HZB was measured to have shifts in resonant frequency of several 100 Hz due to the Nb quadrupole rods being excited by electrical components such as pumps [134, 196]. Whether it is RF cavity testing or small sample testing, it is vital that the level of microphonics

detuning is measured and its main sources are identified.

For the 7.8 GHz bulk Nb Choke Cavity, the minimum cavity bandwidth is typically $\sim$ 1 kHz, assuming an $R_s \approx R_{BCS}$. This is $\approx$ 200 times higher than the level of detuning in the 1.3 GHz TESLA cavities at HZB [195]. Therefore, it was assumed that microphonics would not be a major issue, allowing the simple RF system (shown in Figure 5.8) to be used without a PLL or SEL. However, it was soon discovered that the level of microphonics detuning is higher than that of the LHe SRF test systems. This is thought to be mainly due to the long, movable stainless steel rod between the input coupler and the linear drive on the upper flange of the OVC, which is coupled to the cryocooler noise generated by the periodic motion of its components.

Measurement of the level of microphonics in the system was performed using the VNA. This tracked the shift in S_{11} and/or S_{21} signals with the cavity excited at resonance. Specifically, the phase of these signals ($\angle S_{11}$ and $\angle S_{21}$) was tracked because the amplitude is non-linear in disturbance. By setting a zero span frequency centred at the resonant frequency, f_0, measurements of $\angle S_{11}$ and $\angle S_{21}$ were made as a function of the sweep time to determine the level of frequency detuning (Δf_{shift}). For small frequency shifts, phase shift is linear with frequency shift. The VNA was set to an output power of 0 dBm to avoid the possibility of cavity heating that would lead to additional frequency detuning.

An example of $\angle S_{11}$ and $\angle S_{21}$ measured simultaneously as a function of sweep time is shown in Figure 6.2 with the VNA set to a zero span at single frequency $\approx f_0$. These measurements indicate phase shift detuning up to $\pm 2^\circ$ due to microphonics. With a reduction in microphonics to 0, these phase shifts would tend to 0.

Firstly, the S_{11} signal measured at the VNA as a function of frequency, f, is given from Equation 2.34:

$$S_{11}(f) = \frac{\beta_1 - 1 - iQ_{\text{system}}\delta}{\beta_1 + 1 + iQ_{\text{system}}\delta}, \tag{6.1}$$

where β_1 and Q_{system} can be calculated using Equations 5.29 and 5.20 respec-

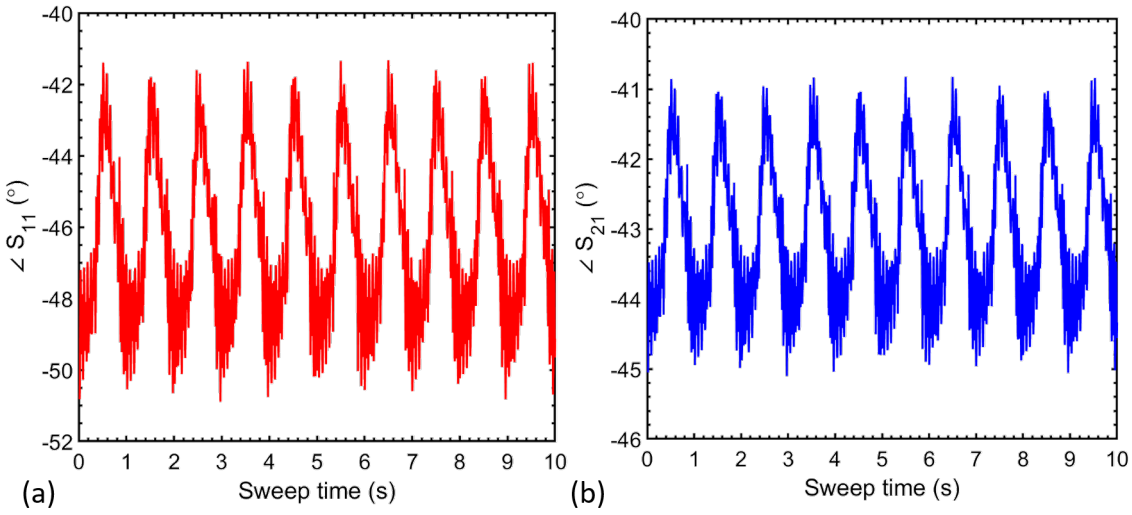

Figure 6.2: Phase data measured at f_0 with zero frequency span over a 10 s sweep time: (a) $\angle S_{11}$, (b) $\angle S_{21}$.

tively. Here, δ is the normalised frequency detuning given by

$$\delta = \frac{f}{f_0} - \frac{f_0}{f} \approx \frac{2\Delta f_{\text{shift}}}{f_0}. \tag{6.2}$$

Equation 6.1 can be separated into its real and imaginary components, therefore $\angle S_{11}$ is given by:

$$\angle S_{11} = -\arctan\left(\frac{2\beta_1 \mathrm{Q}_{\text{system}}\delta}{\beta_1^2 - 1 - (\mathrm{Q}_{\text{system}}\delta)^2}\right), \tag{6.3}$$

which can be re-written as

$$Q^2_{\text{system}}\tan(\angle \mathrm{S}_{11})\delta^2 - 2\beta_1 \mathrm{Q}_{\text{system}}\delta + (1-\beta_1^2)\tan(\angle \mathrm{S}_{11}) = 0. \tag{6.4}$$

Provided $\Delta f_{\text{shift}} \ll f_0$, $\delta^2 \to 0$. Therefore, Equations 6.2 and 6.4 can be combined to give an equation for Δf_{shift} that only requires calculations of $\angle S_{11}$, β_1 and Q_{system}:

$$\Delta f_{\text{shift}} = \frac{f_0(1-\beta_1^2)\tan(\angle \mathrm{S}_{11})}{4\beta_1 Q_{\text{system}}}. \tag{6.5}$$

If, instead, the S_{21} signal is measured, this is represented by

$$S_{21}(f) = \frac{A}{1 + iQ_{\mathrm{L}}\delta}, \tag{6.6}$$

where Q_{L} can be calculated using Equation 5.21 and A is the maximum of S_{21} that occurs at f_0 [197].

From Equation 6.6, $\angle S_{21}$ is given by:

$$\angle S_{21} = \arctan(\mathrm{Q_L}\delta). \tag{6.7}$$

Equations 6.2 and 6.7 can be combined to give a relation between $\Delta f_{\mathrm{shift}}$ and $\angle S_{21}$:

$$\Delta f_{\mathrm{shift}} = \frac{f_0 \tan(\angle \mathrm{S_{21}})}{2Q_{\mathrm{L}}}, \tag{6.8}$$

which is simpler than Equation 6.5 which uses $\angle S_{11}$. Typically, microphonics calculations in this section are performed using S_{21} measurements (unless otherwise stated) due to the simpler calculation method.

Typical levels of $\Delta f_{\mathrm{shift}}$, calculated from measurements in Figure 6.2, are shown in Figure 6.3a (from $\angle S_{11}$) and Figure 6.4a (from $\angle S_{21}$). These show the level of cavity detuning over a sweep time of 10 s. It can be assumed that this level of detuning is constant over longer time periods, provided that the experimental setup does not change between sample tests and there are no sudden sources of external noise. These measurements show a $\Delta f_{\mathrm{shift,max}} \approx \pm 1.5$ kHz, which is consistent with both the S_{11} and the S_{21} calculation methods. These results mean that the input coupler should always be overcoupled to give a cavity bandwidth ≥ 3 kHz (i.e. $Q_{\mathrm{L}} < 2.6 \times 10^6$) to ensure that the cavity remains excited within its bandwidth and stable RF operation is maintained for accurate measurements.

Calculating the fast Fourier transform of the frequency detuning ($|FFT(\Delta f_{\mathrm{shift}})|$) as a function of the sweep time allows the frequency components that contribute to detuning to be determined. These spectra are shown in Figures 6.3b and 6.4b for measurements with $\angle S_{11}$ and $\angle S_{21}$ respectively. As with the frequency shift,

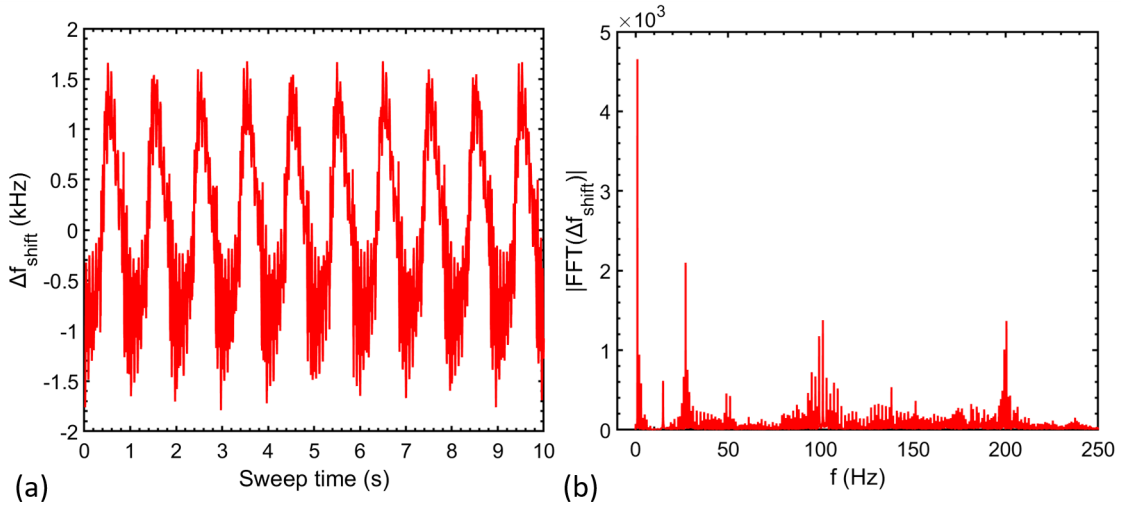

Figure 6.3: Microphonics measurements from $\angle S_{11}$. (a) Δf_{shift} over a 10s sweep time, (b) the FFT of this signal.

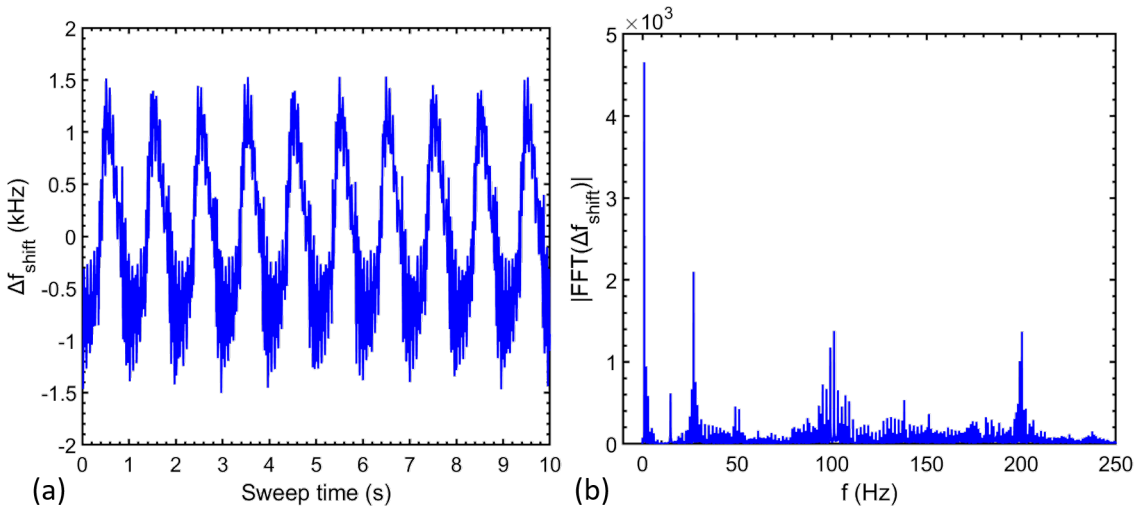

Figure 6.4: Microphonics measurements from $\angle S_{21}$. (a) Δf_{shift} over a 10s sweep time, (b) the FFT of this signal.

the spectra from S_{11} and S_{21} are consistent. In these spectra, there appear to be significant peaks at 1 Hz, 27 Hz, 100 Hz and 200 Hz.

The main vibration sources in the Choke Cavity facility are the cryocooler and vacuum pumps. The dominant peak at 1 Hz is as expected and can be attributed to the 1 Hz cycle of the cold head. The amplitude of this peak is around a factor 2 higher than the next significant frequency source, indicating that it is the dominant source of microphonics. The next largest peak at 27 Hz could be attributed to vibrations through the bellows that connect the top flange of the OVC to the Edwards scroll pump, which has a rotational frequency up to ≈ 1800 rpm (≈ 30 Hz) [198]. The input coupler rod is connected directly to the top flange, which is likely to couple these vibrations through to the input coupler. These scroll pump vibrations could be suppressed by using anti-vibration mounts to absorb or reduce transmission of vibrations to the cryostat.

For the 100 Hz and 200 Hz peaks, detailed vibrational analysis of cryocoolers by Tomaru et al. [199] at the top flange of the cryocooler attributes peaks at these frequencies due to vibrations in the flexible hoses connected to the cryocooler, as well as some smaller peaks between $10 - 100$ Hz. There is a high level of certainty, based on the 1 Hz source and the associated peaks, that the main driver of microphonics is most likely to be the motion of the GM cryocooler that sits within the cryostat. Experimental studies have found that it is possible to suppress GM cryocooler vibrations by suspending the cold head on a separate frame along with using air springs and honeycomb rubber [200].

The results of this analysis highlight that the level of microphonics is approximately 1 order of magnitude higher than the LHe systems previously discussed. Four possible methods to mitigate the effects of microphonics have been identified:

- Reduce the cryocooler vibrations.
- Increase the input coupler depth.
- Restrict movement of the input coupler.

- Use a LLRF control system such as a PLL or SEL.

A Sumitomo GM cryocooler was used for the Choke Cavity facility because it was readily available at the time of the initial build. The other main type of cryocooler is a slightly more expensive PTC. Further analysis by Tomaru et al. [199] compared the vibrations of the cold head (i.e. components mounted to the top flange of the cryostat OVC at room temperature) and the vibrations of the cold stage (i.e. the cryocooler components connected directly to the 4 K stage) of both types of cryocooler. A summary of their vibrational analysis is shown in Figure 6.5. It is clear that the displacement data tracks the 1 s periodic frequency detuning, as was also measured with the Choke Cavity. This confirms the contribution of the cryocooler to microphonics. What is also shown is that the vibration of the cold head for the PTC was two orders of magnitude lower than for the GM cryocooler. This indicates that a significant reduction in microphonics can be achieved by using a PTC for any SRF cavity test facility or LHe-free cavity cryomodule.

Initially, the depth of the input coupler was increased to decrease Q_{e} and β_1 to ensure an increase in $\Delta f_{\mathrm{3dB}} > \Delta f_{\mathrm{shift,max}}$, allowing the Choke Cavity to operate under stable field. Measurements of maximum frequency detuning due to microphonics ($\Delta f_{\mathrm{shift,max}}$) as a function of the position of the input coupler (measured on the linear micrometer drive) are shown in Figure 6.6. A shift in the position of the coupler from $2.4 - 3.4$ mm corresponds to an increase in cavity bandwidth from $\approx 10 - 150$ kHz. These measurements show that the depth of the coupler has little effect on $\Delta f_{\mathrm{shift,max}}$. However, at lower coupling depths, a slight increase in $\Delta f_{\mathrm{shift,max}}$ is observed. The coupler sits inside a Cu block mounted to stage 2 of the cryostat to minimise movement. With the coupler pulled further out, less perturbation of the cavity frequency would be expected. However, the larger detuning could be due to a slight decrease in the mechanical stability of the coupler. Here, the uncertainty in Q_{L} is the main contributor to the uncertainties in $\Delta f_{\mathrm{shift,max}}$. Further details of the uncertainty calculations are shown in Section 6.2.2.

To restrict the movement of the input coupler, Al stiffening brackets were placed

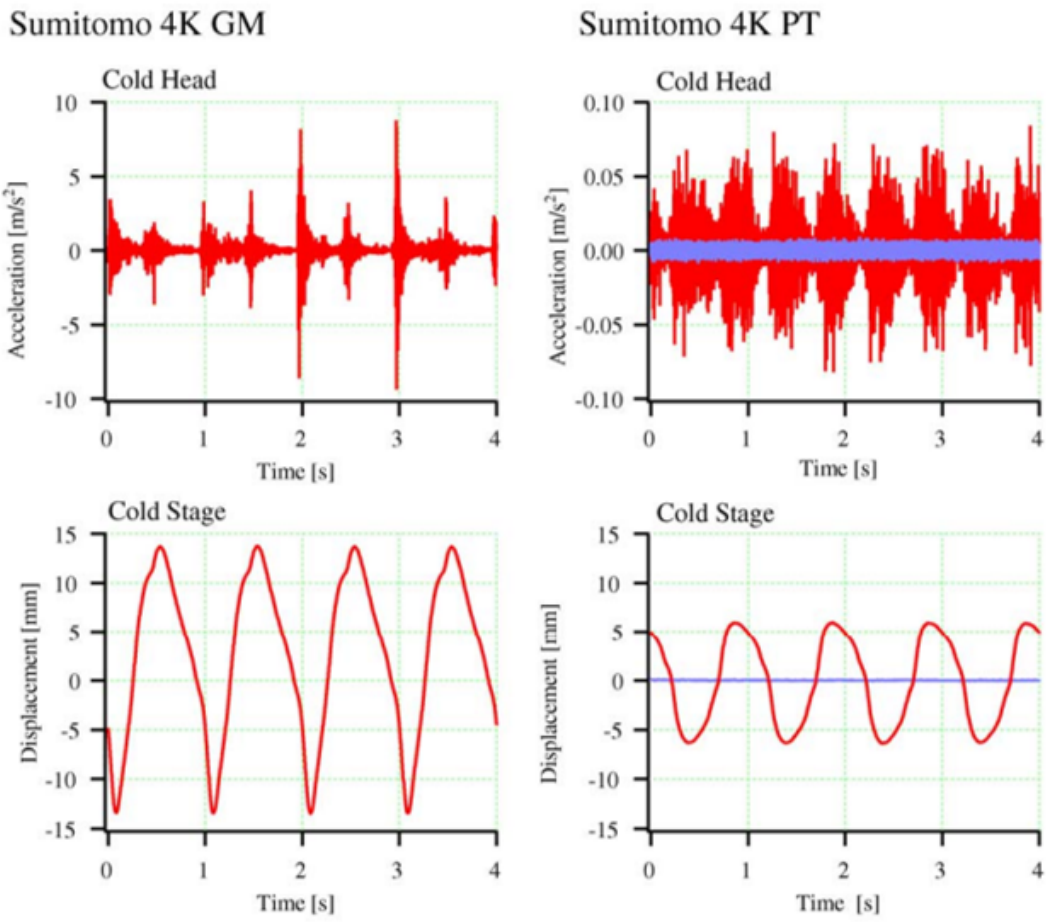

Figure 6.5: Vibration of the cold head and displacement of the cold stage comparing typical Sumitomo GM and PT cryocoolers [199].

around the input coupler, as shown in Figure 6.7. Before adding this, the typical levels of Δf_{shift} were approximately one order of magnitude higher. Further attempts to reduce vibrations may require the use of a cryogenic linear drive mounted directly to stage 2 to reduce the length of the linear drive rod mounted to the input coupler. In addition, the coupler used is made from a semi-rigid coaxial cable. Unlike flexible cables, semi-rigid cables hold their shape and are more resistant to mechanical flexing, therefore minimising movement due to external vibrations.

To reduce the input coupling strength and move the coupler closer to critically coupled, a PLL or SEL should be used. This would increase the power into the cavity and the maximum achievable $B_{\text{s,pk}}$. However, through the use of a variable

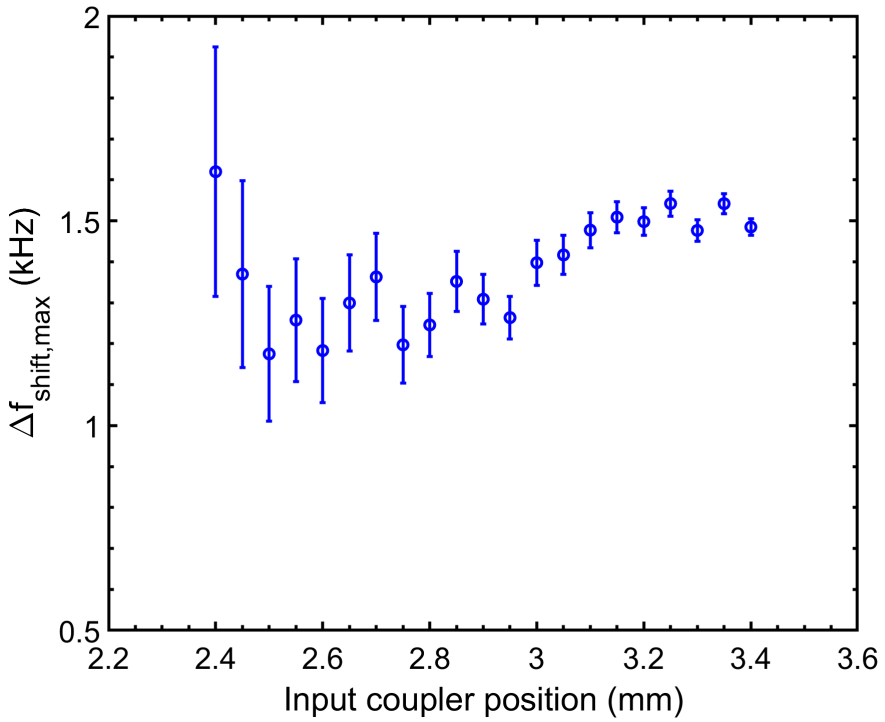

Figure 6.6: Maximum frequency shift due to microphonics over a range of input coupler positions as measured on the linear micrometer drive, where increased coupler position corresponds to more penetration towards the centre of the cavity.

coupler with a wide enough range of coupling depths, these LLRF systems are not necessary for now. With this variable depth input coupler, the easiest step to take was to ensure that the coupler was always adjusted to $\Delta f_{3\mathrm{dB}} > 2 \times \Delta f_{\mathrm{shift,max}}$. A PLL or SEL might also be considered with the use of thin film coated Choke Cavities (e.g. Nb_3Sn/Cu), where the cavity bandwidth might be $< 1\,\mathrm{kHz}$.

6.2.2 Pickup Coupler Q_t Calibrations

The addition of a pickup coupler in the Choke Cavity system means that all stored energy measurements can be made by measuring the transmitted power directly. This simply requires a calibration of Q_t, with full details previously shown in Section 5.3.2. For this, accurate measurements of the S-parameters are needed to calculate

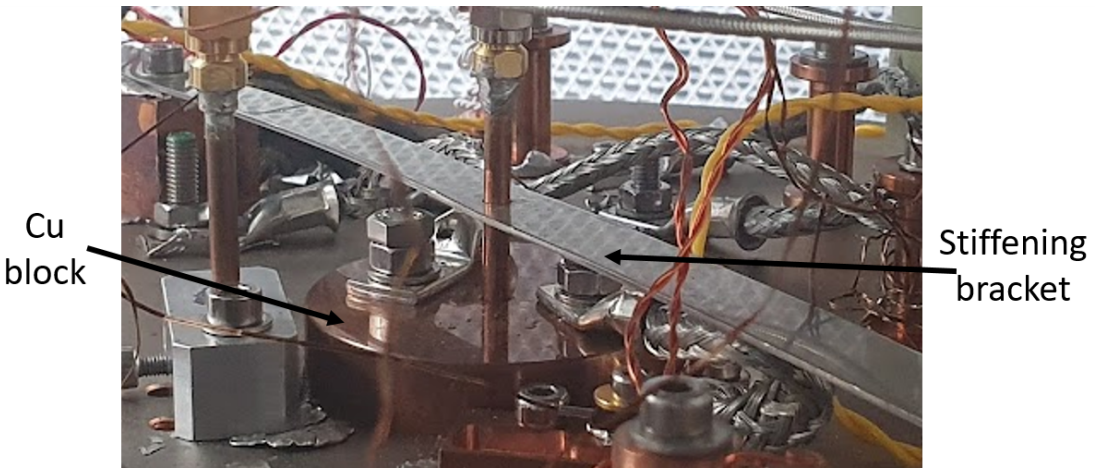

Figure 6.7: A stiffening bracket and Cu block placed around the input coupler.

Q_{L}, β_1 and β_2. Once a measurement of Q_{t} is made at the beginning of a measurement cycle, it is possible to make measurements of R_{s} without a recalibration.

The uncertainty in a measurement of Q_{t} ($\sigma_{Q_{\mathrm{t}}}$) is calculated from Equation 4.6:

$$\left(\frac{\sigma_{Q_{\mathrm{t}}}}{Q_{\mathrm{t}}}\right) = \sqrt{\left(\frac{\sigma_{Q_{\mathrm{system}}}}{Q_{\mathrm{system}}}\right)^2 + \left(\frac{\sigma_{\beta_2}}{\beta_2}\right)^2}, \tag{6.9}$$

where $\sigma_{Q_{\mathrm{system}}}$ denotes the uncertainty in Q_{system} and σ_{β_2} is the uncertainty in β_2. Measurements of Q_{system} are based on measurements of Q_{L}, β_1 and β_2, which all contribute to $\sigma_{Q_{\mathrm{system}}}$.

Firstly, β_2 measurements depend on $|S_{11,\mathrm{min}}|$ and $|S_{21,\mathrm{cav}}|$. Its uncertainty is calculated from Equation 5.24:

$$\sigma_{\beta 2} = \frac{2|S_{21,\mathrm{cav}}|[\sigma_{|S_{21,\mathrm{cav}}|}(|S_{11,\mathrm{min}}|^2 - 1) + 2\sigma_{|S_{11,\mathrm{min}}|}|S_{21,\mathrm{cav}}||S_{11,\mathrm{min}}|]}{(|S_{21,\mathrm{cav}}|^2 + |S_{11,\mathrm{min}}|^2 - 1)}, \tag{6.10}$$

where $\sigma_{|S_{21}|}$ denotes the uncertainty in $|S_{21}|$ and $\sigma_{|S_{11,\mathrm{min}}|}$ is the uncertainty in $|S_{11,\mathrm{min}}|$.

For β_1, measurements depend on $|S_{11,\mathrm{min}}|$, $|S_{11,\mathrm{max}}|$ and β_2. Its uncertainty is calculated from Equation 5.29:

$$\sigma_{\beta 1} = \frac{2(1+\beta_2)(\sigma_{|S_{11,\min}|}|S_{11,\max}| + \sigma_{|S_{11,\max}|}|S_{11,\min}|)}{(|S_{11,\max}| - |S_{11,\min}|)^2} + \frac{\sigma_{\beta 2}(|S_{11,\max}| \pm |S_{11,\min}|)}{|S_{11,\max}| \mp |S_{11,\min}|}, \tag{6.11}$$

where $\sigma_{|S_{11,\max}|}$ denotes the uncertainty in $|S_{11,\max}|$ and the sign changes are: +/- if the input is overcoupled or -/+ if undercoupled.

The S-parameter measurements are made with the Keysight 5024A VNA. The manufacturer quotes an error of ± 0.3 dB for both the reflection and transmission measurements [201]. In addition, external noise coupled through the coaxial cables contributes $\approx \pm 0.05$ dB to the uncertainty (measured fluctuations in $|S_{21}|$ with the cable alone connected to the VNA). The effect of microphonics is typically $< \pm 0.2$ dB measured from the difference between the maxima and minima of a trace with the VNA set to zero frequency span around f_0. Using these uncertainties gives a typical uncertainty of $\approx 20\%$ on both β_1 and β_2.

For Q_{L}, measurements depend on f_0 and Δf. Propagation of uncertainties, Equation 5.21 gives

$$\left(\frac{\sigma_{Q_{\mathrm{L}}}}{Q_{\mathrm{L}}}\right) = \sqrt{\left(\frac{\sigma_{f_0}}{f_0}\right)^2 + \left(\frac{\sigma_{\Delta f_{3\mathrm{dB}}}}{\Delta f_{3\mathrm{dB}}}\right)^2}, \tag{6.12}$$

where σ_{f_0} denotes the uncertainty on f_0 and $\sigma_{\Delta f_{3\mathrm{dB}}}$ denotes the uncertainty on $\Delta f_{3\mathrm{dB}}$.

The frequency measured by the VNA without connections to the ports is accurate to ± 1 Hz, which makes the instrument uncertainty for frequency measurements negligible. The main uncertainty on both f_0 and 3 dB frequencies required for the calculation of $\Delta f_{3\mathrm{dB}}$ is the level of $\Delta f_{\mathrm{shift}}$ due to microphonics. Provided that the input coupler is tuned to a cavity bandwidth $\geq 2\times\ \Delta f_{\mathrm{shift}}$ (for reasons discussed previously in Section 6.2.1), the overall uncertainty on Q_{L} is calculated to be $\approx 7\%$. However, this also requires the correct VNA software settings to be used, as well as a sufficient input coupler depth to satisfy the tuning requirements. The propagation of all these uncertainties leads to an overall uncertainty in Q_{t} of $\approx 20\%$. By reducing the level of microphonics to below the instrumentation error (< 0.05 dB), using the

possible solutions discussed previously in Section 6.2.1, it would be possible to reduce the uncertainty in Q_t to $\approx 14\%$.

The VNA works by initially setting the required frequency range (anything from 0 Hz to 10s of GHz) and the number of frequency sweep points. The VNA then divides the range into a number of sub ranges depending on the number of points. During a sweep, the VNA sends a signal at each frequency sweep point to the DUT and measures the S-parameter response before moving to the next point. The other main setting is the intermediate frequency bandwidth (IFBW) as this controls the measurement resolution but also contributes to the measurement time. A lower IFBW has an increased resolution but a lower measurement speed.

An example of Q_t measurements as a function of the IFBW is shown in Figure 6.8. These measurements were made for three different BWs by changing the depth of the input coupler. As shown, consistent measurements of Q_t are expected for cavity BWs > 3 kHz provided that the IFBW is < 0.5 kHz. For IFBWs up to $\approx 10^3$ kHz, measurements are consistent, provided that the cavity BW is > 20 kHz. Overall, to ensure that narrower cavity BWs can be tested, a the VNA was set up with an IFBW $= 0.5$ kHz with minimum step between sweep points of 0.1 kHz.

If the correct VNA parameters are used, the 3 dB bandwidth method can be used to measure Q_L from the $|S_{21}|$ trace. However, for the example of a 1.3 GHz SRF cavity, this is typically tuned to have a 3 dB bandwidth much less than the level of microphonics, therefore, despite the high resolution of a VNA, its not possible to accurately resolve the Δf_{3dB}. Alternatively, a power decay method is used. This method first relies on the cavity being filled with RF (i.e. the RF switched on at the resonance frequency). After setting cavity on resonance with zero frequency span, the behaviour of the stored energy U in the system is then tracked after the RF is turned off. With RF off, the total power (P_{tot}) is dissipated in the Choke Cavity system (P_{system}) as well as the reverse power out of the input coupler (P_r) and being emitted out of the pickup antenna (P_t). P_{tot} is given by

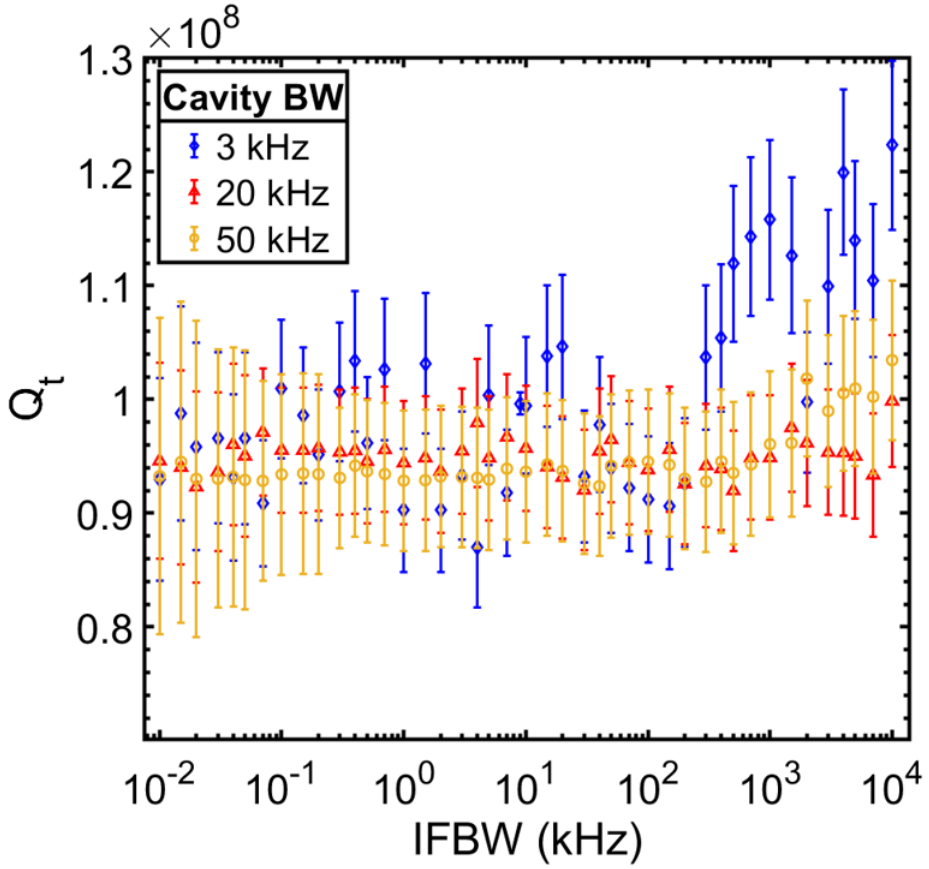

Figure 6.8: Measurements of Q_t as a function of IFBW for three cavity BWs.

$$P_\mathrm{tot} = P_\mathrm{system} + P_\mathrm{r} + P_\mathrm{t}. \tag{6.13}$$

With the RF off, the decay in U over time t is equivalent to the total power loss given by

$$\frac{\mathrm{d}U}{\mathrm{d}t} = -P_\mathrm{tot} = -\frac{\omega_0 U}{Q_\mathrm{L}}, \tag{6.14}$$

where the definition for Q_L given in Equation 5.19 has been used.

The solution to this first-order differential equation is given by

$$U = U_0 \exp\left(-\frac{t}{\tau}\right), \tag{6.15}$$

where U_0 is the initial stored energy and the time constant, τ, is defined as

$$\tau = \frac{Q_{\mathrm{L}}}{\omega_0}. \tag{6.16}$$

Using Equation 6.13 and previous definitions, it is possible to measure the total power emitted after the RF is turned off by measuring P_{system}, P_{r} and P_{t}. As it is difficult to measure P_{system} directly, it is easiest to measure P_{t} through a power sensor (though it would have also been equally possible to measure P_{r}).

After the RF has been switched off, the power decays exponentially, as described by

$$P_{\mathrm{t}} = \frac{\omega_0 U(t)}{Q_{\mathrm{t}}} = a \cdot \exp\left(-\frac{t}{\tau}\right), \tag{6.17}$$

where the constant a is given by

$$a = \frac{\omega_0 U_0}{Q_{\mathrm{t}}}. \tag{6.18}$$

Therefore, fitting measurements of P_{t} as a function of time allow one to calculate τ and hence determine Q_{L} without using a VNA. It can be seen that this method for calculating Q_{L} for a cavity 1.3 GHz, where $\tau \sim 1 - 100\,\mathrm{s}$, is much easier than the VNA 3 dB bandwidth method. The fitting assumes a perfect exponential decay. However, this is often distorted due to effects such as power detector response and noise. Therefore the accuracy of this method is dominated by systematic errors from the choice of fitting-range.

For the Choke Cavity, decay measurements were performed in order to verify the 3 dB bandwidth method. In order to make these measurements, an RF power detector (Mini Circuits ZX47-60LN-S+) replaced the transmitted power meter shown in Figure 5.8. The power detector converts an RF signal to a DC voltage. The DC output can be converted to an average RF power using the manufacturer's calibration data. The DC signal could be tracked in the time domain on a fast oscilloscope (Keysight DSOV084A). For a 7.8 GHz Choke Cavity with variable bandwidth $\sim 1 - 100\,\mathrm{kHz}$, one can expect a $\tau \sim 1 - 150$ µs. The oscilloscope used has a sampling rate of 20 GSa/s, and therefore was sufficient for this purpose.

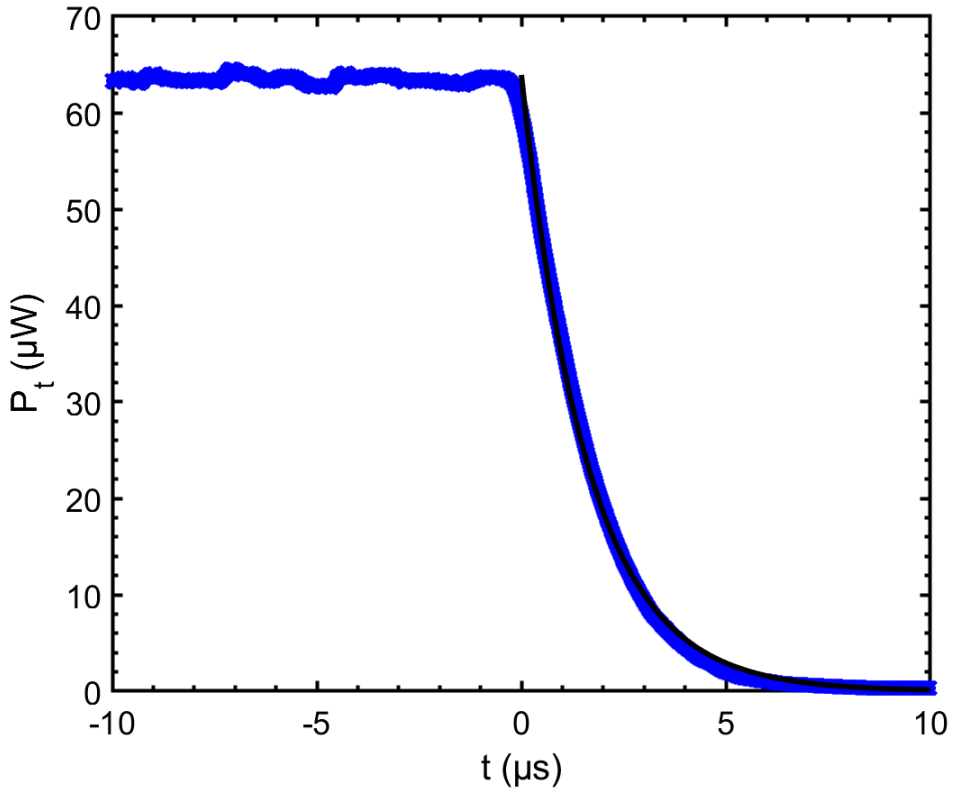

Figure 6.9: An example of a transmitted power decay curve for Nb/Cu DT2.

An example of a transmitted power decay curve, measured on Nb/Cu DT2, is shown in Figure 6.9. This shows a decay over period ~ 10 μs. A fit to Equation 6.17 was performed from $t = 0$. This fit has a $\tau = 1.6$ μs and a $Q_{\mathrm{L}} = 8.0 \times 10^5$. This is consistent with $Q_{\mathrm{L}} = (8.4 \pm 0.6) \times 10^5$ calculated using the 3 dB bandwidth method. The error on Q_{L} from using the decay method was estimated by repeating the fit over different ranges between $t = 0.5\tau$ and 5τ. As a result, the uncertainty on Q_{L} from using this method was estimated to be $\approx 2.5\%$, which was an $\approx 4.5\%$ improvement than using the 3 dB bandwidth method.

This study was extended to include multiple measurements over a range of input coupler depths from $2.4 - 3.4$ mm corresponding to $\Delta f_{3\mathrm{dB}} = 12 - 150$ kHz. Both the 3 dB and the decay methods were used to calculate Q_{L}, as shown in Figure 6.10. These measurements show consistency between the two methods for calculating Q_{L} in the typical bandwidth range that is used for the Choke Cavity measurements.

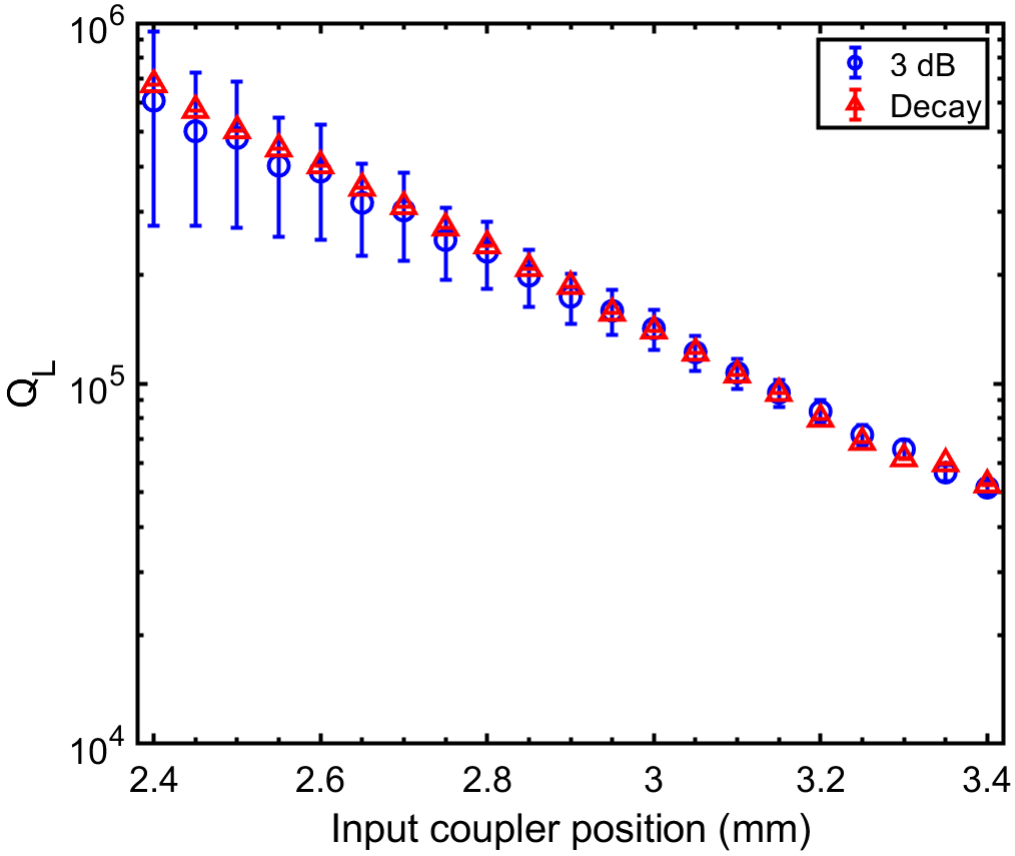

Figure 6.10: Q_L measured over a range of input coupler depths from 2.4 to 3.4 mm, as measured on the linear micrometer drive, where increased coupler position corresponds to more penetration towards the centre of the cavity.

Given the simplicity of the 3 dB method for the Choke Cavity, this was the main method of choice to calculate Q_L for future measurements.

6.3 Sample RF Measurements

6.3.1 Frequency Shift

As a sample is heated from low to high temperature near T_c, the RF penetration depth of the sample surface increases as the magnetic volume increases. This results in a decrease in the resonant frequency, which can be tracked as a function of sample

temperature. The frequency shift, $\Delta f(T_\mathrm{s})$, is given by:

$$\Delta f(T_\mathrm{s}) = f_0(T_\mathrm{s}) - f_0(T_0), \tag{6.19}$$

where T_0 is an arbitrary reference temperature.

For each sample, f_0 was tracked using the VNA connected directly to the RF ports on the test cryostat. A VNA power of 0 dBm was used to avoid possible RF heating of the sample and the possibility of temperature gradients during a measurement. The samples were measured at fixed $T_\mathrm{cav} = 7\,\mathrm{K}$ throughout the temperature sweep to ensure that the frequency shift was only due to a change in T_s. The G10 spacers between the sample and the cavity have a low thermal expansion coefficient, ensuring that there is a constant gap as the temperature increases.

Provided that the input coupler was overcoupled with a cavity bandwidth greater than Δf_shift, f_0 was measured from $|S_{21}|$. Figure 6.11 shows an example of $|S_{21}|$ as a function of frequency over a range of sample temperatures from $T_0 = 6.0\,\mathrm{K}$ to $T_\mathrm{s} > T_\mathrm{c}$ for Nb/Cu DT1. This shows both a decrease in f_0 and an increase in 3 dB bandwidth with T_s, as expected.

To calculate $\Delta f(T_\mathrm{s})$, f_0 must be extracted from data of the type shown in Figure 6.11. Given the higher than expected level of microphonics, the frequency window $\pm 1.5\,\mathrm{kHz}$ around the peak can be noisy, which reduces the accuracy on a measurement of f_0 from simply finding the maximum of the peak. The peak, corresponding to the resonant frequency, was obtained from a Lorentzian fit to the magnitude of Equation 6.6 to smooth out the noise and improve the peak finding:

$$|S_{21}| = \frac{A}{\sqrt{1 + Q_\mathrm{L}^2 \delta^2}}, \tag{6.20}$$

where A is the maximum of S_{21} and δ was previously defined in Equation 6.2. The quality of fit was assessed using the adjusted R^2 value, where values closer to 1 indicate a better fit, and the root mean squared error (RMSE), where lower values denote improved accuracy.

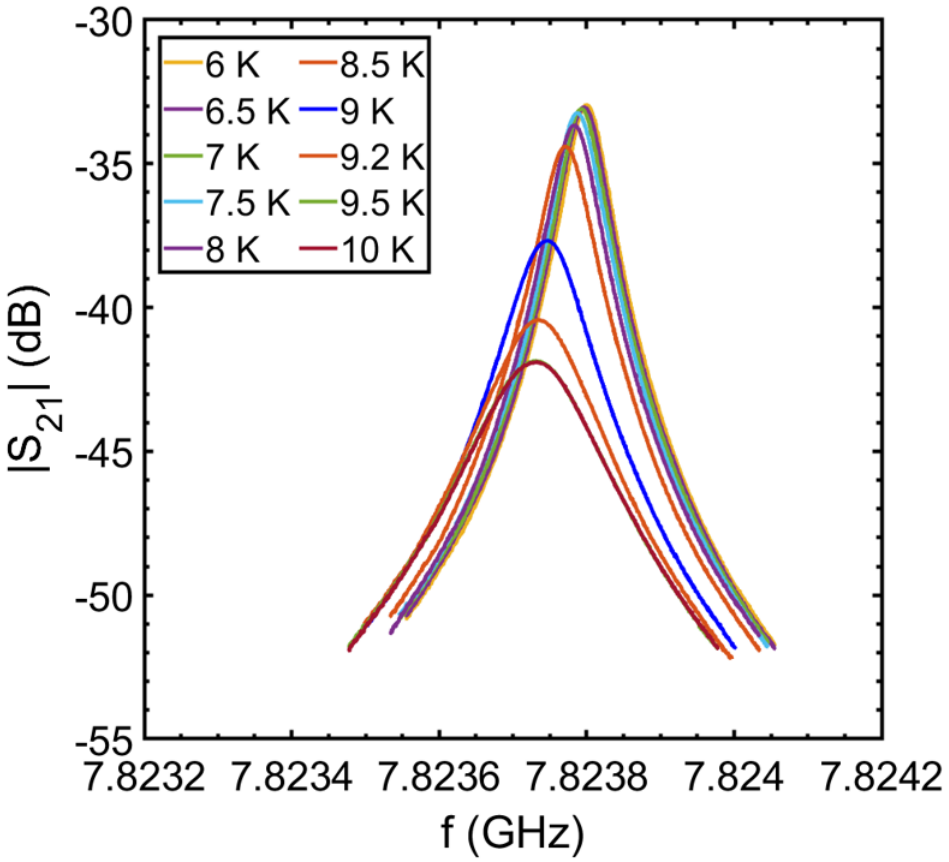

Figure 6.11: $|S_{21}|$ as a function of frequency for sample DT1 with increasing T_s and fixed $T_{cav} = 7\,\mathrm{K}$.

An example of a fit is shown in Figure 6.12, where f_0 and Q_L are free parameters. For the initial fit parameters, an estimate of f_0 is initially measured from $|S_{21,max}|$ and Q_L from a calculation of the 3 dB bandwidth using Equation 5.21. A fitting range of $-4\,\mathrm{dB}$ from $|S_{21,max}|$ is used to avoid uncertainties that may arise from fitting to potential asymmetric sidebands in the $|S_{21}|$ trace at values $\ll |S_{21,max}|$. In this example, the difference between f_0 calculated from $|S_{21,max}|$ and from the fit of $|S_{21}|$ is 0.6 kHz. This difference could be attributed to microphonics detuning causing shifts in f_0 or contributions from nearby choke modes distorting the curve. The fit results, as well as the level of frequency detuning calculated in Section 6.2.1, result in a typical uncertainty of $1.5 - 3.0\,\mathrm{kHz}$ on a measurement of f_0.

Using these analysis techniques, measurements of Δf were made as a function of

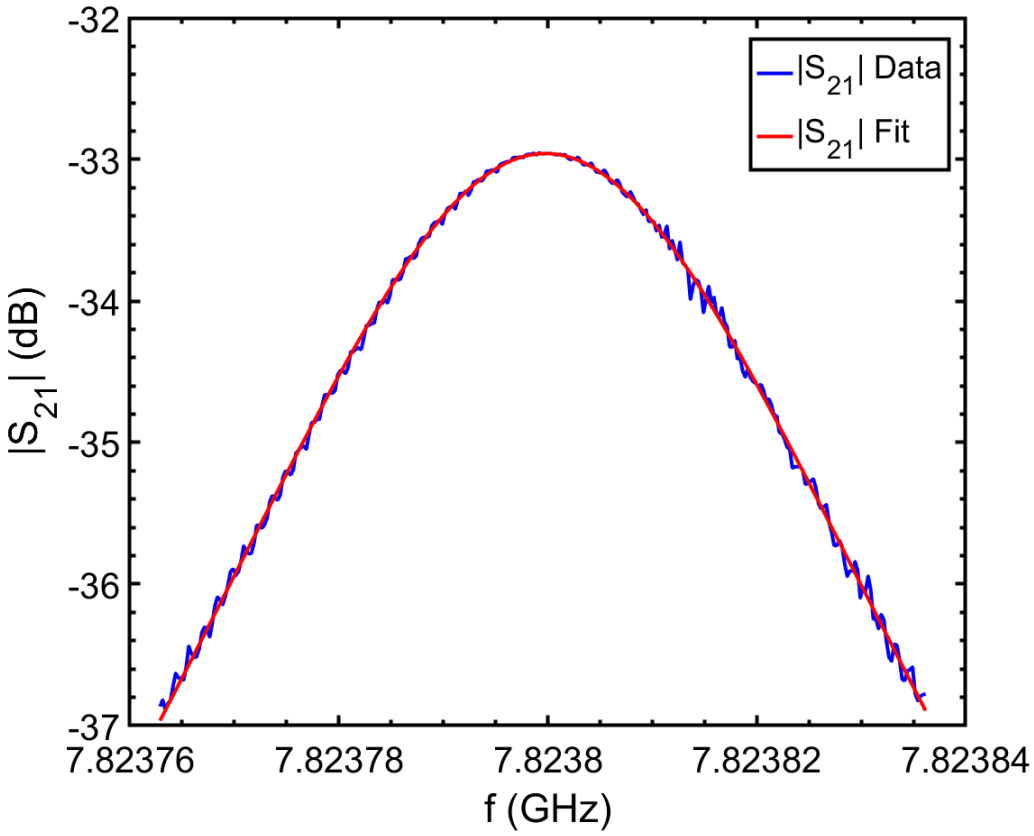

Figure 6.12: $|S_{21}|$ vs f for sample DT1 at $T_s = 6\,\mathrm{K}$ showing the Lorentzian fit to calculate f_0.

T_s for all samples during facility commissioning, as shown in Figure 6.13. The five samples were found to have $T_c \approx 9.2\,\mathrm{K}$ as expected for Nb [53], with Nb/Cu MP2 having the lowest Δf. The presence of slight dips in Δf before T_c has previously been associated with a level of impurities in a degraded sample surface layer that has a penetration depth larger than the normal conducting skin depth [202, 203]. Different levels of dip, most noticeable in the bulk Nb and Nb/Cu DT2 samples, may be the result of different levels of cleanliness in the surface layer of the samples, for example oxygen or nitrogen impurities, but also due to substrate preparation, film oxidation and thermal currents.

To assist in the calculation of T_c for the samples, the first derivative, $\mathrm{d}\Delta f/\mathrm{d}T_s$, was calculated as a function of sample temperature. This is shown in Figure 6.14.

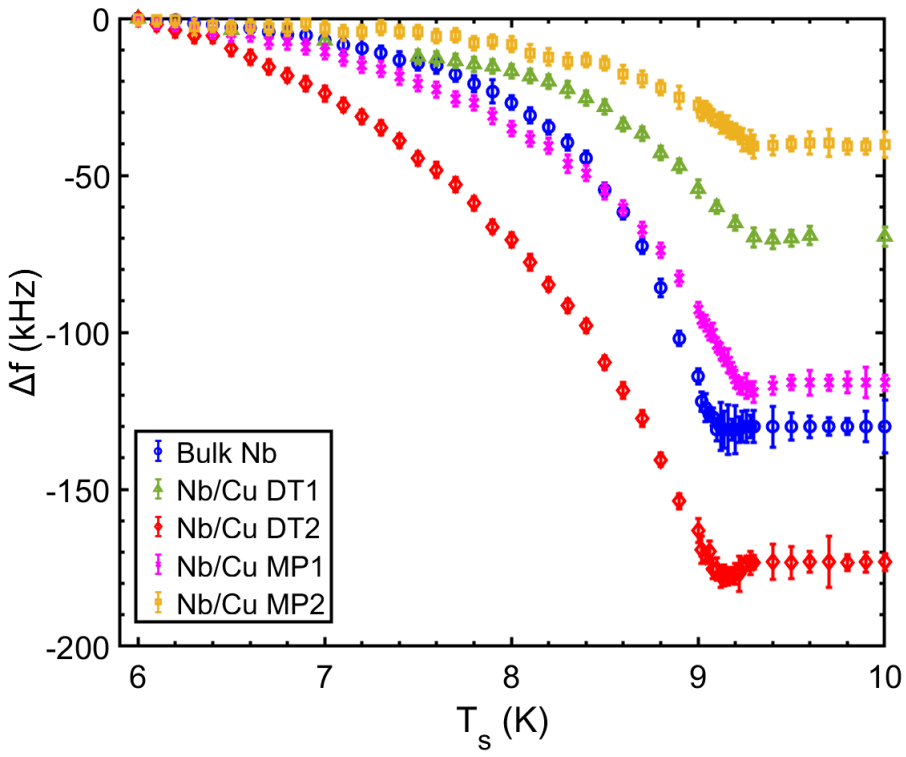

Figure 6.13: The shift in resonant frequency as a function of sample temperature compared at fixed $T_{\mathrm{cav}} = 7\,\mathrm{K}$.

For this, a cubic spline interpolation was used to smooth the data of $\Delta f(T_{\mathrm{s}})$ prior to differentiation. The T_{c} is estimated from the intersection with $\Delta f/\mathrm{d}T_{\mathrm{s}} = 0$ around $T_{\mathrm{s}} = 9.2\,\mathrm{K}$, with care taken for samples that have dips in Δf. Therefore, comparisons with the original $\Delta f(T_{\mathrm{s}})$ data are always required for this method. The values of T_{c} for each sample are summarised later in Table 6.3 in Section 6.3.4.

6.3.2 Penetration Depth

Given that a change in $f(T_{\mathrm{s}})$ can be equated to an increase in the RF penetration depth (defined in Section 2.2.2), the shift in penetration depth, $\Delta\lambda(T_{\mathrm{s}})$, can be calculated. $\Delta\lambda(T_{\mathrm{s}})$ is the difference in penetration depth between two sample temperatures: T_{s} and a reference T_0, where $T_0 < T_{\mathrm{s}}$. Slater's theorem can be used which relates small perturbations in resonance frequency (Δf) of a classical

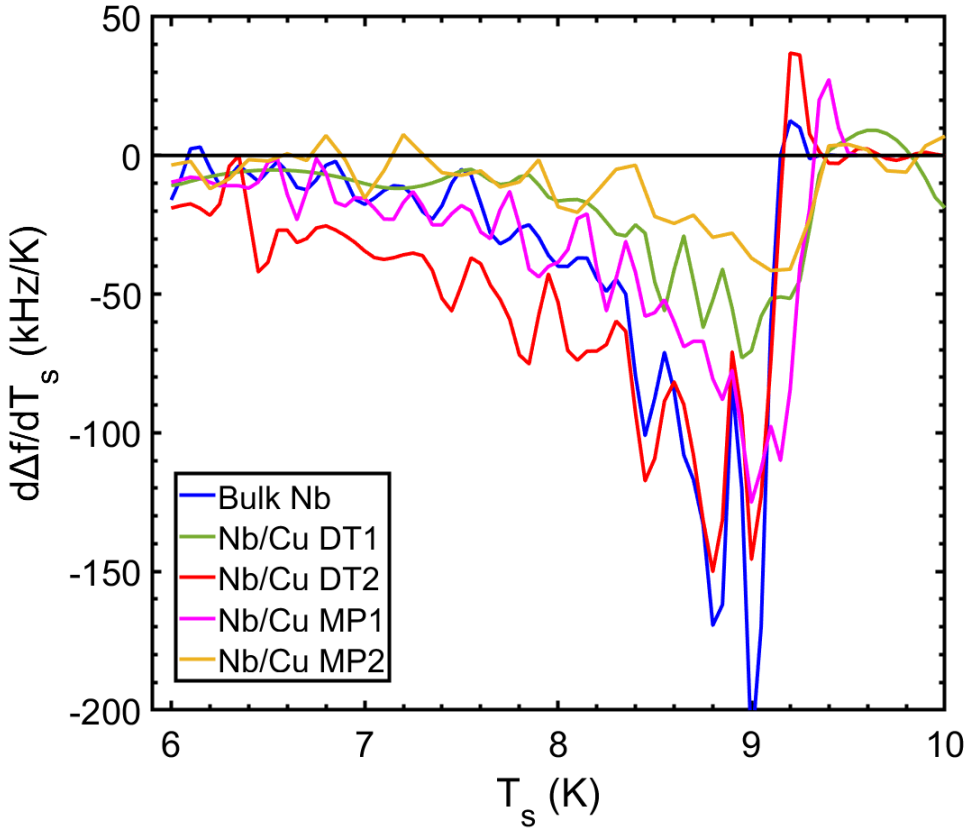

Figure 6.14: The first derivative of the resonant frequency shift as a function of sample temperature for each sample.

oscillator to changes in stored energy (ΔU) [36]:

$$\frac{\Delta U}{U} = \frac{\Delta f}{f}. \tag{6.21}$$

At a perfectly conducting boundary

$$\frac{\Delta f}{f} = \frac{1}{4U}\int_{\Delta V}(\epsilon_0|\boldsymbol{E}|^2 - \mu_0|\boldsymbol{H}|^2)\mathrm{dV}. \tag{6.22}$$

Increasing the temperature of the sample increases the penetration depth which increases the electromagnetic volume. Therefore, $\mathrm{dV} = \mathrm{d}\lambda\mathrm{dA}$. As a result,

$$\begin{aligned}\frac{\Delta f}{f} &= \frac{\Delta\lambda}{4U}\int_{sample}(\epsilon_0|\boldsymbol{E}|^2 - \mu_0|\boldsymbol{H}|^2)\mathrm{dA} \\ &\approx -\frac{\Delta\lambda}{4U}\int_{sample}\mu_0|\boldsymbol{H}|^2\mathrm{dA},\end{aligned} \tag{6.23}$$

the electric field contribution is much less than that of the magnetic field and can be neglected. Using definitions for U (Equation 2.8) and sample geometry factor, G_s (Equation 3.3) Δf to the change in penetration depth ($\Delta\lambda$):

$$\Delta\lambda = \lambda(T_\mathrm{s}) - \lambda(T_0) = -\frac{G_\mathrm{s}}{\pi\mu_0 f_0^2}\Delta f. \tag{6.24}$$

For a sample in the Choke Cavity system, $G_\mathrm{s} = 452\ \Omega$, as calculated using CST [44], which assumes that the sample is homogeneous.

The effective penetration depth at 0 K, λ_0, can be measured by fitting $\Delta\lambda(T_\mathrm{s})$ to the Gorter-Casimir expression, derived from the two-fluid model:

$$\lambda(T_\mathrm{s}) = \frac{\lambda_0}{\sqrt{1-(T_\mathrm{s}/T_\mathrm{c})^n}}, \tag{6.25}$$

where typically $n = 4$ [53].

The effective penetration depth was first calculated using BCS theory via the SRIMP code [56]. Figure 6.15 shows the BCS calculation of the penetration depth using the parameters for bulk Nb: $T_\mathrm{c} = 9.2\,\mathrm{K}$, $\Delta(0)/k_\mathrm{B}T_\mathrm{c} = 1.86$, $\lambda_0 = 32\,\mathrm{nm}$, $\xi_0 = 39\,\mathrm{nm}$ [53]. Least-squares fits to the Gorter-Casimir expression (for the typical case of $n = 4$) were calculated for different values of mean free path, l, from $0.54-540\,\mathrm{nm}$, indicating different sample purities. As l enters the clean limit ($l \gg \xi_0$), the fit appears to be worse close to T_c. In the dirty limit ($l \ll \xi_0$), a good fit is possible at all temperatures. These fits suggest that the Gorter-Casimir expression (with $n = 4$) provides a better estimate of the BCS penetration depth in the dirty limit; however, at temperatures between $6.0 - 8.5\,\mathrm{K}$ the fits follow similar gradients and the Gorter-Caismir expression may be used for both purity ranges.

For the samples tested during commissioning, Figure 6.16 shows measurements of $\Delta\lambda(T_\mathrm{s})$ calculated using Equation 6.24 with the frequency shift results shown in

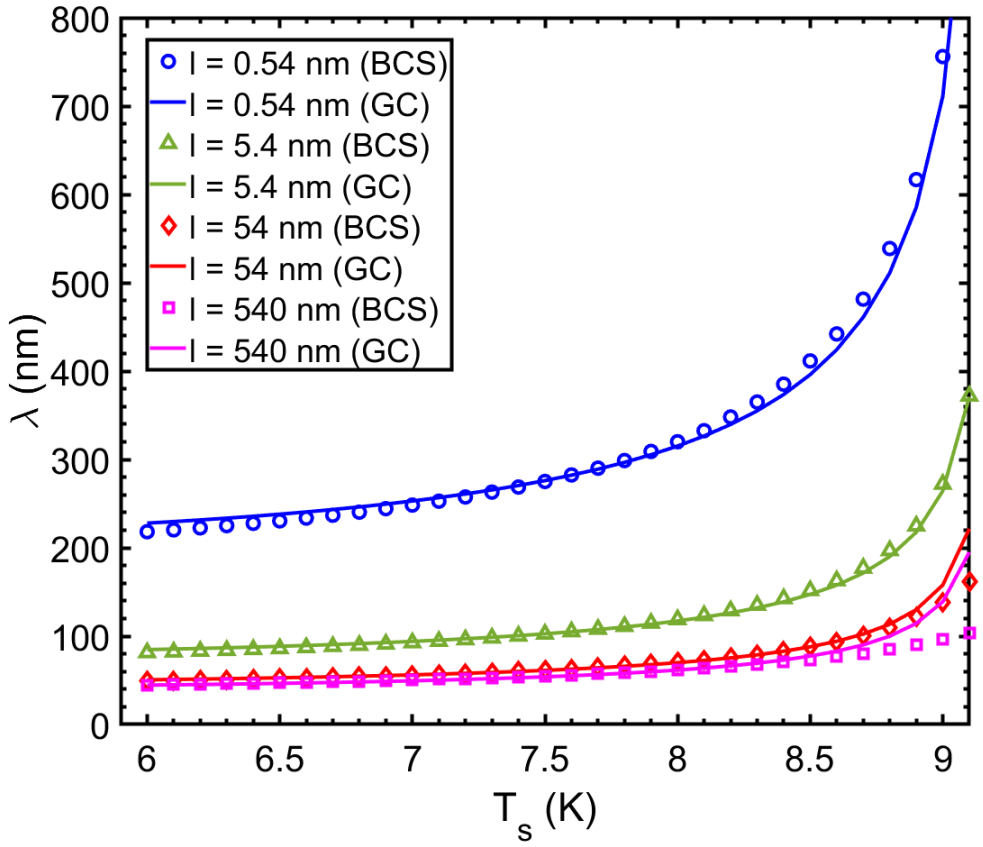

Figure 6.15: Theoretical penetration depth of niobium calculated using BCS theory with the SRIMP code [56] with fits to the Gorter-Casimir equation (with $n = 4$) shown for a range of purities (indicated by different l).

Figure 6.13. Here, $T_0 = 6.0\,\mathrm{K}$. Between $6.0-8.5\,\mathrm{K}$, Nb/Cu MP2, deposited at 530 °C on a MP design 2 Cu substrate, has the lowest penetration shift of 27 nm, while the next lowest shift is 53 nm for the Nb/Cu DT1, deposited at 570 °C on a regular DT Cu disk. The bulk Nb sample and Nb/Cu MP1 have comparable shifts of 102 nm and 103 nm respectively, whilst the Nb/Cu DT2, deposited at 620 °C, is the highest at 205 nm. A least squares fit to Equation 6.25 (with $n = 4$) was performed in the range $6.0\,\mathrm{K} < T_\mathrm{s} < 8.5\,\mathrm{K}$ to try and estimate λ_0. The fits are illustrated in Figure 6.16. Previous experimental data have suggested that this temperature range is suitable for fits to the Gorter-Casimir equation [204].

For the fits, T_c was a fixed parameter, measured from the frequency shift, as

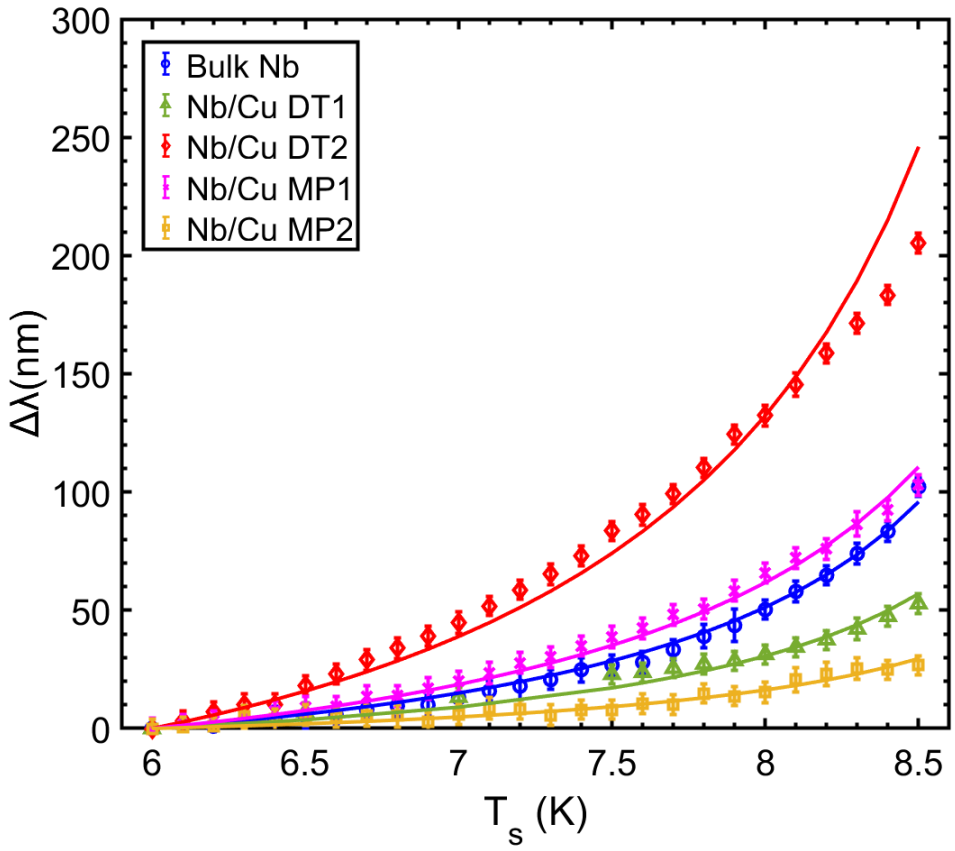

Figure 6.16: The shift in penetration depth as a function of sample temperature for the five samples with least-squares fits to the Gorter-Casimir expression with $n = 4$.

described in Section 6.3.1. It would appear that for the Nb/Cu DT2 sample, the fit of the two-fluid model diverges from the sample above $T_s = 8.5\,\mathrm{K}$ unlike the other four samples. As shown in Figure 6.15, the Gorter-Casimir equation does not provide an equally good fit to all materials and the agreement with the penetration depth calculated using BCS theory is less good for samples in the clean limit close to T_c [204]. It is possible that the $(T/T_c)^4$ dependence in Equation 6.25 is not valid at lower temperatures; therefore, a fit in the range $6.0\,\mathrm{K} < T_s < 8.5\,\mathrm{K}$ may not accurately predict the $\lambda(T)$ dependence at lower temperatures, meaning that it is difficult to obtain λ at 0 K with sufficient accuracy. In addition, the sample l likely changes with penetration depth so it is not constant as penetration depth increases with temperature. This makes it difficult to use a fit over the entire temperature

range to accurately extrapolate to $T_s = 0\,\mathrm{K}$ and measure λ_0. Instead, a dependence on $(T/T_c)^n$ has been investigated, with $1 \leq n \leq 4$, as well as multiple fits over smaller temperature ranges, providing a range of λ_0 [205]. The range of values of λ_0 obtained from the fits is summarised in Table 6.3 in Section 6.3.4.

Here, λ_0 is related to the material-dependent quantities at 0 K: ξ_0, λ_L and l [53] by

$$\lambda_0 = \lambda_L \sqrt{1 + \frac{\pi \xi_0}{2l}}. \tag{6.26}$$

Given the strong correlation of λ_L, ξ_0 and l in Equation 6.26, a unique solution is not possible from fits to $\Delta\lambda(T_s)$ and $R_s(T_s)$ alone. Care should be taken if trying to fit these to the two-fluid model. Further complementing measurements, e.g. B_{c2} measurements by SQUID magnetometry, should be performed as this can provide a relation between values of ξ_0 and l [206]. Instead, l/ξ_0 as a function of λ_L was derived from the values of λ_0, as shown in Figure 6.17. This illustrates the wide parameter space (λ_L, ξ_0, l) that can be used to describe the $\Delta\lambda(T_s)$ relation for each sample and give rise to the sample λ_0. A line for bulk Nb has been shown using theoretical values of $\lambda_L = 32\,\mathrm{nm}$ and $\xi_0 = 39\,\mathrm{nm}$, taken from the literature [53], for $l = 1 - 600$, nm. The intersection of this curve, with the data for each sample, provides an estimate of l assuming bulk-like properties. However, these theoretical values can vary for thin films or even bulk Nb with impurities, making it difficult to extract exact values for the material-dependent parameters via this method. The range of results from these fits highlight that the Choke Cavity alone cannot be used to calculate a unique set λ_L, ξ_0 and l parameters for a sample. The 3 orders of magnitude variation of l/ξ_0 means that it is difficult to separate sample performance based on these parameters. The surface resistance data is therefore vital to compare samples.

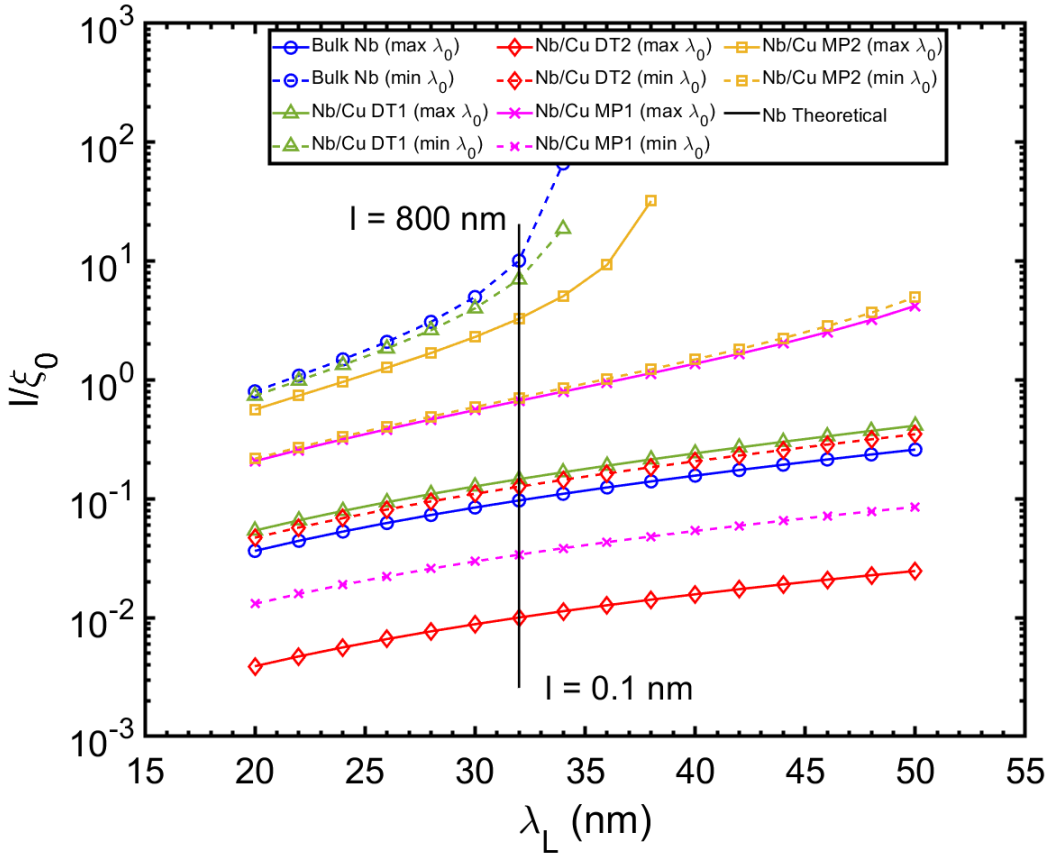

Figure 6.17: l/ξ_0 as a function of λ_L for the five samples. The intersection with theoretical values of $\lambda_L = 32\,\text{nm}$ and $\xi_0 = 39\,\text{nm}$ for bulk Nb is shown. Min and max λ_0 correspond upper and lower bound of λ_0 derived from the Gorter-Casimir fits with $1 \leq n \leq 4$.

6.3.3 Surface Resistance as a function of Sample Peak Magnetic Field

In addition to penetration depth measurements, the main requirement of the Choke Cavity facility is to be able to measure the surface resistance of samples following the RF-DC compensation procedure detailed in Sections 5.3.1 and 5.3.2. Typical SRF cavity tests measure Q_0 (or R_s) as a function of accelerating gradient at fixed cavity temperature. Given that the accelerating gradient is proportional to the peak magnetic field, sample test facilities usually aim to measure R_s as a function of $B_{s,pk}$

to predict the behaviour of thin films at increasing fields, prior to similar coatings being deposited on cavities. Therefore, it is desirable that the Choke Cavity can make similar measurements.

Measurements of $R_s(B_{s,pk})$ at fixed $T_s = 4.2\,K$ are shown in Figure 6.18 for the bulk Nb and Nb/Cu samples. These results show consistent measurements of R_s ranging from 6.7 μΩ for Nb/Cu DT1 to 33.4 μΩ for Nb/Cu MP1 at low $B_{s,pk} < 3\,mT$. For each sample, the uncertainty on R_s decreases slightly as $B_{s,pk}$ increases due to the measurement of larger values of P_{RF}. The contributions to these uncertainties are discussed in detail later in Section 6.5.1.

During commissioning with Nb, a maximum $B_{s,pk} \approx 3\,mT$ was achievable with this facility. It should be noted that this is lower than other sample test facilities compared in Table 3.2. Significantly higher fields are not yet reachable because the Choke Cavity facility is not yet in a radiation-safe test environment. Testing samples with lower R_s at higher RF powers results in an increase in stored energy and higher risk of Bremsstrahlung radiation. Until higher fields can be reached, it is not possible to speculate on the performance of $R_s(B_{s,pk})$ beyond 3 mT for these samples measured at 7.8 GHz. This level of $B_{s,pk}$ is ≈ 30 times lower than typical SRF cavities. A discussion of future upgrades that can be performed to increase these limits is presented later in Section 6.7.

6.3.4 Surface Resistance as a Function of Sample Temperature

In addition to the $R_s(B_{s,pk})$ measurements, surface resistance can also be measured as a function of the sample temperature. For these measurements, the Choke Cavity temperature is kept constant to avoid a drift in stored energy during a measurement.

For each sample, R_s was measured as a function of T_s in the region of $B_{s,pk} < 3\,mT$, shown in Figure 6.19. For these samples, it is possible to compare R_s at $T_s = 4.2$ K. Both DT samples have lower R_s at 4.2 K than the MP samples, which could be due to lower substrate roughness or the effect of being closer to the

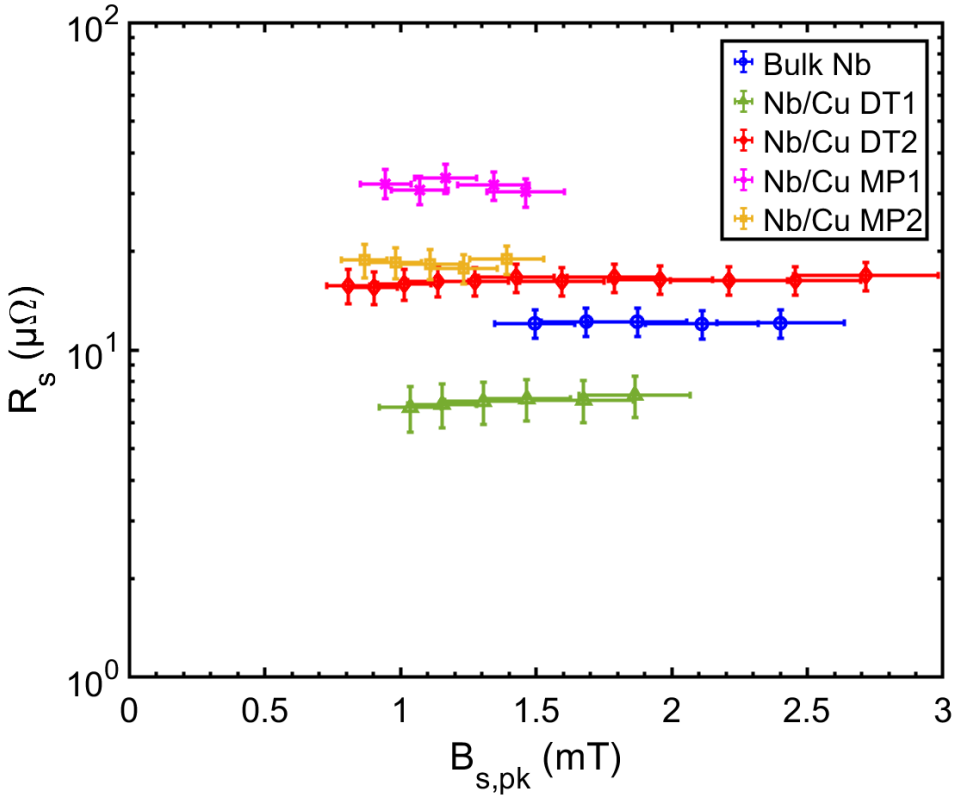

Figure 6.18: R_s vs $B_{s,pk}$ for the five samples compared at fixed $T_s = 4.2\,\mathrm{K}$.

optimal deposition temperatures for Nb. Of the DT samples at this temperature, $R_s = 7.3 \pm 1.0\,\mu\Omega$ for DT1 and $R_s = 16.6 \pm 2.3\,\mu\Omega$ for DT2, which is more than a factor of 2 higher. Sample DT2 was deposited at a higher temperature than DT1. For thin films, this likely increases residual stress and surface roughness [207], which may explain the higher R_s. Of the MP samples, $R_s(4.2\ \mathrm{K}) = 30.6 \pm 4.3\ \mu\Omega$ for MP1 and $R_s(4.2\ \mathrm{K}) = 19.9 \pm 2.8\ \mu\Omega$ for MP2. Despite both undergoing the same deposition parameters, MP2 has a lower R_s at 4.2 K. This could be due to the MP2 sample having less impurities in the film or lower film stress and hence fewer film defects due to the lack of additional heating that is required for In brazing. However, the latter is unlikely to explain the lower R_s for the bulk Nb, DT1 and DT2 samples as no In surface contamination was detected using X-ray photoelectron spectroscopy (XPS). As with SRF cavities, there is a wide variation in performance of samples.

These measurements show an increase in R_s with T_s as expected, with a transition

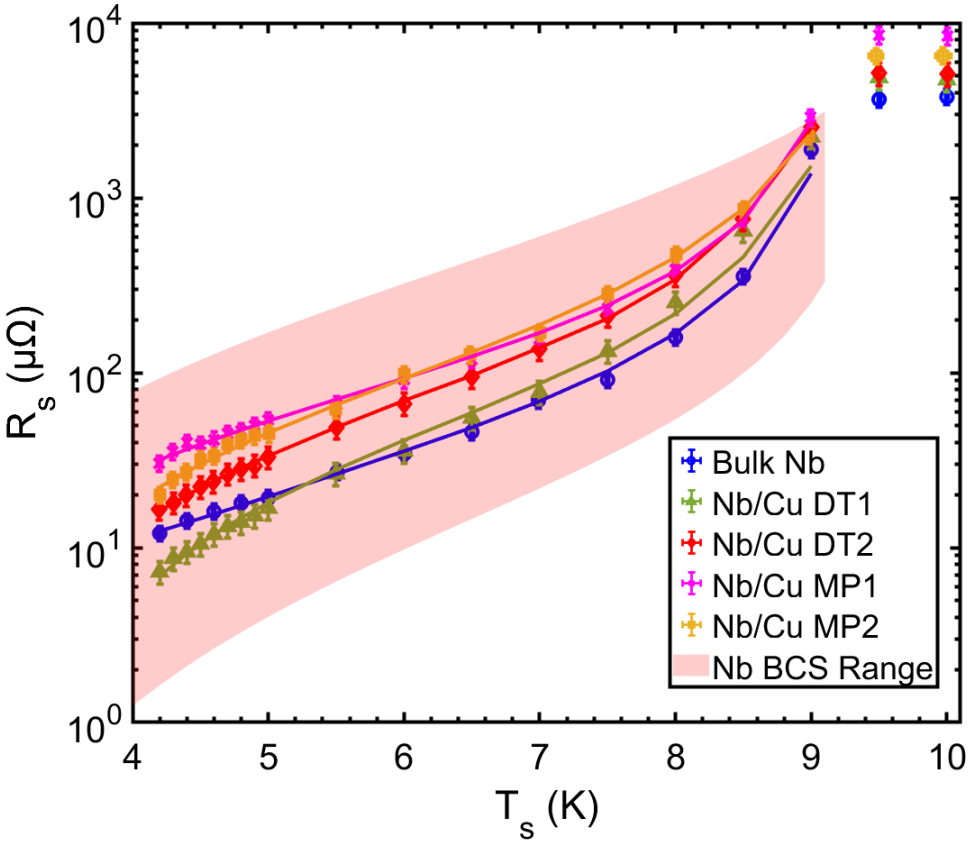

Figure 6.19: $R_s(T_s)$ for the five samples with examples of BCS fits and an illustration of the theoretical BCS resistance range for Nb calculated using the SRIMP code [56] with parameters: $T_c = 9.2\,\mathrm{K}$, $RRR = 1-400$, $\Delta(0)/k_B T_c = 1.5-2.5$, $\lambda_L = 20-50\,\mathrm{nm}$, $\xi_0 = 20-39\,\mathrm{nm}$.

to the normal conducting regime above 9 K. Given that these measurements are at low $B_{s,pk}$, it is possible to derive the superconducting energy gap at 0 K ($\Delta(0)$) by fitting $R_s(T_s)$ to BCS theory in the range $4.2\,\mathrm{K} < T_s < 9.0\,\mathrm{K}$. Examples of fits are illustrated in Figure 6.19. For this process, the WinSuperFit code 2.0 [208], based on the Halbritter code [58], was used with the aim of minimising χ^2 [204]. In addition to measurements of f_0 and T_c, the BCS fits use a range of l, which was derived from λ_0, assuming fixed $\lambda_L = 32\,\mathrm{nm}$ and $\xi_0 = 39\,\mathrm{nm}$ for clean bulk Nb. The low field $R_s(T_s)$ measurements are a combination of a temperature dependent BCS resistance (R_{BCS}) and a temperature independent residual resistance, (R_{res}). Therefore, R_{res}

was also derived from a fit to $R_s(T_s)$ whereby:

$$R_s(T_s) = R_{BCS}(T_s, f_0, \xi_0, \lambda_L\ l, \Delta(0), T_c) + R_{res}. \tag{6.27}$$

The parameters obtained from fits to $R_s(T_s)$, as well as the measurements of $\Delta f(T_s)$ and $\Delta\lambda(T_s)$ in Sections 6.3.1 and 6.3.2 respectively are shown in Table 6.3. As shown in Figure 6.17, different combinations of (λ_L, ξ_0, l) can be used to fit $\Delta\lambda(T_s)$ and $R_s(T_s)$. For the bulk Nb sample, where the literature values of λ_L and ξ_0 have been used, a low surface l is possible due to oxygen disassociation during heat treatment under vacuum [209]. However, the fitting results show a large uncertainty in l. Overall though, the uncertainty on l is typically insignificant to the uncertainty on R_s. This is because R_s is made up of an R_{BCS} component, dominated by an exponential dependence on temperature and energy gap and a quadratic dependence with frequency and an additive R_{res} component $\sim \mu\Omega$.

In addition, it was not possible to perform the full standard treatment process for the bulk Nb sample. The addition of a light BCP after the 600 °C bake could increase l. For the frequency and temperature range of the Choke Cavity, it is expected that R_{BCS} dominates over R_{res}. However, bulk Nb also showed a higher than expected R_{res}, which could be due to contamination during heat treatment.

For the thin film samples, a lower $\Delta(0)$ and higher R_{res} for DT2 compared to DT1 might be due to changes in the sample surface as a result of the higher deposition temperature, whilst the much lower $\Delta(0)$ for the MP2 sample was surprising. In addition, the R_{res} for both MP samples was higher than the DT ones which might be explained by a higher initial MP roughness. The residual resistance is often related to the roughness of the surface and the absence of defects [210]. Previous studies have shown that lower roughness can lead to a more uniform film with fewer defects, which can lower residual resistance [211].

In Figure 6.19, the R_s measurements in the normal conducting state above T_c show a range of R_s for the samples. The R_s measurements for DT1, DT2 and MP2 are within error, making it seem that the these samples have similar l, whilst bulk

Table 6.3: Fit parameters obtained from $\Delta\lambda(T_s)$ and $R_s(T_s)$ (assuming fixed λ_L and ξ_0) measurements of the five samples used for the Choke Cavity facility commissioning.

	Bulk Nb	DT1	DT2	MP1	MP2
T_c (K)	9.28 ± 0.10	9.30 ± 0.10	9.30 ± 0.18	9.43 ± 0.12	9.38 ± 0.13
λ_0 (nm)	$34.4 - 132.8$	$35.4 - 109.6$	$117.2 - 401.8$	$58.6 - 220.1$	$38.9 - 57.4$
λ_L (nm) (fixed)	32	32	32	32	32
ξ_0 (nm) (fixed)	39	39	39	39	39
l (nm)	$4 - 394$	$6 - 274$	$0.4 - 5$	$1.3 - 26$	$28 - 128$
$\Delta(0)/k_BT_c$	2.31 ± 0.02	1.98 ± 0.06	1.78 ± 0.21	1.6 ± 1.23	1.38 ± 0.07
R_{res} ($\mu\Omega$)	6.9 ± 0.5	0.5 ± 0.05	3.9 ± 2.9	4.7 ± 4.5	12.2 ± 3.4

Nb would appear to have higher l whilst MP1 has lower l. At 7.8 GHz, the skin depth is less than the l, suggesting that each sample exists somewhere between the normal skin effect and extreme anomalous skin effect regimes under RF conditions. In this region, it is not possible to use the normal conducting R_s to estimate l, therefore additional techniques should be performed to extract this [212].

Based on these results of fitting, the fittings should only be used as an approximate guide, for the reasons discussed in Section 6.3.2 which details the uncertainties of the BCS parameters at 0 K. Given that BCS parameters can vary, especially for thin films, a range of Nb BCS parameters was also used to plot the theoretical R_{BCS} in Figure 6.19. The parameters used were based on HiPIMS Nb/Cu measurements elsewhere [53, 75]: $T_c = 9.2$ K, $RRR = 1 - 400$, $\Delta(0)/k_BT_c = 1.5 - 2.5$, $\lambda_L = 20 - 50$ nm, $\xi_0 = 20 - 39$ nm. This indicates how the BCS resistance of thin films can vary significantly; however, the Nb samples tested during commissioning were measured to be within this range. Even without knowing the exact BCS parameters, it is still possible to use the Choke Cavity to directly measure $R_s(T_s)$ and compare samples after using different treatment procedures or deposition parameters. This is the primary purpose of the facility, which has been successfully demonstrated during commissioning.

6.4 Measurement Repeatability

During facility commissioning, it was important to demonstrate whether repeated tests with the Choke Cavity using the same samples could achieve consistent results. First, measurements of $R_s(B_{\mathrm{s,pk}})$ at $T_{\mathrm{s}} = 4.2\,\mathrm{K}$ for sample DT2 were made with increasing and decreasing $B_{\mathrm{s,pk}}$ (controlled by the output power of VNA). The results are shown in Figure 6.20. All measurements are consistent, as expected, regardless of whether $B_{\mathrm{s,pk}}$ was increased or decreased. This shows that the $R_{\mathrm{res}}(B)$ effect is small at low fields from $0 - 3\,\mathrm{mT}$. It also indicates that this level of RF power is insufficient to cause significant heating of the sample surface that would affect the reliability of R_{s}.

During any measurement of sample R_{s}, T_{cav} is set to a constant temperature using the temperature controller connected to the Choke Cavity heaters. This temperature is higher than T_{s} to ensure that RF losses on the Choke Cavity are not too high as to cause the cavity temperature to rise during measurement. For sample DT1, measurements of R_{s} as a function of T_{cav} at a fixed $T_{\mathrm{s}} = 4.2\,\mathrm{K}$ were made, as shown in Figure 6.21. The consistency between the measurements demonstrates that R_{s} does not depend on the temperature of the Choke Cavity. For example, at $T_{\mathrm{cav}} = 5.2\,\mathrm{K}$, $R_{\mathrm{s}} = 7.3 \pm 1.1\,\mu\Omega$ and at $T_{\mathrm{cav}} = 5.4\,\mathrm{K}$, $R_{\mathrm{s}} = 7.0 \pm 1.0\,\mu\Omega$. This is as expected because of the good thermal decoupling of the sample and the Choke Cavity.

Another set of repeatability studies looked at the effect of repeated facility cooldowns from room temperature to base temperature. Repeated measurements for the DT1 and DT2 samples were performed after a warm up to room temperature followed by a second cooldown without venting to atmosphere or removing the sample from the facility. The warm up between tests was allowed to proceed naturally without use of heaters to speed up the warm up. The results are shown in Figure 6.22. After repeated thermal cycles and RF calibrations, the measurements demonstrated consistency and repeatability during separate cooldowns. For example, at 4.2 K, $R_{\mathrm{s}} = 7.3 \pm 1.2\,\mu\Omega$ and $7.6 \pm 1.1\,\mu\Omega$ for the two tests of DT1 and $R_{\mathrm{s}} = 16.6 \pm 2.9\,\mu\Omega$ and $16.9 \pm 2.5\,\mu\Omega$ for the two tests of DT2. This indicates

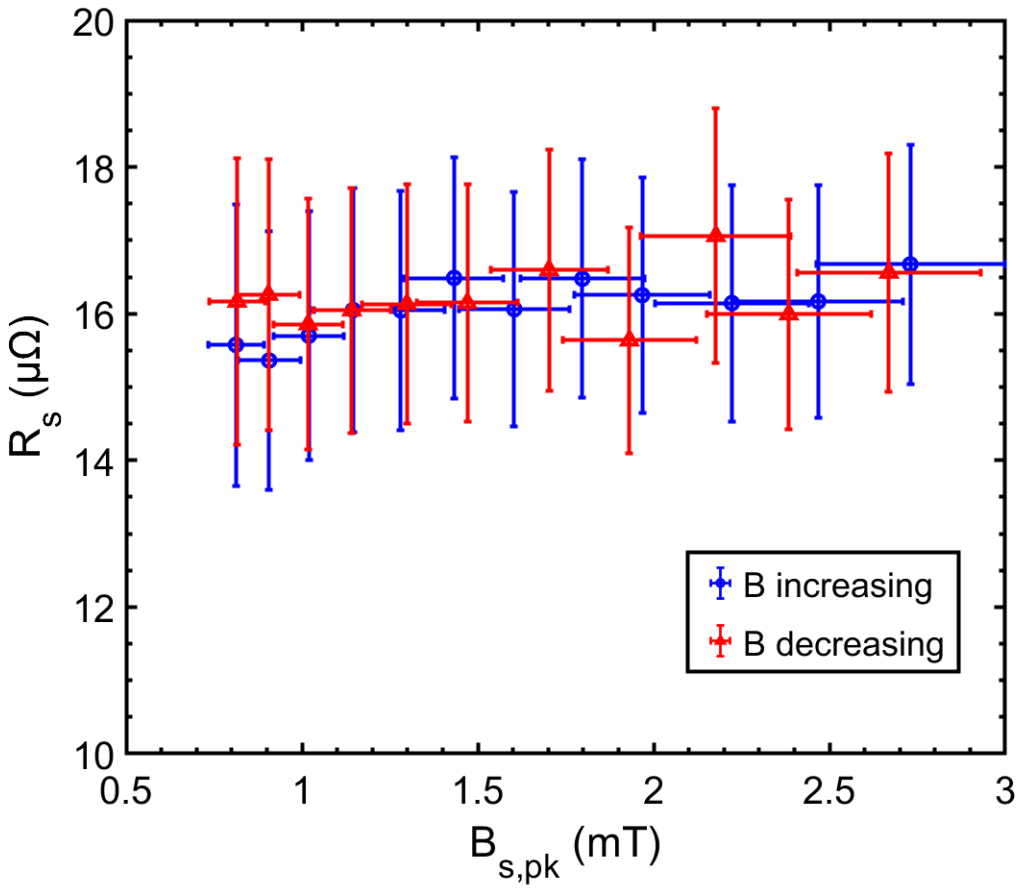

Figure 6.20: R_s vs $B_{s,pk}$ for the Nb/Cu DT2 sample with increasing and decreasing $B_{s,pk}$ field at $T_s = 4.2$ K.

that repeated cooldown cycles have an average uncertainty of $< 2\%$ on sample R_s. This suggests that at least two repeated thermal cycles do not significantly change the surface structure of the films (e.g., from multiple thermal contractions and expansions).

The final set of repeatability measurements looked at five sets of repeated measurements with the MP1 sample, shown in Figure 6.23. Between the first and second cooldowns, the facility was kept under vacuum as with the DT samples. The third set of measurements re-tested the sample after leaving in air for 3 weeks whilst still attached to the sample holder. The fourth test happened after complete removal and reattachment of the sample from the sample holder (which required

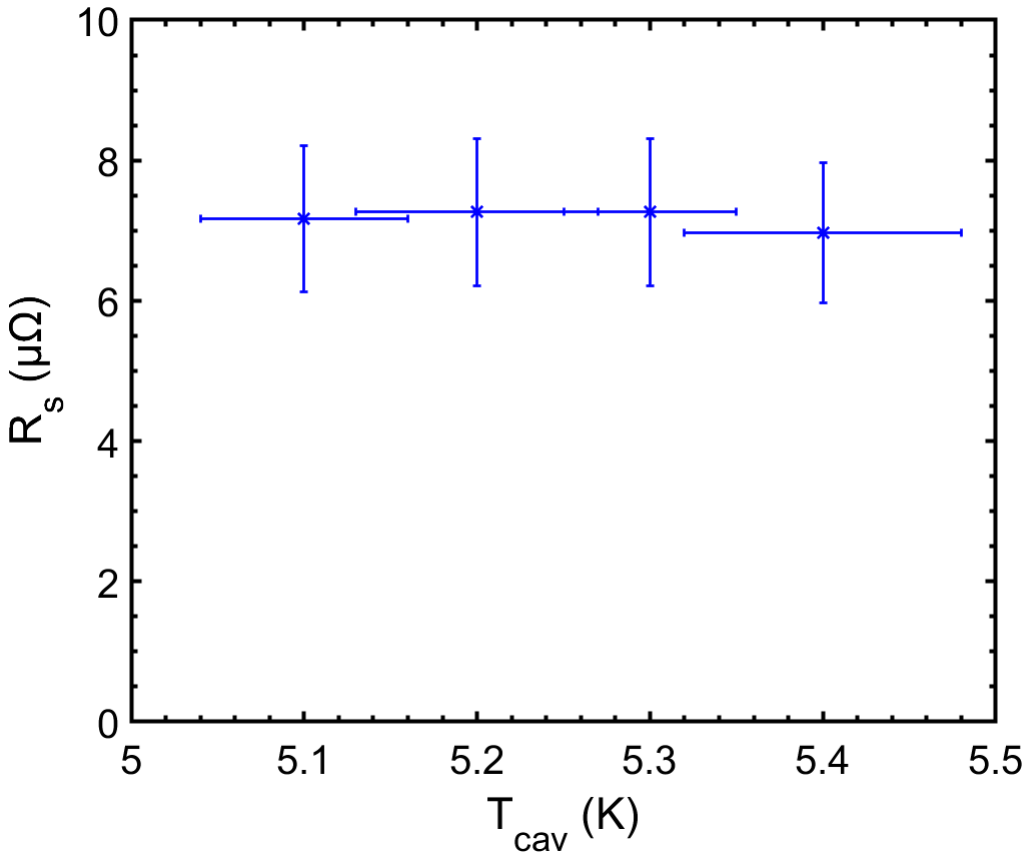

Figure 6.21: $R_{\mathrm{s}}(T_{\mathrm{cav}})$ for Nb/Cu DT1 with fixed $T_{\mathrm{s}} = 4.2\,\mathrm{K}$.

two heating cycles in the In brazing facility, discussed previously in Section 5.2.1). The fifth and final test was after a rapid warm up to room temperature using the stage 2 plate and sample holder heaters to assist. All other warm ups between the first four tests were without assistance from heaters.

As with the DT samples, consistent measurements were observed with repeated cooldowns without sample removal. The third test, after leaving in air, also produced consistent measurements. Therefore, it seems unlikely that leaving Nb in air for short periods causes significant oxidation in the surface layer. The formation of niobium oxides has been shown to decrease Q_0 of cavities at lower fields [213]. The fourth test, after complete removal and reattachment, required another round of sample heating to $\approx 160°\mathrm{C}$ to melt the In between the sample and the sample holder. A slight increase in R_{s} was observed at the lowest temperatures which could be due to

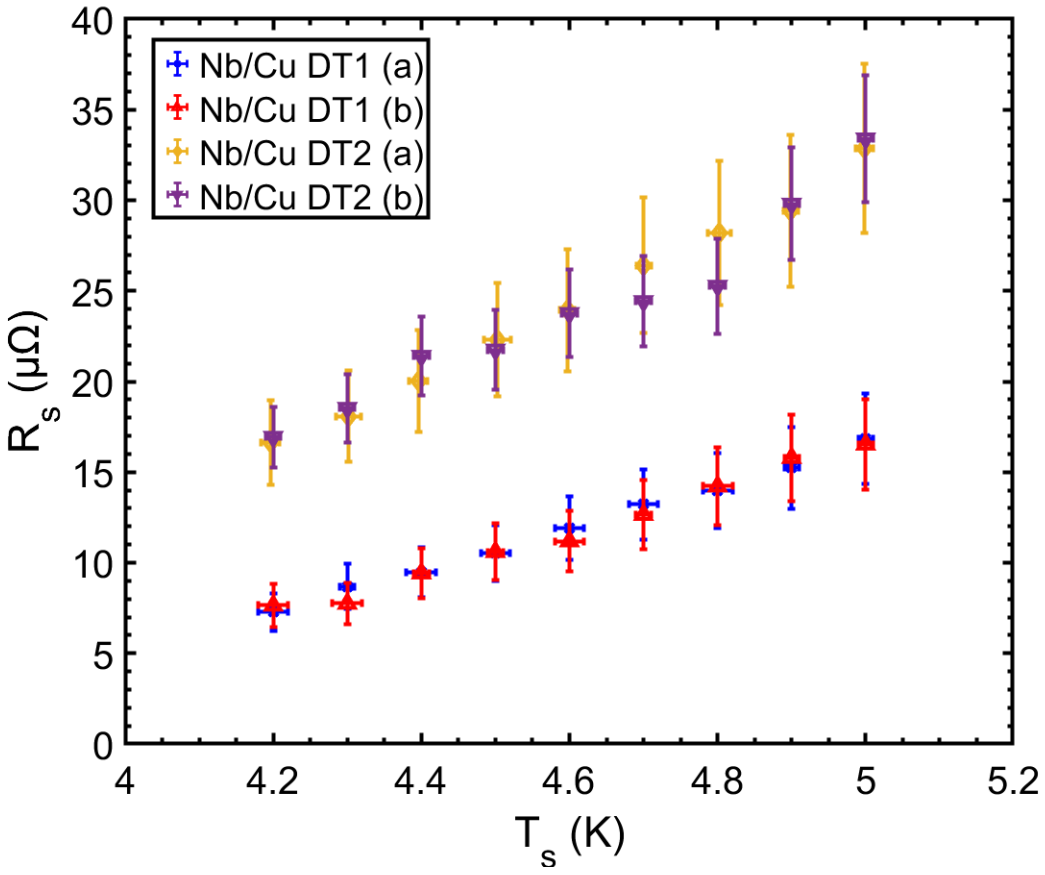

Figure 6.22: $R_s(T_s)$ for two separate cooldowns with Nb/Cu DT1 and DT2: (a) first cooldown, (b) second cooldown.

poor vacuum conditions during a second round of In heating; however, measurement uncertainties make the measurements consistent with the other tests, meaning that it is not possible to conclude the effect of repeated brazing cycles on the sample thin film. Future studies may benefit from analysing the effect of further sample/sample holder brazing cycles. Finally, the rapid heating process, which can cause increased thermal stresses on the film, did not show a significant change in R_s in test 5. This suggests that at least one rapid warm-up of a sample is possible without affecting the reliability of future measurements. Rapid warm-ups are often vital to decrease the total warm-up time and ensure that a sample testing rate of three per week can be maintained.

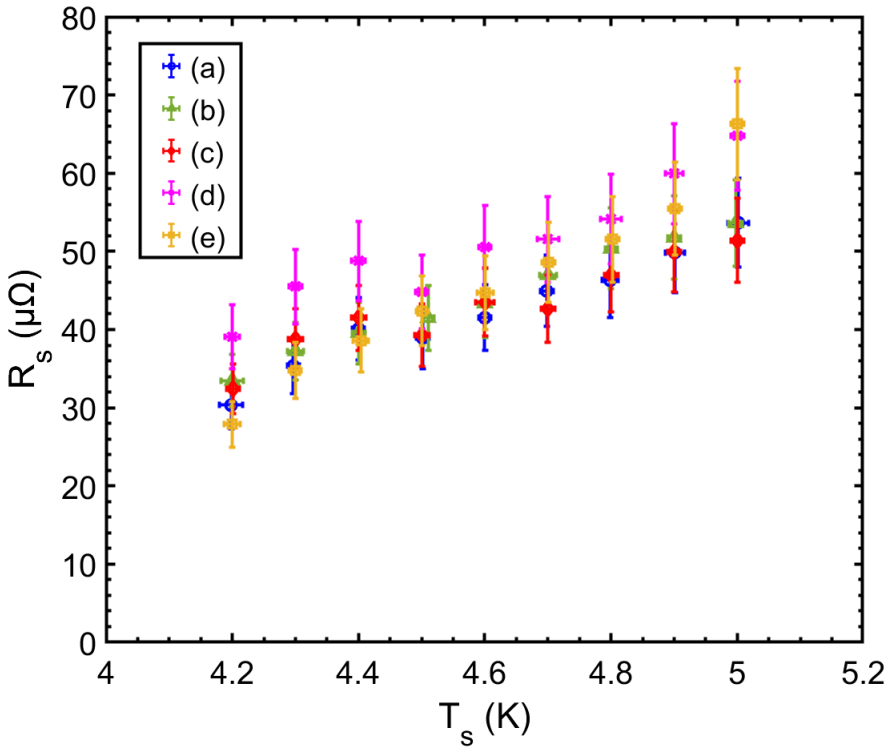

Figure 6.23: $R_{\mathrm{s}}(T_{\mathrm{s}})$ for five separate cooldowns with Nb/Cu MP1: (a) first cooldown, (b) second cooldown without removal, (c) third cooldown after leaving in air, (d) fourth cooldown after removal and reattachment from sample holder, (e) fifth cooldown after rapid warm up.

6.5 Measurement Uncertainties

6.5.1 Surface Resistance and Peak Magnetic Field

Equations 5.11 and 5.10 to calculate R_{s} and $B_{\mathrm{s,pk}}$ show that there are six variables that must be assessed to calculate their overall uncertainties: $\sigma_{R_{\mathrm{s}}}$ and $\sigma_{B_{\mathrm{s,pk}}}$. The contributions of these variables are: the uncertainty in Q_{t} ($\sigma_{Q_{\mathrm{t}}}$), uncertainty in transmitted power ($\sigma_{P_{\mathrm{t}}}$), the uncertainty in the difference in DC heater power (σ_{RF}), uncertainty in resonance frequency (σ_{f_0}) and the uncertainties in the CST calibration constants c_1 and $B_{\mathrm{s,pk,CST}}$, represented by both $\sigma_{c_1/B^2_{s,pk,CST}}$ and $\sigma_{Bs,pk,CST}$.

Firstly, the measurements of Q_{t} are made using the pickup calibration procedure

detailed in Section 5.3.2 with the Keysight 5024A VNA. Details on the uncertainty contributions to Q_t were previously described in Section 6.2.2. The overall uncertainty on a measurement of Q_t is $\approx 20\%$. This requires that the correct VNA settings (i.e. IFBW and number of points) are set correctly before a measurement. By averaging over multiple measurements, it is possible to reduce random errors that may arise and increase the precision of this measurement. However, the instrument errors will dominate, so it is not possible to significantly decrease the 20% error on Q_t.

Measurements of P_t are made using the Keysight E9326A power sensor. The manufacturer quotes a relative accuracy of $\pm$ 0.16 dB for a power measurement with this device [214]. A measurement of P_t also requires the measurement of the RF cable loss of the cable connected to the pickup probe, as well as the measurement of the coupling factor of the directional coupler. Given that cable calibrations are performed with the VNA, an uncertainty of $\pm$ 0.3 dB for RF cable loss is reasonable. Furthermore, P_t reaches steady state after $\approx$ 3 min, after which the measurements are recorded with maximum fluctuations $\approx \pm 0.05$ dBm. A combination of uncertainties leads to an overall uncertainty in P_t of $\pm$ 0.85 dB, which is $\approx 20\%$.

Next, calculating P_{RF} requires measurements of I_{DC} and V_{DC} for the calculation of $P_{DC,1}$ and $P_{DC,2}$. The maximum output current of the Lakeshore 331 temperature controller is 1 A, therefore, for a sample heater resistance of 20 Ω, the maximum measurable voltage drop is 20 V. These are measured with the Multicomp Pro MP730424 multimeter. Within the current and voltage ranges, the manufacturer quotes a worst-case current measurement uncertainty of 0.29% and voltage measurement uncertainty of 0.22% as shown in Figure 6.24 [215]. For the temperature controller heater output, the manufacturer quotes an RMS heater noise of 50 μV + 0.01% of the output voltage. For a sample heater resistance of 20 Ω, this corresponds to a maximum error contribution in a measurement of P_{DC} of 0.2% [216]. The resulting total instrument uncertainty on a measurement of P_{DC} is 0.36%. Furthermore,

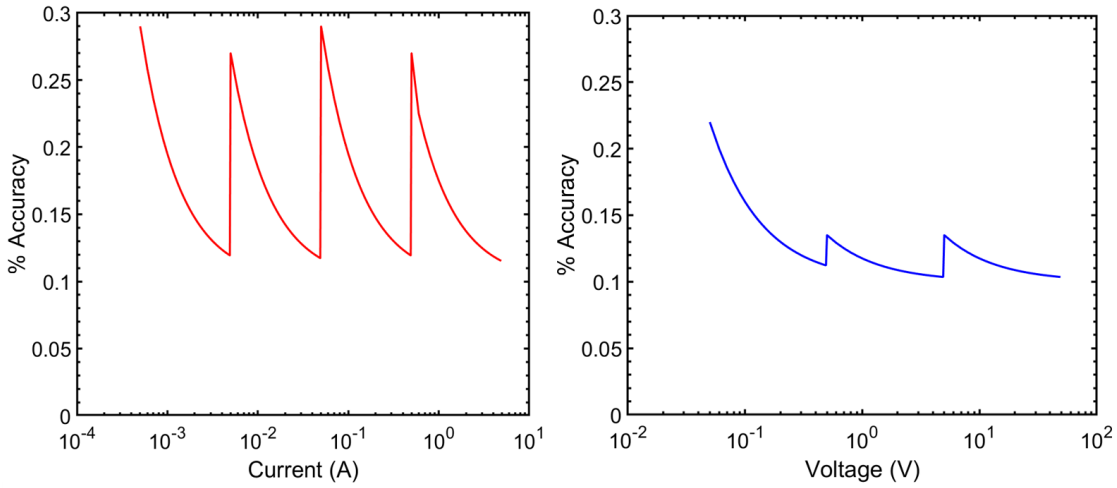

Figure 6.24: Heater current and voltage uncertainties measured with the Multicomp Pro MP730424 multimeter (jumps occur when the multimeter changes range).

due to small steady-state sample temperature fluctuations caused by the stage 2 cold head fluctuations, the heater power fluctuates by ± 1 mW. At steady state, averaging multiple data points and taking the standard deviation, the random error on a measurement of P_{DC} can be reduced to $< 0.5\%$. Combining the three main sources of error on P_{DC} (multimeter uncertainty, RMS heater noise and heater power fluctuations), results in an overall heater accuracy of 0.6%. Therefore, the resulting uncertainty in P_{RF} is generally $< 1\%$, which is much lower than the contributions from Q_{t} and P_{t}, so not an issue.

As explained in Section 6.2.2, the instrumentation error for a measurement of f_0 is negligible. The main source of error is the ±1.5 kHz level of detuning caused by microphonics. As a result, $\sigma_{f_0} \approx 10^{-5}\%$. Therefore, compared to the uncertainties on Q_{t}, P_{t} and P_{RF}, this is negligible and can be excluded from the overall uncertainty calculations, therefore also not an issue.

The final variables that could contribute to the overall uncertainties in R_{s} and $B_{\mathrm{s,pk}}$ are the CST constants c_1 and $B_{\mathrm{s,pk,CST}}$. These constants depend only on the geometry of the Choke Cavity-sample system, therefore, could change if the geometry of the experimental system during a sample test is different from the

original CST model. Two ways the geometry could change are: thermal contractions during cooldown and chemical etching/manufacturing tolerances.

Firstly, when a sample is mounted, the G10 spacers ensure a constant 1 mm gap between the sample and Choke Cavity. Care is always taken to ensure that the sample is pressed tightly against the spacers to maintain this gap. However, during cooldown, thermal contraction of the sample, Choke Cavity and stage 2 plate may lead to a decrease in gap size and diameter of each component, thus changing the gap size and choke parameters. It is possible to estimate these dimensional changes using the equation for linear thermal expansion for each component:

$$\Delta L = L_0 \alpha \Delta T, \tag{6.28}$$

where ΔL is the change in the length of the object, L_0 is the initial object length, α is the linear expansion coefficient and ΔT is the change in temperature.

Nb and Cu have different linear expansion coefficients and therefore expand or contract at different rates. For Nb, $\alpha = 7$ µm/mK and for Cu, $\alpha = 16$ µm/mK [217]. For a cooldown from 298 K to 4 K, a sample of 3 mm thickness can contract by 6 µm if made from bulk Nb and 14 µm if made from Cu relative to the sample surface. Meanwhile, the 12 mm thick bulk Nb Choke Cavity can contract by 26 µm. The Choke Cavity itself is mounted on the underside of the 10 mm thick Cu stage 2 plate and the sample is mounted on top of a 10 mm thick sample holder. These parts can both contract by 47 µm during cooldown relative to the base of the Choke Cavity. A sum of these contractions can result in an estimated maximum increase in gap size of 134 µm due to vertical thermal contractions.

In addition, for the 104 mm diameter bulk Nb Choke Cavity, it can be estimated that thermal contraction reduces the diameter of the cavity by up to 223 µm. The result of thermal contractions of both the thickness and diameter of the Choke Cavity means that the width and height of the chokes and the central cavity may also contract by approximately 223 µm and 26 µm respectively.

Simulations in CST were performed to predict the change in $c_1/B^2_{\mathrm{s,pk,CST}}$ from

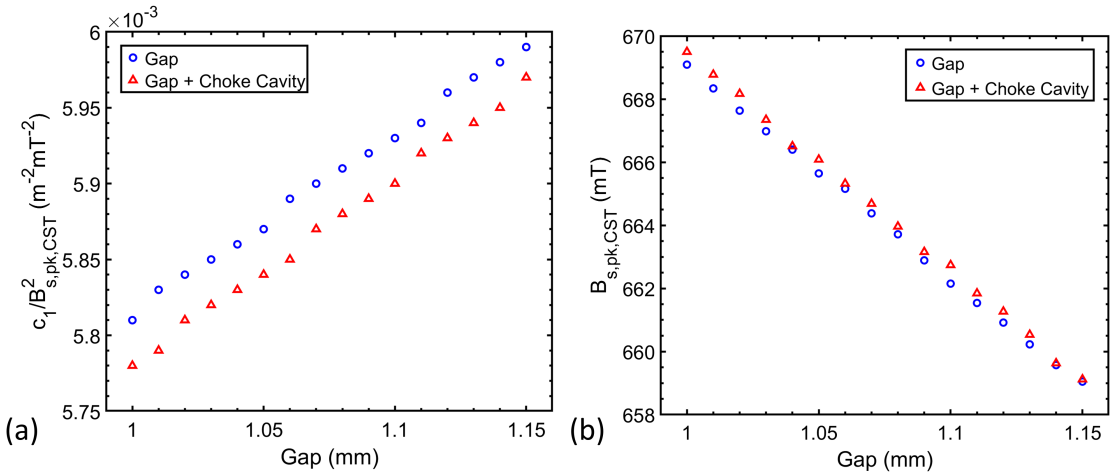

Figure 6.25: Change in CST constants as a function of gap size in the case where only the gap is affected by thermal contraction and the case where both gap and Choke Cavity parameters are affected: (a) $c_1/B^2_{\mathrm{s,pk,CST}}$, (b) $B_{\mathrm{s,pk,CST}}$.

these dimensional changes as R_{s} is dependent on this constant. Simulations also predict the change in $B_{\mathrm{s,pk,CST}}$ alone as $B_{\mathrm{s,pk}}$ is related to this quantity. Changes in $c_1/B^2_{\mathrm{s,pk,CST}}$ are shown as a function of the size of the gap in Figure 6.25a. Meanwhile, the changes in $B_{\mathrm{s,pk,CST}}$ are shown in Figure 6.25b. These are shown for both the case where only the gap increases and the case where both the gap increases and the choke cavity parameters (that is, total diameter and height, choke width and height, central cavity diameter and height) decrease by 223 µm. For both cases, $c_1/B^2_{\mathrm{s,pk,CST}}$ increases by 3.2% and $B_{\mathrm{s,pk,CST}}$ decreases by 1.6%.

Directly after machining at Niowave [187], the bulk Nb Choke Cavity received a BCP surface etch < 20µm to for cleaning up surface damage. A further light BCP etch removing 20 µm of material was performed later by E.Chyhyrynets (INFN) after a high temperature bake for the reasons discussed later in Section 7.1.1. Further CST simulations were performed using an increase in Choke Cavity dimensions as a result of an etch to predict the change in both $c_1/B^2_{\mathrm{s,pk,CST}}$ and $B_{\mathrm{s,pk,CST}}$ as a function of material removed. These results are shown in Figure 6.26. Here, $c_1/B^2_{\mathrm{s,pk,CST}}$ is proportional to the amount of material etched, and increases by 0.4% whilst $B_{\mathrm{s,pk,CST}}$

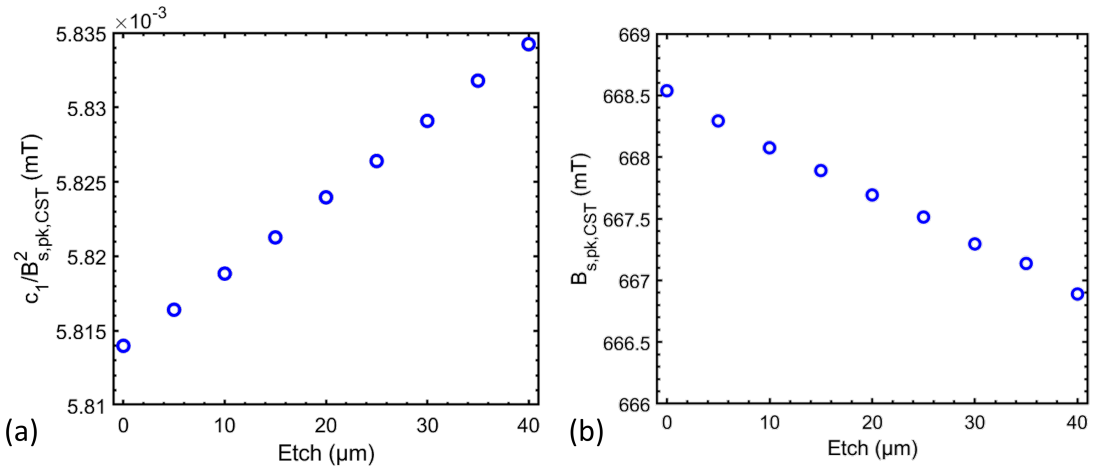

Figure 6.26: Change in CST constants as a function of the material etched: (a) $c_1/B^2_{\mathrm{s,pk,CST}}$, (b) $B_{\mathrm{s,pk,CST}}$.

decreases by 0.2%. Both are much less than the increase due to thermal contractions.

Overall, it is possible to add the effects of thermal contraction and material etching in quadrature. This results in an uncertainty on $c_1/B^2_{\mathrm{s,pk,CST}} \approx 3.2\%$ and uncertainty on $B_{\mathrm{s,pk,CST}} \approx 1.6\%$. However, as with σ_{RF}, these uncertainties are much less than the contributions of Q_{t} and P_{t}.

Taking into account all the uncertainty contributions for the measurements of R_{s}, the propagation of uncertainties in Equations 5.11 and 5.10 gives:

$$\frac{\sigma_{R_{\mathrm{s}}}}{R_{\mathrm{s}}} = \sqrt{\left(\frac{\sigma_{P_{\mathrm{RF}}}}{P_{\mathrm{RF}}}\right)^2 + \left(\frac{\sigma_{Q_{\mathrm{t}}}}{2Q_{\mathrm{t}}}\right)^2 + \left(\frac{\sigma_{P_{\mathrm{t}}}}{2P_{\mathrm{t}}}\right)^2 + \left(\frac{\sigma_{c_1/B^2_{\mathrm{s,pk,CST}}}}{c_1/B^2_{\mathrm{s,pk,CST}}}\right)^2} \approx 14\%, \tag{6.29}$$

where the lowest percentage uncertainty is achievable with multiple measurements of Q_{t}.

Given that the error contribution on Q_{t} and P_{t} dominates over P_{RF}, for $B_{\mathrm{s,pk}}$ measurements, propagation of uncertainties in Equation 5.10 yields a similar result:

$$\frac{\sigma_{B_{\mathrm{s,pk}}}}{B_{\mathrm{s,pk}}} = \sqrt{\left(\frac{\sigma_{Q_{\mathrm{t}}}}{2Q_{\mathrm{t}}}\right)^2 + \left(\frac{\sigma_{P_{\mathrm{t}}}}{2P_{\mathrm{t}}}\right)^2 + \left(\frac{\sigma_{B\mathrm{s,pk,CST}}}{B_{\mathrm{s,pk,CST}}}\right)^2} \approx 14\%. \tag{6.30}$$

6.5.2 Frequency Shift and Penetration Depth

For measurements of $\Delta f(T_\mathrm{s})$ discussed in Section 6.3.1, the main uncertainty contributions are the uncertainty in f_0 at values of T_s. The uncertainty of the instrumentation on a f_0 measurement is negligible for reasons discussed in Section 6.2.2. A measurement of f_0 is typically from a fit to Equation 6.20 and compared to f_0 from the $|S_{21,\mathrm{max}}|$. The difference is typically very small at $10^{-7} - 10^{-5}$%. Therefore, the main uncertainty contribution on each frequency measurement is $\pm 1.5\,\mathrm{kHz}$ due to microphonics. Combining these gives a typical uncertainty on $\Delta f(T_\mathrm{s})$, $\sigma_{\Delta f} \approx 2 - 6\,\mathrm{kHz}$.

The uncertainties in $\Delta f(T_\mathrm{s})$ contribute to the uncertainty in $\Delta\lambda(T_\mathrm{s})$ ($\sigma_{\Delta\lambda}$) from Equation 6.24. Given that the uncertainty on a single measurement of f_0 is negligible, the other uncertainty contribution comes from the geometry factor (G_s) calculated in CST. As shown previously in Section 6.5.1, CST constants dependent on the geometry of the cavity can change due to thermal contractions, chemical etching or sample inhomogeneities (which are difficult to quantify). A maximum increase in G_s of 3.2% is observed due to thermal contractions that cause a change in gap and Choke Cavity parameters, as shown in Figure 6.27a. Meanwhile, a smaller maximum increase of 0.3% in G_s is observed due to chemical etching. Therefore, as with the other CST constants, thermal contractions dominate the overall uncertainty on G_s by 3.2%.

With these uncertainty contributions, the propagation of the uncertainties in Equation 6.24, at $T_\mathrm{s} > 8\,\mathrm{K}$, assuming $T_0 = 6\,\mathrm{K}$, yields

$$\frac{\sigma_{\Delta\lambda}}{\Delta\lambda} = \sqrt{\left(\frac{\sigma_{\Delta f}}{\Delta f}\right)^2 + \left(\frac{\sigma_{G_\mathrm{s}}}{G_\mathrm{s}}\right)^2} \approx 4\%, \tag{6.31}$$

6.5.3 Sample Temperature

For sample temperature measurements, Cernox thermometers and a Lakeshore 331 temperature controller are used. For electronic precision and sensor calibrations, the

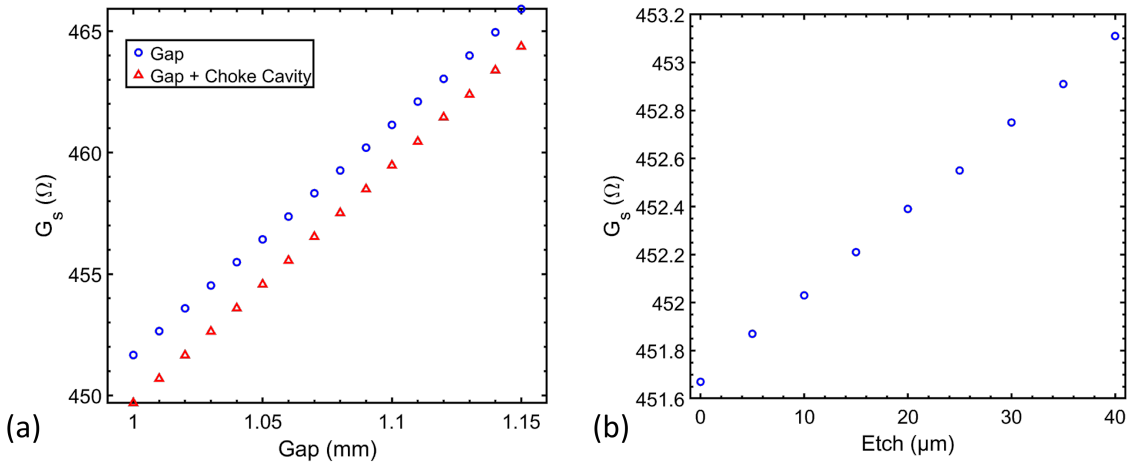

Figure 6.27: Change in the sample geometry factor due to: (a) thermal contractions increasing gap and decreasing Choke Cavity parameters, (b) chemical etch.

manufacturer quotes an instrument uncertainty $\Delta T_{\text{cernox}} = \pm 6.4\,\text{mK}$ in the range of $4.2\,\text{K} < T_\text{s} \leq 10\,\text{K}$ and $\Delta T_{\text{cernox}} = \pm 10.4\,\text{mK}$ in the range of $10\,\text{K} < T_\text{s} \leq 20\,\text{K}$.

Like most of the other facilities described in Section 3.3, these thermometers cannot be mounted directly on the sample. Instead, two thermometers are mounted on the sample holder, positioned approximately 10 mm vertically from the bottom of the sample. Therefore, thermal gradients, denoted as $\Delta T_{\text{gradient}}$, are likely to exist due to contact resistance at the boundary between the sample and the sample holder, as well as the heat distribution within the system. Indium is brazed between the sample and the sample holder to minimise thermal resistance; however, it is still important to account for any temperature gradients horizontally on the sample surface (ΔT_h) and vertically (ΔT_v) between the sample surface and the thermometer. Thermal gradients may exist due to both B-field induced heating on the sample surface and DC heating on the sample holder.

Thermal simulations were performed in CST [44] for a bulk Nb sample at initial $T_\text{s} = 4.2\,\text{K}$ with both imported eigenmode sample surface losses scaled to $B_{\text{s,pk}} = 5\,\text{mT}$ and a DC heating of 36 mW (i.e., what is typically required to maintain $T_\text{s} = 4.2\,\text{K}$) applied to the sample holder. The DC heating was modelled with a heat source on two Cu blocks connected to a Cu sample holder in contact underneath

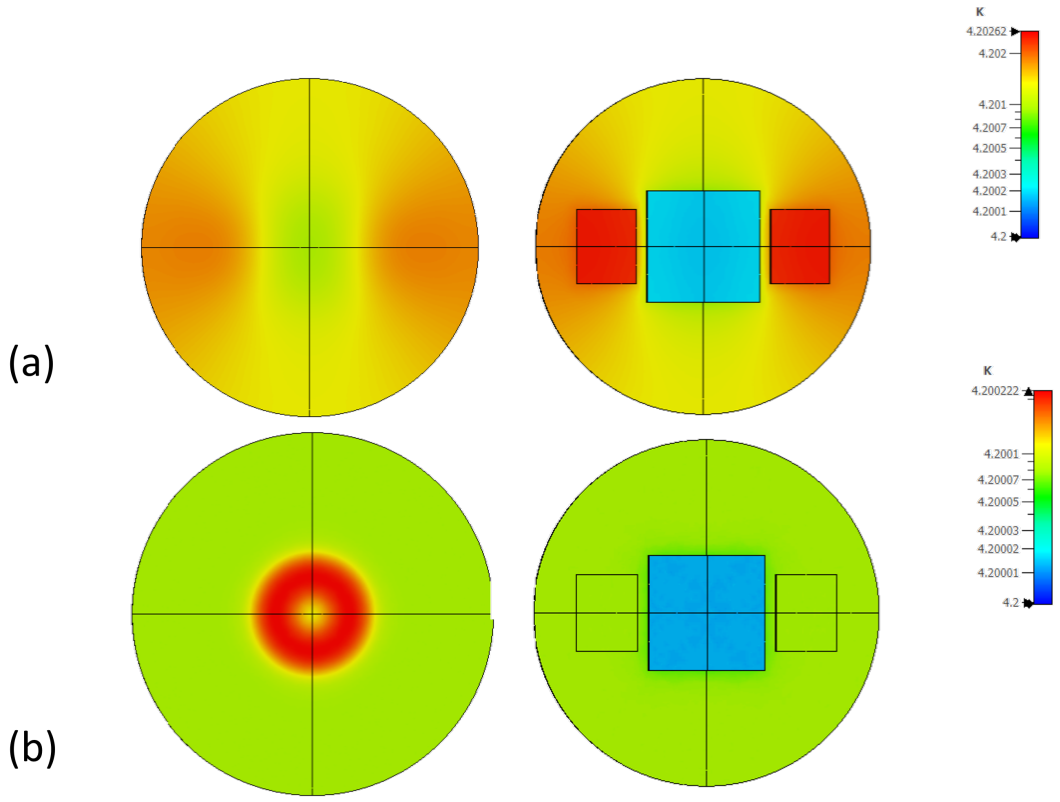

Figure 6.28: Contour plots showing the temperature gradient on both the sample surface and sample holder as a result of: (a) DC heating applied to the sample holder, (b) RF heating to the sample surface.

samples. The resulting temperature contour profiles are shown in Figure 6.28. These illustrate the thermal gradients on both the sample surface and sample holder for both the case with RF heating only and DC heating only. DC heating is concentrated where the heaters are located and RF heating follows the B-field distribution on the sample surface and is maximal at the position of choke 1 where $B_{\mathrm{s,pk}}$ is highest.

The corresponding thermal line profiles at $T_{\mathrm{s}} = 4.2\,\mathrm{K}$ are shown in Figure 6.29. These are shown for the cases with DC heating only from the sample holder, RF heating from the Choke Cavity and the case with a combination of both. The horizontal profile is measured on the sample surface, and the vertical profile is between the maximum temperature on the sample surface and the position on the

sample holder to which the thermometers are mounted. It can be seen that DC heating is approximately maximum ±35 mm from the centre of the sample, since this is the horizontal distance where the heaters are located. The RF heating is maximal at ±12 mm, which is the approximate position of the maximum $B_{\mathrm{s,pk}}$.

For the RF case, the maximum gradients are calculated as $\Delta T_{\mathrm{v}} = \pm\, 0.14\,\mathrm{mK}$ and $\Delta T_{\mathrm{h}} = \pm\, 0.14\,\mathrm{mK}$ at $T_{\mathrm{s}} = 4.2\,\mathrm{K}$. However, the case with DC only heating is higher with $\Delta T_{\mathrm{v}} = \pm\, 0.40\,\mathrm{mK}$ and $\Delta T_{\mathrm{h}} = \pm\, 0.76\,\mathrm{mK}$. This is expected as a result of higher applied powers. A combination of RF and DC results in $\Delta T_{\mathrm{v}} = \pm\, 0.44\,\mathrm{mK}$ and $\Delta T_{\mathrm{h}} = \pm\, 0.83\,\mathrm{mK}$. For a Cu sample, this decreases slightly to $\Delta T_{\mathrm{v}} = \pm\, 0.30\,\mathrm{mK}$ and $\Delta T_{\mathrm{h}} = \pm\, 0.65\,\mathrm{mK}$, due to the higher thermal conductivity of Cu. Figure 6.29(b) shows that the temperature of top of the sample due to RF heating is slightly hotter than the bottom of the sample, i.e. there is a linear temperature gradient over the 3 mm thickness of the sample. There is a slight step at the interface between the sample and sample holder due to thermal contact resistance.

This slight discontinuity at a vertical distance of 3 mm in Figure 6.29(b) may be associated with a horizontal temperature gradient across the boundary between the sample and the sample holder. However, slight gradients may exist at the boundary of the Cu and thin film, which have not been simulated.

At temperatures higher than 4.2 K, the DC power required to reach the higher temperature increases and the RF power dissipated on the sample surface increases, therefore the total heating increases. Figure 6.30 shows the simulated horizontal and vertical temperature gradients as a function of sample temperature for a Nb sample with both RF and DC heating. This shows that the temperature gradient increases with sample temperature up to a maximum $\Delta T_{\mathrm{v}} = \pm\, 20.2\,\mathrm{mK}$ and $\Delta T_{\mathrm{h}} = \pm\, 31.7\,\mathrm{mK}$ at 10 K as a result of the increase in total heating.

Another uncertainty contribution is due to compressor fluctuations that cause variations in the temperature of the cold head. In steady state, these fluctuations (ΔT_{fluc}) were not greater than $\approx \pm\, 5\,\mathrm{mK}$. Furthermore, the temperature difference (ΔT_{diff}) between the two thermometers is not greater than $\approx \pm\, 5\,\mathrm{mK}$.

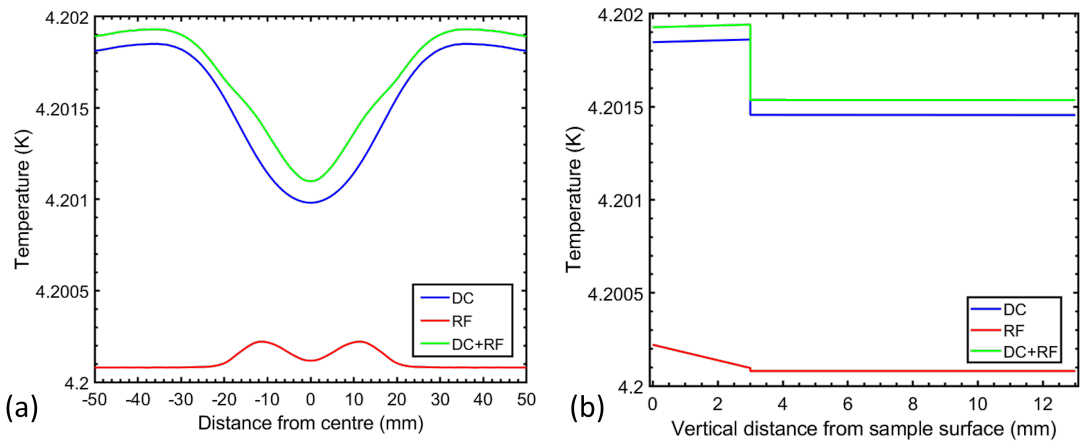

Figure 6.29: Temperature profiles for a Nb sample with DC only heating, RF only heating and a combination of DC and RF heating: (a) horizontally on the sample surface, (b) vertically from the sample surface to where the thermometers are mounted on the sample holder.

Given the calculated uncertainty contributions to the measured temperature, the total uncertainty in temperature (ΔT_{tot}) from $T_{\mathrm{s}} = 4.2 - 10\,\mathrm{K}$ is given by:

$$\Delta T_{\mathrm{tot}} = \sqrt{\Delta T^2_{\mathrm{cernox}} + \Delta T^2_{\mathrm{v}} + \Delta T^2_{\mathrm{h}} + \Delta T^2_{\mathrm{fluc}} + \Delta T^2_{\mathrm{diff}}} \approx \pm\ 10 - 45\ \mathrm{mK} \qquad (6.32)$$

6.5.4 Summary

A summary of the uncertainty contributions of each variable on the measurements of $B_{\mathrm{s,pk}}$, R_{s} and T_{s} is shown in Table 6.4. This provides both systematic (Syst.) and typical levels of random uncertainties (Rand.) on measurements of individual variables. The random error due to repeatability of R_{s} measurements as a function of T_{cav}, $B_{\mathrm{s,pk}}$ (increasing and decreasing at low fields) and due to repeated cooldowns without and with sample removal. The random error due to repeated sample measurements of R_{s} was shown to be less significant than the combination of the other error contributions.

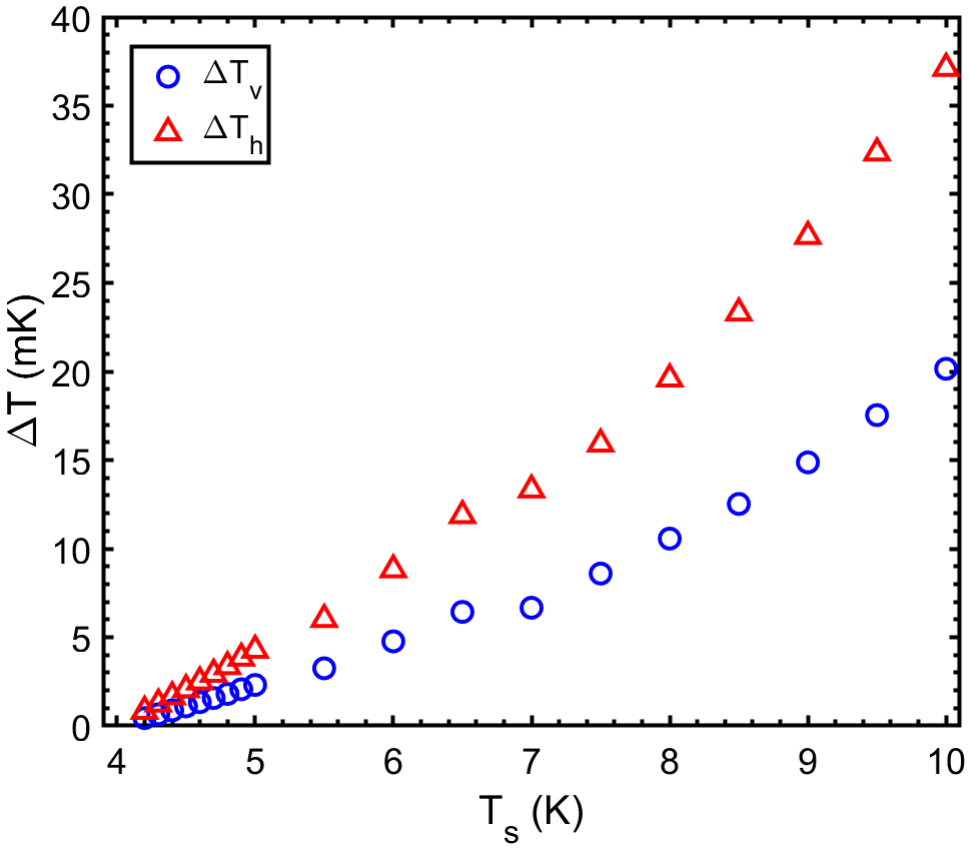

Figure 6.30: Vertical and horizontal thermal gradients for a Nb sample with DC and RF heating as a function of sample temperature.

6.6 Surface Resistance Resolution

The minimum resolvable surface resistance, $R_{\mathrm{s,min}}$, is dependent on the minimum value of P_{RF} that can be resolved. This is given by differentiating Equation 5.11 with respect to $P_{\mathrm{DC},1}$ in the situation where $P_{\mathrm{DC},2} \to 0$, i.e. the case when $P_{\mathrm{RF}} \approx P_{\mathrm{DC},1}$:

$$R_{\mathrm{s,min}} = \frac{c_1 \mu_0^2 \Delta P_{\mathrm{DC},1}}{B_{\mathrm{s,pk}}^2}, \tag{6.33}$$

where $\Delta P_{\mathrm{DC},1}$ is the minimum resolvable heating power.

The smallest resolvable change in the heating power output by the Lake Shore 331 temperature controller is dictated by the heater noise level, which is 13 nW, which would result in a very low $R_{\mathrm{s,min}}$. However, this is not possible, given that the

heater power fluctuates by $\approx \pm 1\,\mathrm{mW}$ as previously stated. Therefore, at 4.2 K, with $B_{\mathrm{s,pk}} = 3\,\mathrm{mT}$, $R_{\mathrm{s,min}} = 0.5\,\mu\Omega$. Consequently, it will be desirable to reach higher fields to reduce $R_{\mathrm{s,min}}$, which will become especially important when measuring thin films with a lower R_{BCS}, such as Nb_3Sn. In the future, the facility will be housed in a radiation test bunker, which will allow higher RF powers to increase $B_{\mathrm{s,pk}}$.

It should be noted that there is practically no limit to the upper value of R_{s} that can be measured with this facility. For example, previous measurements of stainless steel samples at room temperature gave $R_{\mathrm{s}} = 0.17\ \Omega$ [218].

6.7 Summary and Outlook

The sample measurements made with the Choke Cavity during commissioning demonstrate that this facility can be used to characterise and compare the performance of superconducting thin films under RF conditions. Measurements with multiple samples, in particular the Nb/Cu samples deposited at different temperatures, have shown that it is possible to differentiate between samples deposited under different conditions. This means that the Choke Cavity facility is suitable for mass parameter deposition studies and will be the main tool at Daresbury Laboratory for optimising deposition processes in future studies.

Results have shown that measurements of $R_{\mathrm{s}}(T_{\mathrm{s}})$ and $B_{\mathrm{s,pk}}(T_{\mathrm{s}})$ are possible and repeated tests of Nb/Cu samples have demonstrated consistent measurements between cooldowns. In addition, measurements of $\Delta f(T_{\mathrm{s}})$ have shown the ability to estimate T_{c}. These measurements have also proven to be a useful indication of material properties such as the change in penetration depth as well as the level of sample impurities and performance. The main objective in the near future will be to show whether there is any correlation between RF measurements and results from DC tests on the same samples with other facilities previously highlighted in Section 3.1.3.

A key advantage of using the Choke Cavity is that samples can still be measured

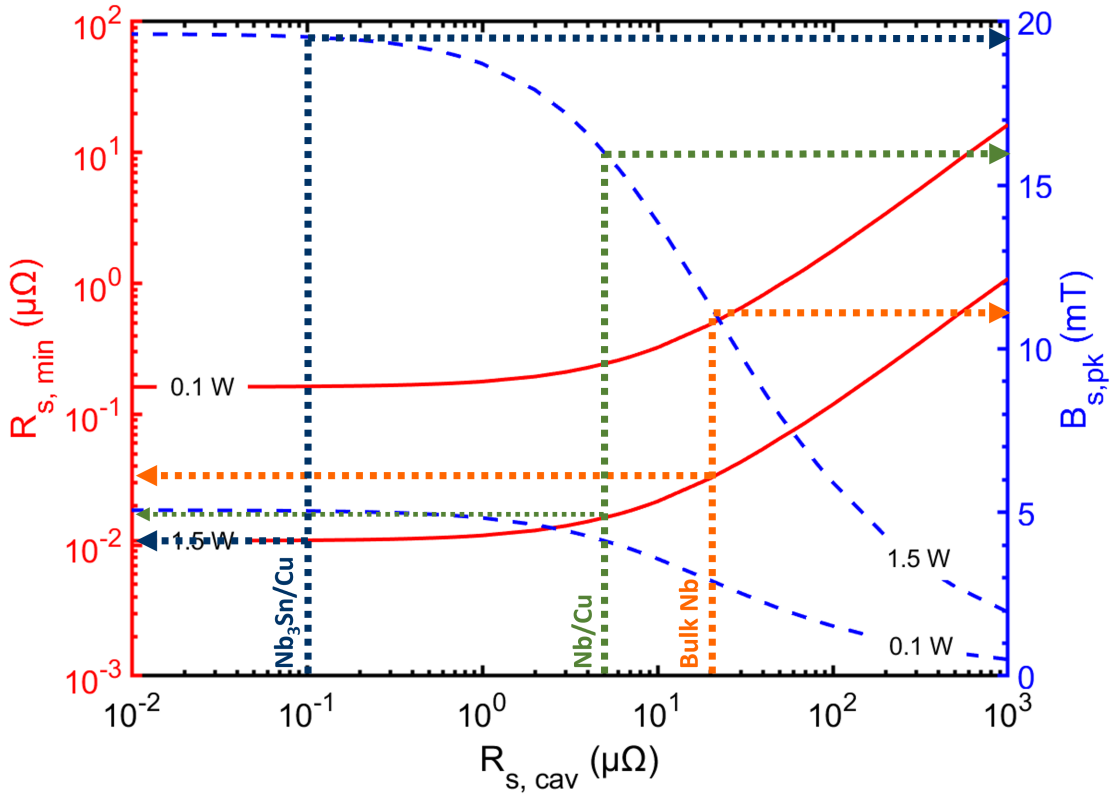

Figure 6.31: $R_{s,min}$ vs $R_{s,cav}$ and $B_{s,pk}$ vs $R_{s,cav}$ for two levels of cavity RF power with a bulk Nb sample. Dashed lines show $R_{s,min}$ and $B_{s,pk}$ for Choke Cavities made from bulk Nb (orange), Nb/Cu (green), Nb_3Sn/Cu (purple).

independently of the quality of the cavity, i.e. the cavity surface resistance ($R_{s,cav}$) does not affect the measurements of sample R_s. This is because the RF losses on the sample are always measured independently of the Choke Cavity. However, a reduction in cavity quality affects the maximum achievable $B_{s,pk}$ given that the ratio of RF power deposited on the sample to the cavity changes. This would then limit $R_{s,min}$ as given in Equation 6.33. Improvements to both $B_{s,pk}$ and $R_{s,min}$ are possible by increasing the input of RF power into the cavity or improving the quality of the Choke Cavity to reduce $R_{s,cav}$. Figure 6.31 illustrates, with a bulk Nb sample, how these improvements can result in a decrease in $R_{s,min}$.

One limitation of using a LHe-free system is that the maximum RF power is

dictated by the cryocooler capacity. For this system, the limit is 1.5 W (though this is slightly reduced due to static heat loads). Powers > 1 W will be achievable once this facility has been moved to a radiation-safe test bunker (scheduled by the end of 2024). Assuming a 1.5 W upper limit, with a bulk Nb cavity operating close to R_{BCS} (i.e. from a full chemical and heat treatment), it is theoretically possible to increase the peak field to $B_{\mathrm{s,pk}} \approx 11\,\mathrm{mT}$, resulting in $R_{\mathrm{s,min}} \approx 0.03\,\mu\Omega$ (represented by the orange lines). In addition, an investigation into the use of TF Nb/Cu Choke Cavities is ongoing. This will allow for slight gains at maximum power: a TF Nb coated Cu choke cavity could reach $B_{\mathrm{s,pk}} \approx 16\,\mathrm{mT}$ and $R_{\mathrm{s,min}} \approx 0.02\ \mu\Omega$ (represented by the green lines) while a TF Nb_3Sn/Cu cavity could reach $B_{\mathrm{s,pk}} \approx 19$ mT with $R_{\mathrm{s,min}} \approx 0.01\ \mu\Omega$ (represented by the purple lines). Further gains might be possible through the use of higher capacity cryocoolers and by using pulsed RF power to increase $B_{\mathrm{s,pk}}$ further. A summary of the performance capabilities after facility commissioning compared to what is achievable with future upgrades is shown in Table 6.5.

Table 6.4: A summary of the Choke Cavity uncertainty contributions.

	Variable	Measurement	Contribution	Syst.	Rand.	Total
$B_{\mathrm{s,pk}}$						**14**%
	Q_{t}	$\lvert S_{11}\rvert$, $\lvert S_{21}\rvert$	VNA	0.3 dB		20%
			Cable loss	0.3 dB		
			External noise		0.05 dB	
			VNA Settings		< 1%	
			Microphonics		< 0.2 dB	
		Q_{L}	Instrument	1 Hz		7%
			VNA Settings		< 1%	
			Microphonics		< 2.5 kHz	
			Repeatability		< 5%	
	P_{t}		Power meter	0.16 dB		20%
			Cable Loss	0.3 dB		
			Fluctuations		0.05 dB	
	$B_{\mathrm{s,pk,CST}}$		Thermal	1.6%		1.6%
			Tolerance	0.2%		
R_{s}						**14**%
	Q_{t}		As above.			20%
	P_{t}		As above.			20%
	P_{RF}	I_{DC}	Multimeter	0.3%		< 1%
		V_{DC}	Multimeter	0.2%		
		P_{DC}	Heater noise		50 µV+0.01%	
			Fluctuations		0.5%	
	$c_1/B^2_{\mathrm{s,pk,CST}}$		Thermal	3.2%		3.2%
			Tolerance	0.4%		
	Repeatability		vs T_{cav}		< 1%	
			vs $B_{\mathrm{s,pk}}$		< 2%	
			without removal		< 1.5%	
			with removal		< 2.2%	
			repeated		< 5.5%	
			cooldown			
$\Delta\lambda$						**4**%
	Δf		Instrument	1 Hz		3.2%
			Microphonics		< 2.5 kHz	
	G_{s}		Thermal	3.2%		3.2%
			Tolerance	0.3%		
T_{s}			Cernox	< 10 mK		$< \mathbf{45}$ mK
			Vert. ΔT	< 20 mK		
			Horiz. ΔT	< 32 mK		
			Fluctuations		< 5 mK	
			Cernox Diff.		< 5 mK	

Table 6.5: Summary of the performance of the Choke Cavity facility after commissioning and with future upgrades.

	Parameter	Present state	With upgrades
Facility	Cavity frequency	7.8 GHz	
	Total time required/sample	2 days	
	Temperature range	$4 - 20$ K	
	Maximum CW RF power	1 W	1.5 W
Measurements	Maximum peak field on sample	3.0 mT	20 mT
	Minimum resolvable R_s	0.5 μΩ	0.01 μΩ
	Typical uncertainty in R_s	14%	

Chapter 7

Thin Film Sample Studies

The main advantages of the Choke Cavity are:

- Two day test per sample meaning rapid RF characterisation and comparison of up to three planar samples per week.
- Using a versatile, cost-effective sample design that can be used for additional cryogenic measurements and material analysis with minimal additional cost and effort.
- Operation in a TM_{010} mode whilst minimising RF leakage with chokes.
- Direct measurements of sample R_s which is not dependent on the cavity R_s.

These benefits mean that the Choke Cavity can provide the main tool for multi parameter optimisation of deposition parameters at Daresbury Laboratory. Previously, thin film optimisation has mainly used the DC techniques discussed in Section 3.1.3.

To demonstrate what can be achieved with the Choke Cavity facility, two sets of thin film sample studies on Cu substrates were performed:

- Nb - the effect of the deposition temperature.
- Nb_3Sn - the effect of target power and Nb buffer layers.

This chapter presents a brief brief introduction to sample preparation the range of additional charaterisation techniques used followed by results from the sample studies.

7.1 Substrate Preparation

7.1.1 Bulk Niobium

After bulk Nb cavity machining, the surface layer is damaged. For the production of cavities, especially, processes such as rolling Nb sheets and stamping the half-cells, can worsen any defects, leading to scratches and bumps on the surface. Given that RF only penetrates $\sim$ 10s of nm into the sample surface, these characteristics will lead increase to an in R_{s}. As detailed in Section 2.3.2, contamination can lead to RF performance limiting effects such as Q-disease, field emission and thermal quenches which increase R_{s} (reducing Q_0) and reduce the maximum E_{acc}.

Cavity treatments start with either physical or chemical polishing to remove the damaged/pollution layer. Physical polishing, for example centrifugal barrel polishing (CBP) or tumbling, rotates the cavity with material inside to polish the surface as the media moves over it [219]. Chemical polishing, such as buffer chemical polishing (BCP) or electropolishing (EP) [220, 221], uses chemical reactions to remove material. Both physical and chemical processes are supplemented with high pressure rinses (HPR) using ultrapure water (UPW) to remove contaminants. With CBP, for example, there is a risk of embedded particles in the cavity surface if not performed carefully. In addition to the dangerous chemicals used for chemical polishing, one issue can arise from hydrogen pollution in the bulk of the material, which can lead to Q disease. It is therefore also necessary to degas the hydrogen from the cavity by heating to temperatures $> 600\,^{\circ}\mathrm{C}$ in a UHV system [222]. After, a light chemical etch to remove a few μm of material is often performed to remove any lossy hydrogen at the surface. Sometimes this is followed by a low temperature bake between $100 - 150^{\circ}\mathrm{C}$ to diffuse oxygen from the lossy niobium pentoxide (Nb_2O_5)

layer on the Nb surface into the bulk.

Most of these treatment processes will not completely remove impurities and may even introduce additional impurities. This means that they are best performed in combination to try and produce the highest quality surface with the optimal RF performance. If using bulk Nb as the substrate for a thin film, the main purpose of the treatment processes is to reduce the surface roughness of the material to improve film adhesion whilst minimising RF losses. However, degassing with heat treatments and removing particulates are still important steps.

For the bulk Nb sample used during facility commissioning in Chapter 6, a BCP was performed at INFN followed by two separate heat treatments at Daresbury Laboratory. Due to the lack of readily available facilities, the order of these treatments performed were non-standard as it was not possible to perform a light BCP after the 600 °C bake to remove potential surface contaminants. Details of the treatments used are presented in this section.

7.1.1.1 Heavy BCP

A BCP was chosen for bulk Nb polishing because it is a simpler process than EP as it does not require electrodes, provides a faster etch rate and has less hydrogen contamination [37]. This process has also proven to be well controllable and very effective for many decades [223]. However, for future use of bulk Nb as a thin film substrate, EP would be a superior process to provide a smoother surface [224]. The BCP uses a mixture of hydrofluoric acid (HF), nitric acid (HNO_3) and phosphoric acid (H_3PO_4). HNO_3 reacts aggressively with Nb, oxidising it to form Nb_2O_5, whilst the HF dissolves the oxide and H_3PO_4 acts a buffer to control the reaction rate. For the Nb disk, these chemicals were used in a volumetric ratio of 1:1:2 as this provides a more controllable etching rate [223]

Before chemical treatment, the sample was washed by ultrasonic cleaning with an aggressive soap solution. The BCP process was performed at INFN for a total of 60 minutes using a simple setup, shown in Figure 7.1. An estimated removal of

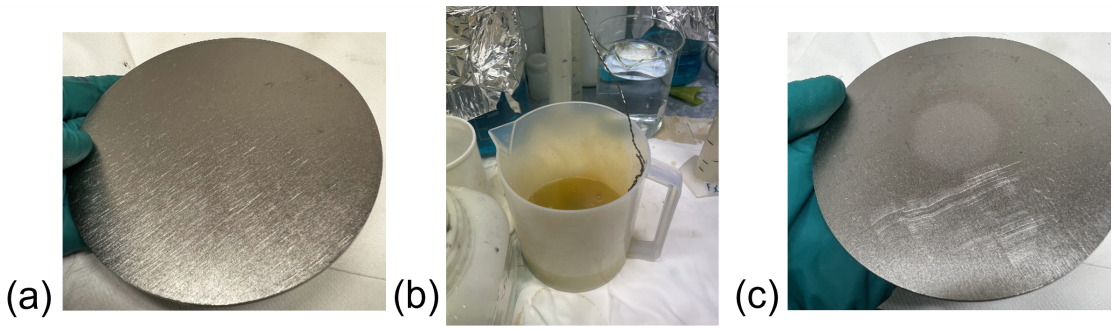

Figure 7.1: The BCP process for the bulk Nb disk: (a) un-polished disk, (b) disk submerged in the BCP solution, (c) post-polished disk. Image courtesy: E. Chyhyrynets (INFN).

100 µm of material was calculated based on previous calibrations.

7.1.1.2 Heat Treatments

After chemical treatment, the Nb disk was cleaned in an ultrasonic bath with UPW prior to being vacuum packed in a clean room and returned to Daresbury Laboratory. At the time of return, it was not possible to perform a high temperature bake. Therefore, a 120 °C bake was performed in UHV for 48 hours using the facility described later in Section 7.2. A low temperature bake between $100 - 150$°C has been shown to reduce both the BCS resistance and the high-field Q-drop that has not been associated with field emission [225]. It is thought that a reduction in BCS resistance of up to 50% at 4.2 K is due to oxygen diffusion from the Nb_2O_5 surface to the bulk, leading to a reduction in the electron mean free path and a modification of the oxide structure. Recent studies also associate a low temperature bake with the decomposition of lossy hydrides within the Nb surface and released hydrogen being trapped by oxygen at vacancies (i.e. lattice defects) forming vacancy-nanohydride complexes [226], thus preventing the formation of nano-hydrides during cooldown. Later, the sample was heated twice at 600 °C, both times for 6 hours, in the same facility under UHV conditions.

7.1.2 Copper

The 100 mm diameter Cu disks used for thin film depositions were cut from a sheet of 3 mm thick rolled OFHC Cu at the Daresbury Laboratory workshop.

Similarly to bulk Nb, the quality of the Cu substrate will affect the RF superconducting properties of a thin film deposited on top [227]. Therefore, all disks had to be polished prior to deposition. Any surface cracks, defects, roughness and impurities can negatively affect the performance of a deposited thin film. Substrate preparation is one of the main research areas in thin film technology. For Cu substrates (both planar and cavities), EP has been the typical method to reduce defects and surface roughness [80, 228]. However, this technique requires harsh mixtures (HF and H_2SO_4 for Nb and H_3PO_4 and butanol for Cu) that present risk to both the user and the environment. As detailed in Section 2.4.1, alternative greener solutions, such as plasma electrolytic polishing (PEP), are being developed using more environmentally friendly diluted salt solutions [85, 86].

At Daresbury Laboratory, a lack of chemical polishing ability at the time of these studies meant that alternative solutions were needed for Choke Cavity sample preparation in order to prepare a high number of samples in a short period of time. For the thin film on Cu samples measured with the Choke Cavity, the goal was to optimise the deposition parameters for future RF cavities and not to evaluate the effect of different polishing techniques. Therefore, the substrate preparation technique chosen had to be highly reproducible to ensure that reliable comparisons could be made between the thin film performance. However, the effect of different polishing techniques more applicable to cavity preparation should form the basis for future studies once the deposition parameters have been optimised.

7.1.2.1 Diamond Turning

Mechanical polishing was decided for the Cu substrate disks as this can be performed using simple processes without the requirements for chemical processes. The technique chosen was diamond turning (DT), performed at STFC RAL Space.

DT is a process that uses a high-speed, precision cutting tool with a single-point diamond tip. It is typically used for high-precision machining of objects that require surface finishes at the level of nanometres to sub-nanometres, e.g. optical components. This process was chosen because of the high-quality, repeatable surface finishes that can be achieved in a short period of time. This made it suitable for preparing many substrates to match the high-volume thin-film preparation and testing provided by the Choke Cavity as well as the requirement for consistent and reliable thin films for sample tests. Having substrates with a consistent surface finish would remove any question marks about the effect of surface preparation on the superconducting measurements, ensuring that the reported results are due to a change in the deposition parameters only.

Each disk was polished for 1 hour using a single-point DT lathe. Isoparaffin was used as the lubricant to control the temperature of the tip and significant deviations in the roughness of the Cu surface that would be caused by temperature deviations. For the DT process, each Cu disk was mounted to the lathe. The lathe is made to rotate at high speeds from 5000 to 18000 rpm whilst the cutting tool is in contact with the Cu surface. During rotation, the tool moves along the horizontal and vertical axes of the disk to cover the entire surface. No additional chemical polishing was performed, however the disks were rinsed with acetone and isopropanol prior to loading in the deposition facility to remove any potential contamination from the isoparaffin. A summary of the DT process is shown in Figure 7.2 showing the quality of a Cu disk before and after polishing.

Roughness measurements of the substrates before and after polishing were performed with a white-light interferometer (WLI). An example of Cu disk roughness measurements before and after DT is shown in Figure 7.3. This shows the removal of machining artifacts after the DT process, resulting in a two orders of magnitude lower roughness. The typical roughness of an unpolished Cu disk was measured to be $S_a \approx 230\,\text{nm}$ and $S_q \approx 350\,\text{nm}$, consistent with typical values for rolled Cu. Measurements of a random selection of five polished disks showed that they had

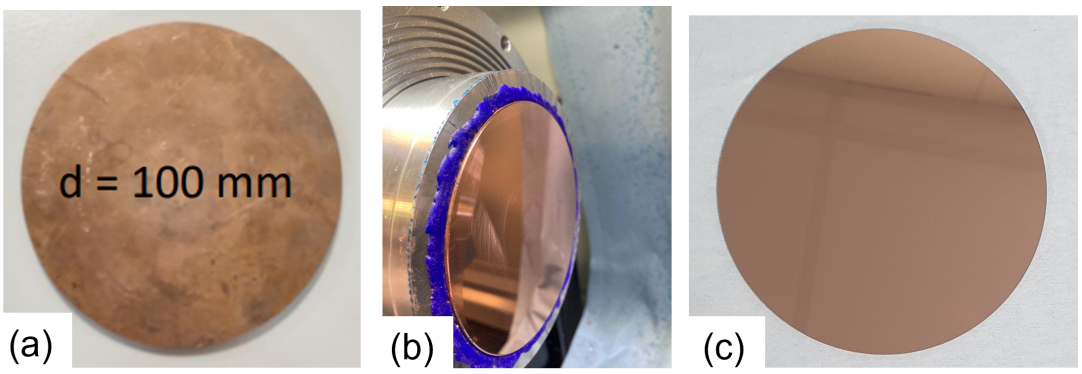

Figure 7.2: The DT process for a Cu disk: (a) un-polished disk, (b) disk secured to the rotating DT lathe, (c) post-polished disk. Image (b) courtesy: M. Beardsley (STFC RAL Space).

been machined to a very high standard with $S_a = 2 - 3\,\text{nm}$ and $S_q = 5 - 6\,\text{nm}$, despite machining grooves being visible after the DT process.

7.1.2.2 Metallographic Polishing

An alternative technique for physical polishing has been developed at IJCLab. The motivation was to provide a cost-effective, safe alternative to lengthy and potentially harmful processes such as BCP and EP [87–90]. This technique, known as metallographic polishing (MP), aims to be a more environmentally friendly method for the preparation of both Nb and Cu substrates [229]. For 1.3 GHz cavities, this technique has been trialled to polish a Nb disk prior to cavity formation [90].

As detailed in Figure 5.11, two different sample and sample holders were designed. Given the added complexity of the bolt holes in the Design 2 sample, it was decided that the DT would not be able to polish the entire surface. Instead, this sample design, along with some disks from Design 1, were treated by MP.

The MP process used a MASTERLAM 1.0 (LAM PLAN production) machine at IJCLab. The recipe for this process consisted of five steps [89]. Each step used gradually smaller diamond abrasives ranging from 125 µm to 1 µm in the final step pressed against the sample with a force up to 300 N. Both the sample holder and the

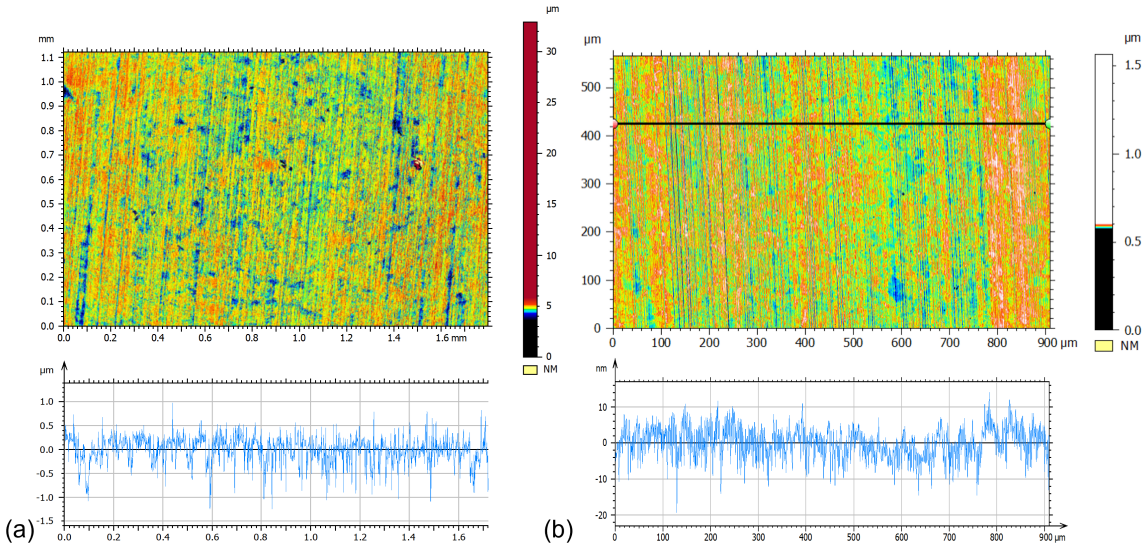

Figure 7.3: Roughness profiles of a typical Cu disk: (a) before DT, (b) after DT.

polishing disks were rotated at up to 150 rpm and each step was performed at times up to 40 mins. UPW cleaning, deionised water/ultrasonic bath cleaning and N_2 gun drying were performed after each step. The total amount of material removed was $130 - 140\,\mu m$. The results of the MP process are shown in Figure 7.4.

As with DT Cu, surface roughness was measured using a WLI. The results in Figure 7.5 show a significant removal of the machining defects from the surface after polishing. The roughness improved significantly from $S_a \approx 230$ nm to $S_a \approx 6$ nm after polishing with an improvement of $S_q \approx 350$ nm to $S_q \approx 20$ nm. Although no machining grooves were visible after polishing, both measurements are higher than those for the DT process with larger variations in roughness height. In addition, it is possible that the larger features in Figure 7.5(b) are particulate inclusions in the surface from the polishing disks, which are not observed after DT. Unfortunately, because of time and staff availability, further polishing steps and development were not possible in the time frame for the MP Cu process. Reduction of the abrasive size to 0.25 µm in a sixth step can potentially lead to reduced roughness and should be investigated. Despite this, at present, this process is more likely to be easier to scale up to polishing larger disks prior to cavity forming. The effect of DT large

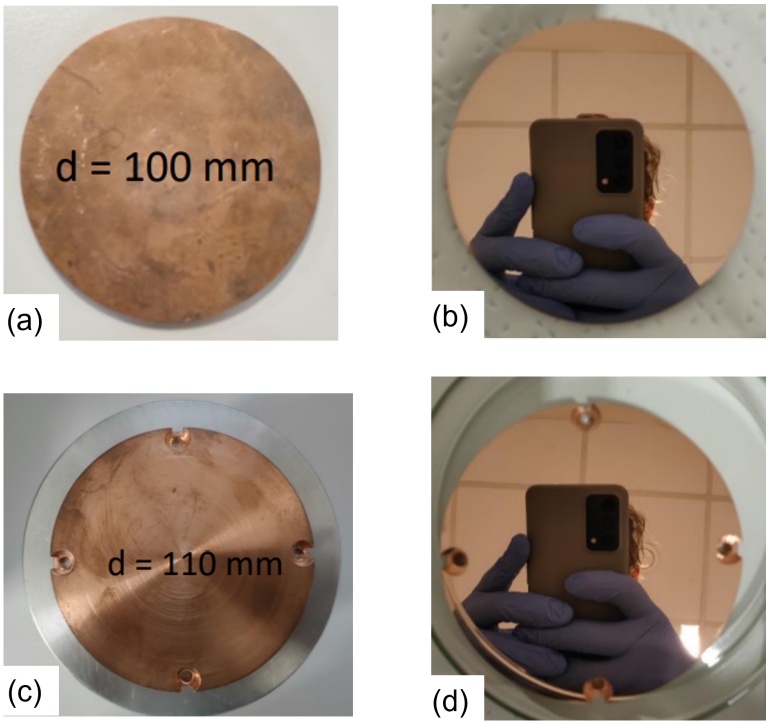

Figure 7.4: MP of Cu disks before and after polishing. Design 1: (a) before MP, (b) after MP; Design 2: (c) before MP, (d) after MP. Image courtesy: O. Hryhorenko (IJCLab).

disks prior to cavity formation after should also be considered in the future.

7.2 Thin Film Deposition

All depositions presented in this chapter and previously in Chapter 6 were performed using the physical vapour deposition (PVD) technique. This technique works by vaporising material from one or more solid or liquid targets to produce a vapour that then travels through a low-pressure plasma before condensing onto the substrate material to form the thin film of the target material.

The main PVD process used for all of the sample depositions is magnetron sputtering. A magnetron consists of the target material (either planar or cylindrical) with magnets mounted underneath. A brief outline of the deposition process is:

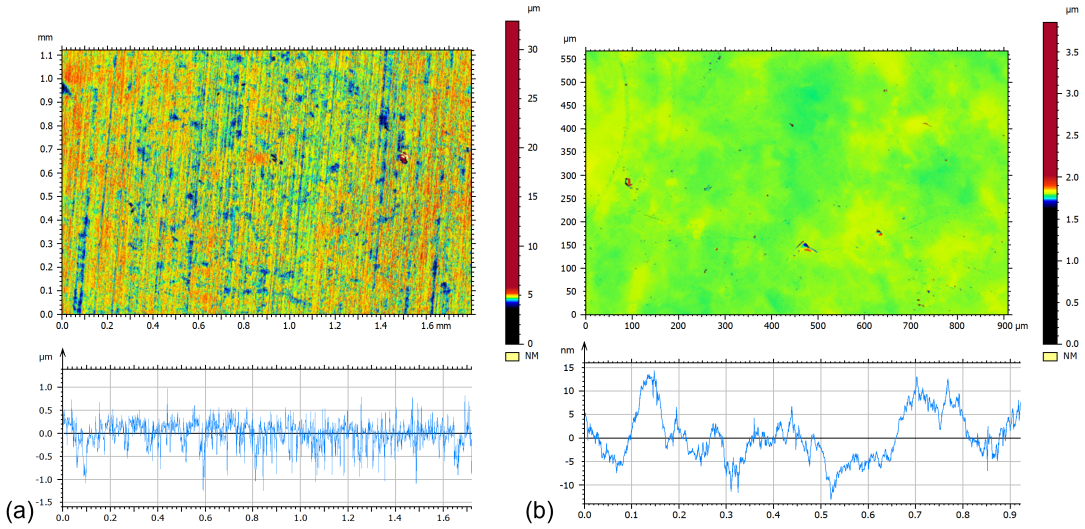

Figure 7.5: The topography image and line profile measured with a WLI showing the roughness of a typical Cu disk: (a) before MP, (b) after MP.

1. A sample is loaded into a vacuum chamber which is then pumped down to UHV conditions ($< 10^{-9}$ mbar).

2. An inert gas (typically argon or krypton) is injected into the vacuum chamber, raising the pressure to $10^{-3} - 10^{-1}$ mbar.

3. A high negative voltage is applied across the target, initiating the field emission of electrons into the vacuum.

4. If the electrons have sufficient energy, they can ionise the inert gas atoms, creating positive ions and secondary electrons. The vacuum now consists of a plasma with positive ions and electrons.

5. These positive ions are accelerated towards the negatively charged target and will cause atoms from the target surface to be ejected into the vacuum upon collision, if the ions have sufficient energy.

6. The magnets underneath the target confine the electrons near the surface to concentrate the plasma close to the target where it is needed most and increase the deposition rate.

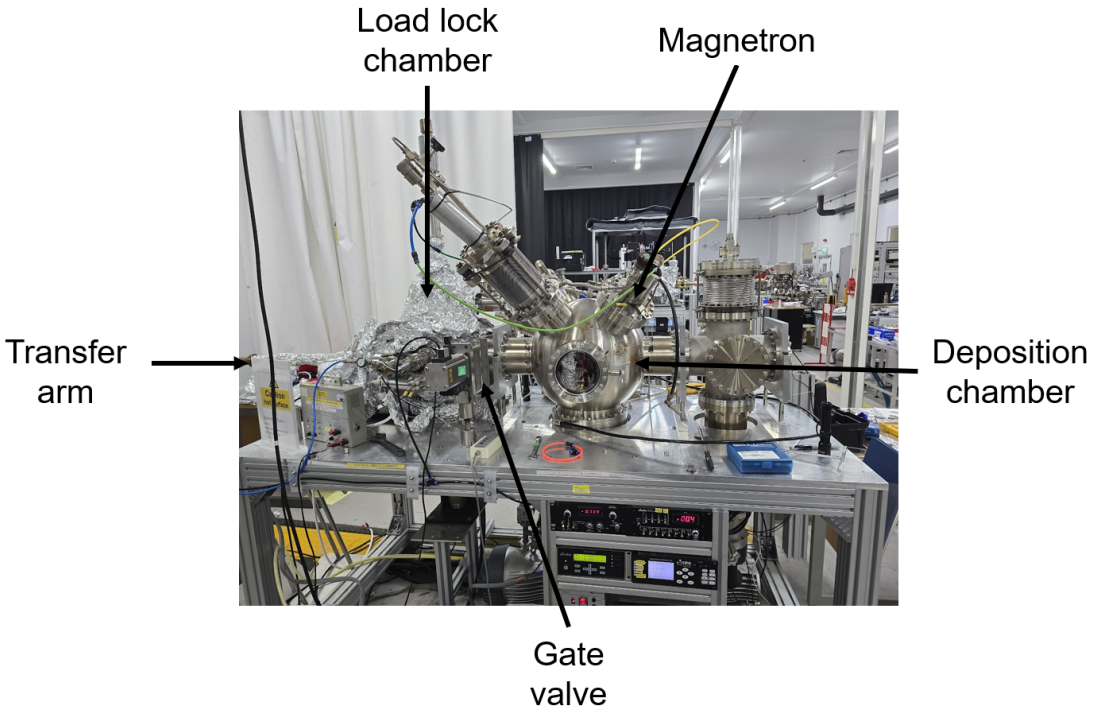

Figure 7.6: The facility at Daresbury Laboratory for planar sample depositions.

7. Thin film deposition, whereby momentum transfer between the incident plasma ions and target atoms provide enough energy for the target atoms to travel to the substrate surface and start forming the thin film.

Both DC and AC voltages (using an RF power supply) can be applied to the target using this method. All the samples presented in Chapters 6 and 7 use DC power supplies via one of two methods:

- Direct current magnetron sputtering (DCMS) - where a constant voltage is applied to the target.

- High power impulse magnetron sputtering (HiPIMS) - which is a type of pulsed DCMS that delivers very short (10s of μs), high frequency ($\sim$ kHz), intense electrical pulses to the target up to three orders of magnitude higher peak power density compared to DCMS [230].

The HiPIMS technique can create a plasma much denser than that generated by DCMS. This can result in denser and smoother coatings with better film adhesion, coverage, lower substrate damage and fewer voids. It may allow for a lower substrate deposition temperature [230]. However, this technique has some disadvantages compared to DCMS. It requires more expensive power supplies, reduces the deposition rate, and can lead to arcing due to high peak voltages.

For all depositions, a previously built custom deposition facility was used at Daresbury Laboratory [113], shown in Figure 7.6). This facility allows for up to seven substrate disks ($50 - 100$ mm diameter) to be loaded at any one time. It is possible to vary multiple DCMS and HiPIMS parameters as well as sample temperature, discharge gas and pressure and deposition time. Having a newly commissioned high-throughput Choke Cavity for RF testing means that the rate of sample testing can now match the rate of sample production.

The main deposition parameters varied were the substrate temperature and the target power. The samples that required heating (excluding the 25 °C/room temperature samples) were preheated at their deposition temperature for 24 hours to outgas and ensure thermal equilibrium. The set temperature was maintained during the deposition. It was not possible to measure the temperature of the sample directly during a deposition because of the rotation of the sample and the risk of surface damage. Therefore, the sample temperature was calibrated during a separate heating cycle with a Cu disk heated at each heater current setpoint for 24 hours and temperature measured with a thermocouple pressed against the centre of the sample.

7.3 Sample Measurement Techniques

An important step after RF measurements was to measure the same samples using superconducting DC techniques and determine whether there is any relation between the results of different measurement techniques. In addition, some surface analysis techniques were performed to understand whether the physical and

chemical structure of the films could be related to the results from superconducting measurements. These measurements used cut outs from the 100 mm sample disks which assumed that the films are uniform across the entire disk. The samples were cut using electrical discharge machining (EDM) in the Daresbury Laboratory workshop, courtesy of S. Bibby-Trevor (STFC).

7.3.1 DC SQUID Magnetometry

A magnetometer is an instrument that is used to measure the behaviour of samples in magnetic fields. Specifically, it is used to measure the magnetic dipole moment ($\boldsymbol{m}$) of the sample. A commonly used laboratory magnetometer is the vibrating sample magnetometer (VSM).

A VSM typically uses a superconducting quantum interference device (SQUID) to measure the sample magnetic moment. A SQUID is a highly sensitive magnetometer that can detect weak magnetic fields. This makes it highly sensitive to small changes in magnetic flux proportional to the change in $\boldsymbol{m}$ of the sample.

The basic principle of operation of a VSM is illustrated in Figure 7.7:

1. A sample, mounted on a rod, is placed between four detection coils (gradiometer) mounted inside a cryostat.

2. A constant magnetic field is applied, and the sample is moved through the test chamber to calibrate the position of the sample.

3. After calibration, a computer-controlled motor moves the sample up and down at low frequencies (10s of Hz) within the detection coil whilst a constant magnetic field is applied. The sample behaves as a point source magnetic dipole. As it moves up and down in the magnetic field, it induces an electric field in the detection coils, generating a small current.

4. The SQUID is coupled to the coils. It is extremely sensitive to small current signals and converts the current to an output voltage.

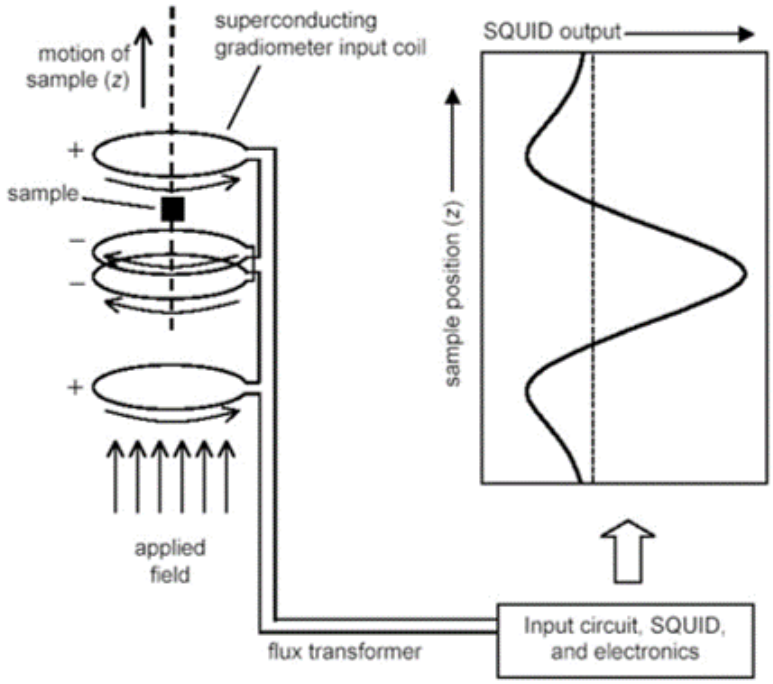

Figure 7.7: A schematic of a SQUID VSM [231].

5. The current generated in the coils is proportional to $\boldsymbol{m}$. The computer analyses the resulting voltage from the SQUID as a function of sample position to calculate $\boldsymbol{m}$.

The main instrument used was the Quantum Design MPMS3 SQUID magnetometer, based at the RAL material characterisation laboratory. The setup for a sample measurement is shown in Figure 7.8. For each test, a separate plastic drinking straw was used to mount the sample. Samples of $5 \times 5\,\mathrm{mm}^2$ were used during mounting, it was vital to ensure the correct position of the sample and parallel alignment with the walls of the straw. If the sample is not parallel to the applied magnetic field, early flux penetration may occur, thus increasing the uncertainty of measurement. The sample straw was mounted on a carbon fibre sample holder rod before being inserted into the cryostat. Inside the system, each sample was orientated the same as shown in Figure 7.7. An automated procedure with an applied magnetic field was performed to measure the sample $\boldsymbol{m}$ prior to a full measurement run. This ensured a proper sample centering between the detection

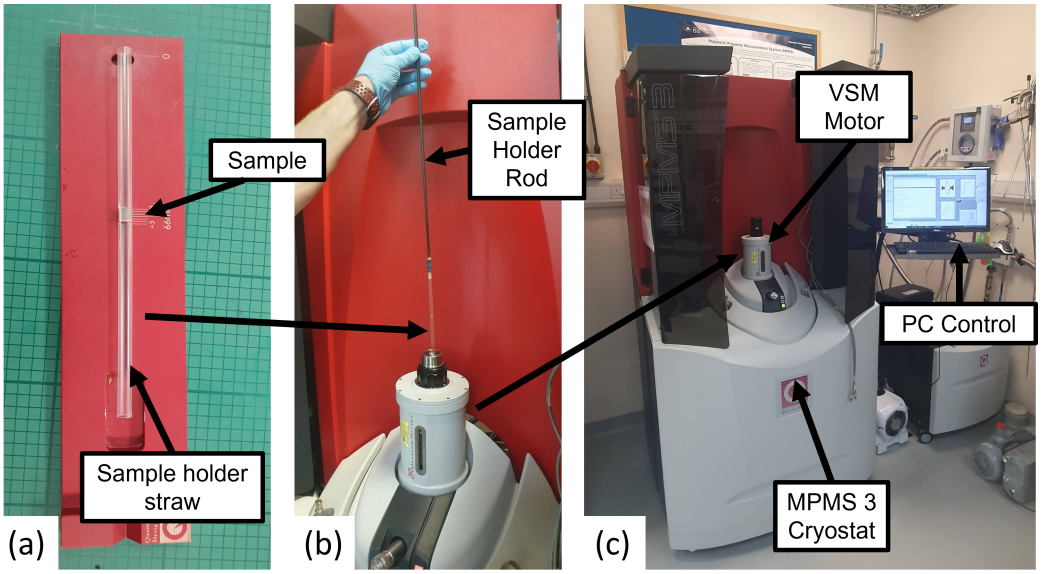

Figure 7.8: The experimental setup and process for a sample measured with the MPMS3: (a) sample mounting and alignment, (b) sample attachment and loading with a sample holder rod, (c) the MPMS3 at RAL.

coils. After alignment, the sample was cooled to the base temperature in < 30 minutes.

The MPMS3 has the potential to operate at magnetic fields up to 7 T and temperatures in the range $1.8-400$ K. It can be used to measure $\boldsymbol{m}$ with sensitivity $\leq 10^{-8}$ emu as a function of the sample temperature or magnetic field. Typical sample measurements were performed as a function of sample temperature from $20-4.2$ K at fixed magnetic fields. The primary use of the VSM was for measurements of the superconducting transition, allowing for calculation of the critical temperature (T_c^{VSM}). This could be compared to measurements of T_c^{RF} from the frequency shift measured by the Choke Cavity, detailed earlier in Section 6.3.1.

For some samples, this technique was also performed on the Quantum Design PPMS measurement system at IEE Bratislava courtesy of E. Seiler and R. Ries (IEE) for further measurement confirmation. For this system, samples of $2.5 \times 2.5\,\mathrm{mm}^2$ were used. Medium-fine sandpaper was used to reduce the thickness to ≈ 1 mm in order to fit the samples into the sample holder.

7.3.2 White-Light Interferometer

As discussed previously, substrate preparation is vital prior to thin film deposition. The level of preparation influences how rough or smooth the surface is, i.e., its roughness. The roughness of the surface ultimately dictates the roughness of the deposited film. Rough surfaces may lead to local field enhancement at some areas of the film, increasing R_s. This could reduce the critical field, leading to early flux entry and early quenching. For a thin film, higher surface roughness has been shown to trigger early vortex penetration in Nb film samples, which may lead to a reduction in E_{acc} [232]. Another study showed a reduction in critical current with increased roughness on Nb thin film strip-line circuits, leading to flux penetration at lower currents, whilst T_c remained constant [233]. However, there is limited data on the minimum required level of roughness for SRF thin films on Cu.

By definition, roughness is the measurement of the deviations of the normal vector of a real surface from its ideal form. It is possible to quantify the level of roughness by measuring irregularities on the surface of the material. The main roughness parameters compared for the samples are:

- S_a = arithmetic mean average.
- S_q = root mean square average roughness.

S_a is a calculation of the absolute average of surface height variations from the mean. S_q is the square root of the average of the squared values of the height variations from the mean. S_a provides a general roughness that is less affected by extreme peaks and troughs, whilst S_q is more sensitive to these irregularities. For thin film SRF, these irregularities can be regions of higher RF losses.

The roughness of the samples was measured using a white-light interferometer (WLI). This technique was used because it does not require physical contact with the sample surface, reducing the chance of film damage before additional characterisation. The basic principle of a WLI is as follows:

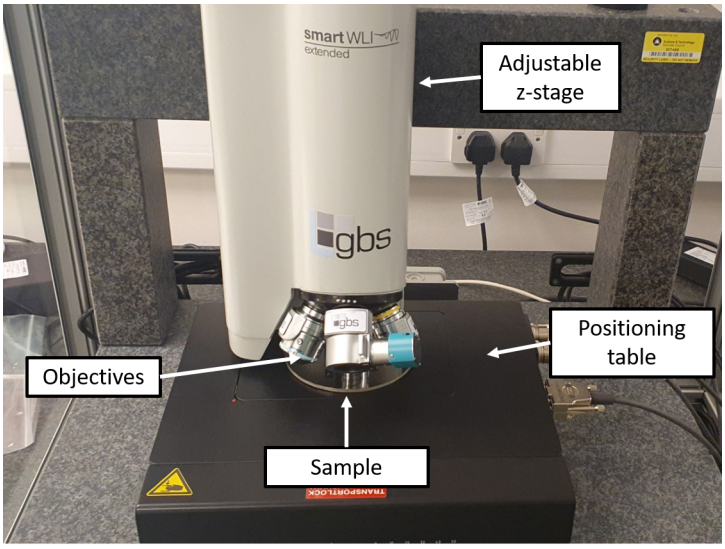

Figure 7.9: The experimental set up for the WLI at Daresbury Laboratory.

1. A light beam passes through a beam splitter and is split into a reference beam and a measurement beam.

2. The reference beam reflects off a mirror whilst the measurement beam reflects off the sample.

3. The two reflected beams then recombine to create an interference pattern on a camera.

The resulting interference pattern can give information about the sample surface. Changes in roughness will change the optical path lengths, thus creating an interference pattern due to a phase difference with the reference beam. The intensity and spacing of the inteference pattern gives details about the height of the peaks and troughs of the sample, thus allowing the roughness parameters to be calculated.

The WLI used was the GBS SmartWLI at Daresbury Laboratory, as shown in Figure 7.9 which allows measurements of S_{a} and S_{q}. Samples were measured prior to cutting. For all measurements, a 20x objective was used that allowed areas of $909.4\ \mu\mathrm{m} \times 567.5\ \mu\mathrm{m}$ to be measured. Typically, at least 7 measurements were taken for each sample at 10 mm intervals from $20-80$ mm from the centre of the sample to

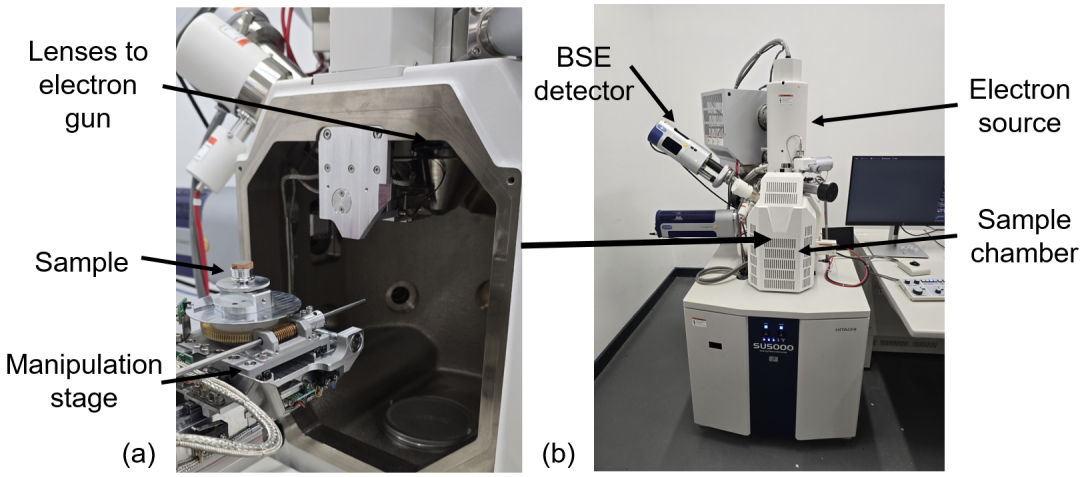

Figure 7.10: The experimental set up for the Hitachi SEM at Daresbury Laboratory: (a) a sample being loaded, (b) some of the features of the SEM.

capture the areas most sensitive to RF heating. The averages S_a and S_q were then calculated. For most samples, this number of measurements gave an approximate idea of the overall roughness of the sample. Due to the time-consuming nature of the measurement procedure, it was not possible to scan each sample in more detail.

7.3.3 Scanning Electron Microscopy and Energy Dispersive X-ray Spectroscopy

Analysing the samples with much higher resolution than the WLI requires a Scanning Electron Microscopy (SEM). This can produce detailed, high-resolution images of the morphology of the sample surface down to a few nm. It works by firing an electron beam from an electron gun on the sample surface. Lenses are used to focus the beam to scan the sample with high resolution. For this, the sample is in a vacuum chamber to prevent electron interactions with other atoms. As the electron beam scans the sample, the electrons interact with the sample atoms. This results in a number of electron-matter interations being produced, including characteristic X-rays, secondary electrons (SE), back-scattered electrons (BSE) and transmitted electrons. Detectors in an SEM mainly detect SE and BSE to create

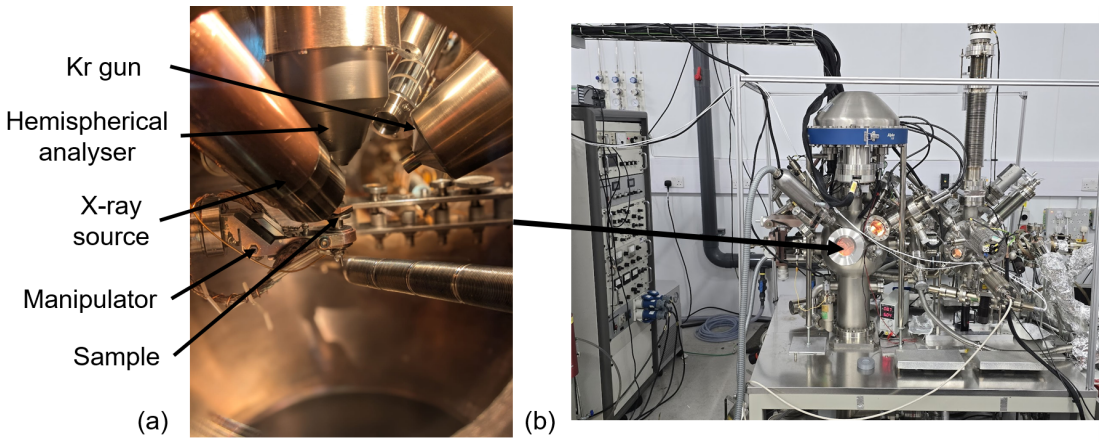

Figure 7.11: The XPS facility at Daresbury Laboratory: (a) a loaded sample and required instruments, (b) the facility.

an image of the sample. The SE are emitted due to inelastic collisions from the top of the sample. BSE are beam electrons due to elastic scatting from deeper within the sample. These detectors can be combined with energy-dispersive X-ray spectroscopy (EDS) to measure the energy of characteristic X-rays to identify and map the elemental composition of the sample.

The SEM used was a Hitachi SU5000, shown in Figure 7.10, at Daresbury Laboratory, courtesy of C. Benjamin (STFC). This is capable for rapid sample exchange and maximum resolution $\sim 1\,\text{nm}$. It can perform SE and BSE imaging as well as EDS. For analysis, samples of $10 \times 10\,\text{mm}^2$ were used. For cross-sectional SEM analysis, each sample was milled with an Ar ion beam using an ArBlade5000 before loading into the SEM.

7.3.4 X-Ray Photoelectron Spectroscopy

To study the surface layer of the samples, X-ray photoelectron spectroscopy (XPS) was used. This technique studies the elemental composition and chemical state up to a few 10s of atomic layers thick. The technique works by irradiating the sample surface with a beam of X-rays of known energy (E_{photon}). By the photoelectric effect, photoelectrons are emitted from the sample surface and the kinetic energy

(E_{KE}) and electron count (intensity) is measured by an electron energy analyser. This energy is related to the electron binding energy (E_{BE}) by

$$E_{\mathrm{BE}} = E_{\mathrm{photon}} - (E_{\mathrm{KE}} + \phi), \tag{7.1}$$

where ϕ is the work function of the atom.

By measuring the kinetic energy and intensity of photoelectrons emitted, a spectrum of intensity as a function of binding energy can be produced. Each element has a unique set of core electron binding energies and some core levels exhibit spin-orbit splitting. Therefore, from the XPS spectra produced, it is possible to identify the elements present in the surface layers of the sample.

As with the SEM measurements, a $10 \times 10\,\mathrm{mm}^2$ sample cut was measured at Daresbury Laboratory, courtesy of C. Benjamin (STFC). This was loaded into a custom-built UHV XPS analysis chamber and mounted on a manipulator stage, shown in Figure 7.11. A non-monochromated 1486.6 eV Al Kα X-ray source is used and a Thermo Alpha 110 hemispherical energy analyser is used to measure the electron energies. The samples were initially measured as loaded. A 5 keV Kr ion source was then used to sputter the surface for 4 hours to remove any potential contaminants on the sample surface before remeasuring. Data analysis was provided by the CasaXPS software package [234].

7.3.5 Secondary Ion Mass Spectrometry

Another technique used to study the surface of the samples is secondary ion mass spectrometry (SIMS). This technique is often used to detect H, C and O at low concentrations $< 5\%$, which is not detectable in XPS. Both H and O are especially problematic for SRF surfaces as they can increase RF losses. SIMS also allows depth profiles of a few μm to be studied with a high elemental detection sensitivity of ppb to ppt level, allowing trace contaminants to be detected throughout the film. This makes it the most sensitive surface analysis technique.

The technique works by focussing a beam of primary ions onto a sample to sputter

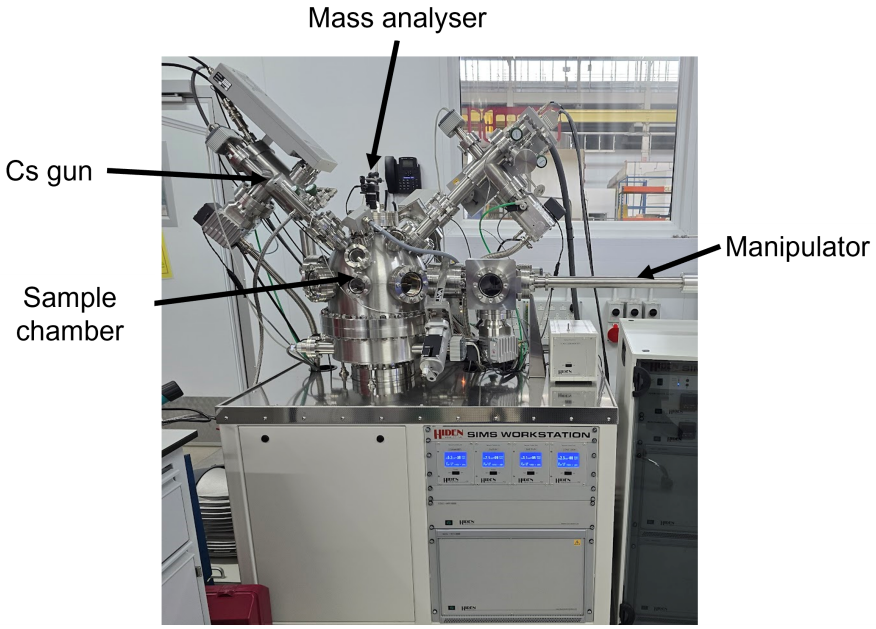

Figure 7.12: The SIMS facility at Daresbury Laboratory.

off atoms and molecules on the surface. This can be performed with short pulsed ion beams with medium intensity to target the first few atomic layers. A time-of-flight (ToF) mass spectrometer is used to determine the mass charge ratio of the ions and characterise the surface composition, whilst a detector (e.g. electron multiplier) records the magnitude of the signal. This makes it relatively non-destructive and is known as static SIMS. A second procedure can be performed in which a caesium or oxygen ion gun is used to sputter the sample and probe the film depth. This is a dynamic SIMS as it permanently damages the surface. A quadrupole mass analyser, tuned for selected masses, will record the mass charge ratio of the ions and map the distribution of elements as the ion beam sputters the surface.

At Daresbury Laboratory $10 \times 10\,\mathrm{mm}^2$ samples were measured in a Hiden SIMS Workstation shown in Figure 7.12, courtesy of R. Valizadeh (STFC). This operates under UHV conditions and uses an Cs ion gun and a Hiden dual-mode MAXIM mass analyser. At the time of measurements, it was not possible to calibrate the sample thickness as a function of the sputtering rate.

7.4 Nb/Cu Samples

A set of Nb/Cu samples were prepared both to demonstrate how the Choke Cavity can be used to help optimise different deposition parameters and, in this case, to investigate the effect of the deposition temperature on the RF performance of Nb/Cu deposited by HiPIMS.

7.4.1 Sample Preparation

This study used 100 mm diameter and 3 mm thick Design 1 DT Cu sample disks without additional chemical treatments. For the depositions, $RRR = 400$ bulk Nb targets were used.

The depositions followed the procedure detailed in Section 7.2. For each deposition, the substrate temperature was varied. With the exception of the sample deposited at room temperature (≈ 25°C), all substrates were heated under UHV conditions at a typical base pressure $P = 2 \times 10^{-9}$ mbar for 20 hours at the required deposition temperature before starting the deposition. The target was then controlled using the Ionautics HiPIMS power supply using the deposition parameters summarised in Table 7.1, with Kr used as the discharge gas. The only variable for the depositions was the deposition temperature. Initially, six samples were deposited at temperatures of 25, 240, 340, 465, 555 and 620 °C. After deposition of the sample at 240°C, it was observed that the target material had worn through to the Cu magnetron mount, likely resulting in Cu contamination of that sample and potentially for previous samples. Therefore, seven additional samples were deposited with a second Nb target at temperatures of: 25, 240, 340, 470, 530, 570 and 620 °C, using the same process as before. These two sets of samples will be referred to as 'Nb/Cu Target 1' and 'Nb/Cu Target 2'. After each deposition, the sample was allowed to cool naturally before removal.

Table 7.1: The deposition parameters for the Nb/Cu effect of deposition temperature study.

Deposition Parameter	Value
Base pressure (mbar)	2×10^{-9}
Initial heating time (h)	20
Initial temperature (°C)	$25 - 620$
Pressure with heating (mbar)	10^{-7}
Average magnetron power (W)	400
Pulse duration (μs)	80
Pulse frequency (kHz)	1
Discharge gas	Kr
Deposition pressure (mbar)	2×10^{-3}
Substrate temperature (°C)	$25 - 620$
Deposition time (h)	4.5

7.4.2 Superconducting Measurements

RF measurements with the Choke Cavity were performed on the uncut sample disks soon after deposition to minimise contamination. Measurements of the resonant frequency shift, from $T_s = 6\,\mathrm{K}$, as a function of sample temperature are shown in Figure 7.13(a) for target 1 and Figure 7.13(b) for target 2. These measurements were made with a VNA power of 0 dBm and $T_{cav} = 7\,\mathrm{K}$. The analysis techniques detailed in Section 6.3.1 were used to calculate f_0 from $|S_{21}|$ at each sample temperature and provide estimates of the RF critical temperature (T_c^{RF}) from $\mathrm{d}\Delta f/\mathrm{d}T_s$.

From the frequency shift alone, it is clear that there are differences between the samples produced with both targets. The thin film Nb should have a T_c close to the theoretical $T_c = 9.2\,\mathrm{K}$ for bulk Nb. However, unexpectedly low transitions to the normal conducting regime at $T_s < 9.2\,\mathrm{K}$ are observed for the samples deposited with target 1 at 25, 240, 340 and 620 °C clearly suggesting that films deposited with this

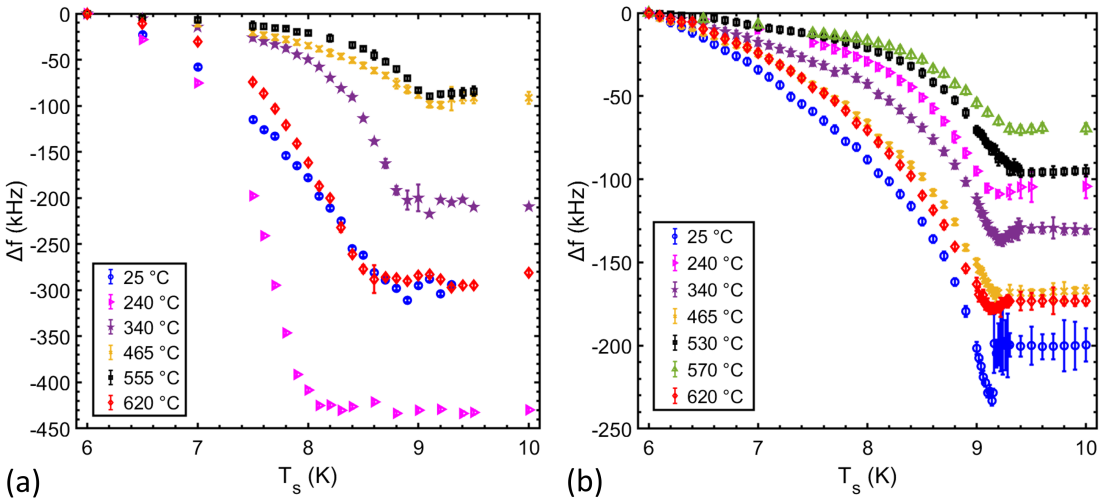

Figure 7.13: The shift in resonant frequency as a function of sample temperature compared at fixed $T_{\mathrm{cav}} = 7\,\mathrm{K}$ for the Nb/Cu samples deposited with: (a) target 1, (b) target 2.

target were contaminated. For target 2, all transitions are close to the theoretical value with a lower range of Δf for the set of samples, suggesting a better quality target. For depositions with both targets, the differences in Δf with the deposition temperature show that the deposition temperature affects the quality of the film, since $\Delta f \propto \Delta\lambda$, as shown previously in Section 6.3.2. In addition, as previously seen in Section 6.3.1, the target 2 samples deposited at 25, 340 and 620 °C all have distinct frequency dips before the transition, suggesting a degraded surface layer for these samples [203]. Given that there is no significant dip present in the other samples, it cannot be certain what the cause of this is and whether this feature is associated with the change in deposition temperature.

The $T_{\mathrm{c}}^{\mathrm{RF}}$ measurements can be compared with measurements of the magnetic moment as a function of the sample temperature performed with the MPMS3 at RAL using the procedure described in Section 7.3.1. An applied magnetic field, $B_{\mathrm{app}} = 5\,\mathrm{mT}$ was used for each test and the samples were cooled at a rate of $1\,\mathrm{K\,min^{-1}}$ from 12 to 4.2 K. The 25 °C target 2 sample could not be measured with any DC or surface analysis due to significant film delamination after cutting. Poor film

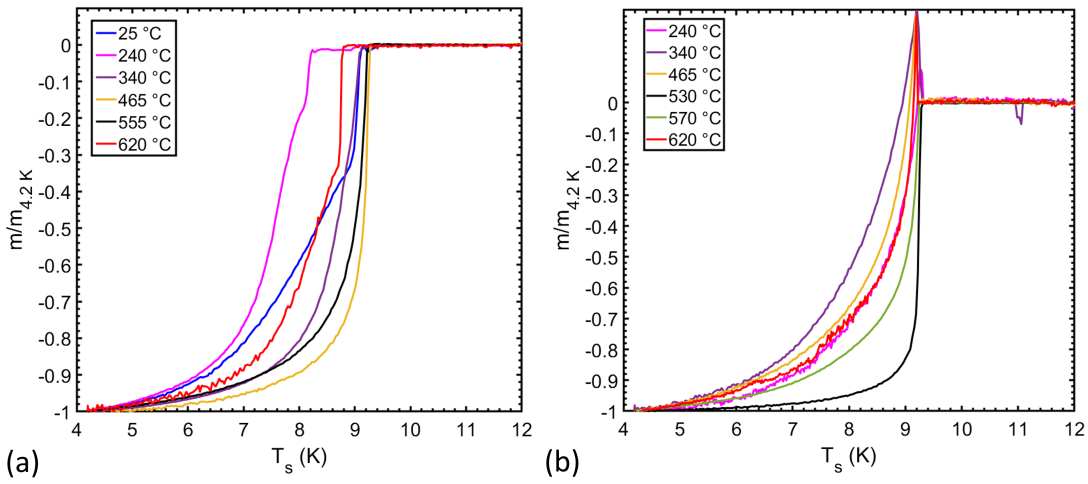

Figure 7.14: The normalised magnetic moment as a function of sample temperature compared at fixed $B_{\mathrm{app}} = 5\,\mathrm{mT}$ for the Nb/Cu samples deposited with: (a) target 1, (b) target 2 (normalised to the magnetic moment at $T_{\mathrm{s}} = 4.2\,\mathrm{K}$, $m_{4.2\mathrm{K}}$).

adhesion was also observed for the target 1 room temperature sample. Both of these demonstrate that room temperature depositions are not viable for a cavity. The critical temperature ($T_{\mathrm{c}}^{\mathrm{VSM}}$) was estimated from the point of onset of the transition, consistent with the method used elsewhere [235]. These measurements are shown in Figure 7.14(a) for target 1 and Figure 7.14(b) for target 2. It can be seen that, as with the RF measurements, a wider range and less overlap of $T_{\mathrm{c}}^{\mathrm{VSM}}$ is observed with the target 1 samples. This might be attributed to a poorer quality target that reduced the film quality for the first set of samples.

As observed with RF measurements, the 240 °C target 1 sample had a lower than expected $T_{\mathrm{c}}^{\mathrm{VSM}}$ likely due to significant contamination after wearing through the target material to the Cu magnetron. More consistent superconducting transitions are observed with the target 2 samples. However, the overshoot in magnetic moment at T_{c} for the 240, 340, 465 and 620 °C samples cannot be fully explained but this could be due do sample misalignment during testing. Fairly wide transitions, with the exception of the 465 and 555 °C target 1 samples and the 530 °C target 2 samples, could be due to a higher level of contamination in these films due to suboptimal

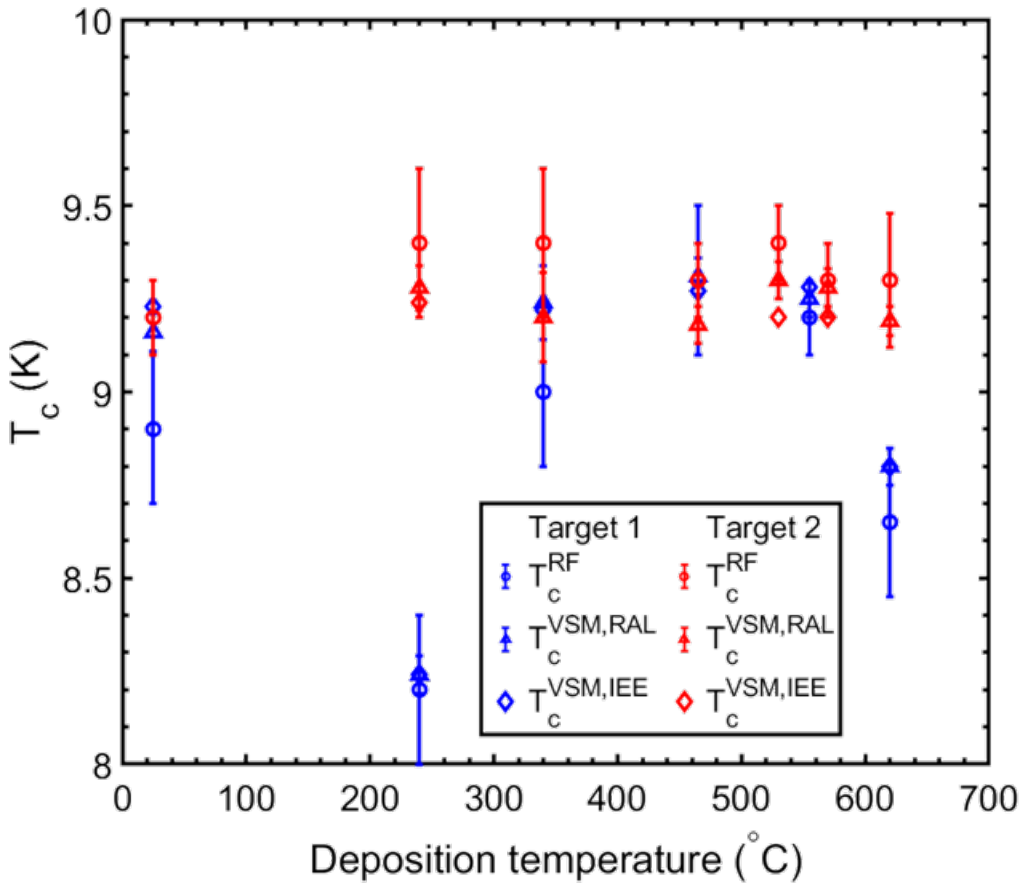

Figure 7.15: A summary of the critical temperature measurements of the Nb/Cu target 1 and target 2 samples. T_c^{RAL} denotes the VSM measurements with the MPMS3 at RAL and T_c^{IEE} denotes the VSM measurements with the PPMS, courtesy of E. Seiler and R. Ries (IEE).

deposition temperatures. It can also be seen that the sharpest transition for the 530 °C target 2 sample had one of the lowest Δf, shown earlier in Figure 7.13(b). However, it cannot be ruled out that any contamination may have been introduced during the EDM cutting.

A summary of the critical temperatures calculated using RF and DC techniques is shown in Figure 7.15. The general consistency between both measurement techniques shows that either method can be reliably used to predict the critical temperature of thin film samples. In addition, some of the samples were also

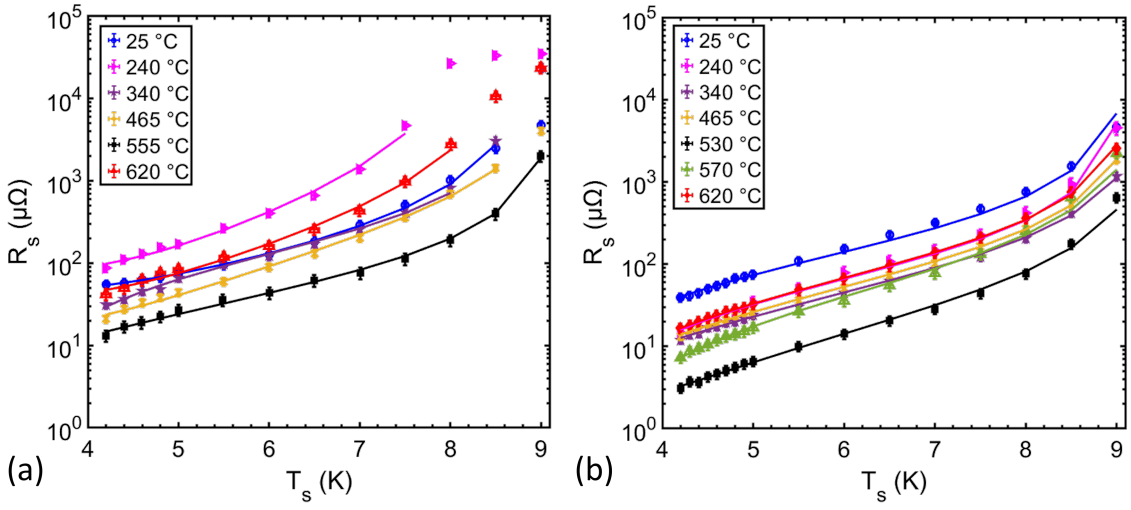

Figure 7.16: The surface resistance as a function of sample temperature compared at low field ($B < 3\,\mathrm{mT}$) with BCS fits for the Nb/Cu samples: (a) target 1, (b) target 2.

measured using the PPMS instrument at IEE, courtesy of E. Seiler and R. Ries. Generally, the measurements between the two sets of VSM measurements are consistent. The smaller samples were not the same in both tests and any discrepancies could be due to slight variations in film quality on the smaller samples as these were cut from different points on the original 100 mm diameter disk. Differences in T_c could also be due to different film thicknesses [116]. In general, the measurements of the target 2 samples are more consistent with T_c typically above 9.2 K. This is consistent with Nb/Cu films measured elsewhere demonstrating T_c between $9.3 - 9.5\,\mathrm{K}$ [116]. No correlation of the critical temperature with the deposition temperature is observed. This is potentially as expected for a single element deposition, as the film stochiometry is likely to remain consistent for a single element deposition, unless contaminants are introduced, e.g., through poor vacuum conditions or significant outgassing from the substrate. If this happens, early flux entry into the superconductor and a lower T_c are possible. However, the sharpest normalised magnetic moment curve in Figure 7.14(b) would suggest an optimal deposition temperature of 530 °C.

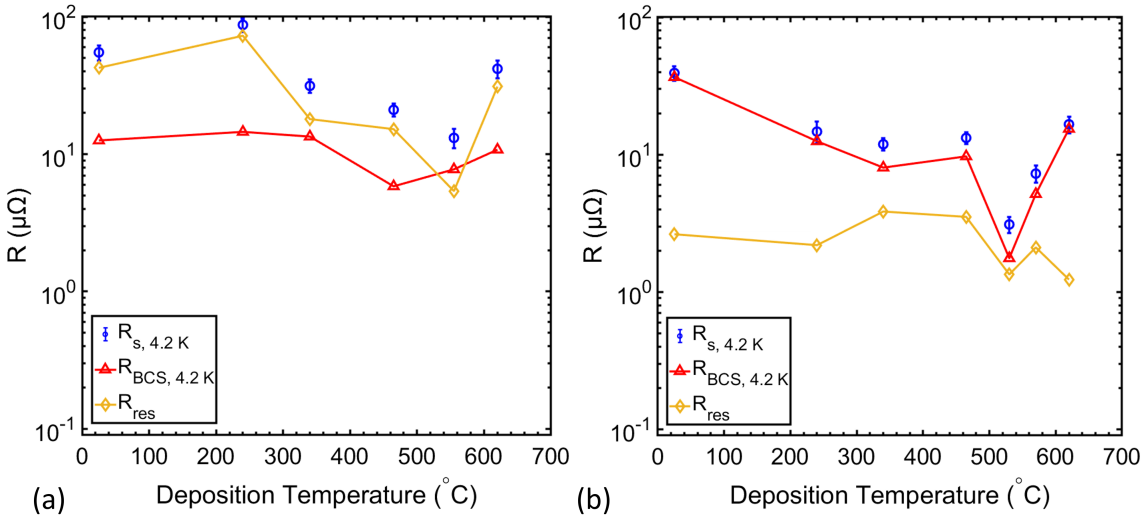

Figure 7.17: Summary of R_s and R_{BCS} at 4.2 K and R_{res} measurements of the Nb/Cu samples as a function of deposition temperature compared at low field ($B < 3$ mT) for: (a) target 1, (b) target 2.

The R_s as a function of sample temperature was also measured for each sample. The measurements of the target 1 samples are shown in Figure 7.16(a) whilst the target 2 are shown in Figure 7.16(b). For all samples, R_s increases with sample temperature as expected. It can be seen that the target 2 samples generally have R_s closer to the theoretical minimum level. For target 1, the sample deposited at 555 °C has the lowest $R_s = 13.1 \pm 2.1\,\mu\Omega$ at 4.2 K. Meanwhile, target 2 was able to deposit a Nb film at 530 °C with a minimum $R_s = 3.1 \pm 0.3\,\mu\Omega$, which is almost an order of magnitude lower. This is in line with the normalised magnetic moment results. For target 1, an early transition between $8 - 8.5$ K is observed for the 240 °C sample, consistent with the lower than expected T_c measurement. For both room temperature samples, a slight flattening of the curve at temperatures close to 4.2 K suggest that the R_s of these two samples is dominated by a large R_{res}.

A comparison of the low field R_s at 4.2 K as a function of deposition temperature is shown in Figure 7.17. Shown in Figure 7.16 are the BCS fits using the procedure outlined in Sections 6.3.2 and 6.3.4 to extract R_{BCS} and R_{res}. These fits assumed fixed $\lambda_L = 32$ nm and $\xi_0 = 39$ nm for clean bulk Nb. Samples with both targets

demonstrate an overall decrease in R_{BCS} at 4.2 K with deposition temperature to a minimum $R_{\mathrm{BCS}} = 5.8\,\mu\Omega$ at 465 °C and $R_{\mathrm{BCS}} = 1.8\,\mu\Omega$ at 530 °C for target 2. Given the trend, the target 2 sample deposited at 465 °C appears to have an R_{BCS} slightly higher than expected but both sets of samples demonstrate an increase in R_{BCS} at higher temperatures above 530 °C. Also shown is R_{res} extracted from the fits. What is clear is that the target 1 samples are dominated by a higher R_{res} on average over a much wider range from $5 - 73\,\mu\Omega$, with the highest being for the 240 °C sample as expected. Meanwhile, target 2 samples are dominated by R_{BCS} with a much smaller range of R_{res} from $1 - 4\,\mu\Omega$ with no apparent dependence on deposition temperature. These results match the variations observed in T_{c}, likely confirming the poorer quality of the target 1 depositions.

Overall, the superconducting measurements showed that the target 1 samples were likely contaminated. From the RF performance of the target 2 samples alone, it can be concluded that the optimal deposition temperature was 530 °C. This suggests that future Nb/Cu depositions in this facility should be optimised around this temperature. It is possible, though, that this can vary between facilities or with different magnetron powers etc. Therefore, it is important to optimise the deposition temperature for each material in every facility, thus demonstrating the importance of a quick RF measurement tool such as the Choke Cavity.

7.4.3 Surface Analysis

Measurements of surface roughness (S_{a} and S_{q}), were made using the WLI detailed in Section 7.3.2 prior to cutting the disks. These measurements are summarised in Figure 7.18(a) for the target 1 samples and Figure 7.18(b) for target 2. For both sets of samples, an overall increase in roughness is observed from the baseline $S_{\mathrm{a}} = 2 - 3\,\mathrm{nm}$ and $S_{\mathrm{a}} = 5 - 6\,\mathrm{nm}$. This is likely due to an expected increase in stresses and grain size of the substrate with increasing temperature. For the target 1 samples, the largest $S_{\mathrm{a}} = 44.3 \pm 3.1\,\mathrm{nm}$ and $S_{\mathrm{q}} = 204.9 \pm 43\,\mathrm{nm}$ for the 555 °C sample which also had the lowest R_{s}. For target 2, the highest roughness is

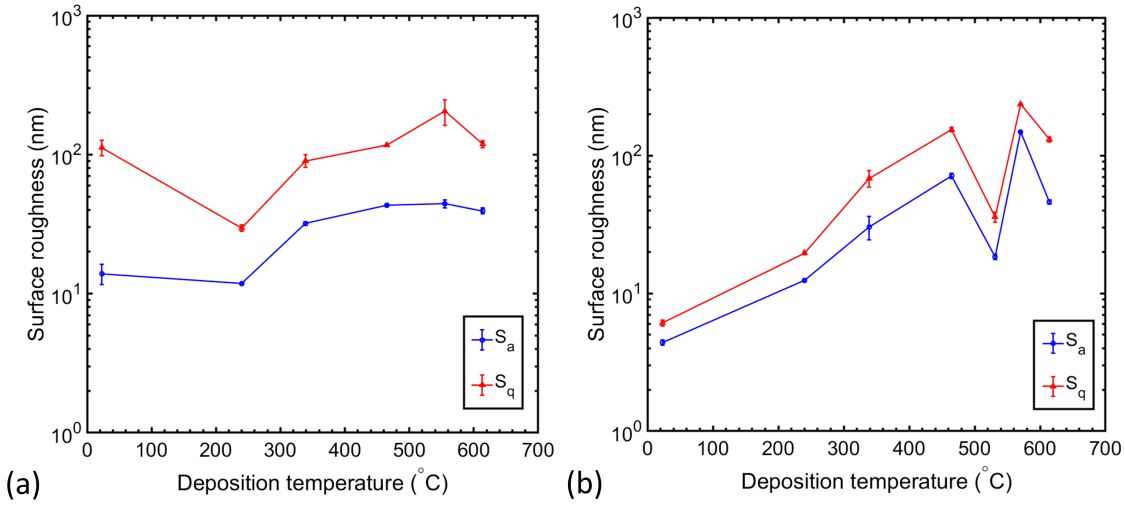

Figure 7.18: Measurements of the average surface roughness, both S_a and S_q, of the Nb/Cu samples deposited with: (a) target 1, (b) target 2.

$S_a = 147.9 \pm 1.7$ nm and $S_q = 235.2 \pm 1.9$ nm for the 570 °C sample. However, this did not exhibit the highest R_s. Meanwhile, a lower S_a and S_q compared to the 340, 465, 570 and 620 °C is observed for the 530 °C sample. This happens to coincide with the lowest R_s of this set. Given that increasing roughness is observed over the range of decreasing R_s for each sample set, it is unlikely that the variation in roughness at this level will explain the differences in low-field RF performance. One disadvantage, however, of this method for measuring roughness is that it assumes a homogeneous film surface by only measuring a few points on each sample.

To study the surface of the samples at higher magnification, the SEM was used, detailed in Section 7.3.3. A selection of SEM images for target 2 are shown in Figure 7.19. The 25 °C sample (Figure 7.19(a)) had the highest R_s. This is likely due to the very small grain size of the film resulting in a large number of regions that could exhibit RF losses. The 530 °C sample (Figure 7.19(c)) had the lowest R_s which could be due to the formation of larger grains and a generally more uniform surface. Due to further heating, the higher 570 °C sample ((Figure 7.19(d)) has larger cracks due to deformation of the Cu surface which is likely to contribute to regions of increased RF losses. Despite larger grains being visible for the 465 °C sample (Figure

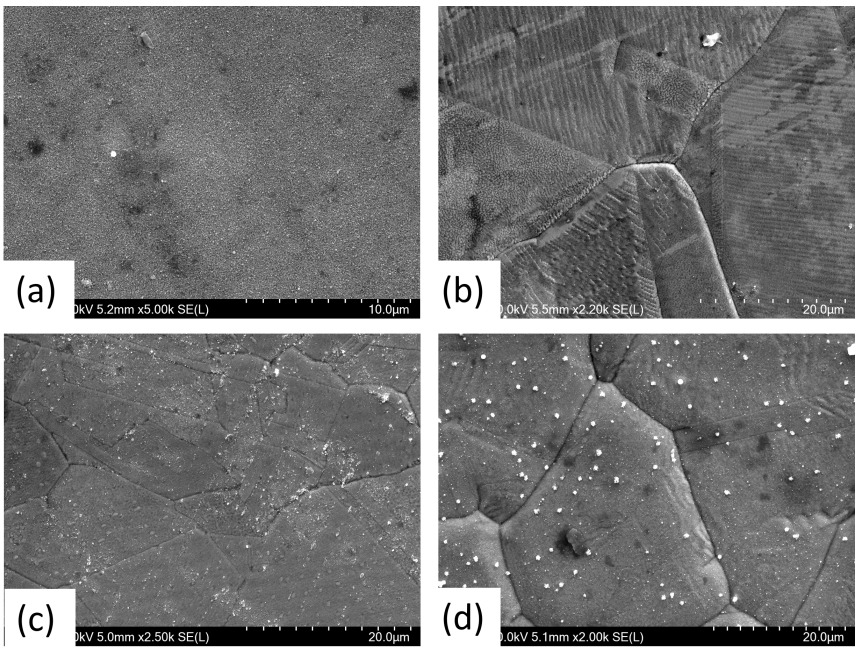

Figure 7.19: SEM images of the Nb/Cu target 2 samples deposited at: (a) 25 °C, (b) 465 °C, (c) 530 °C, (d) 570 °C.

7.19(b)), the film growth appears less uniform, which could explain the slightly higher than expected R_{BCS}. In addition, between 460 and 530 °C there could be increased densification of the film at the surface. Fewer defects in a denser surface would reduce the diffusion of oxygen into the film when exposed to atmosphere, therefore resulting in a thinner evolution of the lossy Nb_2O_5 thus resulting in a lower R_{s}. However, further surface analysis, such as SIMS and electron backscatter diffraction (EBSD) should be performed to study these effects in detail.

All samples appeared to have white specs on the surface, which, according to EDS analysis, correspond to Cu. Given that the samples were only measured after cutting, no conclusion can be made as to whether this was introduced during deposition. It is possible that small Cu particulates in the sample have less effect on low field RF performance, so may have little contribution to the R_{s} measurements anyway.

Ion-beam milling was also performed on each of the $10 \times 10\,\mathrm{mm}^2$ sample cuts,

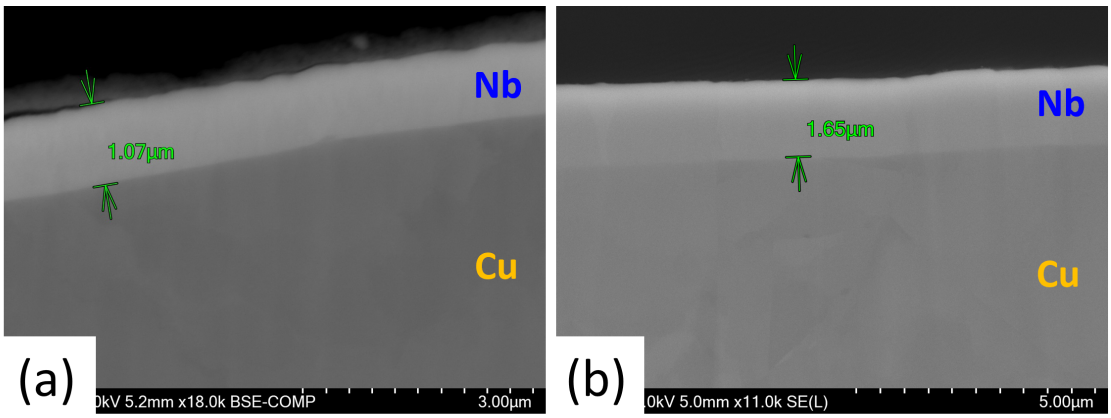

Figure 7.20: Examples of cross-sectional SEM measurements of the Nb/Cu samples deposited with: (a) target 1, (b) target 2.

with typical measurements shown in Figure 7.20. Both the target 1 and target 2 samples exhibited fairly uniform film thicknesses. However, despite attempts to control the thickness by setting the deposition time of each sample at 4.5 hours, the mean thickness was different for the two targets. For target 1, thicknesses ≈ 1 µm were measured whilst target 2 exhibited slightly larger thicknesses ≈ 1.7 µm. Although the same deposition time was used for all samples and the targets were sourced from the same material, the different thicknesses could be due to target 1 having been in the deposition system much longer than target 2. This target could have potentially accumulated more impurities over time, resulting in a decrease in purity and a reduction in the deposition rate as a result. Studies have shown that the deposition rate was higher for the newer target 2 compared with a worn target 1. This could have been due to target purity and thus explain the poorer RF performance with the target 1 samples [236].

XPS analysis was performed to identify the elemental composition. Kr^+ Ion sputtering of the sample surface for 4 hours was performed to remove any potential contamination on the surface and identify only elemental composition in the first few nm of the film. Examples of these results for a range of deposition temperatures are shown in Figure 7.21(a) for target 1 and Figure 7.21(b) for target 2 with (i) Nb 3d,

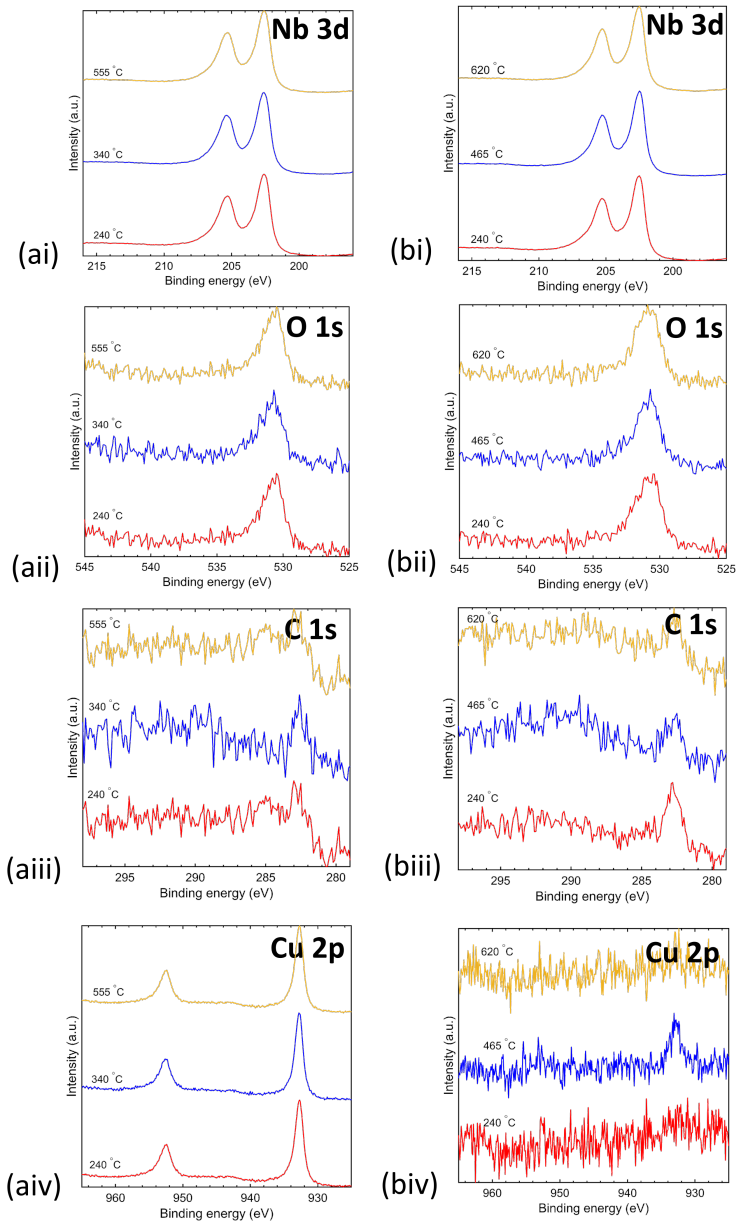

Figure 7.21: Measurements of the XPS core region spectra of a selection of the Nb/Cu samples with: (a) target 1 and (b) target 2, where the spectra for each shown are (i) Nb 3d, (ii) O 1s, (iii) C 1s (iv) Cu 2p.

(ii) O 1s, (iii) C 1s (iv) Cu 2p orbitals. All samples show similar Nb 3d splitting as expected. The O 1s and C 1s peaks in all films are likely due to oxygen and carbon contamination after exposing the sample to atmosphere for some time after cutting.

Most interestingly are the Cu 2p spectra. No significant peaks are present in most the target 2 samples, suggesting very little to no Cu contamination in these films. The exception is a slight peak in the 465 °C, which, along with the SEM image, could explain the slightly higher than expected R_s. The general trend suggests that Cu on the surface observed in the SEM was likely introduced during sample cutting. However, all three target 1 240 °C samples have two significant Cu 2p peaks. The sputtering of the top few monolayers of each film prior to XPS suggests that the Cu in target 1 was introduced during deposition. This Cu contamination could be the cause for the higher R_s in the target 1 samples. There was almost certainly Cu sputtered in the 240 °C sample, explaining the degradation in T_c and R_s. Despite the 555 °C sample being deposited second in the set, Cu is still observed in the surface of the film, suggesting that target 1 was likely contaminated from the outset. Despite this, the target 1 samples were still superconducting under RF conditions, suggesting that trace Cu is not enough to cause sample quenching at low-field RF.

Overall, at low field, it has been demonstrated that the RF performance of two sets of Nb/Cu thin films has a dependence on the deposition temperature. The optimal deposition temperature for both sets of samples deposited in the deposition facility at Daresbury Laboratory was in the range $\approx 340 - 555$ °C. Surface analysis cannot relate this to a surface roughness effect, however SEM analysis suggests an increase in temperature increases the deformation and cracking in the Cu surface, which is likely to have resulted in regions of increased RF losses at the cracks. Chemical analysis with XPS did not show any major differences in film composition with an increase in temperature, however it did highlight the presence of significant Cu contamination for the target 1 samples deposited, despite them still being superconducting. This was likely due to a contaminated target. Little to no presence of Cu in the films for the target 2 samples was observed despite Cu inclusions on the surface detected by SEM suggesting that care should be taken to avoid sample contamination during and after the cutting process.

Excluding the clearly contaminated target 1 samples, the optimal deposition

temperature for Nb/Cu was 530 °C for a film deposited using HiPIMS with average power 400 W, pulse duration 80 µs, pulse frequency 1 kHz and thickness ≈ 1.7 µm. RF measurements at 7.8 GHz showed $R_s = 3.1\,\mu\Omega$ at 4.2 K with $R_{BCS} = 1.8\,\mu\Omega$ and $R_{res} = 1.3\,\mu\Omega$ whilst both DC and RF measurements showed an average $T_c = 9.3$ K.

7.5 Nb_3Sn/Cu Samples

As detailed in Section 2.4.2, cavities coated with alternative superconductors are a must if high Q_0 operation at 4.2 K is to be achieved with higher frequency operation and the potential for high E_{acc} performance exceeding Nb. Having characterised several Nb/Cu thin film samples, the next step was to determine whether the Choke Cavity facility was capable of characterising alternative superconducting thin films with higher T_c and potentially lower R_s. For this, two short studies were performed with thin film Nb_3Sn. The first study looked at single layer Nb_3Sn deposited on Cu. The second study looked at repeating the best performing Nb_3Sn parameters on Cu with a Nb thin film in between. These studies aimed to repeat some previous studies performed at Daresbury Laboratory on Nb_3Sn/Cu deposited by DCMS [105]. These were carried out at a time when RF measurements were not readily available and superconducting measurements were limited to the VSM.

Optimising a Nb_3Sn thin film is much more complicated than Nb due to its multi-elemental composition. Achieving the optimal A15 phase with 25% Sn and 75% Nb, that will improve the RF performance, is usually achieved for temperatures above 930 °C [237]. For thin film depositions on Cu, these temperatures are likely to be problematic as they are close to the melting point of Cu at 1085 °C. Achieving a low R_s and a T_c close to the maximum 18.3 K achieved by magnetron sputtering [238, 239] requires optimisation of the other deposition parameters as the deposition temperature would be set to a value that is much lower than the optimal value.

As with the Nb/Cu samples, depositions for all Nb_3Sn samples were performed with the in-house deposition facility described in Section 7.2. The only change

was the use of an alloy Nb_3Sn planar target mounted on the planar magnetron. This study also used 100 mm diameter and 3 mm thick Design 1 DT Cu sample substrate disks. For each study, initial sample preparation was identical. After the system reached base pressure, $P \approx 2 \times 10^{-9}$ mbar, the substrate was preheated to 620 °C for 20 hours. The substrate was maintained at 620 °C during deposition. Given that a high deposition temperature is required for Nb_3Sn, the maximum heater power possible with this facility was used. Previous studies at Daresbury Laboratory with 650 °C, 450 °C and room temperature depositions showed that the desired stochiometry was only achieved with the 650 °C deposition [105]. The 450 °C deposition exhibited superconducting properties, but with a degraded T_c.

7.5.1 Effect Of Magnetron Power

The first study looked at three samples deposited using DCMS with magnetron powers of 50, 100 and 200 W. The deposition time was 20 hours for the 50 W sample, 10 hours for the 100 W and 4.5 hours for the 200 W. Given that the deposition rate increases with magnetron power, different deposition times were used to ensure that the films had approximately the same thickness. These times were based on previous studies performed with Nb_3Sn depositions on smaller samples in the same facility. DCMS was used instead of HiPIMS to simplify the number of deposition parameters that needed to be controlled. A summary of the deposition parameters used is shown in Table 7.2.

Cross-sectional SEM measurements performed with these samples showed fairly uniform film thicknesses of $2 - 2.3\,\mu m$ for all three samples, as shown in Figure 7.22. However, the 200 W sample showed the presence of Cu in the film from EDS analysis. In addition, large irregularities approximately 1 µm high and 2 µm wide were visible on the surface of the 200 W sample.

Figure 7.23(a) shows R_s as a function of T_s from $4.2 - 9$ K. Both the 50 W and 100 W samples have lower R_s at 4.2 K than the best performing Nb/Cu sample measured in Section 7.4.2, whilst the 200 W sample is comparable with the majority

Table 7.2: The deposition parameters used for the DCMS Nb_3Sn/Cu samples.

Deposition Parameter	Value
Base pressure (mbar)	2×10^{-9}
Initial heating time (h)	20
Initial heating temperature (°C)	620
Pressure with heating (mbar)	10^{-7}
Magnetron power (W)	50, 100, 200
Discharge gas	Kr
Deposition pressure (mbar)	2×10^{-3}
Substrate temperature (°C)	620
Deposition time (h)	20, 10, 4.5

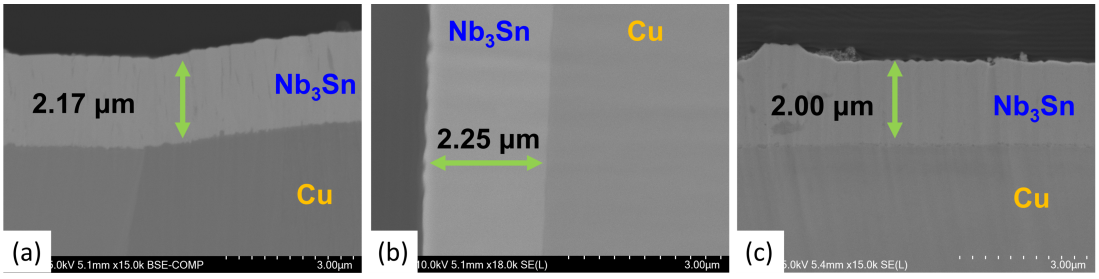

Figure 7.22: Cross-sectional SEM measurements of the DCMS Nb_3Sn/Cu samples: (a) 50 W, (b) 100 W, (c) 200 W.

of Nb/Cu target 2 samples. The best performing sample is the 50 W sample with an $R_s = 0.38 \pm 0.04$ µΩ at 4.2 K, which is one order of magnitude lower than the best Nb/Cu sample. The next best sample is the 100 W sample with $R_s = 2.24 \pm 0.34$ µΩ at the same temperature whilst the 200 W sample is almost one order of magnitude worse with $R_s = 19.62 \pm 2.75$ µΩ. All three samples show a much shallower increase in $R_s(T_s)$ than for Nb/Cu. This is as expected due to the higher expected T_c of the material. For example, the 50 W sample R_s increases by only 6 µΩ over the range of $4.2 - 9$ K. These measurements were made at low $B_{s,pk} < 5$ mT. As with the facility commissioning with Nb samples shown in Section 6.3.3, there no low

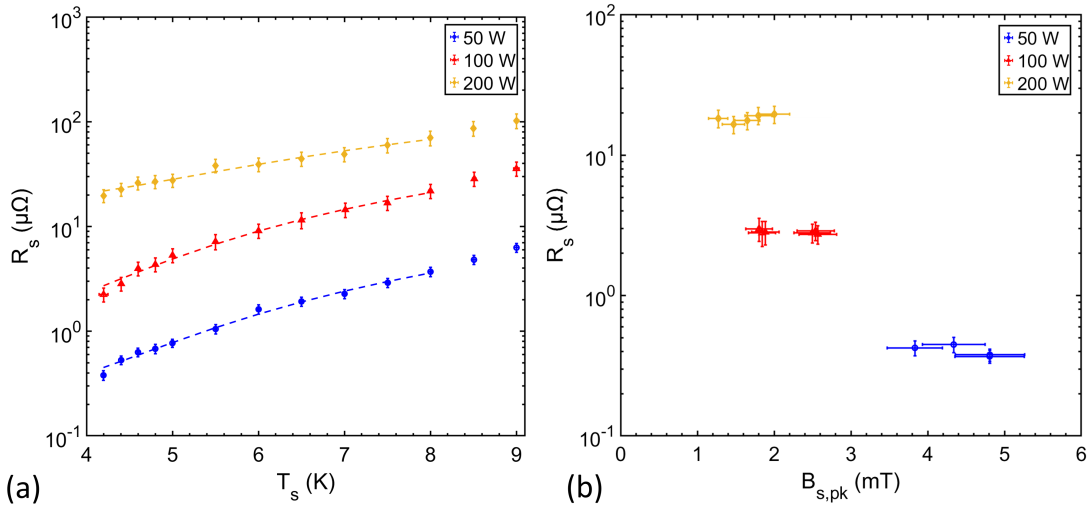

Figure 7.23: Measurements of $R_s(T_s)$ with BCS fits of the DCMS Nb_3Sn/Cu samples deposited with different magnetron powers: (a) as a function of T_s at $B_{s,pk} < 5\,mT$, (b) as a function of $B_{s,pk}$ on the sample at $T_s = 4.2\dot{K}$.

field dependence on R_s at these low fields measured, as shown in Figure 7.23(b). A slightly higher maximum $B_{s,pk} = 5\,mT$ was achievable for the sample 50 W due to the lower R_s and slightly narrower cavity bandwidths used during tests, whilst remaining above the frequency shift due to microphonics.

The T_c of Nb_3Sn can be up to approximately twice that of Nb. Therefore, more measurements of R_s are possible at $T < T_c/2$ with the Choke Cavity where the energy gap $\Delta \to \Delta(0)$. As a result, a least-squares fit of $R_s(T_s)$ to the BCS approximation in Equation 2.52 provides a simpler method to extract an estimate of both $R_{BCS,4.2K}$ and R_{res}. The resulting fits are shown by the dashed lines in Figure 7.23(a).

A summary of the R_s at $T_s = 4.2\,K$ ($R_{s,4.2K}$) as a function of magnetron power is shown in Figure 7.24(a). The raw $R_{s,4.2K}$ measurements suggest that lower magnetron power is required for better RF performance, at least down to 50 W. Also, the values of $R_{BCS,4.2K}$ and R_{res}, derived from the fits in Figure 7.23(a), both show a positive correlation with magnetron power over this range. $R_{BCS,4.2K}$ ranges by an order of magnitude from $0.26 \pm 0.06\,\mu\Omega$ for the 50 W sample to $5.4 \pm 2.2\,\mu\Omega$

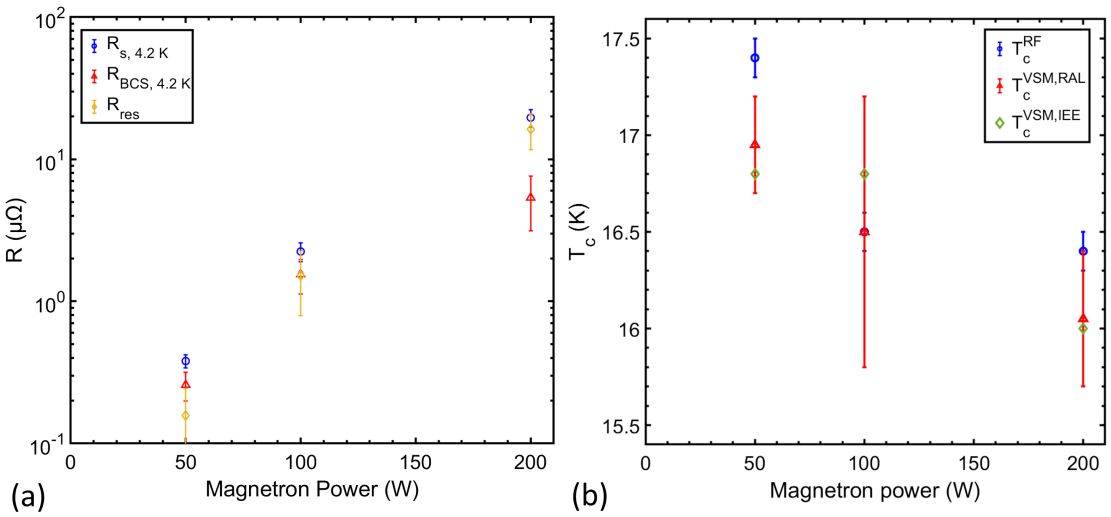

Figure 7.24: Summary of DCMS Nb_3Sn/Cu superconducting sample measurements as a function of magnetron power: (a) R_s and R_{BCS} at 4.2 K and R_{res}, (b) T_c with RF measurements and VSM measurements at RAL and IEE with $B_{app} = 5$ mT.

for the 200 W sample. For the 50 W and 100 W samples, $R_{res} = 0.16 \pm 0.09\,\mu\Omega$ and $1.5 \pm 0.7\,\mu\Omega$ respectively, however the 200 W sample is largely dominated by $R_{res} = 16.3 \pm 4.6\,\mu\Omega$ which is approximately a factor of 3 greater than R_{BCS}.

Critical temperature measurements were also performed. Figure 7.24(b) shows measurements of both T_c^{RF} (from the RF frequency shift) and T_c^{VSM} (from $m(T_s)$), as a function of magnetron power. Both the DC and RF measurements shown the same trend, with consistent measurements observed for the VSM measurements performed at RAL and IEE. The highest T_c was measured to be 17.4 ± 0.1 K for the sample deposited with a 50 W magnetron power whilst the T_c for the 200 W sample was 1 K lower. From the literature, the higher T_c corresponds to a Sn level of $24 - 25\%$, which is close to optimal [237].

Figure 7.25 shows SEM images of the sample surface. Both the 50 W and 100 W samples have similar surface structures with high grain density. There are no significant features to explain why the 50 W sample had slightly better superconducting properties. As with the Nb/Cu target 2 samples deposited at $T \geq 570\,^{\circ}$C, similar small white spots in the images were attributed to Cu with

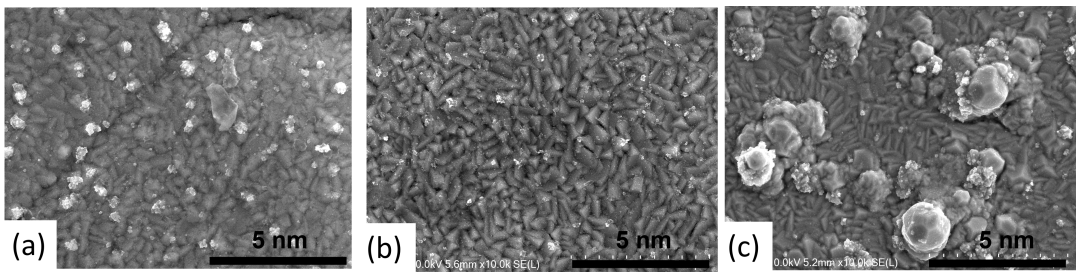

Figure 7.25: SEM images of the Nb_3Sn/Cu samples: (a) 50 W, (b) 100 W, (c) 200 W.

EDS analysis in all samples, suggesting that the presence of Cu could be due to the high substrate temperature during deposition. However, the 200 W sample has a very different surface with the presence of large inclusions of Nb_3Sn on the surface creating a very rough layer. This was also observed in Figure 7.22(c) and could explain the dominant R_{res}.

Dynamic SIMS was also performed on the three samples, as shown in Figure 7.26, to identify elements within the film. The number of counts in the spectra is directly related to the atomic concentration. For the 200 W sample, the worse superconducting performance is likely due to the larger difference between Nb and Sn counts compared to the ratios shown with the 50 W and 100 W samples, suggesting a suboptimal film stoichiometry. Of the other elements, Cu appears to be present on the surface on all samples, as is shown in the SEM images. A decrease in atomic concentration of Cu is observed with increasing sputtering depth for the 50 W and 100 W samples shown in Figure 7.26(a) and Figure 7.26(b). However, there is a significant level of Cu still present in the 200 W sample at increased film depths, which could be an explanation for higher R_{res} and lower T_{c}, as well as the sub-optimal stoichiometry. The presence of Cu was a possible source of higher R_{s} in the Nb/Cu target 1 samples presented previously in Section 2.4.1. Other elements, such as C and O, appear to be high on the surface, likely due to contamination after deposition.

Overall, the results of this short study suggest that Nb_3Sn/Cu deposited with DCMS in the Daresbury Laboratory facility benefit from lower magnetron powers,

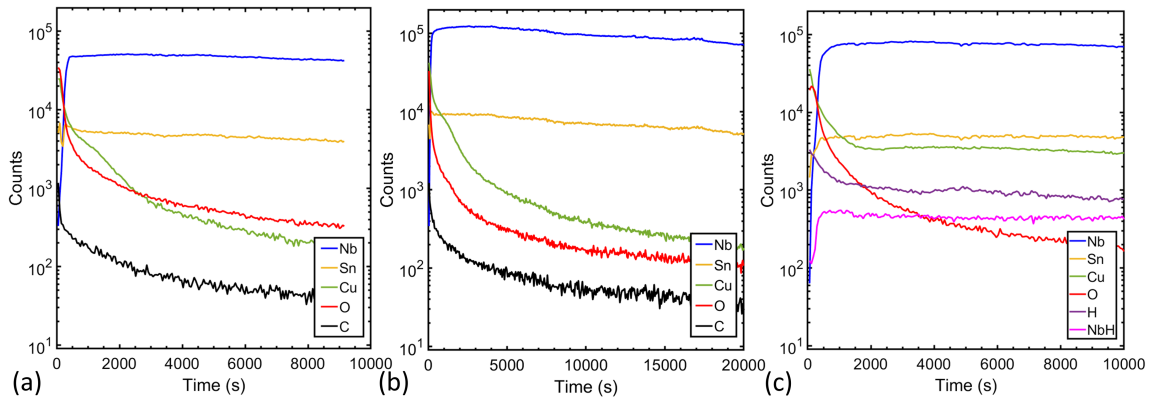

Figure 7.26: Dynamic SIMS measurements of the DCMS Nb_3Sn/Cu samples: (a) 50 W, (b) 100 W, (c) 200 W.

assuming a deposition temperature $\approx 620\,^{\circ}$C. A 50 W magnetron power can achieve dense films with up to two orders of magnitude lower R_s than a 200 W deposition.

7.5.2 Nb_3Sn/Nb Bilayer

Having performed both optimisation studies with Nb and Nb_3Sn thin films, another short study looked to combine the thin film Nb and Nb_3Sn in a bilayer structure. This was to see whether Nb is capable of improving the performance of Nb_3Sn given that, so far, the best performing Nb_3Sn cavities use bulk Nb substrates. For this, two samples were deposited on a DT Cu disk, each with a layer of $\approx$ 2 µm Nb followed by a layer of $\approx$ 1.1 µm Nb_3Sn. In both cases, the Nb film was deposited using 400 W magnetron power and 530 °C deposition temperature as per the best performing sample in Section 2.4.1. After the Nb deposition, the sample was heated to 620 °C before being deposited with the Nb_3Sn layer using DCMS with 50 W magnetron power. Of the two new samples, sample Nb_3Sn/Nb/Cu (1) Nb layer was deposited with DCMS whilst the sample Nb_3Sn/Nb/Cu (2) Nb layer was deposited with HiPIMS. The deposition parameters used are summarised in Table 7.3.

The low-field $R_s(T_s)$ measurements comparing the two samples is shown in Figure 7.27. These measurements show significantly worse RF performance for both bilayers

Table 7.3: The deposition parameters used for the Nb_3Sn/Nb/Cu samples.

Deposition Parameter	**Nb_3Sn DCMS**	**Nb DCMS**	**Nb HiPIMS**
Base pressure (mbar)	2×10^{-9}	2×10^{-9}	2×10^{-9}
Initial heating time (h)	20	20	20
Initial heating temperature (°C)	620	530	530
Pressure with heating (mbar)	10^{-7}	10^{-7}	10^{-7}
Average target power (W)	50	400	400
Pulse duration (μs)			80
Pulse frequency (kHz)			1
Discharge gas	Kr	Kr	Kr
Deposition pressure (mbar)	2×10^{-3}	2×10^{-3}	2×10^{-3}
Substrate temperature (°C)	620	530	530
Deposition time (h)	20	4.5	4.5

with $R_{s,4.2K} = 51.9 \pm 7.5\,\mu\Omega$ for Nb_3Sn/Nb/Cu (1) and $R_{s,4.2K} = 47.1 \pm 6.8\,\mu\Omega$ for Nb_3Sn/Nb/Cu (2). This is approximately one order of magnitude higher that the best Nb/Cu sample from Section 2.4.1 (target 2, 530 °C) with $R_{s,4.2K} = 3.10 \pm 0.42\,\mu\Omega$ and approximately two orders of magnitude higher the 50 W Nb_3Sn/Cu with $R_{s,4.2K} = 0.38 \pm 0.04\,\mu\Omega$. The R_s of both samples appears to be dominated by R_{res}. In addition, a significant 1.3 K degradation in T_c measured from the RF frequency shift between the 50 W single-layer sample and both bilayer samples was measured. A summary of the RF superconducting measurements are shown for comparison in Table 7.4. Both bilayer samples have consistent RF superconducting properties, suggesting that the deposition method for the Nb underlayer does not have a significant effect on the RF performance of the top Nb_3Sn layer.

Figure 7.27 also shows the BCS fits, where the Nb_3Sn/Nb/Cu samples were least-squares fit to the BCS approximation in Equation 2.52. The resulting values of $R_{BCS,4.2\,K}$ and R_{res} are shown in Table 7.4. As expected, both Nb_3Sn/Nb/Cu samples are dominated by a high R_{res} with the highest being Nb_3Sn/Nb/Cu (1)

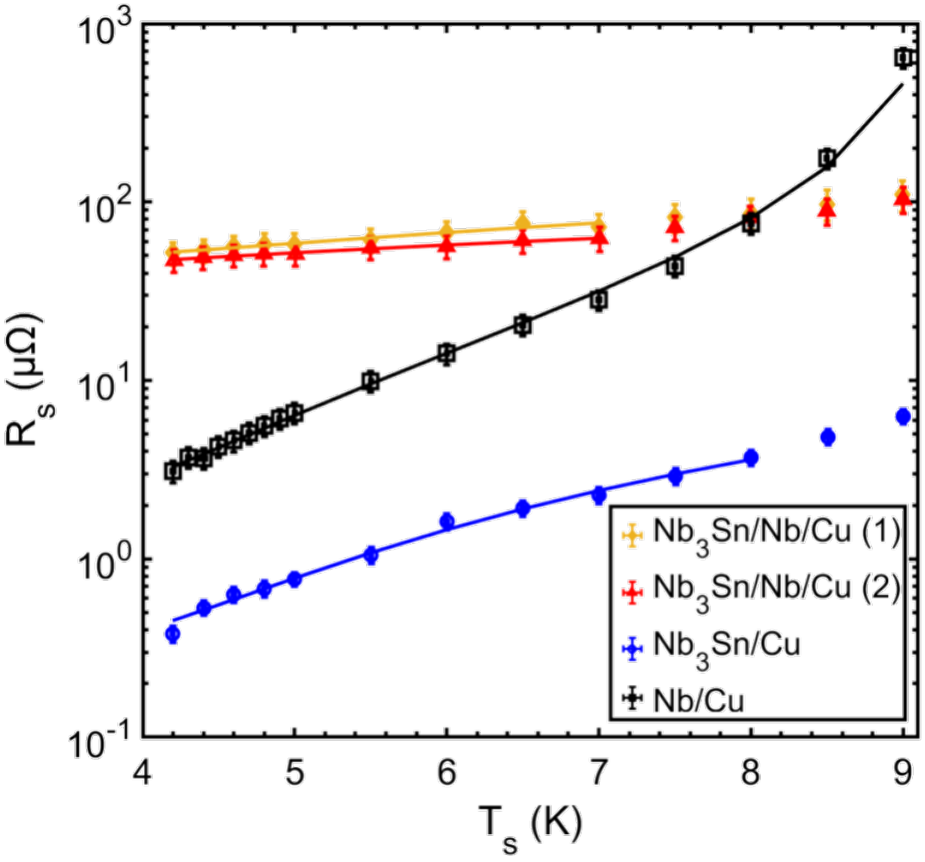

Figure 7.27: $R_s(T_s)$ with BCS fits for the two Nb_3Sn/Nb/Cu bilayer samples compared with the Nb_3Sn/Cu and Nb/Cu samples that exhibited the best superconducting performance.

Table 7.4: A summary of the RF and DC superconducting measurements comparing the Nb_3Sn/Nb/Cu samples with the best single layer Nb_3Sn/Cu and Nb/Cu samples.

Sample	$R_{s,4.2\,K}$ (μΩ)	$R_{BCS,4.2\,K}$ (μΩ)	R_{res} (μΩ)	T_c^{RF} (K)
Nb_3Sn/Nb/Cu (1)	51.9 ± 7.5	10.5 ± 3.3	41.8 ± 10.4	16.1 ± 0.1
Nb_3Sn/Nb/Cu (2)	47.1 ± 6.8	6.5 ± 1.6	41.0 ± 9.4	16.1 ± 0.1
Nb_3Sn/Cu	0.38 ± 0.04	0.26 ± 0.06	0.16 ± 0.09	17.4 ± 0.1
Nb/Cu	3.1 ± 0.42	1.8 ± 0.5	1.3 ± 0.2	9.4 ± 0.1

with $R_{res} = 41.8 \pm 10.4\,\mu\Omega$. This sample also has a slightly higher $R_{BCS,4.2\,K} = 10.5 \pm 3.3\,\mu\Omega$.

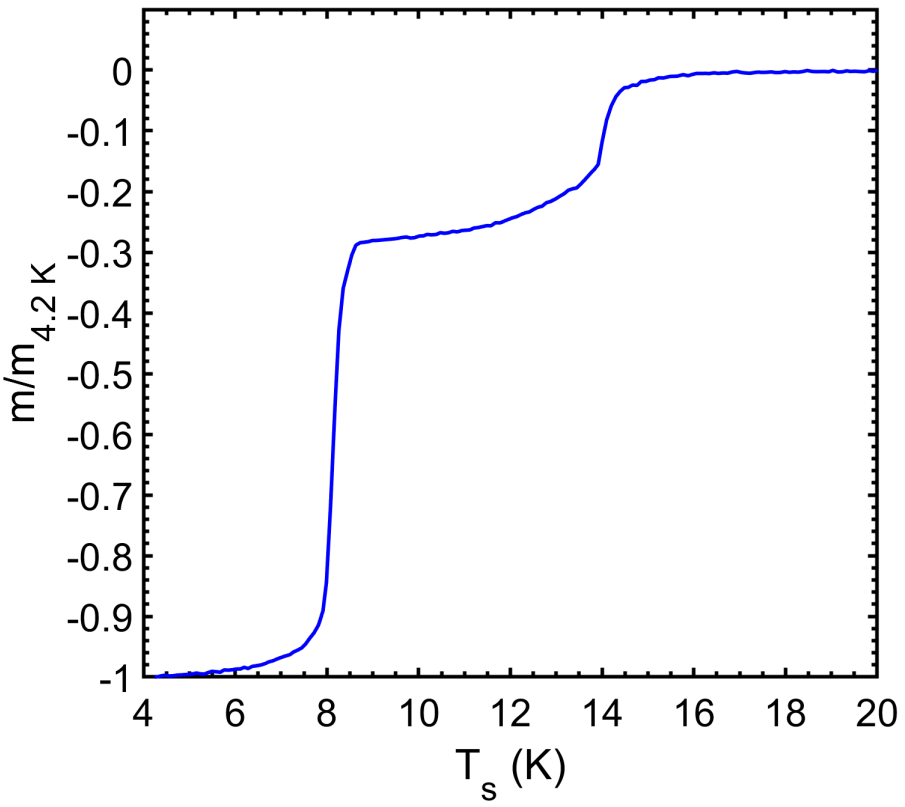

Figure 7.28: The normalised magnetic moment as a function of sample temperature compared at fixed $B_{\mathrm{app}} = 5\,\mathrm{mT}$ for the Nb_3Sn/Nb/Cu (1) sample.

A cut of the Nb_3Sn/Nb/Cu (1) was measured in the MPMS at RAL. Measurements were performed with $B_{\mathrm{app}} = 5\,\mathrm{mT}$ for decreasing temperatures from 20 K to 4.2 K. The results, shown in Figure 7.28, show two distinct superconducting transitions. The onset of transition gives $T_{\mathrm{c}}^{\mathrm{VSM}} \approx 16\,\mathrm{K}$ for the Nb_3Sn layer consistent with the RF measurement. A wide transition suggests that the Nb_3Sn layer is non-homogeneous. Meanwhile, a second transition is observable with $T_{\mathrm{c}}^{\mathrm{VSM}} = 8.25\,\mathrm{K}$, indicating the presence of a degraded Nb base layer. This is consistent with the $T_{\mathrm{c}}^{\mathrm{RF}}$ measurement.

A cut of the Nb_3Sn/Nb/Cu (1) sample was studied with XPS after 4 hours of Kr^+ ion sputtering of the sample surface. As with the Nb/Cu samples, O 1s and C 1s peaks were observed are likely due to oxygen and carbon contamination after exposing the sample to air. The three main spectra of interest are shown in Figure

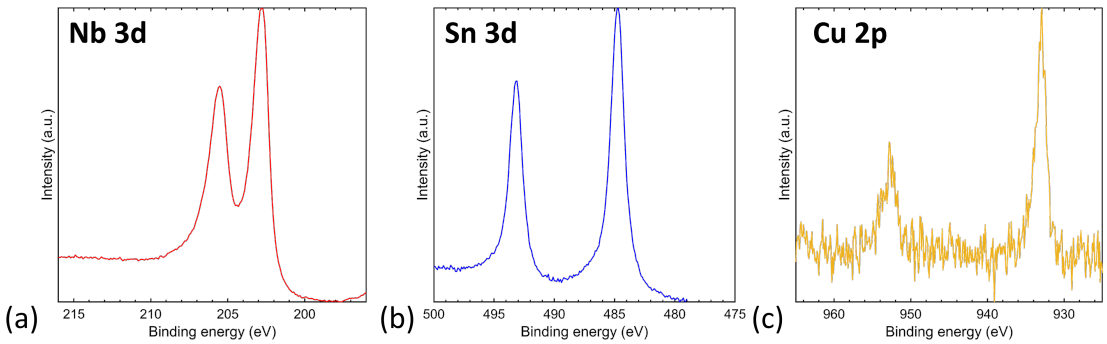

Figure 7.29: Measurements of the XPS core region spectra of a selection of the Nb_3Sn/Nb/Cu (1) sample showing: (a) Nb 3d, (b) Sn 3d (c) Cu 2p.

7.29. The Nb 3d and Sn 3d splittings are observed as expected for a Nb_3Sn surface. However, Cu peaks are also observed in the surface layer despite the surface layer being approximately 3µm thick on top of the Cu substrate. The Nb/Cu target 2 samples previously analysed suggest that this Cu is not due to sample contamination after cutting. Another cut of the Nb_3Sn/Nb/Cu (1) sample was also studied with the SEM, as shown in Figure 7.30. The surface of this sample appears to be very irregular with white blobs of Nb_3Sn on the surface confirmed by EDS. The large peak on the centre of the image is confirmed to be mostly Cu protruding through the surface of the film. These features (approximately 5 µm and 10 µm long) feature in many places on the surface. This Cu, also observed by the XPS, was introduced during the deposition procedure and is likely to be one explanation for higher R_{res} and lower T_c as these features were not observed in the single layer Nb_3Sn samples. Therefore, these bilayer samples were not good.

Previous bilayer studies saw a worse film growth for the bilayer than for the single layer [105]. These studies showed non-homogenous growth and diffusion of Cu from the substrate that was not present in the single-layer growth. This could be a possible explanation for a degradation in superconducting performance and should be studied further. With a much worse superconducting performance than the single Nb_3Sn layer deposited with the same parameters, more research is needed

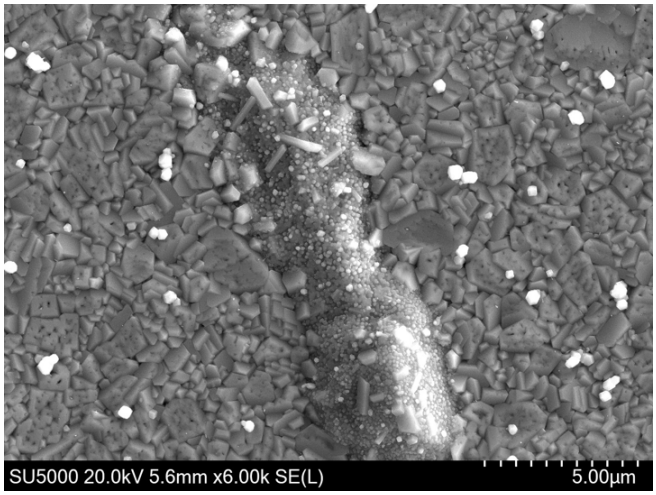

Figure 7.30: An SEM image of the Nb_3Sn/Nb/Cu (1) sample.

to investigate these differences and see whether such layers of materials are worth the effort for cavity depositions. Studies at INFN report improvements in T_c with a thicker 30 µm Nb layer [240], therefore different thicknesses of the Nb layer might be considered in future studies. In addition, research at CERN is ongoing to investigate the effect of a tantalum under layer to act as a diffusion barrier to Cu [241].

Chapter 8

Conclusions

8.1 Choke Cavity Facility

The aim of this work was to utilise a previously designed RF resonator and develop it into a cryogenic facility able to measure the RF performance of thin film superconducting planar samples. Importantly, one of the main goals was to ensure that the facility could test samples with a high throughput rate, thus exceeding that rate of other similar facilities elsewhere. For this, an existing cryogenic facility was modified.

8.1.1 Choke Cavity

The resonator/test cavity that was used to test samples had been previously designed at Lancaster University and Daresbury Laboratory and was later manufactured at Niowave [187]. The cavity, which became known as the Choke Cavity, was made from $RRR = 400$ bulk Nb, operated at 7.8 GHz and was originally designed to test planar samples up to 100 mm in diameter. The unique feature of this test cavity was the addition of three quarter-wavelength RF chokes acting as band-stop filters that allow a sample to be mounted underneath the cavity with a physical gap, whilst ensuring that RF leakage is minimised. The physical gap meant that the sample and cavity could be thermally isolated meaning that their temperature could be controlled and

measured independently, allowing for an RF-DC compensation method to be used to measure the R_s of samples. The aim was to avoid using the alternative end-plate replacement method [122] that risks sample contamination and unreliable R_s measurements due to the requirement a reference sample made from the same ingot of material and treated in the same way as the test cavity.

Prior to developing this facility, the Choke Cavity was rigorously simulated in CST [44] to evaluate the electromagnetic performance of this design and determine whether the position and number of chokes are sufficient to minimise RF leakage. For this, the aim was to maximise Q_{system} - a quantity which combines the total Ohmic losses in the Choke Cavity with non-Ohmic (radiative) losses through the sample-cavity gap. Should Q_{system} be dominated by leakage, significant redesign of the cavity might have to be considered.

The initial set of simulations, analysing the performance of the Choke Cavity, looked at a design with a central elliptical cavity and just one choke. This showed that design is very sensitive to small variations in the choke dimensions. For example, a change in choke depth by $\pm 0.01\,\text{mm}$ with fixed gap or a change in choke radial position by $\pm 0.05\,\text{mm}$ with fixed width would be enough to reduce Q_{system} by one order of magnitude due to increased leakage beyond the choke, thus reducing the maximum peak sample magnetic field ($B_{\text{s,pk}}$). This study concluded that such a test cavity design must have at least one extra choke to mitigate leakage.

The addition of an extra two chokes to the model, demonstrated that a three choke bulk Nb design can maintain a $Q_{\text{system}} = 8.4 \times 10^6$ at $4.2\,\text{K}$, which is limited by Ohmic losses. By comparison, a two choke model also benefitted from reduced leakage but was more sensitive to variations in choke parameters. For the three choke design, the radiative losses were 3 orders of magnitude lower, suggesting that the only way to significantly increase Q_{system} further would be to reduce the frequency, minimum measurement temperature or change the Choke Cavity to a material with lower theoretical R_{BCS} (e.g. Nb_3Sn/Cu). Given the difficulties in these further modifications, it was decided that work should continue with the bulk Nb three

choke design.

Further cavity optimisation looked at the size of the sample-cavity gap. The orignal design was for a 2.1 mm gap. Further simulations showed that smaller gaps would increase the percentage of RF power dissipation on the sample to maximise $B_{\mathrm{s,pk}}$. A gap of 1 mm was decided as this would lead to 34% RF heating on the sample (for a Nb sample), 2% higher than the sample heating with a 2.1 mm gap. This also corresponds to an $\approx 10\%$ increase in the maximum attainable $B_{\mathrm{s,pk}}$. Ideally RF heating on the sample would be maximised further, but would again require a Choke Cavity with lower R_{BCS}.

The final simulations looked at optimising the position for RF couplers into the cavity. The input would be positioned in the centre of the central cavity to maximise coupling to the E-field. However, positioning the pickup was more difficult due to the complex cavity shape. The only viable positions were to insert the pickup into a choke. Positioning in the first choke demonstrated an 8% reduction in RF heating on the sample whilst the second and third chokes showed no change. Given the much weaker coupling in the third choke, the second choke was chosen. Further simulations highlighted potential difficulties due to the appearance of Fano resonances whilst a pickup is inserted in choke 2. These arise due to the destructive interference of two modes close to each other. However, the mode separation was measured to be ≈ 300 MHz, which is much higher than the few kHz bandwidth expected with the cavity, therefore a pickup in choke 2 was confirmed.

Overall, the final Choke Cavity design demonstrated Q_{system} close to 10^7 and a tolerance up to 2 mm on the choke 1 depth of the final design, which was sufficient for the original manufacturing tolerances and post-manufacture chemical etching. Unlike the Surface Impedance Characterisation (SIC) system at JLab [166], the design of the Choke Cavity means that any issues with the chokes post-manufacture, causing higher than expected radiative losses, would not affect sample measurements, as the losses would radiate out of the system. Also, compared to the quadrupole resonators (QPR) [40, 133–136], the Choke Cavity is able to test a

much simpler sample design that is more more versatile for future measurements.

8.1.2 Cryogenic Facility

To test samples with the Choke Cavity, significant modifications were made to an existing cryogenic facility that was originally designed and built at Daresbury Laboratory. This system uses a LHe-free cryocooler. This is a major benefit over other test facilities, most of which use liquid cryogenics, as it avoids potential supply issues with liquid cryogens and allows for safer and easier operation. In this facility, the Choke Cavity is mounted to the stage 2 plate which is cooled by the cold head whilst a sample is mounted underneath with a separate cooling pathway to the Choke Cavity. The downside of not using liquid cryogens was that the minimum temperature possible on the sample was $T_s = 3.6\,\mathrm{K}$ and the maximum RF power was limited by the cold head capacity. However, given that the main aim was to quickly test and compare alternative materials with higher T_c, this was deemed sufficient.

The main modification required the design of a new sample holder for accurate temperature control and measurements of the sample being tested because attaching thermometers, heaters and heat links directly to the sample is difficult. The original sample holder had poor thermalisation with the sample. A new sample holder was designed which could be indium brazed to the centre of the sample to maximise thermal conductance. Given potential issues with thermal gradients, this sample holder was later upgraded (design 1) to cover a much wider area of the sample to achieve better temperature control, alignment and thermal distribution. An alternative sample holder (design 2) was also designed to be tested with a bespoke sample disk. The sample and sample holder can be bolted without the requirement for indium brazing, thus simplifying sample preparation. Modifications to the sample mounting stage increased the maximum sample size to 130 mm diameter whilst also improving the mechanical stability of the sample during testing to minimise vibrations.

In the future, the Choke Cavity facility should aim to prioritise the bolted

design 2 samples as this minimises the risk of sample contamination after deposition. Despite no indium contamination being detected on design 1 samples, there is still a slight risk of contamination during the brazing process in a separated vacuum chamber, which should aim to be avoided.

Additional modifications resulted in the use of G10 to maintain the 1 mm sample-cavity gap because of its low thermal conductivity and good mechanical properties. An improved thermometry and heater system allowed for more accurate temperature control of the sample with the use of Cernox thermometers and heaters connected to a PID temperature controller with more simplified wiring. New heat links to the sample holder were designed to increased the thermal path between the sample and cavity whilst ensuring that a detectable change in temperature with applied heater power was sufficient for the RF-DC compensation to be used.

As well as the cryogenic design, a new RF system was built. Unfortunately, during the period of this work, the system could not be housed in a radiation safe bunker, therefore RF power into the cavity was limited to 1 W. This meant that sufficient fixed attenuators were required at the amplifier input. However, given that the Choke Cavity has a wide bandwidth ($\approx 1\,\mathrm{kHz}$), the system could use a VNA instead of requiring a more complex LLRF control system. Though, the latter should be considered if future Choke Cavity upgrades are able to achieve a smaller cavity bandwidth that is less than the frequency shift due to microphonics.

8.1.3 Commissioning

With the new Choke Cavity facility, an experiment operation procedure was developed to test samples at the highest possible throughput rate. With an easy to open system and simple vacuum operation, it was deemed possible to load a sample and pump down to $< 10^{-4}\,\mathrm{mbar}$ in less than 6 hours. With the ability to remote control the compressor, cooldown could be achieved overnight with the following day dedicated for a full set of sample measurements. Initially only $R_\mathrm{s}(T_\mathrm{s})$ at fixed $B_\mathrm{s,pk}$ and $R_\mathrm{s}(B_\mathrm{s,pk})$ at fixed T_s were going to be made. However, there was enough

measurement time in a day to also measure the resonant frequency shift (Δf) as a function of T_s at fixed cavity temperature (T_cav) to extract T_c and the change in penetration depth ($\Delta\lambda$). The addition of extra heaters in the system allow for rapid warm up overnight meaning that a sample change could be made the day after testing, allowing for a high throughput rate of up to 3 samples to be achieved per week. By comparison, a QPR throughput rate is typically 1 or 2 samples per month. Up until now, RF characterisation at Daresbury Laboratory has these other facilities, therefore optimisation studies have not been possible.

Facility commissioning used one bulk Nb sample and four thin film Nb/Cu samples. Two of the Cu substrates were diamond turned (DT) whilst the other two were metallographically polished (MP) prior to deposition (including one alternative design 2 sample disk) The effect of microphonics was initially investigated, which is a common issue with SRF cavity testing. Through S-parameter measurements with the VNA the resonant frequency shift due to microphonics was measured to be $\approx \pm 1.5\,\mathrm{kHz}$. This was initially an order of magnitude higher prior to the addition and tightening of brackets around the input coupler. Unfortunately, this level of microphonics is significantly larger than LHe test systems due to significant vibrations generated by the mechanical 1 Hz cycle of the cold head. Vibrational analysis confirmed this as the main source along with vibrations from the vacuum pumps and flexible hoses in the system. As well as steps made to reduce the vibrations of the input coupler, any future test facility must use a pulse-tube cryocooler instead of a GM cryocooler to help reduce vibrations by up to 2 orders of magnitude.

The first set of measurements demonstrated was $\Delta f(T_\mathrm{s})$ which showed a clear relation between the variables. Calculations of $d\Delta f/dT_\mathrm{s}$ showed $T_\mathrm{c} \approx 9.2\,\mathrm{K}$ as expected for all five samples. As well as T_c, $\Delta\lambda(T_\mathrm{s})$ was also extracted from the fact that $\Delta\lambda \propto \Delta f$. Attempts were made to fit the data to the Gorter-Casimir expression which is derived from the two-fluid model. However, results showed that this equation does not provide a good fit for all samples. For samples in the clean

limit ($l \gg \xi_0$) the fit is less good close to T_c. In addition, extracting λ_0 proved to be difficult as the sample mean free path (l) likely changes with penetration depth. Multiple fits were performed with different temperature dependences of the two-fluid model to produce a range of λ_0. However, this demonstrated that it was not possible to assess sample parameters with any precision based on the measurement observables of R_s and Δf. Further fits were attempted to extract other material properties (λ_L, ξ_0, l), however it was clear that if a unique set of these parameters are to be extracted for a sample tested with the Choke Cavity, further complementing measurements are required, as detailed in [206].

Further sample measurements demonstrated that it was possible to compare $R_s(B_{s,pk})$ at fixed T_s. These measurements demonstrated that R_s is independent of $B_{s,pk}$ at low $B_{s,pk} < 3\,\mathrm{mT}$. However, little can be said about the $R_s(B_{s,pk})$ sensitivity at higher fields due to $B_{s,pk}$ being limited to 3 mT. Measurements of $R_s(T_s)$ at fixed $B_{s,pk}$ showed an increase of R_s with T_s as expected, within the BCS range for Nb, before a transition to the normal conducting regime above 9 K. BCS fits to extract R_{res} demonstrated a higher R_{res} for the MP samples, which could be a result of the polishing technique potentially introducing particulate inclusions in the surface from the polishing disks and a higher initial roughness. A comparison of samples with different preparation techniques should be performed prior to cavity depositions which are more likely to be chemically polished than DT.

Commissioning also looked at repeatability studies with the design 1 sample holder that requires indium brazing. Measurements of $R_s(B_{s,pk})$ demonstrated consistent measurements regardless of whether $B_{s,pk}$ was increased or decreased. Consistent measurements of $R_s(T_{cav})$ demonstrated good thermal decoupling of the sample and Choke Cavity. Repeated $R_s(T_s)$ for the DT samples, concluded that the samples are not affected by repeated cooldowns without disconnecting the sample and sample holder. For the MP sample, repeated $R_s(T_s)$ measurements also demonstrated repeatability after rapid warm up, dismounting the sample completely and keeping in air for a short time before remounting and cooling down. A re-test

after repeating the indium brazing process, i.e. heating the sample to disconnect it from the sample holder before reheating to re-braze to the sample holder resulted in a slight increase in R_s which could be associated with the vacuum conditions during this process, but further investigations should be performed.

During commissioning, the measurement uncertainties were identified. Typical uncertainties in R_s and B_s are both 14% dominated by the uncertainty in Q_t and P_t (both $\approx$ 20%). The main contributions are systematic uncertainties from RF measurements and cable losses. The random uncertainties on measurements of R_s were estimated during the repeatability studies. For repeating with different T_cav the uncertainty was 1%, repeating with different $B_\mathrm{s,pk}$ was 2%, repeating without sample removal was 1.5% and repeating with sample removal was 2.2%. The uncertainty in temperature was calculated to be $< \pm 45\,\mathrm{mK}$ with contributions from the Cernox uncertainty, temperature gradients calculated in CST and random fluctuations and differences between the two thermometers during a measurement.

It is likely the dominant 20% uncertainties on both Q_t and P_t could be reduced with targeted improvements. For Q_t, the largest uncertainties arise from S-parameter measurements. Whilst instrumentation errors are unavoidable, the impact of microphonics could be mitigated by reducing cryocooler-induced vibrations or further constraining input coupler motion. Such measures could suppress the $\pm 0.2\,\mathrm{dB}$ shifts to below the level of external noise, lowering the uncertainty on Q_t to $\approx$ 14%. For P_t, the main uncertainty is the determination of cable losses, both internal and external. Locating the power sensor directly at the cryostat feedthrough, e.g. via an RF switch, would largely reduce the influence of the external cable loss uncertainty, potentially reducing the overall uncertainty on Q_t to $\approx$ 13%. Taken together, these refinements suggest that the uncertainties on R_s and B_s could be decreased to $\approx$ 10%.

8.2 Sample Studies

8.2.1 Nb/Cu

Facility commissioning with Nb samples demonstrated that the Choke Cavity is an effective tool to be used that can be used at Daresbury Laboratory to compare samples and assist with the optimisation of thin film deposition parameters. As a result, several thin film samples were prepared at Daresbury laboratory to be studied. These studies all used 100 mm diameter OFHC Cu disks that were DT at STFC RAL space to an average roughness ≈ 3 nm. This was done to remove the effect of substrate preparation from the studies and ensure that only the effect of changing deposition parameters was investigated. Investigating the effect of substrate preparation should be considered in the future.

The first study looked at the effect of the deposition temperature on the superconducting performance of Nb/Cu samples deposited by HiPIMS at 400 W. A range of sample temperatures were investigated from 25 °C to 620°C (the maximum achievable in the Daresbury facility). Two sets of samples (target 1 and target 2) were prepared after it was observed that the Nb target material had worn through to the Cu magnetron for the set of samples with target 1.

A clear dependence of R_s with deposition temperature was observed with both sets of samples. The overall R_s of the target 2 samples was lower than the target 1, indicating a possible difference in target quality. Of the target 1 set, the last sample, deposited at 240 °C, had higher than expected R_s likely due to Cu inclusions in the film. Fitting the low-field $R_s(T_s)$ data to extract R_{BCS} at 4.2 K and R_{res}, despite the target quality issues, showed that both sets of samples exhibited a decrease in R_{BCS} with overall optimal RF performance achievable for deposition temperatures in the range $340 - 555$ °C. For the higher quality target 2 set, a much smaller R_{res} from $1 - 4\,\mu\Omega$ was observed whilst the target 1 samples were dominated by a higher R_{res} from $5 - 73\,\mu\Omega$. In addition, excluding the 240 °C target 1 sample, the highest R_{BCS} for both sets was for the sample deposited at room temperature (≈ 25 °C).

Visual inspection also found some film delamination, suggesting that optimal film adhesion is only possible with substrate heating. At higher deposition temperature, R_{BCS} increases which could be due to sub-optimal film growth as the Cu surface starts to deform.

Additional superconducting measurements in a VSM at RAL showed differences in T_{c} between the two targets. The target 2 samples had more consistent T_{c} measurements ranging from $9.1 - 9.4\,\mathrm{K}$, whilst the target 1 had a much wider variation from $8.3 - 9.3\,\mathrm{K}$, with the lower end being the 240 °C sample. Both were consistent with T_{c} measured from the RF frequency shift. For the better quality set of target 2 samples, there was no correlation between T_{c} and deposition temperature as expected for single element depositions. Further tests in a VSM at IEE demonstrated consistent results, with slight variations likely due to different sample cuts being taken from different regions across the large sample disk.

Various surface analysis techniques were also performed on the samples. Roughness measurements with a WLI at Daresbury Laboratory were not sufficient to explain the differences, possibly due to the lack of points measured on the large samples. However, elemental analysis with XPS at Daresbury Laboratory showed clear differences between target 1 and target 2. The main difference being the presence of significant Cu 2p peaks for the target 1 sample. Given that samples were ion beam sputtered for 4 hours, these Cu signals were likely due to Cu mixed in the Nb film and not Cu contamination on the surface from cutting. Cu was almost certainly sputtered during the 240 °C target 1 deposition. Potentially, due to the thickness of the target for the previous depositions, Cu was sputtered for all samples in this set. The lack of Cu in the target 2 samples suggests that the Cu in the film was unlikely to be from the substrate heating.

The better performing target 2 samples were studied in further detail with an SEM at Daresbury Laboratory. This highlighted clear changes to the surface structure with an increase in deposition temperature. There is a clear increase in grain size with deposition temperature, with the smallest grains being for the 25 °C

sample, likely explaining the higher RF losses. The optimal RF performance for the 530 °C sample is likely due to larger grains and a more uniform surface whilst larger cracks and defects appear for the 570 °C sample. The higher than expected R_{BCS} for the 465 °C sample could be due to irregularities on the surface, the cause of which are unknown. Cross-sectional SEM measurements also highlighted that the target 1 samples were $\approx 0.7\,\mu\mathrm{m}$ thinner than target 2 samples despite all samples being deposited for 4.5 h. This can likely be explained the increased target wear causing a reduction in deposition rate.

Overall, this study highlighted that the deposition temperature does affect the RF performance of Nb/Cu samples and the differences in R_{s} between good and bad samples can be resolved with the Choke Cavity. If T_{c} measurements alone were performed with the VSM, these differences in target 2 samples would not be detectable. Excluding the contaminated target 1 samples, the optimal deposition temperature was 530 °C. This was based on this sample having the lowest $R_{\mathrm{BCS,4.2\,K}}$ vs deposition as well as the low $\Delta f(T_{\mathrm{s}})$ correlating with the sharpest transition in normalised magnetic moment.

Future studies should focus on depositions around 530 °C but also investigate the effect of target wear or age that was not considered prior to this study. Also, future studies might consider some surface analysis directly after deposition to analyse the effect of sample cutting on post RF-measurements. If samples are cut for future analysis, more samples could be tested to investigate the uniformity of the sample disks.

8.2.2 Nb_3Sn/Cu

A second set of studies investigated Nb_3Sn on Cu. This is presently the most promising alternative material to replace bulk Nb and allow for 4.2 K operation and higher E_{acc}. However, thin film Nb_3Sn/Cu has yet to match or exceed the performance of Nb_3Sn/Nb produced by Sn vapour diffusion.

For this study, three single-layer Nb_3Sn/Cu samples were all deposited by DCMS

at 620 °C. This deposition temperature was based on previous studies at Daresbury Laboratory that showed that the highest temperature achievable in the system was required to optimise the stochiometry and T_c [105]. However, prior to the Choke Cavity project, no RF measurements were possible until now. Given that deposition temperature was fixed, the effect of magnetron power was investigated with samples produced at 50 W, 100 W and 200 W. A variation in deposition time ensured that all three samples were approximately the same thickness.

RF measurements showed that the Nb_3Sn/Cu benefit from lower magnetron powers, assuming a fixed deposition temperature ≈ 620 °C. Extracting R_{BCS} at 4.2 K showed an increase in R_{BCS} with magnetron power with 50 W being optimal for the samples studied. The 50 W sample demonstrated an R_s approximately one order of magnitude lower than the best Nb/Cu sample studied. The 50 W and 100 W samples had $R_{res} < 1\,\mu\Omega$ however the 200 W sample was dominated by an $R_{res} \approx 16\,\mu\Omega$. Both RF and VSM T_c also demonstrated a dependence on the magnetron power, with the 50 W sample demonstrating T_c 1 K higher (at 17.4 K) compared to the 200 W sample.

Measurements of $R_s(B_{s,pk})$ were also made at $T_s = 4.2$ K. A combination of lower R_s than Nb and slightly narrower cavity bandwidths during tests allowed for a maximum $B_{s,pk} = 5$ mT to be reached, which was slightly higher than during commissioning with Nb. No field dependence on R_s was detectable at these low fields. Further facility upgrades, such as moving to a bunker, using pulsed RF, thin film coated Choke Cavity, should all be considered to allow for R_s measurements at slightly higher $B_{s,pk}$. With the current cryocooler, $B_{s,pk} = 20$ mT could be achieved with these upgrades, thus overlapping with the lower fields of the QPR.

SEM analysis showed similar high grain density for the 50 W and 100 W samples. However, the worse superconducting performance of the 200 W sample could be explained by smaller grains and the present of large Nb_3Sn inclusions in the surface creating a very rough layer. Also, SIMS analysis showed much higher concentration of Cu in the 200 W film which, like the Nb/Cu target 1 samples, could also be a source of higher R_s.

Overall, this study demonstrated that the RF performance of Nb_3Sn/Cu produced by DCMS can be optimised by reducing the magnetron power (at least down to 50 W). The results of this study also show that the Choke Cavity is able to measure high T_c alternative superconductors. As this study only looked at the effect of one deposition parameter, future studies might consider whether further improvements can be achieved at even lower magnetron powers or identify other parameters that can reduce R_s and increase T_c of Nb_3Sn further. Surface analysis during this study also highlighted that the preparation of contamination free samples is the limiting issue.

8.2.3 Nb_3Sn/Nb/Cu

Two additional Nb_3Sn samples were investigated with a layer of Nb between the Nb_3Sn and Cu to see whether this could improve the Nb_3Sn growth and subsequent RF performance. For the Nb layer, the best deposition temperature was used as determined by the Nb/Cu samples. One of the samples was deposited with 400 W DCMS and other with 400 W HiPIMS. The Nb_3Sn layers were both 50 W DCMS.

The RF performance of this study demonstrated a degradation in RF performance compared to both Nb and Nb_3Sn single layers. R_s was approximately two orders of magnitude higher the single layer Nb_3Sn sample due to a dominant $R_{res} \approx 40\,\mu\Omega$, independent of the deposition method for the Nb layer. Also, T_c (both RF and DC) was approximately 1.3 K lower compared with the single layer Nb_3Sn sample. The VSM measurement of one of the samples demonstrated two transitions corresponding to the bilayer structure. The Nb transition was also lower than expected at 8.25 K suggesting that this layer was degraded.

Unlike the 50 W single-layer sample, both XPS and SEM analysis of the bilayers showed significant levels of Cu in the film. The SEM also showed Cu protruding through the film, creating a non-uniform surface as well as irregular Nb_3Sn growth in places. As with the Nb_3Sn single layer samples, the preparation of contamination free bilayer samples is a major issue. To understand the cause of this, many more

samples must be prepared and the effect of other deposition parameters must be investigated.

The reasons for worse bilayer performance compared to the Nb_3Sn single layers should be investigated further. However, these results are consistent with previous studies at Daresbury Laboratory (albeit without RF measurements) [105]. Understanding the interaction between each layer and the substrate is important before attempting Nb_3Sn depositions on Cu cavities. Tracking Cu diffusion in future samples could also help in the optimisation process.

8.3 Future Work

The Choke Cavity facility has been shown to be an effective tool that can be used as the primary tool for optimising thin film deposition parameters at Daresbury Laboratory. However, there are some future facility upgrades that could be made. These include:

- Moving the facility to a newly built radiation test bunker will lift the RF power limitations, allowing for higher input powers and the possibility of pulsed RF.
- Using Nb_3Sn coated Cu Choke Cavities to reduce the cavity surface resistance and increase the percentage of power dissipated on the sample, allowing for higher $B_{\mathrm{s,pk}}$.
- Using pulse-tube cryocoolers to reduce microphonics and consider higher capacity cryocoolers on the market (e.g., 5 W pulse-tube cryocoolers are now available at Cryomech).
- Using a modified sample holder to measure the dependence of the surface resistance on trapped flux (a known source of residual resistance) and ways of reducing the effects of possible losses. This can be done by integrating Hall probes to the sample holder and investigating the effect of magnetic shielding whilst monitoring the ambient B-field.

- Improve Q_{system} by addressing cleaning of the Choke Cavity assembly.
- Active monitoring of microphonics.
- Improve precision in RF measurements to constrain errors.

A valuable next step to bridge the gap between planar and curved geometries is to perform depositions on split 6 GHz cavity tests using the same planar magnetron setup allowing for direct comparisons. These cavities have the advantage of being able to visually inspect film quality and perform the RF test. It is also possible that cylindrical magnetron configurations can also be used to deposit on planar samples allowing for Choke Cavity tests prior to more traditional closed 1.3 GHz cavity tests. All superconducting measurements on planar samples should inform future 1.3 GHz cavity depositions.

Given the quick turnaround time with the Choke Cavity, this opens up the possibility for many interesting sample studies. Most importantly, this will give a direct indication of film performance under RF conditions, which is the most important indicator of whether the deposition parameters are worth repeating on a cavity. Some ideas of future studies based on this work that are worth considering are:

- Investigating the effect of substrate preparation on RF performance with fixed deposition parameters. The samples studied in this work were prepared by DT or MP to achieve low, consistent roughness. However, cavity treatment typically uses other techniques, such as electropolishing and centrifugal barrel polishing. As these methods are continuously improved, and newer techniques such as plasma electrolytic polishing are being developed, it will be important to understand the effect of these techniques on RF performance.
- More studies should be performed on Nb_3Sn thin films as this is the most promising alternative material. Further research on the effect of Nb buffer layers should be performed to understand why the RF performance differs

from that of single layers. However, all Nb_3Sn studies should first aim to resolve the issues surrounding Cu contamination.

- Compare the RF performance of planar magnetron depositions on both Choke Cavity samples and both split and closed cavities. The latter is worth investigating due the current difficulties in manufacturing cylindrical targets made of alternative materials.

- Investigate whether DC field penetration measurements can predict RF measurements, and whether there is any correlation between results. For this, the Daresbury Laboratory magnetic field penetration facility [119] has recently been upgraded to measure 100 mm diameter samples (i.e. without cutting), with under high parallel DC magnetic fields up to 600 mT and reduced field leakage with magnetic shielding.

Appendix A

Sample Holder Drawings

A.1 Choke Cavity

Section 4 discussed the development of the Choke Cavity from an intial 3.9 GHz 2 choke design to the final 7.8 GHz 3 choke design. CST simulations were performed on different iterations of the design to demonstrate its effectiveness in measuring the RF properties of planar samples whilst minimising RF leakage. A technical drawing of the final Choke Cavity design is shown in Figure A.1.

A.2 Sample Holders

Section 5.2.1 discussed the design of new sample holders that would be mounted to samples for accurate temperature measurement and control. This section first shows the technical drawing for the initial sample holder redesign in Figure A.2.

Further development led to a final iteration of sample holders. The first was the Design 1 sample holder, which must be indium brazed to the sample disk. The technical drawing is shown in Figure A.3. The second was the Design 2 sample holder, which is bolted to a bespoke sample design. The technical drawing of this sample holder is shown in Figure A.4 whilst the bespoke sample is shown in Figure A.5.

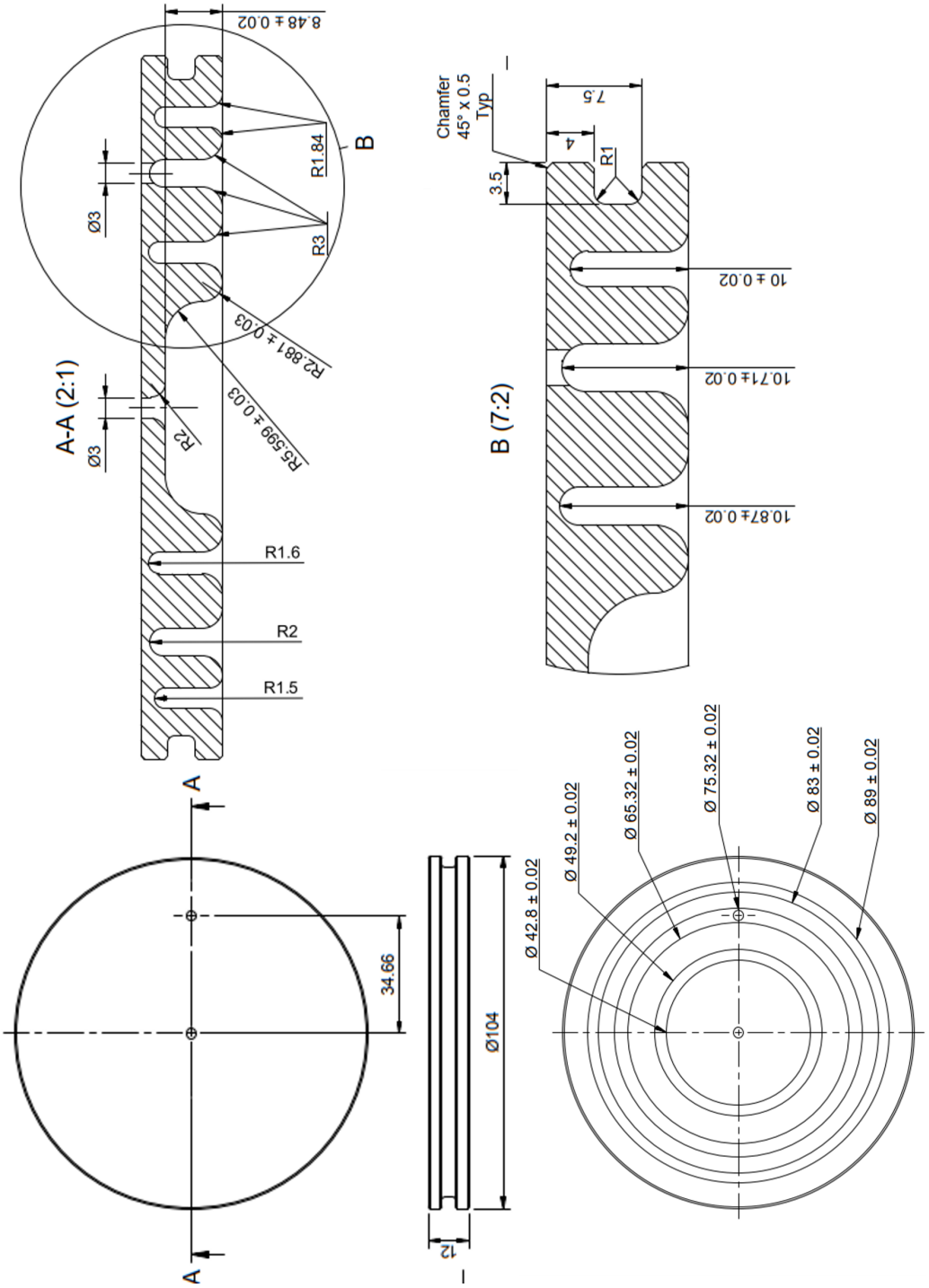

Figure A.1: The Choke Cavity.

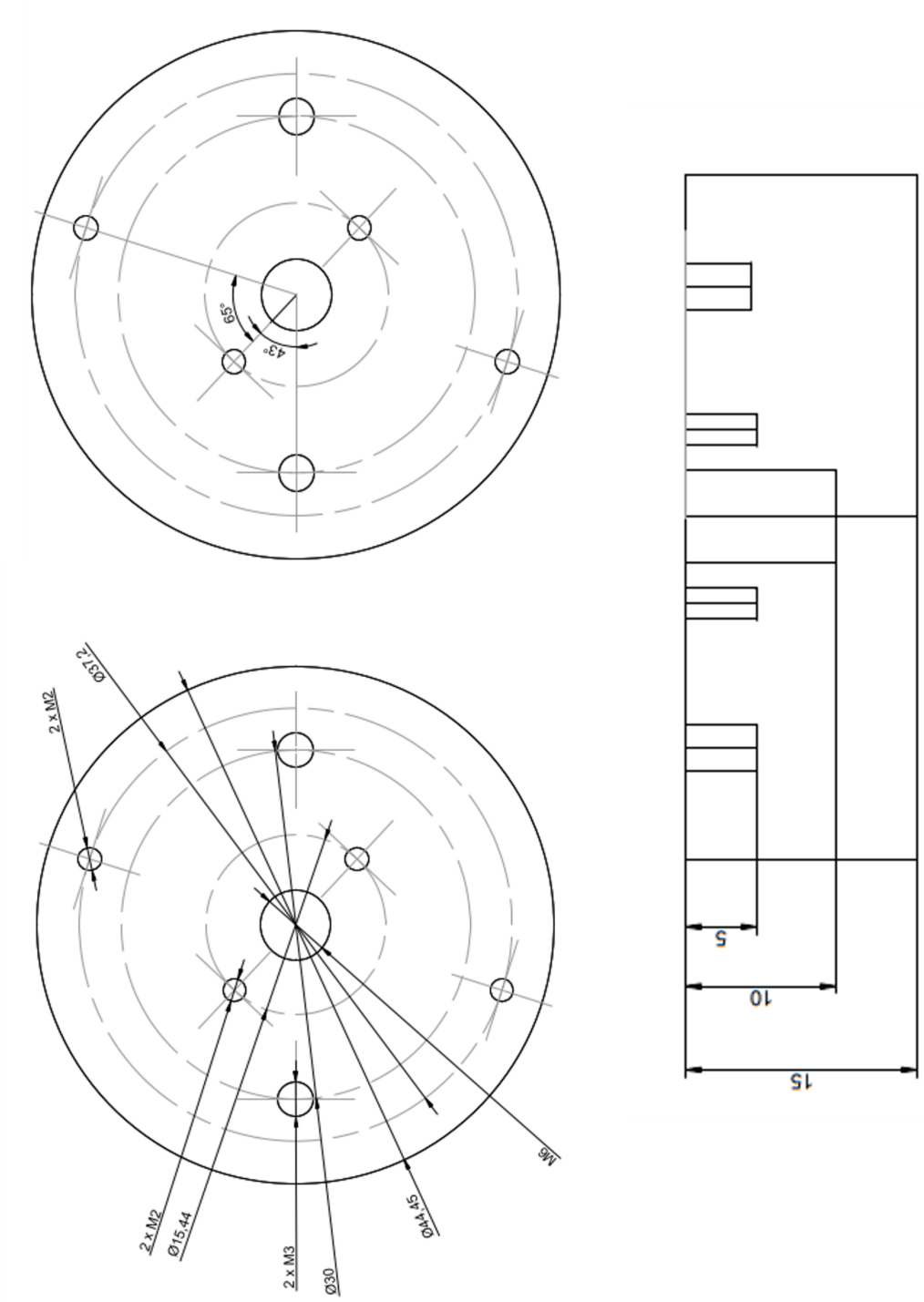

Figure A.2: The first redesign of the sample holder.

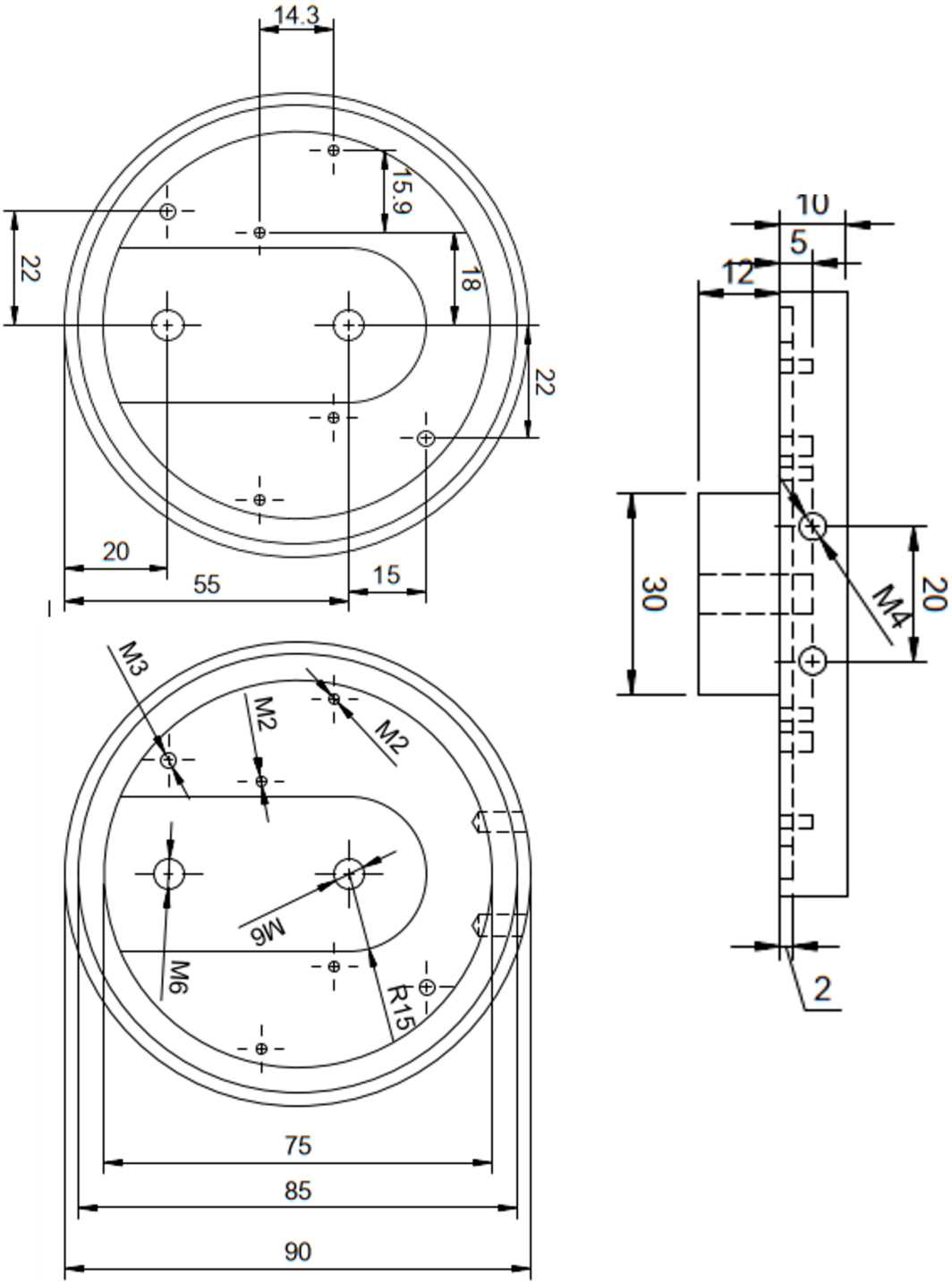

Figure A.3: The Design 1 sample holder.

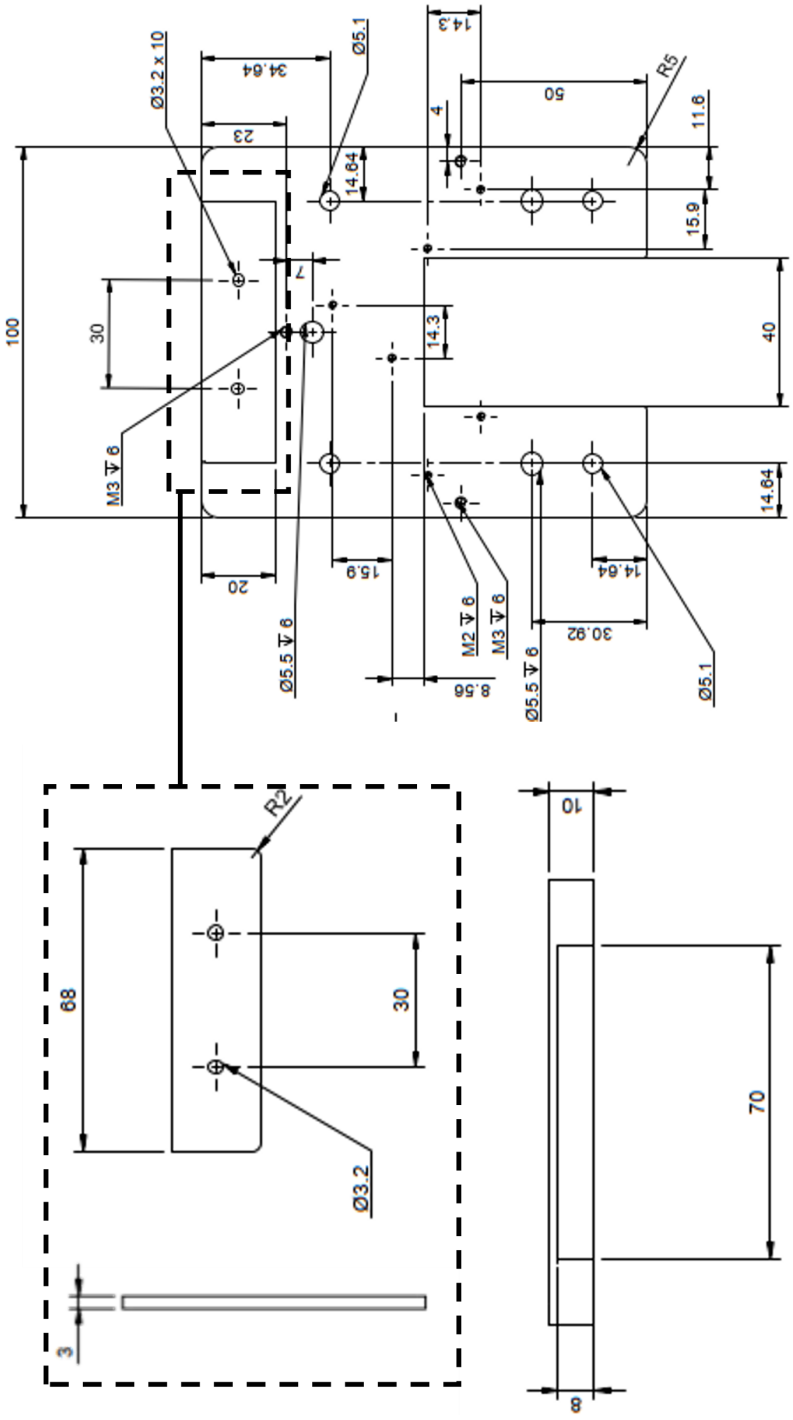

Figure A.4: The Design 2 sample holder.

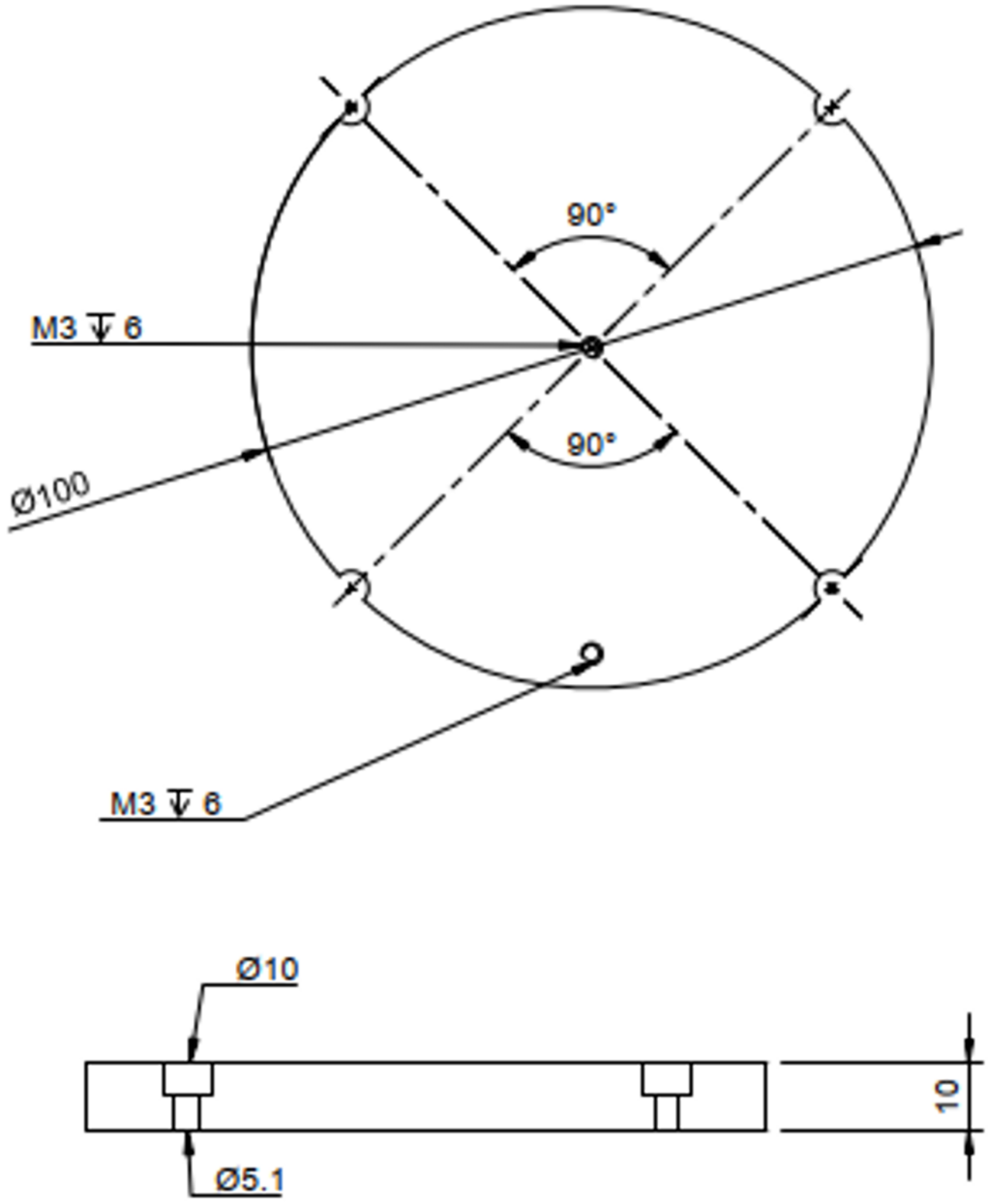

Figure A.5: The Design 2 sample.

References

[1] D. Seal, O. B. Malyshev, P. Goudket, et al. "A high throughput facility for the RF characterisation of planar superconducting thin films". In: *Superconductor Science and Technology* 37.11 (Oct. 2024), p. 115012. DOI: 10.1088/1361-6668/ad7643.

[2] D. Seal, C. Benjamin, O. B. Malyshev, et al. "Upgraded multiprobe sample inserts for thin film SRF cavity developments". In: *Proc. 15th International Particle Accelerator Conference (IPAC '24)* (Nashville, TN, USA). May 2024, pp. 2775–2778. DOI: 10.18429/JACoW-IPAC2024-WEPS38.

[3] C. Benjamin, R. Valizadeh, D. Seal, et al. "V_3Si: an alternative thin film material for superconducting RF cavities". In: *Proc. 15th International Particle Accelerator Conference (IPAC'24)* (Nashville, TN, USA). May 2024, pp. 2779–2781. DOI: 10.18429/JACoW-IPAC2024-WEPS39.

[4] D. Seal, G. Burt, J. A. Conlon, et al. "Optimisation of Niobium Thin Film Deposition Parameters for SRF Cavities". In: *Proc. 21st International Conference on RF Superconductivity (SRF'23)* (Grand Rapids, MI, USA). June 2023, pp. 253–258. DOI: 10.18429/JACoW-SRF2023-MOPMB062.

[5] N. Leicester, G. Burt, D. Seal, et al. "Development and testing of split 6 GHz cavities with niobium coatings". In: *Proc. 21st International Conference on RF Superconductivity (SRF '23)* (Grand Rapids, MI, USA). June 2023, pp. 51–55. DOI: 10.18429/JACoW-SRF2023-MOPMB001.

[6] C. Benjamin, G. Burt, D. Seal, et al. "Deposition and Characterisation of V_3Si Films for SRF Applications". In: *Proc. 21st International Conference on RF Superconductivity (SRF'23)* (Grand Rapids, MI, USA). Sept. 2023, pp. 84–87. DOI: 10.18429/JACoW-SRF2023-MOPMB011.

[7] C. Pira, O. Azzolini, D. Seal, et al. "Progress in European Thin Film Activities". In: *Proc. 21st International Conference on RF Superconductivity (SRF'23)* (Grand Rapids, MI, USA). June 2023, pp. 607–614. DOI: 10.18429/JACoW-SRF2023-WECAA01.

[8] D. Seal, C. Benjamin, G. Burt, et al. "Characterisation Facilities For Evaluating Superconducting Thin Films For SRF Cavities". In: *Proc. 14th International Particle Accelerator Conference (IPAC'23)* (Venice, Italy). May 2023, pp. 2983–2986. DOI: 10.18429/JACoW-IPAC2023-WEPA141.

[9] T. Sian, J. Conlon, D. Seal, et al. "Split 6 GHz SRF thin film cavities". In: *Proc. 14th International Particle Accelerator Conference (IPAC '23)* (Venice, Italy). May 2023, pp. 3074–3077. DOI: 10.18429/JACoW-IPAC2023-WEPA185.

[10] C. Benjamin, R. Valizadeh, D. Seal, et al. "V_3Si Thin Films for SRF Applications". In: *Proc. 14th Internation Particle Accelerator Conference (IPAC'23)* (Venice, Italy). Sept. 2023, pp. 3071–3073. DOI: 10.18429/JACoW-IPAC2023-WEPA184.

[11] T. Sian, G. Burt, D. Seal, et al. "Split thin film SRF 6 GHz cavities". In: *Proc. 31st International Linear Accelerator Conference (LINAC '22)* (Liverpool, UK). Sept. 2022, pp. 814–817. DOI: 10.18429/JACoW-LINAC2022-THP0GE09.

[12] D. Seal, O. B. Malyshev, R. Valizadeh, et al. "RF Characterisation of Bulk Niobium and Thin Film Coated Planar Samples at 7.8 GHz". In: *Proc. 31st International Linear Accelerator Conference (LINAC '22)* (Liverpool, UK). Sept. 2022, pp. 818–821. DOI: 10.18429/JACoW-LINAC2022-THP0GE10.

[13] C. Z. Antoine, S. Berry, D. Seal, et al. "Thin Film Activities in the IFAST Program". In: *Proc. 65th ICFA Adv. Beam Dyn. Workshop High Luminosity Circular e e Colliders (eeFACT2022)* (Frascati, Italy). Sept. 2022, pp. 818–821. DOI: 10.18429/JACoW-eeFACT2022-WEYAS0104.

[14] D. Seal, T. Sian, O. B. Malyshev, et al. "First RF Measurements of Planar SRF Thin Films with a High Throughput Test Facility at Daresbury Laboratory". In: *Proc. 13th International Particle Accelerator Conference (IPAC'22)* (Bangkok, Thailand). June 2022, pp. 1283–1286. DOI: 10.18429/JACoW-IPAC2022-TUPOTK033.

[15] O. B. Malyshev, P. Goudket, D. Seal, et al. "Main Highlights of ARIES WP15 Collaboration". In: *Proc. 20th International Conference on RF Superconductivity (SRF'21)* (East Lansing, MI, USA). June 2021, p. 571. DOI: 10.18429/JACoW-SRF2021-WEPFDV007.

[16] D. Seal, T. Sian, O. B. Malyshev, et al. "A Low Power Test Facility for SRF Thin Film Testing with High Sample Throughput Rate". In: *Proc. 20th International Conference on RF Superconductivity (SRF'21)* (East Lansing, MI, USA). June 2021, p. 100. DOI: 10.18429/JACoW-SRF2021-SUPFDV016.

[17] R. Valizadeh, A. Hannah, D. Seal, et al. "Synthesis of Nb and Alternative Superconducting Film to Nb for SRF Cavity as Single Layer". In: *Proc. 20th International Conference on RF Superconductivity (SRF'21)* (East Lansing, MI, USA). 20. June 2022, p. 893. DOI: 10.18429/JACoW-SRF2021-FROFDV06.

[18] P. J. Bryant. "A Brief History And Review Of Accelerators". In: *CERN Accelerator School: Course on General Accelerator Physics*. 1992, pp. 1–16. DOI: 10.5170/CERN-1994-001.1.

[19] H. P. Singh and M. Kumar. "Applications of Particle Accelerators in Various Industries and Biophysics-A Review". In: *International Journal of Medical and Allied Health Sciences* 01.02 (Dec. 2021), pp. 40–43. DOI: 10.54618/IJMAHS.2021122.

[20] A. J. Antolak. "Overview of Accelerator Applications for Security and Defense". In: *Reviews of Accelerator Science and Technology* 08 (2015), pp. 27–36. DOI: 10.1142/S1793626815300029.

[21] L. Evans and P. Bryant. "LHC Machine". In: *Journal of Instrumentation* 03.08 (Aug. 2008), S08001. DOI: 10.1088/1748-0221/3/08/S08001.

[22] M. Nunes. *Hadron Therapy Physics and Simulations*. New York, NY: Springer New York, 2014, pp. 35–63. DOI: 10.1007/978-1-4614-8899-6_3.

[23] R. J. Van de Graaff, K. T. Compton, and L. C. Van Atta. "The Electrostatic Production of High Voltage for Nuclear Investigations". In: *Phys. Rev.* 43.03 (Feb. 1933), pp. 149–157. DOI: 10.1103/PhysRev.43.149.

[24] J. D. Cockcroft and E. T. S. Walton. "Experiments with High Velocity Positive Ions. (I) Further Developments in the Method of Obtaining High Velocity Positive Ions". In: *Proc. Roy. Soc. Lond. A* 136 (1932), pp. 619–630. DOI: 10.1098/rspa.1932.0107.

[25] T. W. Aitken. "The Daresbury tandem. A review 1970-92". In: *Nuclear Instruments and Methods in Physics Research Section A: Accelerators, Spectrometers, Detectors and Associated Equipment* 328.01 (1993), pp. 10–24. DOI: https://doi.org/10.1016/0168-9002(93)90593-7.

[26] R. Wideröe. *Uber ein neues Prinzip zur Herstellung hoher Spannungen*. Ed. by W. Rogowski. Berlin, Heidelberg: Springer Berlin Heidelberg, 1929, pp. 157–176. DOI: 10.1007/978-3-662-40440-9_14.

[27] E. W. Snedden et al. "Specification and design for full energy beam exploitation of the compact linear accelerator for research and applications". In: *Phys. Rev. Accel. Beams* 27.04 (Apr. 2024), p. 041602. DOI: 10.1103/PhysRevAccelBeams.27.041602.

[28] E. O. Lawrence and N. E. Edlefsen. "On the production of high speed protons". In: *Science* 72.1867 (1930), p. 376.

[29] V. I. Veksler. "A new method of accelerating relativistic particles". In: *Comptes Rendus de l'Académie des Sciences de l'URSS* 43.08 (1944), pp. 329–331.

[30] E. M. McMillan. "The Synchrotron—A Proposed High Energy Particle Accelerator". In: *Phys. Rev.* 68.05-06 (Sept. 1945), pp. 143–144. DOI: 10.1103/PhysRev.68.143.

[31] D. H. Tomboulian and P. L. Hartman. "Properties of Synchrotron Radiation". In: *Phys. Rev.* 102.6 (1956), pp. 1423–1447. DOI: doi:10.1103/PhysRev.102.1423.

[32] D. J. Holder, P. D. Quinn, and N. G. Wyles. "The SRS at Daresbury Laboratory: a Eulogy to the World's First Dedicated High-energy Synchrotron Radiation Source". In: *11th European Particle Accelerator Conference (EPAC'08)* (Genoa, Italy). July 2008, pp. 2133–2135. URL: https://jacow.org/e08/papers/WEPC062.pdf.

[33] M. Altarelli. "Physics with third generation synchrotron sources". In: *Physica Scripta* 1994.T55 (Jan. 1994), pp. 9–13. DOI: 10.1088/0031-8949/1994/T55/001.

[34] M. W. Poole et al. "The DIAMOND Project: An Advanced Light Source for the UK". In: *Proc. 19th Particle Accelerator Conference (PAC'01)* (Chicago, IL, USA). June 2001, pp. 227–229. URL: https://jacow.org/p01/papers/TOPA004.pdf.

[35] H. Chapman. "Fourth-generation light sources". In: *IUCrJ* 10 (Apr. 2023), pp. 246–247. DOI: 10.1107/S2052252523003585.

[36] T. Junginger. "Investigations of the surface resistance of superconducting materials". PhD thesis. University of Heidelberg, July 2012.

[37] H. Padamsee, J. Knobloch, and T. Hays. *RF Superconductivity for Accelerators*. 2nd. Wiley-VCH, 2008.

[38] D. Bafia et al. "Gradients of 50 MV/m in TESLA shaped cavities via modified low temperature bake". In: *Proc. 19th International Conference on RF Superconductivity (SRF'19)* (Dresden, Germany). June 2019, pp. 586–591. DOI: 10.18429/JACoW-SRF2019-TUP061.

[39] A-M. Valente-Feliciano. "Superconducting RF materials other than bulk niobium: a review". In: *Superconductor Science and Technology* 29.11 (Sept. 2016), p. 113002. DOI: 10.1088/0953-2048/29/11/113002.

[40] E. Chiaveri et al. "The Quadrupole Resonator, Construction, RF System, Field Calculations and First Applications". In: *Proc. 6th European Particle Accelerator Conference (EPAC'98)* (Stockholm, Sweden). June 1998, pp. 1852–1854. URL: https://jacow.org/e98/papers/TUP041B.pdf.

[41] J. K. Sekutowicz. "Superconducting Elliptical Cavities (arXiv:1201.2598)". 2022.

[42] D. Proch. "The TESLA Cavity: Design Considerations and RF Properties". In: *Proc. 6th International Conference on RF Superconductivity (SRF'93)* (Newport News, VA, USA). Oct. 1993, pp. 382–397. URL: https://jacow.org/SRF93/papers/SRF93G01.pdf.

[43] B. Aune et al. "Superconducting TESLA cavities". In: *Phys. Rev. ST Accel. Beams* 3 (9 Sept. 2000), p. 092001. DOI: 10.1103/PhysRevSTAB.3.092001.

[44] *CST Studio Suite*. https://www.3ds.com/products-services/simulia/products/cst-studio-suite/. Accessed: 06-11-2024.

[45] J. R. Delayen and K. W. Shepard. "Tests of a superconducting rf quadrupole device". In: *Applied Physics Letters* 57.5 (July 1990), pp. 514–516. DOI: 10.1063/1.103636.

[46] S. Calatroni. *A Mathematica Notebook for the calculation of the anaomalous skin effect in copper*. Tech. rep. CERN, CH-1211 Geneva, Switzerland, 2020.

[47] G. E. H. Reuter and E. H. Sondheimer. "The theory of the anomalous skin effect in metals". In: *A. Mathematical and Physical Sciences* 195 (Dec. 1948), pp. 336–364. DOI: 10.1098/rspa.1948.0123.

[48] H. K. Onnes. "The Resistance of Pure Mercury at Helium Temperatures". In: *Commun. Phys. Lab. Univ. Leiden* 12 (1911).

[49] H. K. Onnes. "The sudden disappearance of the ordinary resistance of tin, and the super-conductive state of lead". In: *Commun. Phys. Lab. Univ. Leiden* 133 (May 1913).

[50] W Meissner and R Ochsenfeld. "Ein neuer Effekt bei Eintritt der Supraleitfähigkeit". In: *Naturwissenschaften* 21 (1933), pp. 787–788.

[51] C. J. Gorter and H. B. G. Casimir. In: *Z.Techn. Physik* 15 (1934), p. 539.

[52] F. London and H. London. "The electromagnetic equations of the supraconductor". In: *Proceedings of The Royal Society A: Mathematical, Physical and Engineering Sciences* 149 (1935), pp. 71–88. DOI: 10.1098/rspa.1935.0048.

[53] J. P. Turneaure, J. Halbritter, and H. A. Schwettman. "The surface impedance of superconductors and normal conductors: The Mattis-Bardeen theory". In: *Journal of Superconductivity* 4.5 (Oct. 1991), pp. 341–355.

[54] J. Bardeen, L. N. Cooper, and J. R. Schrieffer. "Microscopic Theory of Superconductivity". In: *Phys. Rev.* 106 (1 Apr. 1957), pp. 162–164. DOI: 10.1103/PhysRev.106.162.

[55] J. Bardeen, L. N. Cooper, and J. R. Schrieffer. "Theory of Superconductivity". In: *Phys. Rev.* 108 (5 Dec. 1957), pp. 1175–1204. DOI: 10.1103/PhysRev.108.1175.

[56] M. Liepe. *SRIMP*. Accessed: 06-11-2024. 2012. URL: https://www.classe.cornell.edu/~liepe/webpage/researchsrimp.html.

[57] B. Bonin. "Materials for superconducting cavities". In: *CAS - CERN Accelerator School:Superconductivity in Particle Accelerators, CERN-96-03* (May 1995).

[58] J Halbritter. "FORTRAN-PROGRAM FOR THE COMPUTATION OF THE SURFACE IMPEDANCE OF SUPERCONDUCTORS." In: (1970). URL: https://www.osti.gov/biblio/4102575.

[59] C. P. Bean and J. D. Livingston. "Surface Barrier in Type-II Superconductors". In: *Phys. Rev. Lett.* 12 (1 Jan. 1964), pp. 14–16. DOI: 10.1103/PhysRevLett.12.14.

[60] D. Reschke. *Limits in Cavity Performance*. Tutorial, 13th International Conference on RF Superconductivity (SRF'07). Oct. 2007.

[61] U. Klein and D. Proch. "Multipactoring in Superconducting RF Structures". In: *Conference on Future Possibilities for Electron Accelerators* (Charlottesville, VA, USA). Jan. 1979.

[62] W. Weingarten. "Superconducting Cavities". In: *CERN Accelerator School, RF Engineering for Particle Accelerators, CERN 92-03* (1996), p. 318.

[63] H. Padamsee. "Calculations for breakdown induced by "Large defects" in superconducting niobium cavities". In: *IEEE Transactions on Magnetics* 19.3 (1983), pp. 1322–1325. DOI: 10.1109/TMAG.1983.1062561.

[64] R. H. Fowler and L. Nordheim. "Electron emission in intense electric fields". In: *Proc. Roy. Soc. Lond. A* 119 (1928), pp. 173–181. DOI: 10.1098/rspa.1928.0091.

[65] R. J. Noer. "Microscopic Studies of Field Emission From RF Cavity Surfaces". In: *6th International Conference on RF Superconductivity (SRF'93)* (CEBAF, Newport News, Virginia, USA). Oct. 1993, pp. 47–65.

[66] B. Aune et al. “Degradation of Niobium Superconducting RF Cavities During Cooling Time”. In: *Proc. 15th International Linear Accelerator Conference (LINAC’90)* (Albuquerque, NM, USA, Sep. 1990). Sept. 1990, pp. 253–255. URL: https://jacow.org/l90/papers/MO472.pdf.

[67] P. Dhakal. “Nitrogen doping and infusion in SRF cavities: a review”. In: *Physics Open* 5 (2020), p. 100034.

[68] A-M. Valente-Feliciano et al. “Next-generation superconducting RF technology based on advanced thin film technologies and innovative materials for accelerator enhanced performance and energy reach (arXiv:2204.02536)”. Apr. 2022.

[69] C. Antoine. “R&D in superconducting RF: thin film capabilities as a game changer for future sustainability”. In: *Proc. 14th International Particle Accelerator Conference (IPAC’23)* (Venice, Italy). May 2023, pp. 21–26. DOI: 10.18429/JACoW-IPAC2023-MOYD3.

[70] C. Benvenuti, N. Circelli, and M. Hauer. “Niobium films for superconducting accelerating cavities”. In: *Applied Physics Letters* 45.5 (1984), pp. 583–584. ISSN: 00036951. DOI: 10.1063/1.95289.

[71] O. S. Brüning et al. *LHC Design Report*. CERN Yellow Reports: Monographs. Geneva: CERN, 2004. DOI: 10.5170/CERN-2004-003-V-1.

[72] F. Gerigk. “Superconducting RF at CERN: Operation, Projects, and R&D”. In: *IEEE Transactions on Applied Superconductivity* 28.4 (2018), pp. 1–5. DOI: 10.1109/TASC.2018.2792528.

[73] S. Aull et al. “On the Understanding of Q-Slope of Niobium Thin Films”. In: *Proc. 17th International Conference on RF Superconductivity (SRF’15)* (Whistler, Canada). Sept. 2015, pp. 494–500. URL: https://jacow.org/SRF2015/papers/TUBA03.pdf.

[74] V. Palmieri et al. "The Way of Thick Films toward a Flat Q-curve in Sputtered Cavities". In: *Proc. 18th International Conference on RF Superconductivity (SRF'17)* (Lanzhou, China). July 2017, pp. 378–381. DOI: 10.18429/JACoW-SRF2017-TUYBA03.

[75] M. Arzeo et al. "Enhanced radio-frequency performance of niobium films on copper substrates deposited by high power impulse magnetron sputtering". In: *Superconductor Science and Technology* 35.5 (Apr. 2022), p. 054008. DOI: 10.1088/1361-6668/ac5646.

[76] M. C. Burton et al. "RF Results of Nb Coated SRF Accelerator Cavities via HiPIMS". In: *Proc. 29th International Linear Accelerator Conference (LINAC '18)* (Beijing, China). Sept. 2018. DOI: 10.18429/JACoW-LINAC2018-TUPO042.

[77] M. C. Burton et al. "RF Results of Nb Coated SRF Accelerator Cavities via HiPIMS". In: *Proc. 18th International Conference on RF Superconductivity (SRF'17)* (Lanzhou, China). July 2017, pp. 535–538. DOI: 10.18429/JACoW-SRF2017-TUPB066.

[78] S. Leith et al. "HiPIMS deposition of superconducting Nb thin films onto Cu substrates". In: *Vacuum* 212 (2023), p. 112041. DOI: https://doi.org/10.1016/j.vacuum.2023.112041.

[79] W. Venturini Delsolaro and A. Miyazaki. "Seamless Quarter Wave Resonators for HIE ISOLDE". In: *Proc. 29th International Linear Accelerator Conference (LINAC'18)* (Beijing, China). Sept. 2018, pp. 292–296. DOI: 10.18429/JACoW-LINAC2018-TU1A05.

[80] L. Vega Cid et al. "Seamless 1.3 GHz Copper Cavities for Nb Coatings: Cold Test Results of Two Different Approaches". In: *Proc. 20th International Conference on RF Superconductivity (SRF'21)* (East Lansing, MI, USA). July 2021, p. 498. DOI: 10.18429/JACoW-SRF2021-TUPTEV009.

[81] D. Ford et al. "Additive Manufacturing of Pure Niobium and Copper Using Laser Powder Bed Fusion for Particle Accelerator Applications". In: *Proc. 21st International Conference on Radio-Frequency Superconductivity (SRF'23)* (Grand Rapids, MI, USA). June 2023, pp. 872–875. DOI: 10.18429/JACoW-SRF2023-WEPWB119.

[82] F. Peauger et al. "SWELL and Other SRF Split Cavity Development". In: *Proc. 31st International Linear Accelerator Conference (LINAC '22)* (Liverpool, UK). Sept. 2022, pp. 300–304. DOI: 10.18429/JACoW-LINAC2022-TU1AA04.

[83] K. Scibor et al. "SWELL 1.3 GHz Cavity fabrication approach and machining". In: *Proc. 14th International Particle Accelerator Conference (IPAC'23)* (Venice, Italy). May 2023.

[84] A-M. Valente-Feliciano. "Nb Films: Substrates, Nucleation Crystal Growth". In: *Proc. 15th International Conference on RF Superconductivity (SRF'11)* (Chicago, IL, USA). July 2011, pp. 332–342. URL: https://jacow.org/SRF2011/papers/TUIOB06.pdf.

[85] C. Pira et al. "Plasma Electrolytic Polishing as a Promising Treatment Replacement of Electropolishing in the Copper and Niobium Substrate Preparation for SRF". In: *Proc. 20th International Conference on RF Superconductivity (SRF'21)* (East Lansing, MI, USA). 20. Oct. 2022, p. 718. DOI: 10.18429/JACoW-SRF2021-THOTEV06.

[86] E. Chyhyrynets et al. "Plasma Electrolytic Polishing Technology Progress Development for Nb and Cu Substrates Preparation". In: *Proc. 21st International Conference on RF Superconductivity (SRF '23)* (Grand Rapids, MI, USA). 21. June 2023, pp. 75–79. DOI: 10.18429/JACoW-SRF2023-MOPMB009.

[87] O. Hryhorenko et al. "Metallographic Polishing Pathway to the Future of Large Scale SRF Facilities". In: *Proc. 19th International Conference on RF*

Superconductivity (SRF '19) (Dresden, Germany). July 2019, pp. 828–832. DOI: 10.18429/JACoW-SRF2019-THP002.

[88] O. Hryhorenko et al. "Investigation of an Alternative Path for SRF Cavity Fabrication and Surface Processing". In: *Proc. 20th International Conference on RF Superconductivity (SRF'21)* (East Lansing, MI, USA). July 2021, p. 319. DOI: 10.18429/JACoW-SRF2021-MOPFDV001.

[89] O. Hryhorenko et al. "Recent Advances in Metallographic Polishing for SRF Application". In: *Proc. 21th Int. Conf. RF Supercond. (SRF'23)* (Grand Rapids, MI, USA). June 2023, pp. 646–650. DOI: 10.18429/JACoW-SRF2023-WEIXA06.

[90] O. Hryhorenko et al. "Exploring Innovative Pathway for SRF Cavity Fabrication". In: *Proc. 21th International Conference on RF Superconductivity (SRF'23)* (Grand Rapids, MI, USA). June 2023, pp. 680–684. DOI: 10.18429/JACoW-SRF2023-WEPWB050.

[91] S Keckert et al. "Critical fields of Nb3Sn prepared for superconducting cavities". In: *Superconductor Science and Technology* 32.7 (May 2019), p. 075004. DOI: 10.1088/1361-6668/ab119e.

[92] T. Junginger et al. "Critical Fields of SRF Materials". In: *Proc. 9th International Particle Accelerator Conference (IPAC'18)* (Vancouver, Canada). May 2018, pp. 3921–3924. DOI: 10.18429/JACoW-IPAC2018-THPAL118.

[93] A. Godeke. *Nb_3Sn for radio frequency cavities*. Tech. rep. Lawrence Berkeley National Lab.(LBNL), Berkeley, CA (United States), 2006.

[94] M. U. Liepe K. Howard and Z. Sun. "Thermal annealing of DC sputtered Nb_3Sn and V_3Si thin films for superconducting radio-frequency cavities". In: *J. Appl. Phys* 134 (Dec. 2023), p. 225301. DOI: 10.1209/5.0185404.

[95] Y. Wang, T. Plackowski, and A. Junod. "Specific heat in the superconducting and normal state (2–300 K, 0–16 T), and magnetic susceptibility of the 38 K superconductor MgB2: evidence for a multicomponent gap". In: *Physica*

C: Superconductivity 355.3 (2001), pp. 179–193. DOI: https://doi.org/10.1016/S0921-4534(01)00617-7.

[96] F. Laube et al. "Superconducting energy gap distribution of MgB2 investigated by point-contact spectroscopy". In: *Europhysics Letters* 56.2 (Oct. 2001), p. 296. DOI: 10.1209/epl/i2001-00519-4.

[97] S. M. Deambrosis et al. "A15 Superconductors: An Alternative to Niobium for RF Cavities". In: *Proc. 12th International Workshop on RF Superconductivity SRF'05* (Ithaca, NY, USA). July 2005, pp. 205–209. URL: https://jacow.org/SRF2005/papers/TUA13.pdf.

[98] R.A. Rimmer et al. *Next Generation SRF accelerators based on Nb_3Sn.* Tech. rep. LOI Snowmass, 2021.

[99] S. Posen and D. L. Hall. "Nb_3Sn superconducting radiofrequency cavities: fabrication, results, properties, and prospects". In: *Superconductor Science and Technology* 30.3 (Jan. 2017). DOI: 10.1088/1361-6668/30/3/033004.

[100] P. Kneisel et al. "Nb3Sn Layers on High-Purity Nb Cavities with Very High Quality Factors and Accelerating Gradients". In: *Proc. 5th European Particle Accelerator Conference (EPAC'96)* (Sitges, Spain). June 1996, pp. 2085–2087.

[101] S. Posen and M. Liepe. "Advances in development of Nb_3Sn superconducting radio-frequency cavities". In: *Phys. Rev. ST Accel. Beams* 17.11 (Nov. 2014), p. 112001. DOI: 10.1103/PhysRevSTAB.17.112001.

[102] S. Posen et al. "Advances in Nb_3Sn superconducting radiofrequency cavities towards first practical accelerator applications". In: *Superconductor Science and Technology* 34.2 (Jan. 2021), p. 025007. DOI: 10.1088/1361-6668/abc7f7.

[103] A. Gurevich. "Enhancement of RF breakdown field of superconductors by multilayer coating". In: *Applied Physics Letters* 88 (Feb. 2006), p. 012511.

[104] N. M. Verboncoeur et al. "Next-Generation Nb_3Sn Superconducting RF Cavities". In: *Proc. 31st International Linear Accelerator Conference (LINAC'22)* (Liverpool, UK). 31. Oct. 2022, pp. 305–309. DOI: 10.18429/JACoW-LINAC2022-TU1AA06.

[105] R. Valizadeh et al. "PVD Depostion of Nb_3Sn Thin Film on Copper Substrate from an Alloy Nb_3Sn Target". In: *Proc. 10th International Particle Accelerator Conference (IPAC'19)* (Melbourne, Australia). May 2019, pp. 2818–2821. DOI: 10.18429/JACoW-IPAC2019-WEPRB011.

[106] F. B. Lockwood Estrin et al. "Using HiPIMS to Deposit V_3Si Superconducting Thin Films". In: *Proc. 20th International Conference on RF Superconductivity (SRF'21)* (East Lansing, MI, USA). June 2022.

[107] S. Wilde et al. "High Power Impulse Magnetron Sputtering of Thin Films for Superconducting RF Cavities". In: *Proc. 17th International Conference on RF Superconductivity (SRF'15)* (Whistler, Canada). Sept. 2015, pp. 647–650. URL: https://jacow.org/SRF2015/papers/TUPB040.pdf.

[108] A. Hannah et al. "A First 6 GHz Cavity Deposition with B1 Superconducting Thin Film at ASTeC". In: *Proc. 13th International Particle Accelerator Conference IPAC'22* (Bangkok, Thailand). July 2022, pp. 1279–1282. DOI: 10.18429/JACoW-IPAC2022-TUPOTK031.

[109] P. Pizzol et al. "CVD Deposition of Nb Based Materials for SRF Cavities". In: *Proc. 7th International Particle Accelerator Conference (IPAC'16)* (Busan, Korea). June 2016, pp. 2241–2244. DOI: 10.18429/JACoW-IPAC2016-WEPMB056.

[110] P. Pizzol et al. "Atomic Layer Deposition of Niobium Nitride from Different Precursors". In: *Proc. 8th International Particle Accelerator Conference (IPAC'17)* (Copenhagen, Denmark). May 2017, pp. 1094–1097. DOI: 10.18429/JACoW-IPAC2017-MOPVA100.

[111] N. Misra, A. N. Hannah, and R. Valizadeh. "Facile Deposition of Superconducting MgB_2 Thin Films on Substrates: A Comparative Investigation of Electrochemical Deposition and Magnetron Sputtering Techniques". In: *Proc. 10th International Particle Accelerator Conference (IPAC'19)* (Melbourne, Australia). May 2019, pp. 2984–2986. DOI: 10.18429/JACoW-IPAC2019-WEPRB070.

[112] O. B. Malyshev et al. "First Results of Magnetic Field Penetration Measurements on Multilayer S-I-S Structures". In: *Proc. 7th International Particle Accelerator Conference (IPAC'16)* (Busan, Korea). May 2016, pp. 2245–2247. DOI: 10.18429/JACoW-IPAC2016-WEPMB057.

[113] S. Wilde. "Development of superconducting thin films for use in SRF cavity applications". PhD thesis. Loughborough University, Dec. 2018.

[114] Xie D. et al. "Deposition of titanium films on complex bowl-shaped workpieces using DCMS and HiPIMS". In: *Surface and Coatings Technology* 442 (July 2022), p. 128192. DOI: https://doi.org/10.1016/j.surfcoat.2022.128192.

[115] R. S. Rastogi, V. D. Vankar, and K. L. Chopra. "Simple planar magnetron sputtering source". In: *Review of Scientific Instruments* 58.8 (Aug. 1987), pp. 1505–1506. DOI: 10.1063/1.1139388.

[116] A. Bianchi et al. "Thickness effect on superconducting properties of niobium films for radio-frequency cavity applications". In: *Superconductor Science and Technology* 37.8 (June 2024), p. 085005. DOI: 10.1088/1361-6668/ad59ce.

[117] O. B. Malyshev et al. "A facility for magnetic field penetration measurements on multilayer S-I-S structures". In: *Proc. 17th International Conference on RF Superconductity (SRF'15)* (Whistler, Canada). Sept. 2015, pp. 716–719. DOI: 10.18429/JACoW-SRF2015-TUPB059.

[118] O. B. Malyshev et al. "Design, Assembly and Commissioning of a New Cryogenic Facility for Complex Superconducting Thin Film Testing". In: *Proc. 9th International Particle Accelerator Conference (IPAC'18)* (Vancouver, Canada). Apr. 2018, pp. 3859–3861. DOI: 10.18429/JACoW-IPAC2018-THPAL089.

[119] D. A. Turner et al. "A facility for the characterisation of planar multilayer structures with preliminary niobium results". In: *Superconductor Science and Technology* 35.9 (July 2022), p. 095004. DOI: 10.1088/1361-6668/ac7fbf.

[120] L. Smith et al. "Investigation, using Nb foils to characterise the optimal dimensions of samples measured by the magnetic field penetration facility". In: *Proc. 21st International Conference on RF Superconductivity (SRF'23)* (Grand Rapids, MI, USA). June 2023, pp. 88–91. DOI: 10.18429/JACoW-SRF2023-MOPMB012.

[121] P. Goudket, T. Junginger, and B. P. Xiao. "Devices for SRF material characterization". In: *Superconductor Science and Technology* 30.1 (Nov. 2016), p. 013001. DOI: 10.1088/0953-2048/30/1/013001.

[122] Y. Bruynseraede et al. "Surface-resistance measurements in TE_{011}-mode cavities of superconducting indium, lead and an indium-lead alloy at low and high RF magnetic fields". In: *Physica* 54.1 (1971), pp. 137–159. DOI: https://doi.org/10.1016/0031-8914(71)90066-8.

[123] A. Bianchi and W. Venturini Delsolaro. "Temperature mapping on a niobium-coated copper superconducting radio-frequency cavity". In: *Sci. Rep.* 13.1 (May 2023), p. 17075. DOI: 10.1038/s41598-023-44021-w.

[124] M. Ge et al. "A temperature-mapping system for multi-cell SRF accelerating cavities". In: *Proc. North American Particle Accelerator Conference (NA-PAC'13)*. Sept. 2015.

[125] T. E. Oseroff, M. Liepe, and Z. Sun. "Sample Test Systems for Next-Gen SRF Surfaces". In: *Proc. 20th International Conference on RF Superconductivity (SRF'21)* (East Lansing, MI, USA). Oct. 2022, p. 357. DOI: 10.18429/JACoW-SRF2021-TUOFDV07.

[126] C. D. Nantista et al. "Test bed for superconducting materials". In: *Proc. 21st Particle Accelerator Conference (PAC'05)* (Knoxville, TN, USA). May 2005, pp. 4227–4229. URL: https://jacow.org/p05/papers/WPAT089.pdf.

[127] J. Guo et al. "Cryogenic RF Material Testing with a High-Q Copper Cavity". In: *AIP Conference Proceedings* 1299.1 (Nov. 2010). DOI: 10.1063/1.3520338.

[128] Y. Xie, J. H. Hinnefeld, and M. Liepe. "Design of a TE-Type Cavity for Testing Superconducting Material Samples". In: *Proc. 14th International Conference on RF Superconductivity (SRF'09)* (Berlin, Germany). Sept. 2009, pp. 281–285. URL: https://jacow.org/SRF2009/papers/TUPPO034.pdf.

[129] N. J. Pogue et al. "Ultra-Gradient Test Cavity for Testing SRF Wafer Samples". In: *IEEE Transactions on Applied Superconductivity* 21.3 (June 2011), pp. 1903–1907. DOI: 10.1109/TASC.2010.2088091.

[130] S. C. Huang et al. "The Electromagnetic Optimization of TE-sample Host Cavity at IMP". In: *Proc. 29th International Linear Accelerator Conference (LINAC'18)* (Beijing, China). Sept. 2018, pp. 852–854. DOI: 10.18429/JACoW-LINAC2018-THPO069.

[131] X. Wang et al. "Development of a TE-mode sample host cavity". In: *Proc. 15th International Particle Accelerator Conference (IPAC'24)* (Nashville, TN, USA). May 2024, pp. 2795–2797. DOI: 10.18429/JACoW-IPAC2024-WEPS45.

[132] M. Ribeaudeau et al. "Surface Resistance Measurements of Superconducting Samples with Vacuum Insulated Thermometers". In: *Proc. 6th European Particle Accelerator Conference (EPAC'98)* (Stockholm, Sweden). June 1998, pp. 1873–1875. URL: https://jacow.org/e98/papers/TUP05B.pdf.

[133] V. del Pozo Romano et al. "Redesign of CERN's Quadrupole Resonator for Testing of Superconducting Samples". In: *Proc. 18th International Conference on RF Superconductivity (SRF'17)* (Lanzhou, China). July 2017, pp. 420–422. DOI: 10.18429/JACoW-SRF2017-TUPB016.

[134] S. Keckert et al. "Characterizing materials for superconducting radiofrequency applications—A comprehensive overview of the quadrupole resonator design and measurement capabilities". In: *Review of Scientific Instruments* 92.6 (June 2021), p. 064710. DOI: 10.1063/5.0046971.

[135] R. Monroy-Villa et al. "Status of the new quadrupole resonator for SRF R&D". In: *Proc. 20th International Conference on RF Superconductivity (SRF'21)*. June 2022, pp. 751–755. DOI: 10.18429/JACoW-SRF2021-THPFDV001.

[136] B. P. Xiao et al. "Note: Radio frequency surface impedance characterization system for superconducting samples at 7.5 GHz". In: *Review of Scientific Instruments* 82.5 (May 2011), p. 056104. DOI: 10.1063/1.3575589.

[137] S. G. Tantawi et al. "Superconducting materials testing with a high-Q copper RF cavity". In: *Proc. 22nd Particle Accelerator Conference (PAC'07)* (Albuquerque, NM, USA). June 2007, pp. 2370–2372. URL: https://jacow.org/p07/papers/WEPMS018.pdf.

[138] A. Canabal et al. "Critical magnetic field determination of superconducting materials". In: *Proc. 11th European Particle Accelerator Conference (EPAC'08)* (Genoa, Italy). June 2008, pp. 919–921. URL: https://jacow.org/e08/papers/MOPP157.pdf.

[139] J. Guo et al. "A Cryogenic RF Material Testing Facility at SLAC". In: *Proc. 1st International Particle Accelerator Conference (IPAC'10)* (Kyoto, Japan). May 2010, pp. 3049–3051. URL: http://accelconf.web.cern.ch/IPAC10/papers/WEPEC073.pdf.

[140] J. Guo et al. "Cryogenic RF Material Testing at SLAC". In: *Proc. 24th Particle Accelerator Conference (PAC'11)* (New York, NY, USA). Mar. 2011, pp. 1030–1032. URL: https://jacow.org/PAC2011/papers/TUP102.pdf.

[141] J. Guo et al. "Testing the RF Properties of Novel Superconducting Materials". In: *Proc. 15th International Conference on RF Superconductivity (SRF'11)* (July 2011), pp. 325–329. URL: https://accelconf.web.cern.ch/SRF2011/papers/tuiob03.pdf.

[142] P. B. Welander, M. A. Franzi, and S. G. Tantawi. "Cryogenic RF Characterization of Superconducting Materials at SLAC With Hemispherical Cavities". In: *Proc. 17th International Conference on RF Superconductivity (SRF'15)* (Whistler, Canada). Sept. 2015, pp. 735–738. URL: https://jacow.org/SRF2015/papers/TUPB065.pdf.

[143] H. Oikawa et al. "Design Study of a Test Cavity for Evaluating RF Critical Magnetic Field of Thin-Film Superconductor". In: *Proc. 28th International Linear Accelerator Conference (LINAC'160)* (East Lansing, MI, USA). May 2017, pp. 852–854. DOI: 10.18429/JACoW-LINAC2016-THPLR006.

[144] H. Oikawa, H. Hayano, and T. Higashiguchi. "Design Study of Mushroom Shaped Cavity for Evaluation of RF Critical Magnetic Field of Thin-film Superconductor". In: *Proc. 18th International Conference on RF Superconductivity (SRF'17)* (Lanzhou, China). July 2017, pp. 914–916. DOI: 10.18429/JACoW-SRF2017-THPB077.

[145] H. Oikawa et al. "Fabrication of Nb Mushroom Shaped Cavity for Evaluation of Multi-layer Thin-film Superconductor". In: *Proc. 29th International Linear*

Accelerator Conference (LINAC'18) (Beijing, China). Sept. 2018, pp. 454–457. DOI: 10.18429/JACoW-LINAC2018-TUP0053.

[146] H. Oikawa, T. Higashiguchi, and H. Hayano. "Design of niobium-based mushroom-shaped cavity for critical magnetic field evaluation of superconducting multilayer thin films toward achieving higher accelerating gradient cavity". In: *Japanese Journal of Applied Physics* 58.2 (Jan. 2019), p. 028001. DOI: 10.7567/1347-4065/aaf46a.

[147] D. L. Hall et al. "Development and Performance of a High Field TE-Mode Sample Host Cavity". In: *Proc. 16th International Conference on RF Superconductivity (SRF'13)* (Paris, France). Sept. 2013, pp. 985–987. URL: https://epaper.kek.jp/SRF2013/papers/thp038.pdf.

[148] D. L. Hall et al. "SRF Material Performance Studies using a Sample Host Cavity". In: *Proc. 5th International Particle Accelerator Conference (IPAC'14)* (Dresden, Germany). June 2014, pp. 2638–2640. DOI: 10.18429/JACoW-IPAC2014-WEPRI065.

[149] J. T. Maniscalco et al. "Recent Results from the Cornell Sample Host Cavity". In: *Proc. 17th International Conference on RF Superconductivity (SRF'15)* (Whistler, Canada). Sept. 2015, pp. 626–628. URL: https://jacow.org/SRF2015/papers/TUPB030.pdf.

[150] J. T. Maniscalco, D. L. Hall, and M. Liepe. "RF Performance Studies of Thin-Film Superconductors Using a Sample Host Cavity". In: *Proc. 6th International Particle Accelerator Conference (IPAC'15)* (Richmond, VA, USA). May 2015, pp. 3462–3463. DOI: 10.18429/JACoW-IPAC2015-WEPTY076.

[151] N. Pogue, C. E. Reece, and P. M. McIntyre. "Ultimate-Gradient SRF Test Cavity and Low Loss Tangent Measurements in Ultra Pure Sapphire". In: *Proc. 25th International Linear Accelerator Conference (LINAC'10)*

(Tsukuba, Japan). Sept. 2010, pp. 842–844. URL: https://jacow.org/LINAC2010/papers/THP038.pdf.

[152] J. K. Comeaux. "Testing and Simulation of the SRF Wafer Test Cavity for the Characterization of Superconductors and Heterostructures". MA thesis. Texas A&M University, Aug. 2014.

[153] N. J. Pogue et al. "First Results of the SRF Wafer Test Cavity for the Characterization of Superconductors". In: *IEEE Transactions on Applied Superconductivity* 25.3 (Oct. 2015), pp. 1–4. DOI: 10.1109/TASC.2014.2362415.

[154] E. Mahner et al. "A new instrument to measure the surface resistance of superconducting samples at 400 MHz". In: *Review of Scientific Instruments* 74.7 (July 2003), pp. 3390–3394. DOI: 10.1063/1.1578157.

[155] T. Junginger, W. Weingarten, and C. Welsch. "Extension of the measurement capabilities of the quadrupole resonator". In: *Review of Scientific Instruments* 83.Jun (June 2012), p. 063902. DOI: 10.1063/1.4725521.

[156] R. Monroy-Villa et al. "Design and Fabrication of a Quadrupole-Resonator for Sample R&D". In: *Proc. 19th International Conference on RF Superconductivity (SRF'19)* (Dresden, Germany). June 2019, pp. 838–841. DOI: 10.18429/JACoW-SRF2019-THP004.

[157] R. Monroy-Villa et al. "Commissioning of the UHH Quadrupole Resonator at DESY". In: *Proc. 21st International Conference on RF Superconductivity (SRF'23)* (Grand Rapids, MI, USA). June 2023, pp. 952–959. DOI: 10.18429/JACoW-SRF2023-THCAA02.

[158] S. Aull et al. "High Resolution Surface Resistance Studies". In: *Proc. 16th International Conference on RF Superconductivity (SRF'13)* (Paris, France). Sept. 2013, pp. 785–788. URL: https://jacow.org/SRF2013/papers/WEIOC01.pdf.

[159] R. Kleindienst, J. Knobloch, and O. Kugeler. "Development of an Optimized Quadrupole Resonator at HZB". In: *Proc. 16th International Conference on RF Superconductivity (SRF'13)* (Paris, France). Sept. 2013, pp. 614–616. URL: https://jacow.org/SRF2013/papers/TUP074.pdf.

[160] R. Kleindienst et al. "Commissioning Results of the HZB Quadrupole Resonator". In: *Proc. 17th International Conference on RF Superconductivity (SRF'15)* (Whistler, Canada). Sept. 2015, pp. 930–936. URL: https://jacow.org/SRF2015/papers/WEA1A04.pdf.

[161] S. Keckert et al. "Design and First Measurements of an Alternative Calorimetry Chamber for the HZB Quadrupole Resonator". In: *Proc. 17th International Conference on RF Superconductivity (SRF'15)* (Whistler, Canada). Sept. 2015, pp. 739–743. URL: https://jacow.org/SRF2015/papers/TUPB067.pdf.

[162] S. Keckert et al. "Surface Resistance Characterization of Nb_3Sn Using the HZB Quadrupole Resonator". In: *Proc. 18th International Conference on RF Superconductivity (SRF'17)* (Lanzhou, China). July 2017, pp. 863–866. DOI: 10.18429/JACoW-SRF2017-THPB053.

[163] S. Keckert et al. "The Challenge to Measure nΩ Surface Resistance on SRF Samples". In: *Proc. 9th International Particle Accelerator Conference (IPAC'18)* (Vancouver, Canada). Apr. 2018, pp. 2812–2815. DOI: 10.18429/JACoW-IPAC2018-WEPML049.

[164] D. B. Tikhonov et al. "Superconducting Thin Films Characterization at HZB with the Quadrupole Resonator". In: *Proc. 19th International Conference on RF Superconductivity (SRF'19)* (Dresden, Germany). June 2019, pp. 616–620. DOI: 10.18429/JACoW-SRF2019-TUP073.

[165] S. Bira et al. "Geometry Optimization for a Quadrupole Resonator at Jefferson Lab". In: *Proc. 21st International Conference on RF Superconductivity*

(SRF'23) (Grand Rapids, MI, USA). June 2023, pp. 670–673. DOI: 10.18429/JACoW-SRF2023-WEPW048.

[166] L. Phillips et al. "A sapphire loaded TE011 cavity for surface impedance measurements - design, construction, and commissioning status". In: *Proc. 12th International Workshop on RF Superconductivity (SRF'05)* (Ithaca, NY, USA). July 2005, pp. 349–351. URL: https://jacow.org/SRF2005/papers/TUP46.pdf.

[167] B. Xiao et al. "Commissioning of the SRF surface impedance characterization system at Jefferson Lab". In: *Proc. 23rd Particle Accelerator Conference (PAC'09)* (Vancouver, Canada). May 2009, pp. 2144–2146. URL: https://jacow.org/PAC2009/papers/WE5PFP061.pdf.

[168] B. Xiao. "Surface impedance of superconducting radio frequency (SRF) materials". PhD thesis. College of William & Mary - Arts & Sciences, Aug. 2012.

[169] B. Xiao et al. "RF surface impedance measurement of polycrystalline and large grain Nb disk sample at 7.5 GHz". In: *Proc. 14th International Conference on RF Superconductivity (SRF'09)* (Berlin, Germany, Sep. 2009). Sept. 2009, pp. 305–308. URL: https://jacow.org/SRF2009/papers/TUPPO042.pdf.

[170] B. P. Xiao et al. "RF surface impedance characterization of potential new materials for SRF-based accelerators". In: *Proc. 26th International Linear Accelerator Conference (LINAC'12)* (Tel Aviv, Israel, Sep. 2012). Sept. 2012, pp. 312–314. URL: https://jacow.org/LINAC2012/papers/MOPB060.pdf.

[171] G. V. Eremeev et al. "Characterization of superconducting samples with SIC system for thin film developments: status and recent results." In: *Proc. 16th International Conference on RF Superconductivity (SRF'13)* (Paris, France). Sept. 2013, pp. 599–602. URL: https://jacow.org/SRF2013/papers/TUP070.pdf.

[172] B. P. Xiao et al. "Surface impedance measurements of single crystal MgB2 films for radiofrequency superconductivity applications". In: *Superconductor Science and Technology* 25.9 (July 2012), p. 095006. DOI: 10.1088/0953-2048/25/9/095006.

[173] B. Xiao and C. E. Reece. "RF surface impedance of a two-band superconductor". In: *Physical Review Accelerators and Beams* 22.5 (May 2019). DOI: 10.1103/PhysRevAccelBeams.22.053101.

[174] R. A. Lukaszew et al. "Proof of concept thin films and multilayers toward enhanced field gradients in SRF cavities". In: *Proc. 16th International Conference on RF Superconductivity (SRF'13)* (Paris, France). Sept. 2013, pp. 782–784. URL: https://jacow.org/SRF2013/papers/WEIOB02.pdf.

[175] S. Sosa-Guitron et al. "Measurements of RF properties of thin film Nb_3Sn superconducting multilayers using a calorimetric technique". In: *Proc. 17th International Conference on RF Superconductivity (SRF'15)* (Whistler, Canada). Sept. 2015, pp. 720–722. URL: https://jacow.org/SRF2015/papers/TUPB060.pdf.

[176] M. Juillard et al. "Superconducting Surface Resistance Measurements with a TE011 Cavity". In: *Proc. 2nd European Particle Accelerator Conference (EPAC'90)* (Nice, France). June 1990, pp. 1106–1109.

[177] M. Fouaidy et al. "New results on RF properties of superconducting niobium films using a thermometric system". In: *Proc. 8th European Particle Accelerator Conference (EPAC'02)* (Paris, France). June 2002, pp. 2229–2231. URL: https://jacow.org/e02/papers/THPDO038.pdf.

[178] G. Martinet et al. "Development of a TE011 cavity for thin-films study". In: *Proc. 14th International Conference on RF Superconductivity (SRF'09)* (Berlin, Germany). Sept. 2009, pp. 293–296. URL: https://jacow.org/SRF2009/papers/TUPPO039.pdf.

[179] G. Martinet. "Results on Bulk Niobium Surface Resistance Measurement With Pillbox Cavity on TE011 and TE012 Modes". In: *Proc. 19th International Conference on RF Superconductivity (SRF'19)* (Dresden, Germany). June 2019, pp. 833–837. DOI: 10.18429/JACoW-SRF2019-THP003.

[180] C. Z. Antoine, J.-C. Villegier, and G. Martinet. "Study of nanometric superconducting multilayers for RF field screening applications". In: *Applied Physics Letters* 102.10 (Mar. 2013), p. 102603. DOI: 10.1063/1.4794938.

[181] S. Keckert et al. "Commissioning of a New Sample Test Cavity for Rapid RF Characterization of SRF Materials". In: *Proc. 21st International Conference on RF Superconductivity (SRF'23)* (Grand Rapids, MI, USA). June 2023, pp. 410–413. DOI: 10.18429/JACoW-SRF2023-TUPTB013.

[182] T. Shintake. "The Choke Mode Cavity". In: *Journal, Japanese Related, Applied Physics* 31.11A (1992), p. L1567. DOI: 10.1143/JJAP.31.L1567.

[183] T. Shintake H. Matsumoto and H. Hayano. "High Power Test of HOM-Free Choke-Mode Damped Accelerating Structure". In: *Proc. 17th International Linear Accelerator Conference (LINAC'94)* (Tsukuba, Japan). Aug. 1994, pp. 293–295. URL: https://accelconf.web.cern.ch/l94/papers/MO-91.pdf.

[184] T. Shintake et al. "The First Wakefield Test on the C-Band Choke-Mode Accelerating Structure". In: *18th Particle Accelerator Conference (PAC'99)* (New York, NY, USA). Mar. 1999, pp. 3411–3413. URL: https://jacow.org/p99/papers/FRA14.pdf.

[185] P. Goudket et al. "Test cavity and cryostat for SRF thin film evaluation". In: *6th International Particle Accelerator Conference (IPAC'15)* (Richmond, VA, USA). May 2015, pp. 3232–3234. DOI: 10.18429/JACoW-IPAC2015-WEPHA052.

[186] U. Fano. "Effects of Configuration Interaction on Intensities and Phase Shifts". In: *Phys. Rev.* 124 (6 Dec. 1961), pp. 1866–1878. DOI: 10.1103/PhysRev.124.1866.

[187] *Niowave Inc.* https://www.niowaveinc.com/.

[188] G. Jiang et al. "Understanding and optimization of the coating process of the radio-frequency Nb3Sn thin film superconducting cavities using tin vapor diffusion method". In: *Applied Surface Science* 643 (2024), p. 158708. DOI: https://doi.org/10.1016/j.apsusc.2023.158708.

[189] P. Goudket et al. "First Full Cryogenic Test of the SRF Thin Film Test Cavity". In: *18th International Conference on RF Superconductivity (SRF'17)* (Lanzhou, China). July 2017, pp. 644–646. DOI: 10.18429/JACoW-SRF2017-TUPB104.

[190] O. B. Malyshev et al. "The SRF Thin Film Test Facility in LHe-Free Cryostat". In: *19th International Conference on RF Superconductivity (SRF'19)*. June 2019, pp. 612–614. DOI: 10.18429/JACoW-SRF2019-TUP070.

[191] P Duthil. *Material Properties at Low Temperature*. Apr. 2013. DOI: 10.5170/CERN-2014-005.77.

[192] S. S. Courts, P. R. Swinehart, and C. J. Yeager. *A New Cryogenic Diode Thermometer*. Tech. rep. Westerville, OH, 43082, USA: Lake Shore Cryotronics, Inc.

[193] M. Keikha et al. "Microphonic Noise Cancellation in Super-Conducting Cavity". In: *45th Annual Conference of the IEEE Industrial Electronics Society (IECON 2019)*. Oct. 2019, pp. 449–454. DOI: 10.1109/IECON.2019.8927105.

[194] N. Banerjee et al. "Microphonics Studies of the CBETA Linac Cryomodules". In: *Proc. 8th International Particle Accelerator Conference (IPAC'17)* (Copenhagen, Denmark). May 2017, pp. 1138–1141. DOI: 10.18429/JACoW-IPAC2017-MOPVA122.

[195] A. Neumann et al. "Analysis and active compensation of microphonics in continuous wave narrow-bandwidth superconducting cavities". In: *Phys. Rev. ST Accel. Beams* 13 (8 Aug. 2010), p. 082001. DOI: 10.1103/PhysRevSTAB.13.082001.

[196] R. Kleindienst. "Radio frequency characterization of superconductors for particle accelerators". PhD thesis. University of Siegen, Sept. 2017.

[197] Z. Ma. "Ginzton Labs Report No. 5298". PhD thesis. Stanford University, 1995.

[198] *nXDS Scroll Pump Manual*. Edwards. Apr. 2012.

[199] T. Tomaru et al. "Vibration analysis of cryocoolers". In: *Cryogenics* 44.5 (May 2004), pp. 309–317. DOI: 10.1016/j.cryogenics.2004.02.003.

[200] Xiang Guan et al. "Experimental study on vibration reduction of a cryogen-free dilution refrigerator system pre-cooled by a GM cryocooler". In: *Cryogenics* 142 (2024), p. 103911. DOI: https://doi.org/10.1016/j.cryogenics.2024.103911.

[201] *Streamline Series Vector Network Analyzer (A-models) Data Sheet*. Keysight. Apr. 2024.

[202] D. Bafia et al. "Investigation of Frequency Behavior Near Tc of Niobium Superconducting Radio-Frequency Cavities". In: *Proc. 19th International Conference on RF Superconductivity (SRF'19)* (Dresden, Germany). June 2019, pp. 112–117. DOI: 10.18429/JACoW-SRF2019-MOP031.

[203] D. Bafia et al. "Investigating the anomalous frequency variations near T_c of Nb SRF cavities". In: *Proc. 20th International Conference on RF Superconductivity (SRF'21)* (East Lansing, MI, USA). June 2021, pp. 885–892. DOI: 10.18429/JACoW-SRF2021-FROFDV03.

[204] G. Ciovati. "Investigation of the superconducting properties of niobium radio-frequency cavities". PhD thesis. Old Dominion University, Aug. 2005.

[205] B.W. Langley et al. "Magnetic penetration depth measurements of superconducting thin films by a microstrip resonator technique". In: *Review of Scientific Instruments* 62.7 (July 1991), pp. 1801–1812. DOI: 10.1063/1.1142425.

[206] A. Miyazaki and W. Venturini Delsolaro. "Determination of the Bardeen Cooper Schrieffer material parameters of the HIE-ISOLDE superconducting resonator". In: *Superconductor Science and Technology* 32.2 (Jan. 2019), p. 025002. DOI: 10.1088/1361-6668/aaf049.

[207] H. Li et al. "Effects of deposition temperature on structure, residual stress and corrosion behavior of Cr/TiN/Ti/TiN films". In: *Ceramics International* 47.24 (Dec. 2021), pp. 34909–34917. DOI: https://doi.org/10.1016/j.ceramint.2021.09.032.

[208] G. Ciovati and B. Xiao. *WinSuperfit Version 2.0*. Last accessed 01.07.24. 2010.

[209] S. Posen et al. "Ultralow Surface Resistance via Vacuum Heat Treatment of Superconducting Radio-Frequency Cavities". In: *Phys. Rev. Applied* 13 (Jan. 2020), p. 014024. DOI: 10.1103/PhysRevApplied.13.014024.

[210] C. Benvenuti et al. "Study of the Residual Resistance of Superconducting Niobium Films at 1.5 GHz". In: *9th Workshop on RF Superconductivity (SRF'99)* (Santa Fe, NM, USA). Nov. 1999, pp. 550–554. URL: https://jacow.org/SRF99/papers/THA004.pdf.

[211] C. Benvenuti et al. "Study of the surface resistance of superconducting niobium films at 1.5 GHz". In: *Physica C: Superconductivity* 316.3 (1999), pp. 153–188. DOI: https://doi.org/10.1016/S0921-4534(99)00207-5.

[212] W. Singer, A. Ermakov, and X. Singer. *RRR-Measurement Techniques on High Purity Niobium*. Tech. rep. TTC-Report 2010-02, 2010.

[213] A. Romanenko and D. I. Schuster. "Understanding Quality Factor Degradation in Superconducting Niobium Cavities at Low Microwave Field Amplitudes". In: *Phys. Rev. Lett.* 119 (Dec. 2017), p. 264801. DOI: 10.1103/PhysRevLett.119.264801.

[214] *E4416A/E4417A EPM-P Series Power Meters and E-Series E9320 Peak and Average Power Sensors Data Sheet*. Keysight. Apr. 2024.

[215] *Bench Top Digital Multimeter Multicomp Pro MP730424 Datasheet*. Multicomp Pro. Nov. 2013.

[216] *User's Manual Model 331 Temperature Controller*. Lakeshore. May 2009.

[217] The Engineering Toolbox. *Thermal Expansion - Linear Expansion Coefficients*. https://www.engineeringtoolbox.com/linear-expansion-coefficients-d$_9$5.*html*. Last accessed 11.09.24.

[218] O. B. Malyshev et al. "RF surface resistance study of non-evaporable getter coatings". In: *Nuclear Instruments and Methods in Physics Research Section A: Accelerators, Spectrometers, Detectors and Associated Equipment* 844 (2017), pp. 99–107.

[219] T. Higuchi. "Development of a New Surface Treatment Method for Superconducting Cavities Using a New Mechanical Polishing and Electropolishing without Hydrogen Adsorption (Q-Disease)". PhD thesis. The Graduate University for Advanced Studies at KEK, 2002.

[220] P. Kneisel. "Surface Preparation of Niobium". In: *1st International Conference on RF Superconductivity (SRF'80)* (Karlsruhe, Germany). July 1980. URL: https://jacow.org/srf80/papers/SRF80-2.pdf.

[221] D. Bloess. "Chemistry and Surface Treatment". In: *Proc. 2nd International Conference on RF Superconductivity (SRF'84)* (Geneva, Switzerland). July 1984. URL: https://jacow.org/srf84/papers/SRF84-23.pdf.

[222] H. Ito et al. "Influence of furnace baking on Q–E behavior of superconducting accelerating cavities". In: *Progress of Theoretical and Experimental Physics* 2021 (Apr. 2021), 071G01. DOI: 10.1093/ptep/ptab056.

[223] Y. Jung et al. "Analysis of BCP Characteristics for SRF Cavities". In: *Proc. 5th International Particle Accelerator Conference (IPAC'14)* (Dresden, Germany). June 2014, pp. 2549–2551. DOI: 10.18429/JACoW-IPAC2014-WEPRI034.

[224] K. Saito et al. "Superiority of Electropolishing over Chemical Polishing on High Gradients". In: *Proc. 9th International Conference on RF Superconductivity (SRF'97)* (Padova, Italy). Oct. 1997, pp. 795–813. URL: https://jacow.org/SRF97/papers/SRF97D02.pdf.

[225] G. Ciovati et al. "Effect of Low Temperature Baking on Niobium Cavities". In: *Proc. 11th International Conference on RF Superconductivity (SRF'03)* (Lübeck, Germany). Sept. 2003, pp. 562–571. URL: https://jacow.org/SRF2003/papers/WE014.pdf.

[226] M. Wenskat et al. "Vacancy-Hydrogen Interaction in Niobium during Low-Temperature Baking". In: *Sci. Rep.* 10.8300 (May 2020). DOI: 10.1038/s41598-020-65083-0.

[227] C. Pira et al. "Impact of the Cu Substrate Surface Preparation on the Morphological, Superconductive and RF Properties of the Nb Superconductive Coatings". In: *Proc. 19th International Conference on RF Superconductivity (SRF'19)* (Dresden, Germany). June 2019, pp. 935–940. DOI: 10.18429/JACoW-SRF2019-THP041.

[228] A. Carlini and A.-M. Valente-Feliciano. "Electropolishing Copper Substrates for Niobium Thin-Film Coatings in SRF Technologies". In: *APS Meeting Abstracts*. Vol. 3. Oct. 2009.

[229] O. Hryhorenko et al. "An Innovative Approach of Surface Polishing for SRF Cavity Applications". In: *Journal of Manufacturing and Materials Processing* 7.2 (Mar. 2023). DOI: 10.3390/jmmp7020062.

[230] A-M. Valente-Feliciano. "HiPIMS: a New Generation of Film Deposition Techniques for SRF Applications". In: *16th International Conference on RF Superconductivity (SRF'13)* (Paris, France). Sept. 2013, pp. 754–760. URL: https://jacow.org/SRF2013/papers/WEIOA01.pdf.

[231] R. Black and F. Wellstood. *The SQUID Handbook: Applications of SQUIDs and SQUID Systems*. Vol. 2. Wiley, Aug. 2006, pp. 391–440. DOI: 10.1002/9783527609956.ch12.

[232] R. Ries et al. "Superconducting properties and surface roughness of thin Nb samples fabricated for SRF applications". In: *Journal of Physics: Conference Series* 1559.1 (June 2020), p. 012040. DOI: 10.1088/1742-6596/1559/1/012040.

[233] J. Bower et al. "Effect of Surface Roughness on Thin Film Niobium Coatings". In: *IEEE Transactions on Applied Superconductivity* 17.2 (July 2007), pp. 768–771. DOI: 10.1109/TASC.2007.898722.

[234] N. Fairley et al. "Systematic and collaborative approach to problem solving using X-ray photoelectron spectroscopy". In: *Applied Surface Science Advances* 5 (Sept. 2021), p. 100112. DOI: 10.1016/j.apsadv.2021.100112.

[235] R. Ries et al. "Improvement of the first flux entry field by laser post-treatment of the thin Nb film on Cu". In: *Superconductor Science and Technology* 34.6 (Apr. 2021), p. 065001. DOI: 10.1088/1361-6668/abf54d.

[236] N. D. Madsen et al. "Controlling the deposition rate during target erosion in reactive pulsed DC magnetron sputter deposition of alumina". In: *Surface and Coatings Technology* 206.23 (July 2012), pp. 4850–4854. DOI: https://doi.org/10.1016/j.surfcoat.2012.05.070.

[237] A. Godeke. "A review of the properties of Nb_3Sn and their variation with A15 composition, morphology and strain state". In: *Superconductor Science and Technology* 19.8 (June 2006), R68. DOI: 10.1088/0953-2048/19/8/R02.

[238] C. T. Wu, R. T. Kampwirth, and J. W. Hafstrom. "High-rate magnetron sputtering of high T_c Nb_3Sn films". In: *Journal of Vacuum Science and Technology* 14.1 (Jan. 1977), pp. 134–137. DOI: 10.1116/1.569104.

[239] R. Kampwirth, J. Hafstrom, and C. Wu. "Application of high rate magnetron sputtering to the fabrication of A-15 compounds". In: *IEEE Transactions on Magnetics* 13.1 (Aug. 1976), pp. 315–318. DOI: 10.1109/TMAG.1977.1059445.

[240] D. Fonnesu et al. "Influence of the Coating Parameters on the $T_c$of Nb_3Sn Thin Films on Copper Deposited via DC Magnetron Sputtering". In: *Proc. 21st International Conference on RF Superconductivity (SRF'23)* (Grand Rapids, MI, USA). June 2023, pp. 92–95.

[241] S. Leith A. T. Perez Fontenla C. P. A. Carlos et al. "Development and Characterisation of Advanced Coatings for High Energy Physics Applications". In: *Proc. 14th International Particle Accelerator Conference (IPAC'23)* (Venice, Italy). May 2023, pp. 3006–3009. DOI: 10.18429/JACoW-IPAC2023-WEPA150.